The VERITAS Bright Moonlight Program

Sean Griffin
Physics Department
McGill University
Montreal, Quebec
Canada

December 10, 2015

A thesis submitted to
McGill University
in partial fulfilment of the requirements
for the degree of Doctor of Philosophy

Ex Astris, Scientia.

"We choose to go to the moon in this decade and do the other things, not because they are easy, but because they are hard." - John F. Kennedy

Abstract

In gamma-ray astronomy using Imaging Atmospheric Cherenkov Telescopes (IACTs), the amount of observing time available is limited by a number of factors. One such factor is that the telescope cameras are made of photomultiplier tubes (PMTs) and are thus highly sensitive to light. The sky is 100 times brighter during full Moon than new Moon at the wavelengths most relevant to ground-based gamma-ray astronomy; the increased noise in the data stream due to moonlight photons both degrades the data quality and, more importantly, accelerates ageing of the PMTs. Thus, IACTs have historically been limited to observing during clear, moonless nights, or on nights where the moon is only partially illuminated and low in the sky.

There are two approaches to circumventing the limits imposed by moonlight: observing using reduced PMT gains, or by using UV bandpass filters to block out parts of the moonlight spectrum. The *VERITAS* experiment, which consists of four IACTs at the Whipple Observatory in southern Arizona, was typically limited to when the moon was $\lesssim 35\%$ illuminated. Using two new observing modes (one based on each of the aforementioned methods), *VERITAS* is in principle able to observe through the full Moon. The end result is an additional $\sim 29\%$ observing time in a year, of which half has a data quality comparable to standard dark time data for the purposes of many of the *VERITAS* science goals.

In this work, the two observing modes will be thoroughly described. In order to produce analysis tools for the bright moonlight data, extensive data/Monte Carlo comparisons have been made to verify the detector model. Studies of the resulting energy threshold, array sensitivity, and systematic errors are also presented. Finally, the first science results from the *VERITAS* Bright Moonlight Program are presented: the detection of a flare from the blazar *1ES 1727+502*.

Résumé

En astronomie gamma utilisant les réseaux de télescopes Tcherenkov (Imaging Atmospheric Cherenkov Telescopes (IACTs)), le temps disponible pour l'observation est limité par un certain nombre de facteurs. Par exemple, les caméras du télescope sont composées de tubes photomultiplicateurs (PMT) et donc très sensibles à la lumière. Dans les longueurs d'ondes les plus pertinentes pour l'astronomie gamma, le ciel est 100 fois plus lumineux durant la pleine lune que pendant la nouvelle lune. L'augmentation du bruit dans les données en raison de photons au clair de lune dégrade la qualité des données et, plus important encore, accélère le vieillissement des PMT. Ainsi, les IACTs ont historiquement été contraints d'observer uniquement durant les nuits claires, sans lune, ou durant les nuits où la lune est seulement partiellement illuminée et basse dans le ciel.

Il existe deux approches pour contourner les limites imposées par le clair de lune: réduire les gains des PMT, ou utiliser des filtres à ultraviolet pour bloquer certaines parties du spectre électromagnétique. L'observatoire *VERITAS*, qui exploite quatre IACTs à l'Observatoire Whipple dans le sud de l'Arizona, est généralement limité à des lunes illuminées à un maximum de 35%. Grace à l'utilisation de ces deux nouveaux modes d'observation, *VERITAS* est en principe maintenant capable d'observer même pendant la pleine lune, bien qu'en pratique les quelques jours aux alentours de la pleine lune sont généralement réservés à l'entretien du télescope. Le résultat final est une augmentation de 29% du temps d'observation par année, dont la moitié est à peu près égale en qualité aux standards de période sombre en ce qui concerne la plupart des objectifs scientifiques de *VERITAS*.

Dans ce travail, les deux modes d'observation sont décrits en détails. Afin de produire des outils d'analyse pour les données «clair de lune», de nombreuses comparaisons entre les données et des simulations Monte Carlo ont été faites pour vérifier le modèle de détecteur. Les études du seuil d'énergie résultant, la sensibilité de l'observatoire et les erreurs systématiques sont également présentées. Enfin, les premiers résultats scientifiques du programme

d'observation en clair de lune sont présentés: la détection d'une éruption provenant du blazar *1ES 1727+502*.

Acknowledgements

During my time as a graduate student, I have had the opportunity to work with some fantastic and interesting people. The following is a non-exhaustive list of those who have helped me over the past few years. I apologize in advance should anyone be omitted.

My supervisor, D. Hanna, took a chance on a young undergraduate who had mediocre grades but was quite motivated and interested in *VERITAS*. Thanks to him, I now know (amongst other things) that when producing multiple plots I should always use the same scales on the axes, how to tell when there's something wrong with error bars, and that when you're unplugging a high voltage cable, only use one hand in case you get electrocuted. I am very grateful for the opportunities that he has given me, the confidence that he has had in my abilities, and the skills he has helped me develop.

Thanks to K. Ragan for his assistance over the past few years and for effectively becoming my second supervisor. His help, in particular in the last months of producing this work, is greatly appreciated.

Thanks to J. Holder who allowed me to work with him in Delaware for the better part of six months (and paid to bring me back once my fellowship had ended), who allowed me to effectively lead a new project, and who was always trying to push me out of my comfort zone and to be more confident in my abilities.

This work would not have been possible without the help of R. Bird, with whom I have worked very closely over the past two years. The many nights of drinking fancy beers have helped produced this work.

I must thank A. McCann and M. McCutcheon for teaching me everything I know about life as a graduate student in *VERITAS*, and helping me through some of the more difficult periods of graduate school. My office mates (past and present) S. Archambault, A. MacLeod, T. Lin, and J. Tyler have all helped spark interesting discussions.

B. Zitzer has been a big help, in particular by teaching me about the science done in

gamma-ray astronomy. I must also thank D. Staszak, for convincing me to relax and for having faith that I will make it through this difficult phase in my career. A. O'Faoláin de Bhróithe has helped me understand more than a few things, and never made me feel bad about not knowing some bit of knowledge that most people consider commonplace. Thanks also to A. Furniss and M. Cerruti for helping me understand blazar physics.

Thanks to the crew at the Whipple Observatory, Jack, George, Danny, and Caesar, for keeping things light and the atmosphere pleasant.

I must remark that I have had some phenomenal teachers over the past twenty five years of schooling who have always encouraged me to follow my passion and pursue a career as a scientist.

Finally, I would be remiss if I did not acknowledge the unquantifiable support that I have received from my friends, family, and loved ones that has allowed me to get to this point in my life.

This research is supported by grants from Natural Sciences and Engineering Research Council of Canada (NSERC), Centre de recherche en astrophysique du Québec (CRAQ), Fonds de recherche du Québec – Nature et technologies (FRQNT), and the McGill Graduate office. In addition, *VERITAS* is supported by grants from the U.S. Department of Energy Office of Science, the U.S. National Science Foundation and the Smithsonian Institution. We acknowledge the excellent work of the collaborating institutions in the construction and operation of the instrument.

The *VERITAS* Collaboration is grateful to Trevor Weekes for his seminal contributions and leadership in the field of VHE gamma-ray astrophysics, which made this study possible.

List of Original Contributions

The following is a non-exhaustive list of projects and contributions to *VERITAS* performed by the author during his tenure as a PhD-level graduate student.

Work Pertaining Directly to this Thesis

The main focus of this thesis, the *VERITAS* Bright Moonlight Program, required intensive work with the *VERITAS* simulations and analysis packages. The author produced detector configuration files and analysis tools for the collaboration to use with the new data products. The author worked very closely with another *VERITAS* collaborator, R. Bird from University College Dublin, on this project. Each step in the work has been rigorously cross-checked by both parties. The author co-wrote the proposals for calibration time such that the new detector configuration could be well-understood.

The author spent a considerable amount of time writing software to model the optical effects of the UV filters on the *VERITAS* detector in order to adjust the detector model. This work was essential in understanding the UV filter detector model.

The author also contributed the primary analysis and *VERITAS*-related text to the first publication [1] resulting from the Bright Moonlight Program, a summary of which is given at the end of this thesis.

A publication pertaining to the Bright Moonlight Program is currently being prepared; both the author of this thesis and R. Bird are the lead authors.

Work Away from the University

Since 2009, the author has spent over 250 days at the *VERITAS* site. This was done in the context of observing (usually as the shift leader or "czar") or often as part of the day crew. The author has participated in a number of significant upgrades to the telescopes, specifically

the relocation of a telescope in 2009 (during his M.Sc.) and the upgrade of the telescope cameras in 2012.

The author was the recipient of a bursary sponsored by the FRQNT that allowed him to work at the University of Delaware with Prof. J. Holder from late October 2013 to May 2015. During this trip, the author led the design and construction of a new, ultra-low cost prototype gamma-ray telescope known as "El Cheapo". During this trip, the author spent two weeks working at the NASA Goddard Spaceflight Centre working on the telescope pointing system with Dr. J. Perkins.

Presentations

The author gave several talks at yearly CRAQ meetings on the status of *VERITAS*, novel calibration methods, or other projects (such as El Cheapo). The author has also presented his research regularly at *VERITAS* collaboration meetings; this was vital to the development of the Bright Moonlight Program.

The work on a novel telescope relative calibration method (not discussed in this thesis) were presented as a poster at the 2013 Canadian Association of Physicists meeting (Montreal, Canada) and at the International Cosmic Ray Conference (Rio de Janeiro, Brazil) as a poster the same year.

The author represented the *VERITAS* collaboration at the *Fermi-HAWC-VERITAS* Analysis Workshop at the University of Maryland in February 2014 and gave a talk on *VERITAS* calibration methods.

At the 2014 Canadian Association of Physicists meeting (Sudbury, Canada) the author gave a presentation on the *VERITAS* upgrade and bright moonlight program; this talk won the award for best student presentation in the Division of Instrumentation and Measurement Physics (DIMP).

The work in this thesis was presented at the 2015 International Cosmic Ray Conference (The Hague, Netherlands) as a contributed talk.

Awards

2014–2015	Graduate Excellence Award ($5,000)
2014 / 06	CAP DIMP Prize for Best Student Oral Presentation ($200)
2013–2014	FRQNT Stage International ($14,650)
2013–2014	Alexander McFee Fellowship ($10,000)
2012–2013	Molson & Hilton Hart Fellowship ($10,000)
2012-2015	Travel and mobility awards totalling $9,050

Conventions

In this thesis, definitions have been colored in green and the underlying assumptions of any statements have been colored blue. This thesis makes extensive use of clickable cross-references and citations.

The bibliography has been designed to allow articles, websites, and technical documents to be easily accessed via the [ADS] and [LINK] fields included for most bibliography entries.

Some figures have been acquired via private communication with *VERITAS* collaboration members. In such cases, the creator of said figure has been indicated.

There are no published references for some of the software packages used in this thesis. In such a case, a website URL has been used to refer to a public website containing either the source code or documentation.

Contents

List of Figures

List of Tables

Chapter 1

Introduction

"The beginning in every task is the chief thing."

Plato, *The Republic*

1.1 Gamma-Ray Astronomy

Gamma-ray astronomy is one of the youngest fields of astronomy owing to the fact that astrophysical gamma rays are absorbed by the Earth's atmosphere. Thus, the field could not develop until detectors could be deployed outside of the atmosphere (either on high-altitude balloons or space-based instruments). The field of ground-based gamma-ray astronomy is said to have been started with the 1958 paper, "*On Gamma-ray Astronomy*" by P. Morrison [2]. It was postulated in the early 1960s that the Cherenkov light from astrophysical gamma rays interacting with the Earth's atmosphere could be used as a probe into this energy regime.

The first detection of very high energy (VHE) ($E \gtrsim 100$ GeV) gamma rays from an astrophysical source (the Crab Nebula, which has since become the standard candle in the field) was made by the Whipple Collaboration in 1989 [3]. At the time, the Whipple 10-m telescope, shown in Figure 1.1, had been operating for 20 years in various configurations at the Whipple Observatory on Mount Hopkins in Arizona. Since then, significant strides have been made in the field of gamma-ray astronomy, and the number of sources is now over 150 [4].

At the time of writing, there are three major ground-based observatories operating. In the southern hemisphere is the High Energy Stereoscopic System (*H.E.S.S.*), which operates five telescopes (four 12-m telescopes and one 28-m telescope) in Namibia [5]. In the northern

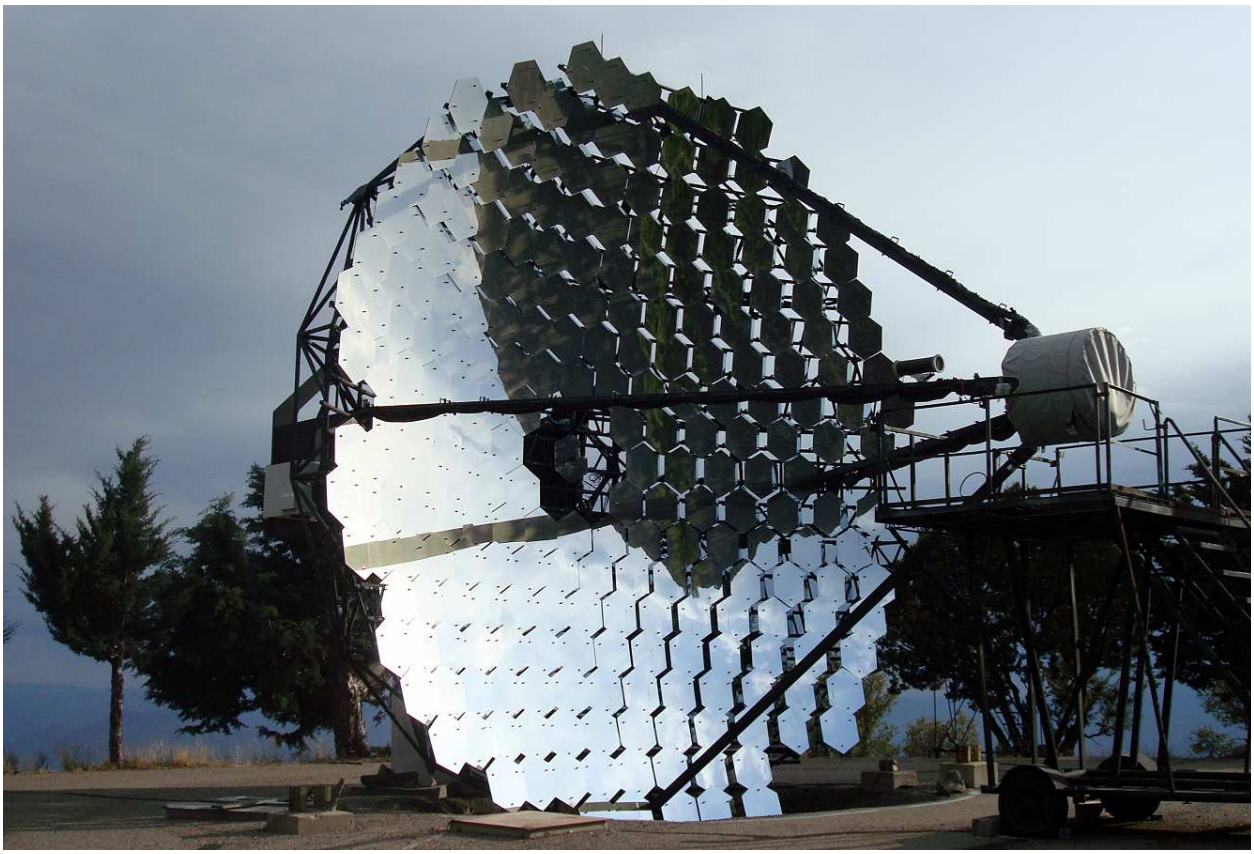

Figure 1.1: The Whipple 10-m telescope in 2010. A 10-m tessellated reflector focuses light onto a photomultiplier camera. This picture was taken shortly before the 10-m was decommissioned after $\sim$ 40 years of service.

hemisphere are two observatories. The first is the Major Atmospheric Gamma Imaging Cherenkov (*MAGIC*) array, which operates two 17-m telescopes in the Canary Islands [6]. The second is the Very Energetic Radiation Imaging Telescope Array System (*VERITAS*) [7], which operates four 12-m telescopes in the southern US. Images of the three observatories are shown in Figure 1.2. *VERITAS* is the experiment used in this thesis and will be discussed in Chapter 3.

1.2 The Moon

In general, after factoring in effects like poor weather (which on average removes $\sim$ 50% of the observing time) there are only $\sim$ 1000 hours of observing time per year available to experiments like *VERITAS*. The gamma-ray fluxes from astrophysical sources are in general very low; there are only a handful of sources with fluxes strong enough to be detected in less than an hour. Due to this, observing campaigns of gamma-ray source candidates are

Figure 1.2: **Top**: The *H.E.S.S.* array. Image credit: *H.E.S.S.* collaboration. **Middle**: The *MAGIC* telescopes. The smaller telescope to the right is the *FACT* telescope [8], a prototype gamma-ray telescope. Image credit: *MAGIC* collaboration. **Bottom**: The *VERITAS* array. Image credit: *VERITAS* collaboration.

typically of order 50 hours long[1], or longer depending on the specific science goals of the measurement, which equates to enough time to observe ~ 20 targets a year. This effectively puts a hard limit on the science throughput of the experiment. In practice, more sources are observed since some science goals do not require exposures to be as deep as others, but this is not always the case. Thus, additional observing time allows for more targets to be observed, or measurements requiring deep exposures to be made (such as measurements of the extragalactic background light, discussed in Section 10.3).

All current- and past-generation gamma-ray telescopes use cameras which are extremely sensitive to light, to the level where too much light can destroy the detector. The Moon (Figure 1.3) can brighten the sky significantly (at some wavelengths by two orders of magnitude, as will be shown in Chapter 5). Thus, historically, ground-based gamma-ray observatories were restricted to clear, moonless nights. However, this did not stop the gamma-ray astronomy pioneers from attempting to develop new methods of increasing the amount of time available for observing. Several methods, including the use of solar-blind cameras, liquid UV-transparent filters and reducing camera sensitivity by underpowering the camera elements have been tried in the past; a discussion of these historical attempts will be given in Chapter 6. *VERITAS* has also adopted two new observing modes along the same lines as these; the implementation and results of the new observing modes are the main focus of this work.

1.3 Thesis Overview

In Chapter 2, the principles behind ground-based gamma-ray astronomy are discussed as is a history of both space-based and ground-based gamma-ray observatories. Chapter 3 describes the *VERITAS* experiment and the technology behind ground-based gamma-ray astronomy. Chapter 4 describes the ideas behind the analysis of VHE gamma-ray data analysis and provides a brief discussion of one of the *VERITAS* analysis packages.

The remaining chapters are where the author provided the majority of the original contributions in this work. Chapter 5 provides a quantitative overview of the different contributing components to the brightness of the night sky. Chapter 6 describes the *VERITAS* observing strategy and provides an overview for the content in Chapters 7 to 9 which contain the main results of this thesis. The results of a standard *VERITAS* analysis are compared to the two novel observing modes designed to allow *VERITAS* to operate under bright skies. Finally, the applications and first science results of the bright moonlight program are presented in Chapter 10.

[1] The 50 hours originates from the amount of time any given source spends at small zenith angles ($z \lesssim 30°$) under dark skies.

Figure 1.3: The full Moon. Image credit: "FullMoon2010" by Gregory H. Revera. Licensed under CC BY-SA 3.0 via Wikimedia Commons.

Chapter 2

Gamma-Ray Astronomy

The Earth's atmosphere is opaque to gamma rays. Thus, gamma-ray astronomy requires either putting a detector in space (which is both costly and subject to severe size restrictions) or constructing a ground-based observatory which takes advantage of the physics that occurs when a high-energy gamma ray interacts with atoms in the Earth's atmosphere. In this chapter, the principles of ground-based gamma-ray astronomy are discussed with a description of current and past observatories, followed by a brief history of space-based observatories and the current state of the field.

2.1 Ground Based

2.1.1 Air Showers

2.1.1.1 Gamma-Ray Induced Air Showers

When a gamma ray (the primary, that is, the original particle of astrophysical origin) enters the Earth's atmosphere, it quickly interacts with the electric field of atmospheric nuclei and converts into an electron and a positron:

$$\gamma_{\mathrm{HE}} + p_{\mathrm{atmosphere}} \rightarrow p'_{\mathrm{atmosphere}} + e^+ + e^-. \tag{2.1}$$

This is called Bethe-Heitler pair production [9] and is the dominant reaction for gamma rays with energies greater than ~ 10 MeV. The equation for pair production can also be written as

$$\gamma_{\mathrm{HE}} + \gamma_{\mathrm{atmosphere}} \rightarrow e^+ + e^- \tag{2.2}$$

where the second photon is a virtual photon from the interaction in the Coulomb field of the nucleus.

The electrons and positrons will continue to propagate through the atmosphere and produce high energy photons via bremsstrahlung radiation. Over a characteristic length scale known as a radiation length, an electron (or positron) will have its energy reduced to $1/e$ of its original energy via bremsstrahlung radiation. The radiation length is given to good approximation by [10, Equation 6.76]

$$\xi_0 = \frac{716.4 \cdot A}{Z(Z+1)\ln(287/\sqrt{Z})} \text{ g cm}^{-2} \tag{2.3}$$

where Z and A are the atomic and mass numbers of the medium, respectively. The units here are consistent with a density multiplied by a path length; the main idea is that the radiation length has more to do with the amount of material being traversed than an actual distance. The vertical thickness of the atmosphere in these units is ~ 1000 g cm^{-2} and the radiation length in air is 37.1 g cm^{-2} [11]. Hence, the atmosphere is ≈ 27 radiation lengths thick.

For a sufficiently energetic primary, the secondary photons will *also* have enough energy to pair produce. The new electron/positron pairs also emit bremsstrahlung photons and the process continues in a cascade called an air shower. This type of air shower is referred to as an electromagnetic (EM) air shower. A cartoon of an EM air shower is given in Figure 2.1. The process continues until the ionization losses and radiation losses become equal. This point is called the shower maximum which is where the maximum number of particles (N_{max}) are present, after which the cascade begins to die off. The height of shower maximum is denoted H_{max}.

2.1.1.2 Cosmic-Ray Induced Air Showers

The above treatment can also be applied to cosmic ray (CR) primaries (*i.e.* charged particles). The cosmic ray flux is dominated by protons, with a smaller component ($\sim 9\%$) of alpha particles and about 1% heavy elements such as iron. In the case of cosmic rays, the air shower development is not purely electromagnetic but rather hadronic in nature and is thus referred to as a hadronic air shower.

As the cosmic ray collides with the upper atmosphere, it interacts and the production of π mesons dominates. These decay into other particles causing a cascade similar to the one

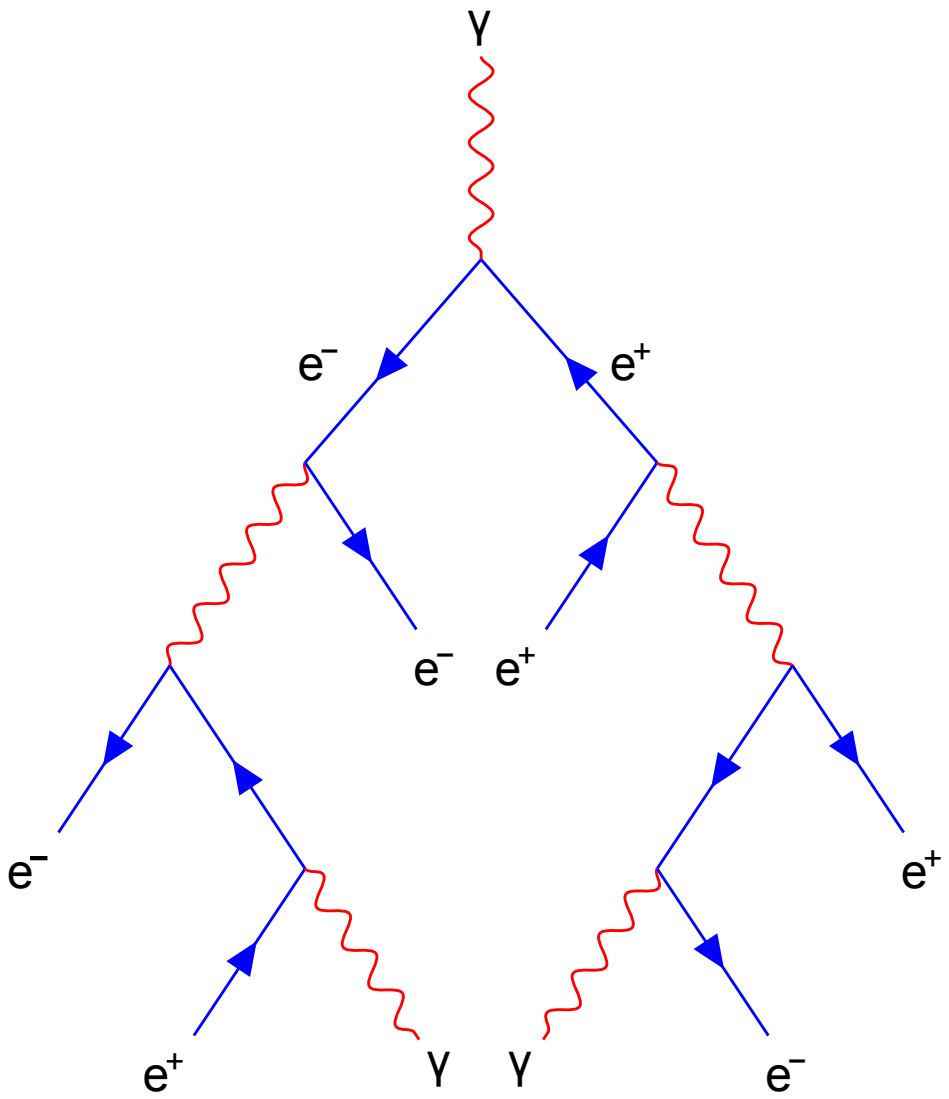

Figure 2.1: A cartoon of a gamma-ray-induced air shower. The gamma-ray primary undergoes pair production, and the subsequent particles emit a high energy photon via bremsstrahlung radiation due to the presence of molecules in the atmosphere. These photons then go on to pair produce, and the process repeats.

mentioned above. The different interactions dominating in a hadronic air shower are:

$$\begin{aligned}
p + p \;&\rightarrow\; \pi \;+\; \chi \\
&\quad\; \pi^0 \;\rightarrow\; \gamma \;+\; \gamma \\
&\quad\; \pi^+ \;\rightarrow\; \mu^+ \;+\; \nu_\mu \\
&\qquad\quad\; \mu^+ \;\rightarrow\; e^+ \;+\; \nu_e \;+\; \bar{\nu}_\mu \\
&\quad\; \pi^- \;\rightarrow\; \mu^- \;+\; \bar{\nu}_\mu \\
&\qquad\quad\; \mu^- \;\rightarrow\; e^- \;+\; \bar{\nu}_e \;+\; \nu_\mu .
\end{aligned} \tag{2.4}$$

Other interactions, such as proton and neutron production are also possible, but not explicitly listed here. In addition to this, charged pions will often scatter before decaying.

The first term is known as neutral pion decay, where the π^0 decays almost immediately ($t \sim 9 \times 10^{-17}$ s) into two photons (this is the main decay; other decays are at least 90 times less likely to occur [12]). The two produced gamma rays go on to produce electromagnetic showers.

The second and third decays are charged pion decays. The charged pion decay products are neutrinos and muons (for more information see e.g. [13]), the latter of which can decay into electrons (or positrons) and another neutrino. A cartoon of these interactions is given in Figure 2.2.

There are also cosmic-ray electrons which produce an effectively irreducible background for ground-based gamma-ray observatories, since an electron will produce an electromagnetic shower. Technically, it should be possible to identify *some* of the electrons because on average they interact one half radiation length before gamma rays do (see [14]). However, since the cosmic ray electron flux is low (100 times less than other cosmic ray primaries) and isotropic, cosmic ray electrons are largely ignored. It is possible that in some energy ranges they will become the limiting factor for the next generation of gamma-ray observatories; with advanced analysis techniques and large arrays providing many views of the same air shower, the ability to separate hadronic showers from electromagnetic showers will mean that cosmic ray electrons will constitute an irreducible background, since they look like gamma-ray-induced showers.

2.1.1.3 Differences Between Cosmic-Ray and Gamma-ray Initiated Showers

Gamma-ray initiated showers are more compact than hadron-initiated ones. This is because the electron/positron pairs are strongly beamed in the direction of the primary. The propagation of electrons is dominated by Coulomb scattering and the pair production products do not generally acquire much transverse momentum: the cascade has a length of ~ 10 km but is only a few 10s of metres wide. In contrast, components of hadronic showers

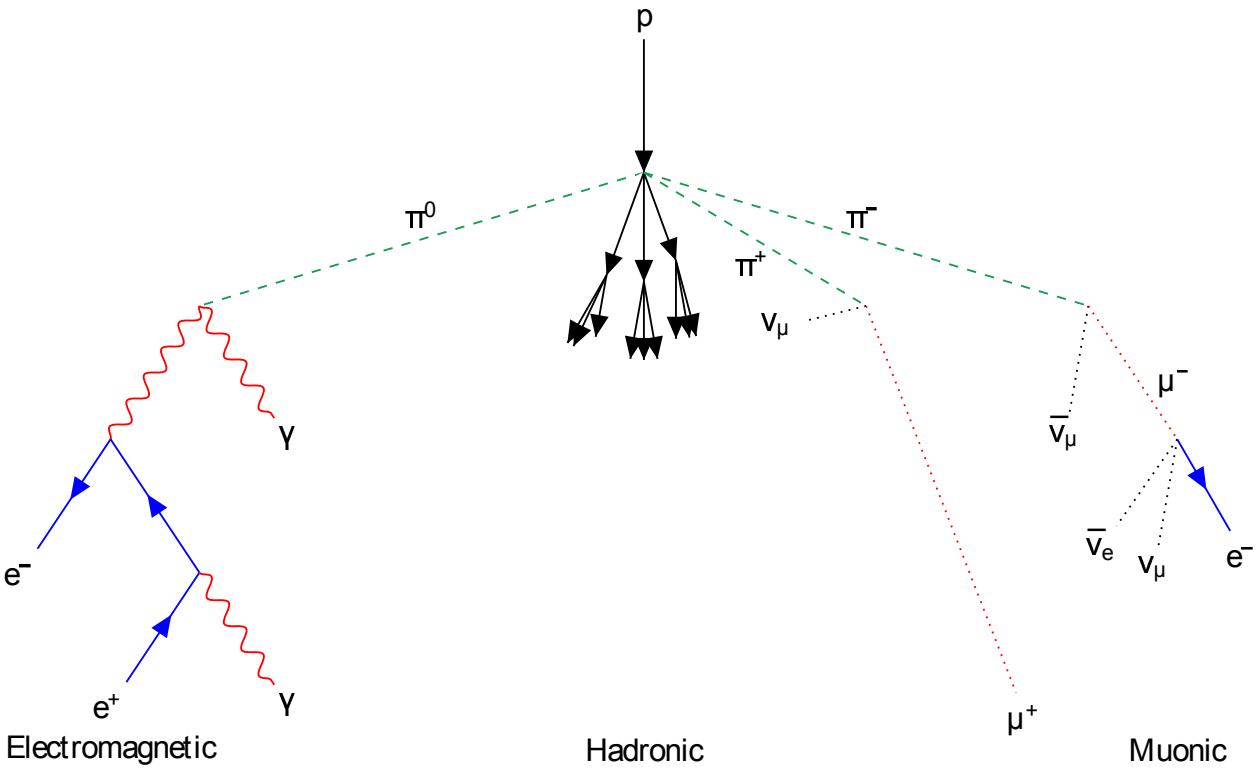

Figure 2.2: A cartoon of a hadron-induced air shower with the various shower components indicated. An important difference between hadronic and purely electromagnetic air showers is that the components in a hadronic shower can have large transverse momenta, producing an air shower which is largely asymmetric. This image is not by any means to scale; features have been exaggerated to aid the eye.

can have considerable transverse momentum. To demonstrate this, results of air shower simulations for a gamma ray, a proton, and an iron nucleus are shown in Figure 2.3. The hadronic showers are much more extended than the gamma-ray shower. When performing an analysis, this fact becomes an important feature for rejecting background events.

2.1.2 Cherenkov Radiation

Cherenkov radiation, sometimes spelled Čerenkov radiation, is electromagnetic radiation produced by a dielectric medium when a charged particle moves through it faster than the speed of light in said medium. It is named after Pavel A. Cherenkov who shared the 1958 Nobel Prize in Physics for its discovery (made in 1934) with Ilya Frank and Igor Tamm who explained the phenomenon.

For a dielectric medium with an index of refraction n, the speed of light in the medium is reduced to c/n. As a charged particle moves through the medium with speed v its electric

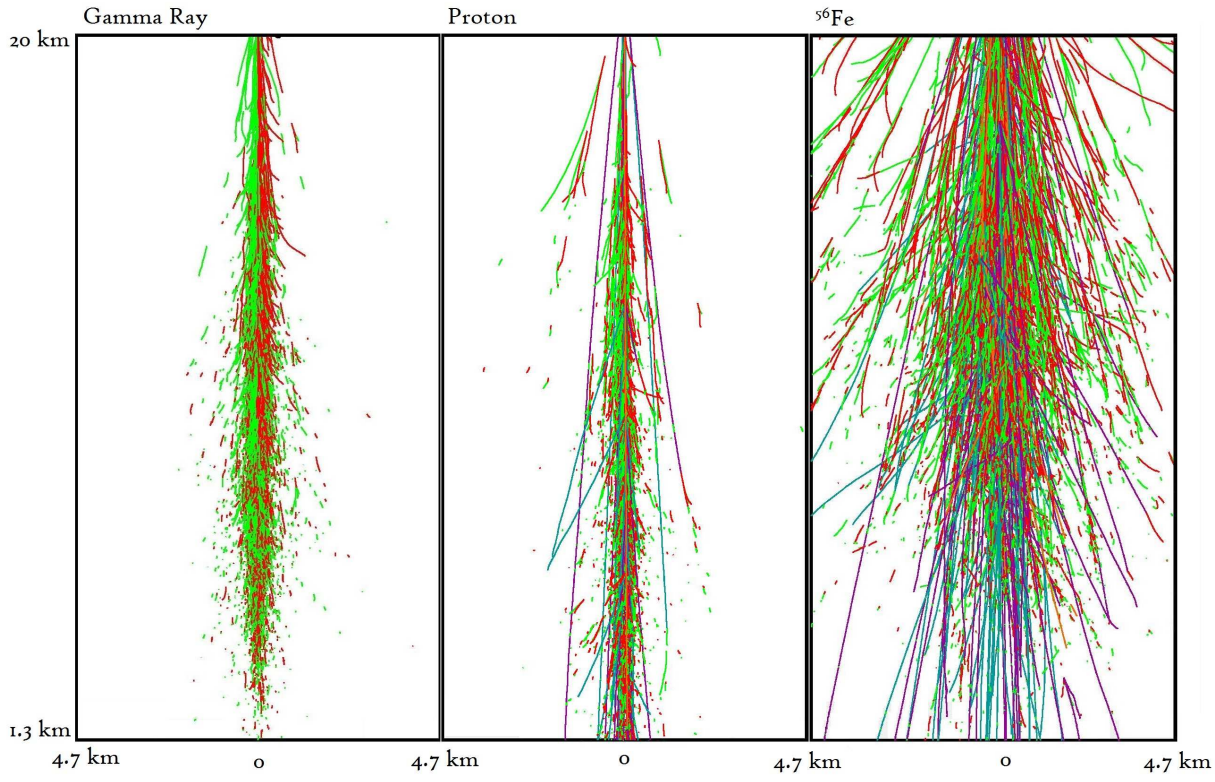

Figure 2.3: Simulated tracks for charged particles in air showers induced by three different primaries with energy $E = 10^5$ GeV. The different colors correspond to different kinds of particles. Electrons (positrons) are shown in green (red), positive (negative) muons are shown in purple (turquoise), and positive (negative) pions are given in maroon (dark green). Image credit: M. Kertzmann

field propagates at c/n in spherical shells around the particle. This has the effect of polarising nearby atoms. As the particle continues to propagate through the medium, the atoms in the medium depolarise. If $v \ll c/n$, the polarisation is roughly symmetric and there is no net electric field. However, if $v > c/n$, the electric field of the charged particle propagates more slowly than the particle itself. This has the effect of a net induced dipole in the medium trailing the charged particle. When the medium relaxes and depolarises, it emits photons for which there is constructive interference at a particular angle, the Cherenkov angle (defined below), and coherent radiation, known as Cherenkov radiation, is produced along a wavefront trailing the particle.

The Cherenkov emission constructively interferes in a cone whose geometry is defined in

Figure 2.4. The opening angle of the cone is given by

$$\cos\theta = \frac{(c/n)t}{vt} = \frac{1}{n\beta}, \tag{2.5}$$

where $\beta \equiv v/c$ and t is time. It follows that for a given refractive index, there is a threshold velocity $\beta_t = 1/n$ below which there is no Cherenkov emission. Also, the frequency dependence of n limits Cherenkov emission to UV and lower frequencies: $\beta_t = 1/n$ can only be satisfied for $n > 1$ since at high frequencies $n < 1$ (as is the case for, e.g. x-rays). Also, it follows that there is a maximum Cherenkov angle $\cos(\theta_{\max}) = 1/n$.

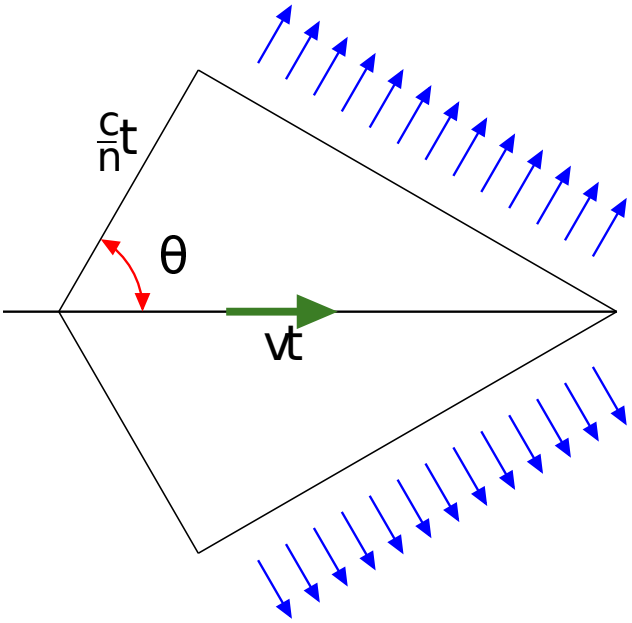

Figure 2.4: The geometry of Cherenkov emission (the angles have been exaggerated). The green arrow represents the velocity vector of the ultra-relativistic particle. θ is the Cherenkov angle.

The number of photons emitted by a charged particle (with charge Ze) per unit path length per unit wavelength is

$$\frac{d^2N}{dxd\lambda} = \frac{2\pi\alpha Z^2}{\lambda^2}\left(1 - \frac{1}{\beta^2 n^2(\lambda)}\right). \tag{2.6}$$

where α is the fine structure constant. There is a strong dependence on λ; Cherenkov radiation comprises mostly UV and blue photons, with some of the emission at longer wavelengths.

At blue/UV wavelengths, $n(\lambda)$ is essentially constant (for measurements taken at sea level see [15]), thus, for the specific case for an electron, the total number of Cherenkov photons with wavelengths $\lambda_1 < \lambda < \lambda_2$ produced after the electron has traversed a path l, is

$$N = 2\pi\alpha l\left(\frac{1}{\lambda_1} - \frac{1}{\lambda_2}\right)\left(1 - \frac{1}{\beta^2 n^2}\right). \tag{2.7}$$

Based on this, it is possible to calculate roughly how many Cherenkov photons will be produced in an air shower and determine roughly what the flux on the ground will be. For a highly energetic primary, $\beta \approx 1$ for the majority of the shower and for a 100 GeV shower, the maximum number of particles occurs at about 10 km above sea level [11]. At this altitude, the air has a refractive index $n \approx 1.000\,096$ [16]. Thus, the Cherenkov cone opening angle (as determined by Equation 2.5) is $\theta \approx 0.8°$. Note that at sea level (*i.e.* where the air is more dense and n is larger) θ also increases (e.g. the Cherenkov angle is $\theta \approx 1.3°$ at sea level). The Cherenkov photon densities, and several other useful numbers, for several gamma-ray energies is given in Table 2.1.

Energy (TeV)	H_{max} (km)	N_{max}	ρ (photons m^{-2})
0.01	12.8	1.6×10^1	2.7×10^{-1}
0.1	10.3	1.3×10^2	4.6×10^0
1	8.4	1.1×10^3	7.4×10^1
10	6.8	1.0×10^4	1.1×10^3
100	5.5	9.3×10^4	1.6×10^4
1000	4.4	8.6×10^5	1.9×10^5

Table 2.1: Table of the height of shower maximum H_{max}, the maximum number of particles in the shower N_{max}, and the Cherenkov photon density at sea level ρ. The data in this table are taken from Table 2.1 in [11].

Cherenkov photons from an air shower all arrive at the ground within a few nanoseconds of each other in a "flash" of light. Due to the fact that the shower secondaries are propagating faster than the speed of light, the first photons to hit the ground are the last ones to be produced – one is seeing the end of the air shower before the beginning.

By placing a telescope within the light-pool and sampling the air shower, one can gain information about the primary which created it. This is the principle of the Imaging Atmospheric Cherenkov Technique (IACT); a cartoon of the principle is given in Figure 2.5. In essence, the atmosphere is being used as a giant calorimeter: the telescope is used to measure the amount of energy deposited by actively imaging the Cherenkov flash from air showers. Having multiple telescopes yields a stereoscopic view of the same shower, thus providing more information from which to reconstruct the information pertaining to the primary. Details on the acquisition and analysis of such data will be presented later in Chapters 3 and 4, respectively.

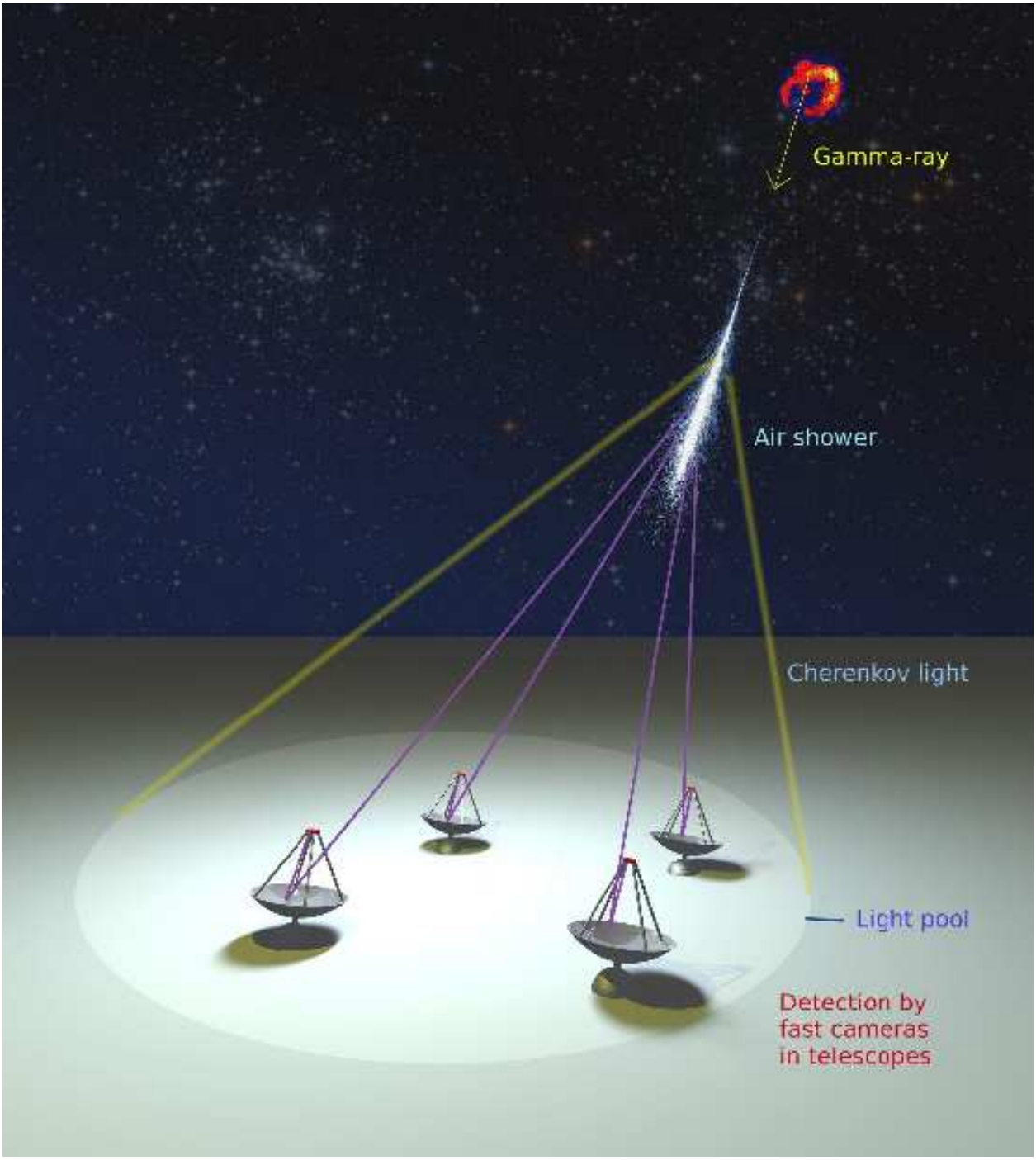

Figure 2.5: By using multiple telescopes, spaced such that they are all within the expected Cherenkov light pool from a gamma-ray primary, it is possible to make stereoscopic measurements of the same air shower, which greatly increases sensitivity and resolution. Image credit: Figure 4.1 in [17]

2.1.3 Discerning Gamma-rays from Cosmic Rays

It was stated in Section 2.1.1.3 that air showers are much more compact for gamma-ray primaries than hadron primaries. This translates into very different distributions in Cherenkov photons on the ground. A cartoon illustrating some of the differences is given in Figure 2.6. The distribution of Cherenkov photons at the ground level for three different simulated primaries (photon, proton, and iron nucleus) can be seen in Figure 2.7. On average, hadronic showers produce "clumpier" and less uniform distributions of Cherenkov photons on the ground; this means that an image of a hadronic shower will look different from a photon-induced one. Thus, imaging air showers and quantifying their shapes provides a powerful discriminator when separating gamma rays from cosmic rays in the analysis (this will be discussed in Chapter 4).

2.1.4 History of IACT Telescopes

It has already been presented that the first very high energy (VHE) gamma ray source detection was by made by the *Whipple* collaboration which operated a 10-m telescope at the Whipple observatory in southern Arizona [19]. The 10-m operated for over 40 years (in one capacity or another), and was finally decommissioned in 2012 and dismantled in 2013, marking the end of an era in gamma-ray astronomy.

The next major experiment was *HEGRA*. The *HEGRA* collaboration pioneered stereoscopic observations of air showers [20]. *HEGRA* operated in the Canary Islands (at what is now the *MAGIC* site) from 1992 to 2002. The first *HEGRA* telescope (a prototype, CT1, with a smaller mirror) was installed in 1992, and the second was installed in 1993 (CT2). Between 1995 and 1996, four more telescopes were installed (CT3-CT6). CT2-CT6 were identical[1], with a collection area of 8.5 m^2 (equivalent of a 1.6-m diameter telescope). They were arranged in a square with 100 m to a side and a fifth telescope in the centre. *HEGRA* was decommissioned in the early 2000s when the manpower for the construction of the *H.E.S.S.* and *MAGIC* telescope arrays was required.

The early 21st century saw the birth of three IACT arrays: *H.E.S.S.* (2002 for the *H.E.S.S.*-I telescopes, 2012 for *H.E.S.S.*-II), *MAGIC* (2004 for *MAGIC*-I, 2009 for *MAGIC*-II), and *VERITAS* (full array operations in 2007), which have already been presented.

The next generation of ground-based gamma-ray observatory is known as the Cherenkov Telescope Array (*CTA*) [21] which is expected to be a a factor of 10 better than current-generation arrays. CTA will operate telescopes with a number of sizes[2]:

[1] After upgrades were made to CT2.

[2] At the time of writing, the number of CTA telescopes has not yet been finalised.

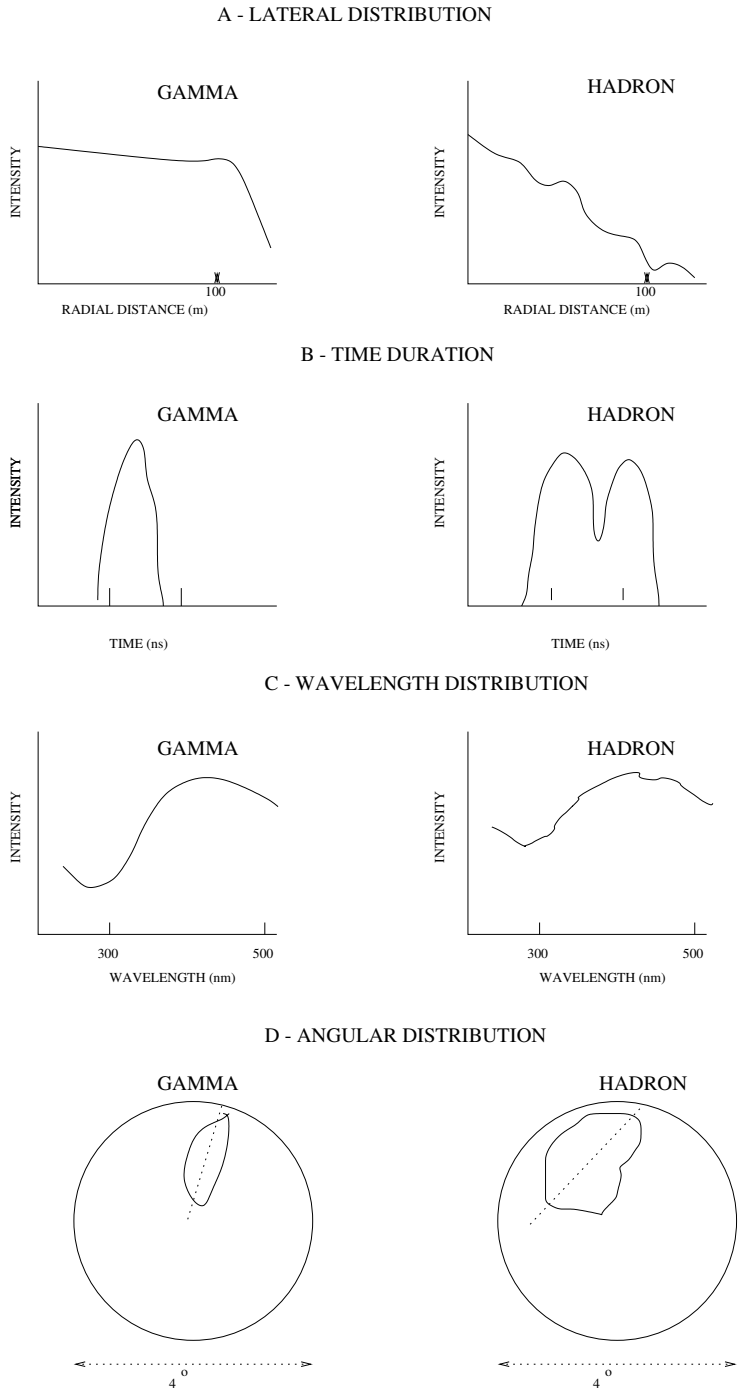

Figure 2.6: Cartoon of the different distributions pertaining to Cherenkov emission for a number of parameters for gamma rays (**left**) and hadrons (**right**). The distributions for hadrons are in general less uniform. Image credit: Figure 2.8 in [11].

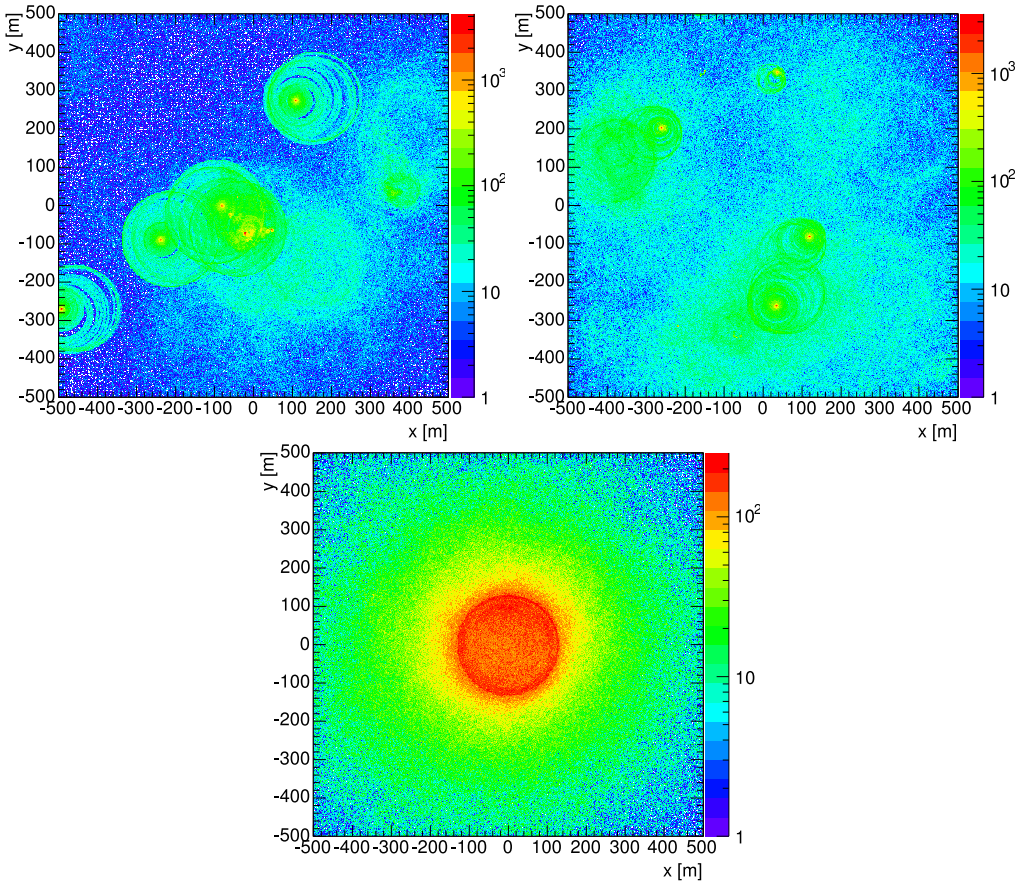

Figure 2.7: Simulated Cherenkov photon densities on the ground for three different primaries: a 500 GeV proton (**top left**), a 500 GeV iron nucleus (**top right**) and a 300 GeV gamma ray (**bottom**). The photon density for the gamma ray is largely uniform within the Cherenkov light pool (radius 120 m), whereas the hadronic showers are asymmetric and contain structures due to (e.g.) the Cherenkov emission from muons (which manifests as rings). Image credit: Figure 3-7 in [18].

- 4 large size telescopes: 23-m diameter telescopes designed to have an energy threshold of 20 GeV.
- 24 mid size telescopes: 10 to 15-m diameter telescopes. These will be most sensitive between 100 and 1 TeV.
- 72 small size telescopes: 4 to 6-m diameter telescopes with a large field of view and sensitivity above 10 TeV.

At the time of writing, there are more than 1000 people working on CTA; it can almost be thought of as the Large Hadron Collider of gamma-ray astronomy. As of the time of writing, prototype telescopes and cameras are being commissioned and the array is expected to come on-line at some point in the late 2010s.

2.1.5 Pointed versus Non-Pointed Instruments

Non-pointed instruments operate very differently than pointed (*i.e.* telescope-based) instruments. Non-pointed instruments generally fall into the category of particle detectors as they do not image the Cherenkov light from the shower; they instead rely on detecting the effects of the particle cascade passing through the apparatus.

The general idea is to place detectors (often tanks of water, or one massive water tank) at high altitudes such that secondary air-shower particles pass through the tanks and produce Cherenkov radiation in the water. Once again, by measuring the deposited Cherenkov light, one can determine information about the primary.

Detectors like this have a very large field of view (zenith angles $\lesssim 50°$) but their sensitivity is much lower than that of pointed instruments. However, due to the nature of the detector, they can be run 24 hours a day and are not affected by poor weather, since it is no longer photons that need to propagate to the detector but the high energy particles themselves (which will not be scattered by clouds).

The large field of view of non-pointed instruments allows for highly extended sources to be easier studied. While pointed instruments (such as *VERITAS*) are much more sensitive (see Figure 2.8), they have a limited field of view. Hence, it is difficult for a telescope to observe the full extent of some sources such as diffuse gamma-ray emission from the galactic plane, or the Geminga pulsar wind nebula, from which the Milagro experiment [22] detected extended VHE emission [23]. The size of the extension is $2.8° \pm 0.8°$ diameter – this is comparable to the entire field of view of current-generation gamma-ray observatories and hence makes observations with a pointed instrument difficult.

The next-generation water Cherenkov experiment being brought online at the time of writing is the High-Altitude Water Cherenkov Observatory (*HAWC*) [24, 25]. *HAWC* is an array of 300 instrumented water tanks located near Puebla, Mexico, at an altitude of 4100 m and is shown in Figure 2.9. Due to the nature of the experiment (and other water-Cherenkov experiments), *HAWC* is exposed to 2/3 of the sky during any given 24-hour period. Thus, the experiment is continuously building up exposure on the entire visible sky.

In the case of transient events, the large field of view and continuous exposure gives non-pointed instruments a huge advantage. Phenomena such as gamma-ray bursts (GRBs), which typically have prompt emission that quickly dies out, have the potential to be detected as long as the experiment is running, whereas pointed instruments like *VERITAS* need to slew to the target, which can take minutes in some cases. This can be long enough to completely miss the event; transients like GRBs have characteristic timescales of only a few seconds. That being said, non-pointed instruments have poor sensitivity; *HAWC* requires ~ 1 day to detect the Crab Nebula, whereas *VERITAS* can do this in < 1 minute. Thus, the advantages

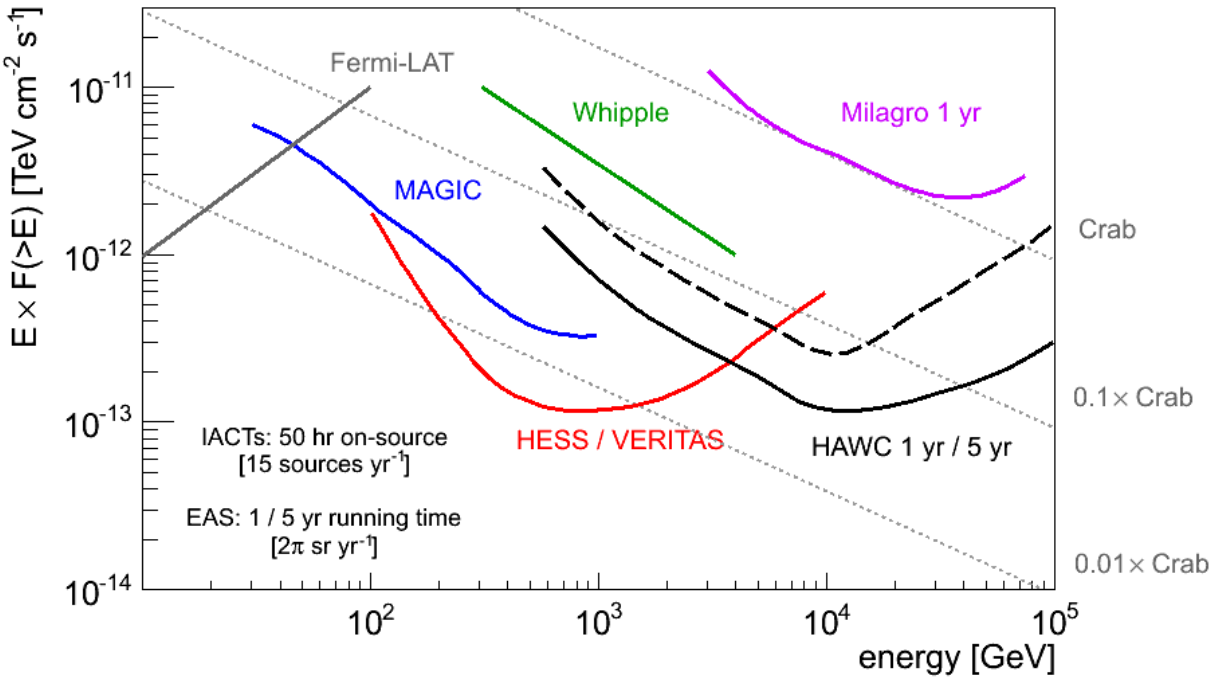

Figure 2.8: Sensitivity of various gamma-ray observatories a function of energy and integration time. At high energies, experiments like *HAWC* are more sensitive than pointed instruments based on typical exposures for IACT telescopes. Image credit: *HAWC* collaboration.

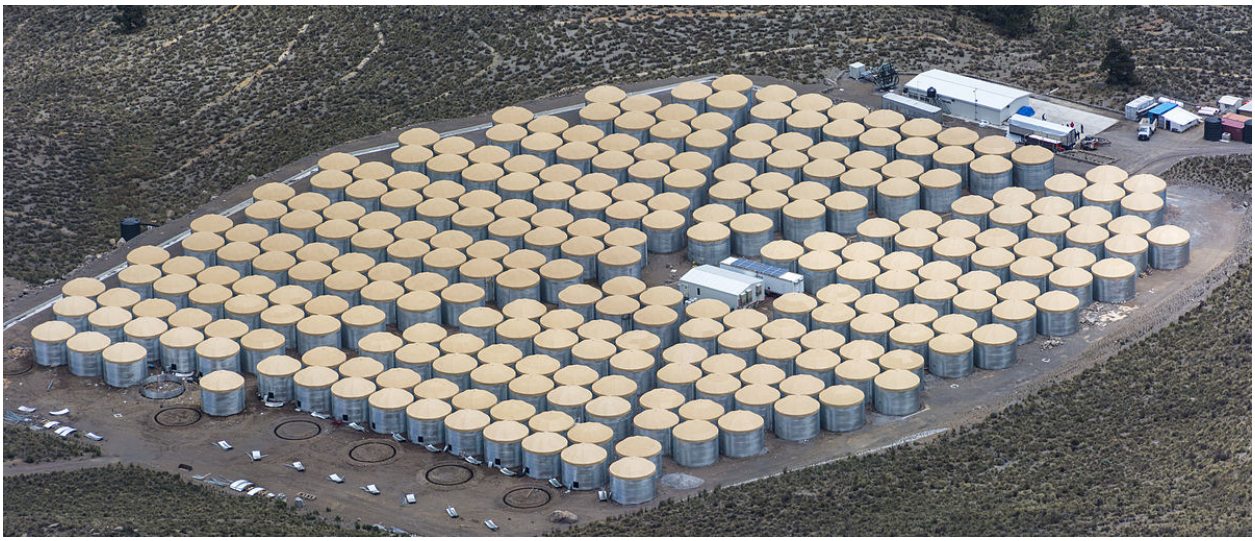

Figure 2.9: The *HAWC* experiment prior to completion (a few tanks in the bottom left are still missing). Image credit: "HAWC from LMT Aug 19 2014 01" by Jordan A. Goodman. Licensed under CC BY-SA 4.0 via Wikimedia Commons

of one detector type over the other depend on the specific science goals targeted.

2.2 Space-based Experiments

2.2.1 History

The first orbital gamma-ray telescope was on the *Explorer XI* satellite which was launched on April 27, 1961. It operated until November that year, in that time detecting 22 gamma rays and $\approx 22,000$ cosmic ray events [26]. The gamma rays were distributed isotropically, offering the first insight into a diffuse gamma-ray background.

The first significant detection of gamma-ray emission from the Galaxy was detected by the *Orbiting Solar Observatory 3* (*OSO-3*). *OSO-3* was launched on March 8, 1967 and was designed to measure gamma rays at energies $E > 50$ MeV. During its time in orbit *OSO-3* detected 621 gamma rays, and a significant (10.4σ) concentration along the galactic plane, with enhanced emission around the galactic centre [27].

The first detection of GRBs (which are now known to be among the most violent events in the Universe) was made on July 2, 1967. This discovery was actually made by US military *Vela* satellites which were were designed to search for terrestrial gamma-ray emission due to nuclear testing. After it was determined that the strange signals could not be of terrestrial or solar origin (using timing information between the different instruments) the results were published, ushering in a new field of gamma-ray observations [28].

The *Small Astronomy Satellite 2* (*SAS-2*) was launched on November 15, 1972. It was designed to measure the distribution of galactic and extragalactic gamma rays between 20 and 30 MeV. SAS-2 succeeded in detecting gamma rays from the Crab Nebula, Vela X (a pulsar wind nebula), and Geminga (also a pulsar wind nebula) [29, 30].

The next major gamma-ray mission was *Cos-B*, a European mission launched on August 9, 1975. This mission resulted in the creation of the 2GC Catalogue which contained a list of 25 gamma-ray sources with emission above 100 MeV [31].

The *Compton Gamma Ray Observatory (CGRO)*, shown in Figure 2.10, was the second of NASA's "Great Observatories"[3]. It was launched from Space Shuttle *Atlantis* during STS-37 on April 5, 1991 and carried four instruments covering an unprecedented range in energies, from 20 keV to 30 GeV. At the time, *CGRO* was the heaviest payload (17 tons) to be deployed from a Space Shuttle. During the mission, *CGRO*'s high-gain antenna failed to deploy, which demonstrated the usefulness of having humans in space; astronauts J. L. Ross

[3]The other three being the Hubble Space Telescope (UV/visible light), the Spitzer Space Telescope (IR), and Chandra X-ray Observatory (X-rays).

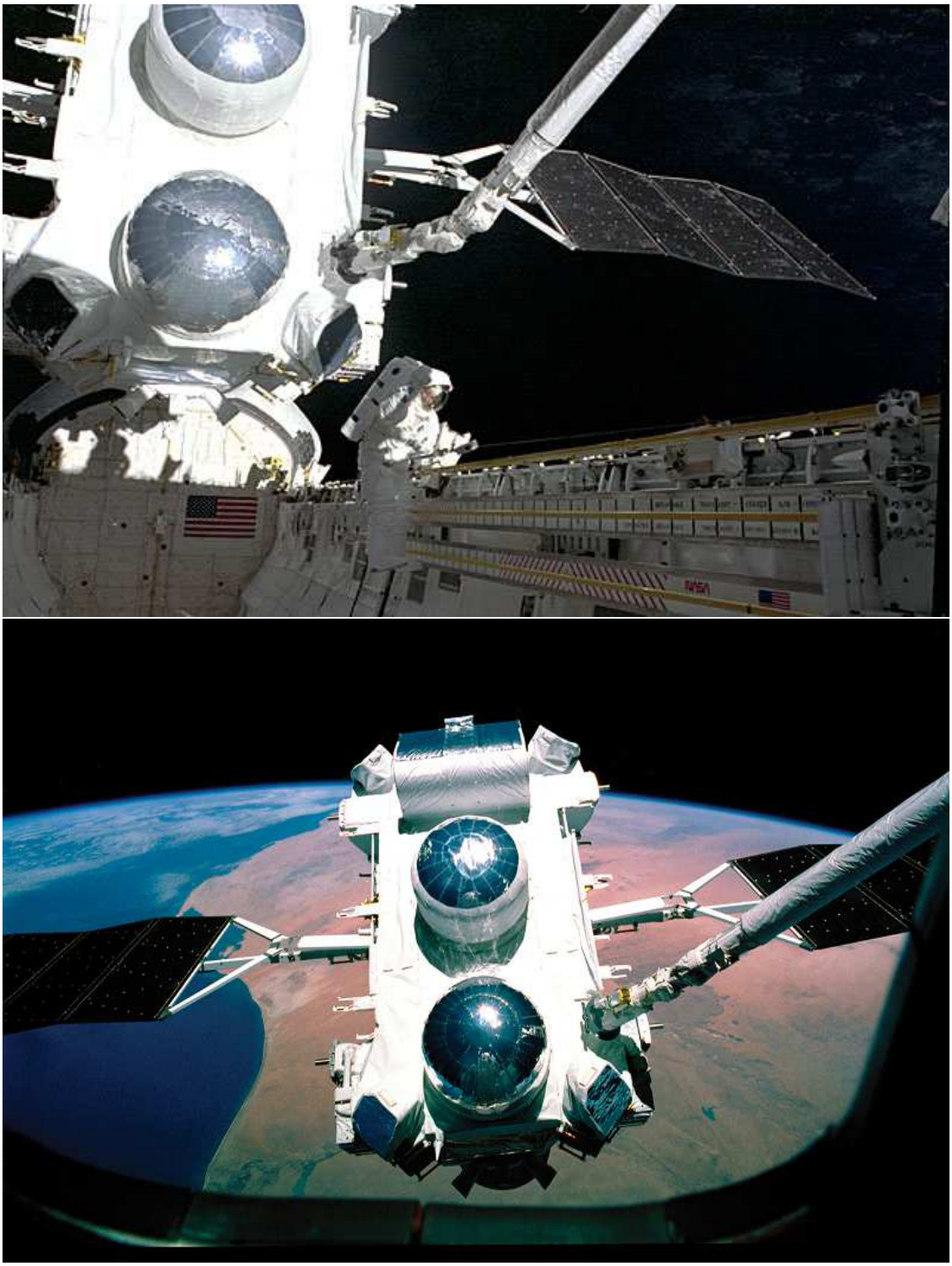

Figure 2.10: **Top**: Deployment of *CGRO* from Space Shuttle *Atlantis*. Astronaut J. Apt can be seen directly below the Shuttle Remote Manipulator System (the "Canadarm"). CGRO is roughly the same size as a school bus. Image credit: NASA / Crew of STS-37. **Bottom**: Another view of *CGRO* shortly before release. Image credit: NASA / Crew of STS-37.

and J. Apt performed a spacewalk and were able to successfully deploy the antenna, saving the mission.

2.2.2 The *Fermi* Mission

The current workhorse in the field of gamma-ray astronomy below 100 GeV is the *Fermi* mission. It was launched on June 11, 2008, and was known prior to launch as *GLAST* (Gamma-ray Large Area Space Telescope). It is shown in its launch configuration in Figure 2.11. *Fermi* comprises two components, the Gamma-ray Burst Monitor (GBM) [32] and the Large Area Telescope (LAT) [33] which probe different energy gamma rays and have different science goals. Since beginning its mission, *Fermi* has detected a huge number of gamma-ray sources (of which the vast majority are new discoveries); the most recent catalogue includes 3033 sources [34].

2.2.2.1 The Large Area Telescope

The LAT is a pair production telescope. When a gamma ray enters the instrument, it can pair-produce in the detector's pair conversion material (tungsten foil). The electron and positron then propagate through the detector, producing ions in silicon strip detectors which allow the particle trajectories to be tracked. The particles then arrive in a calorimeter where the energy of the pair is measured. Cosmic rays can be rejected using a an anticoincidence detector, which is a layer of plastic scintillator tiles encasing the detector. When a charged particle traverses the scintillator, it produces light which can be recorded and used to discriminate gamma rays from cosmic rays. Using information from the anticoincidence detector, the silicon trackers, and the calorimeter, the energy of the gamma ray can be determined. A diagram of the inside of the LAT is shown in Figure 2.12.

The LAT is 0.72 m deep by 1.8 m square and has an effective area in the centre of the field of view of ~ 7000 cm^2 at 1 GeV. It is sensitive to gamma rays between 20 MeV and 300 GeV. The LAT has a large field of view ($\sim 20\%$ of the sky at any given time) and sees the entire sky every two orbits[4].

2.2.2.2 The Gamma-ray Burst Monitor

The GBM is a very different detector. It comprises twelve sodium iodide (NaI) scintillators (12.7 cm diameter by 1.27 cm thick) and two bismuth germanate (BGO) scintillators (each 12.7 cm diameter by 12.7 cm thick). The NaI detectors are sensitive from a few keV to 1 MeV and are designed to identify GRB locations and provide triggers. The BGO are sensitive over

[4]One orbit takes 96 minutes.

Figure 2.11: The *Fermi* satellite in its launch faring in 2008. The LAT is the large silver "box" in the centre of the picture; the cylindrical GBM instruments can also be seen below it. Image credit: "First half of the payload fairing is installed around GLAST" by NASA/Jim Grossmann - Licensed under Public Domain via Wikimedia Commons

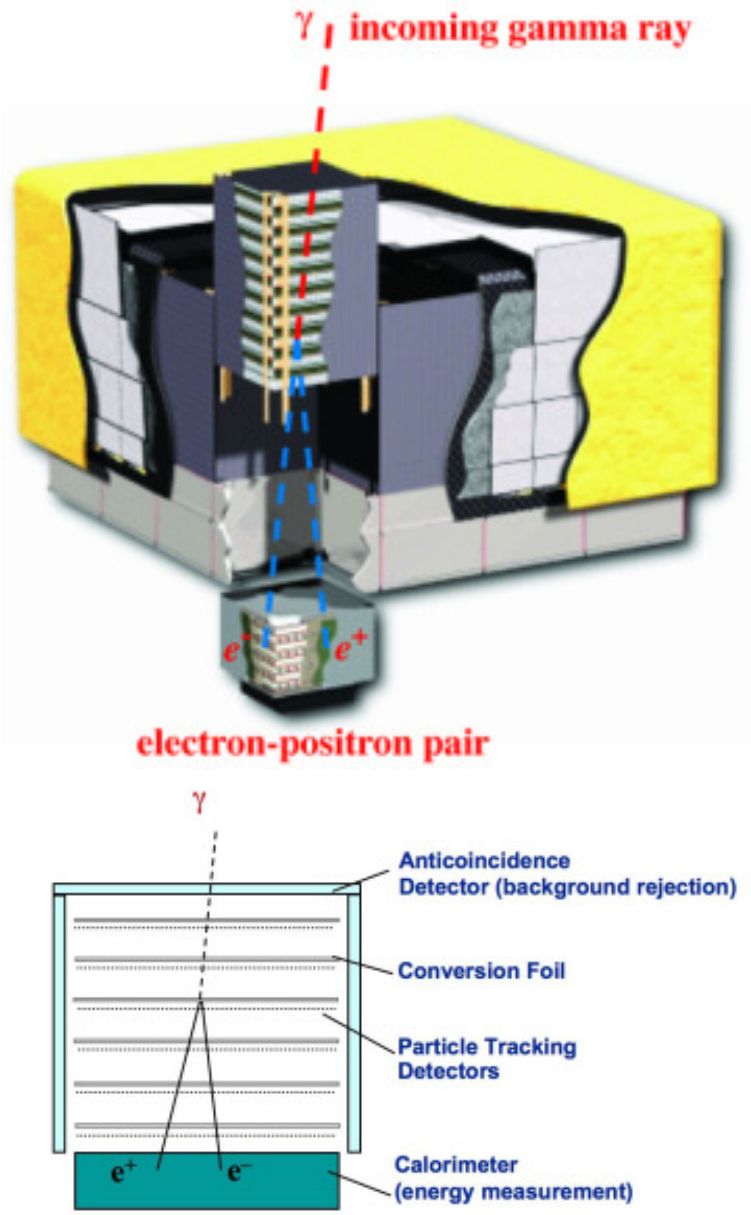

Figure 2.12: **Top**: Cutaway of the *Fermi*-LAT instrument. The LAT is made of 16 modular "towers", each containing 18 tungsten pair-conversion layers and 16 planes of silicon tracker per "tower". Each of the 16 calorimeters consists of 8 layers of CsI scintillator. The anticoincidence shielding is made of 89 individual segments which cover the outside of the instrument. Image credit: NASA/GSFC. **Bottom**: Principles of a pair-production telescope. The different components are described in the main text. Image credit: NASA/GSFC.

the range 150 keV to 40 MeV. The detectors can see the entire unocculted sky at any given time and the GBM generates triggers for ~ 250 GRBs a year.

2.3 Summary

In this chapter, the physics behind ground-based gamma-ray astronomy and the imaging atmospheric Cherenkov technique have been presented. It has been shown that hadronic and electromagnetic air showers differ in a number of quantifiable ways; this becomes important when searching for astrophysical gamma rays. The next chapters will describe how to measure Cherenkov light and subsequently reconstruct information about the primary which produced the corresponding air shower. This allows astrophysical studies of gamma-ray sources to be made.

Chapter 3

The *VERITAS* Experiment

Veritas, meaning truth, was the Roman goddess of truth, a daughter of Saturn and the mother of Virtue.

VERITAS, the **V**ery **E**nergetic **R**adiation **I**maging **T**elescope **A**rray **S**ystem, is an array of four Imaging Atmospheric Cherenkov telescopes located at the F. L. Whipple Observatory in southern Arizona (31.675° N, 110.952° W, 1270 m above sea level). Each telescope was built sequentially beginning with the prototype telescope in 2003. The experiment's official "first light" was in 2007, however, observations were made before that using the partially completed array.

In summer 2009, in order to increase the sensitivity of the experiment, one of the telescopes (Telescope 1) was relocated[1]. The before and after pictures can be seen in Figure 3.1 and a diagram of the two configurations is shown in Figure 3.2. The move was necessitated by the fact that due to the proximity of Telescope 1 (denoted T1, and similarly for the other four telescopes) and Telescope 4 in the old configuration, they typically had very similar views of air showers. Thus, the advantage of a multiple views of an air shower was largely lost for this telescope pair (the benefits of a stereoscopic view are discussed later in Chapter 4).

Historically, *VERITAS* was never supposed to be built at the Whipple Observatory basecamp. It was supposed to be installed at the Kitt Peak Observatory (also in southern Arizona), but due to political reasons when the funding for *VERITAS* was approved, the collaboration no longer had access to the site at Kitt Peak. The prototype telescope (now

[1] Anecdotally, the author's first task as a graduate student on *VERITAS* was to dig up old signal cables from a cable trench between the telescope and its electronics trailer. This came as a surprise since digging with one's hands isn't something one trains for while pursuing a B.Sc. in physics.

Figure 3.1: **Top**: The old array configuration. **Bottom**: The new array configuration, with T1 (foreground) in its new position. Image credit: *VERITAS* Collaboration.

Telescope 1) was constructed in the lower yard of the basecamp, and Telescopes 2, 3, and 4 followed. Given that the basecamp was not part of the original design plan, the telescopes were installed where there was space to put them, as opposed to being installed in ideal locations.

3.1 Anatomy of a *VERITAS* Telescope

Each *VERITAS* telescope is functionally identical and made up of five major components indicated in Figure 3.3:

- Positioner: For telescope pointing.
- Reflector / Dish: The mirrors of the telescope.
- Optical Support Structure (OSS): Supports the reflector.
- Camera box: Contains the telescope focal plane instrumentation.

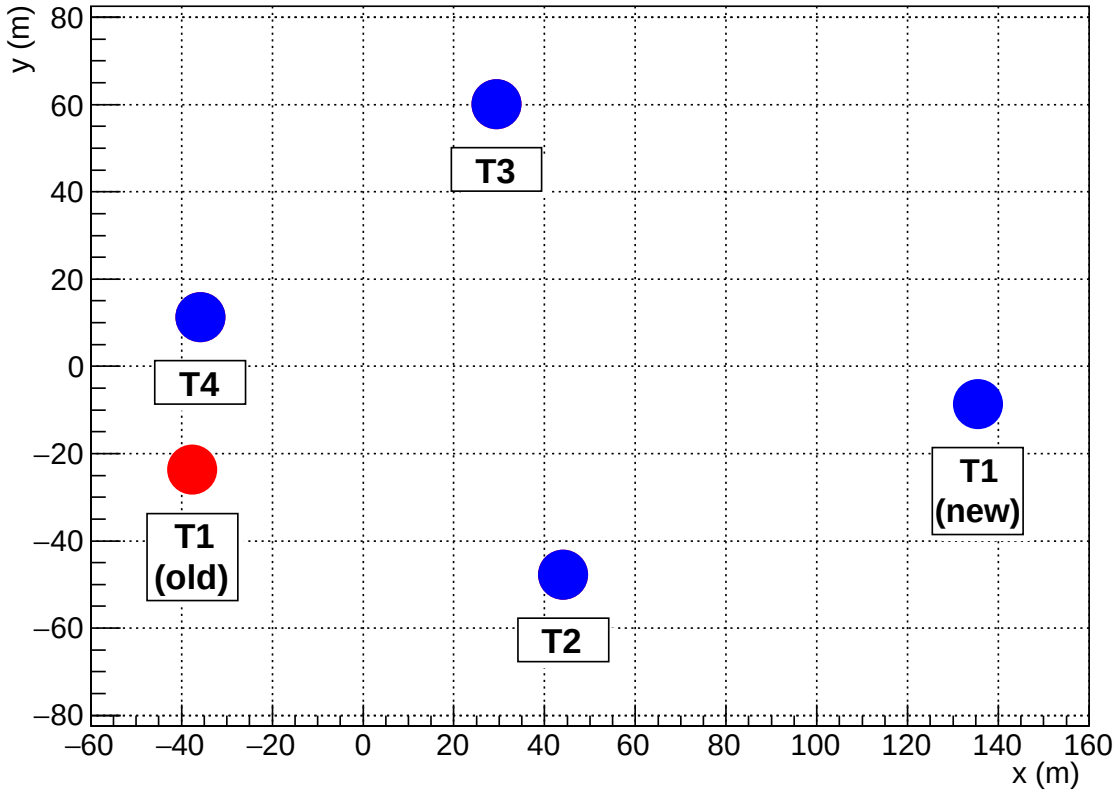

Figure 3.2: The relative positions of the telescopes viewed from directly above before (red) and after (blue) the T1 move. The marker sizes are roughly the size of a *VERITAS* dish.

- Electronics trailer: Contains camera readout electronics and monitoring systems.

In the subsequent sections of this chapter, the functions of the different components mentioned here will be described.

3.2 Focal Plane Instrumentation

Each telescope is equipped with a camera consisting of 499 photomultiplier tubes (PMTs). A PMT is a device that uses the photoelectric effect, wherein when light interacts with a metal (or semiconductor) in a vacuum, electrons are ejected from the material. This effectively allows one to convert a photon into an electric signal which can be digitised. A diagram of a PMT is given in Figure 3.4.

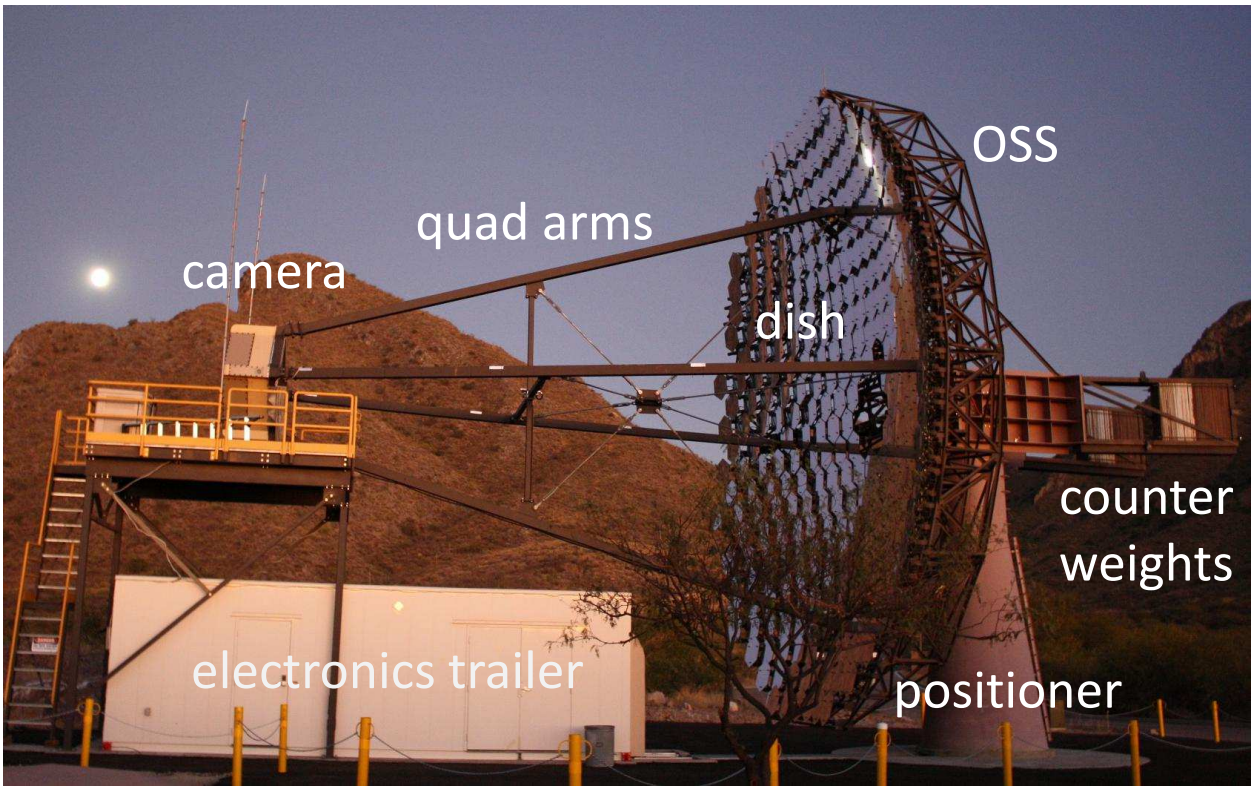

Figure 3.3: Telescope 1 with the different telescope components indicated.

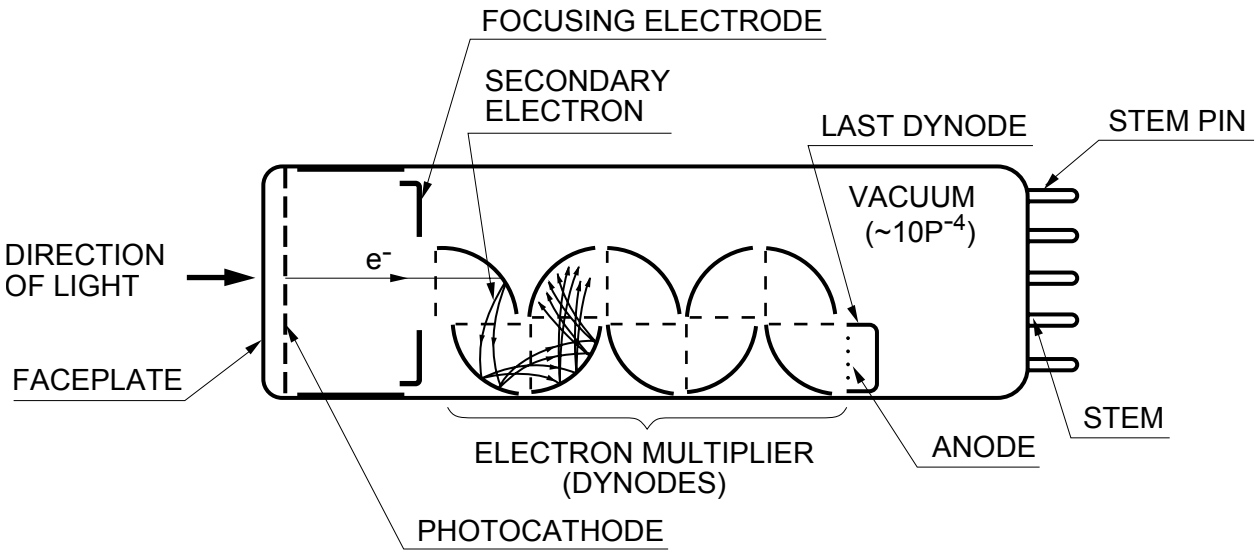

Figure 3.4: Diagram of a photomultiplier tube. When a photon hits the PMT photocathode, there is a wavelength-dependent probability that due to the photoelectric effect an electron will be ejected from the photocathode. When the photoelectron hits the first dynode, it has enough energy to eject multiple electrons from the dynode, which are then accelerated toward the second dynode and the process repeats. The end result is a measureable pulse of charge at the PMT anode. Image credit: Figure 2-1 in [35].

3.2.1 PMT Theory of Operation

3.2.1.1 The Photocathode

In a PMT, the first interaction occurs when a photon arrives at the PMT entry window, which is often (but not always) made from UV-transparent glass. On the interior of the glass is material called the photocathode. The purpose of the photocathode is to convert a photon into an electron, referred to as a photoelectron (p.e.). The quantum efficiency (QE) is the wavelength-dependent efficiency at which incoming photons are converted into photoelectrons:

$$\mathrm{QE}(\lambda) = \frac{N_{p.e.}(\lambda)}{N_{phot}(\lambda)}. \tag{3.1}$$

This conversion is achieved via the photoelectric effect wherein an electron can be ejected from the photocathode material if the absorbed photon carries more energy than the electron binding energy (also known as the work function) of the material. For typical photocathode materials, this is a few eV [36, p. 12-124]. A diagram of this is shown in Figure 3.5. In order to eject an electron, the incoming photon must have enough energy to move the electron from the valence band to the conduction band and over the electron affinity level. The electron affinity can be thought of as a measure of the ability of the atoms to retain their electrons.

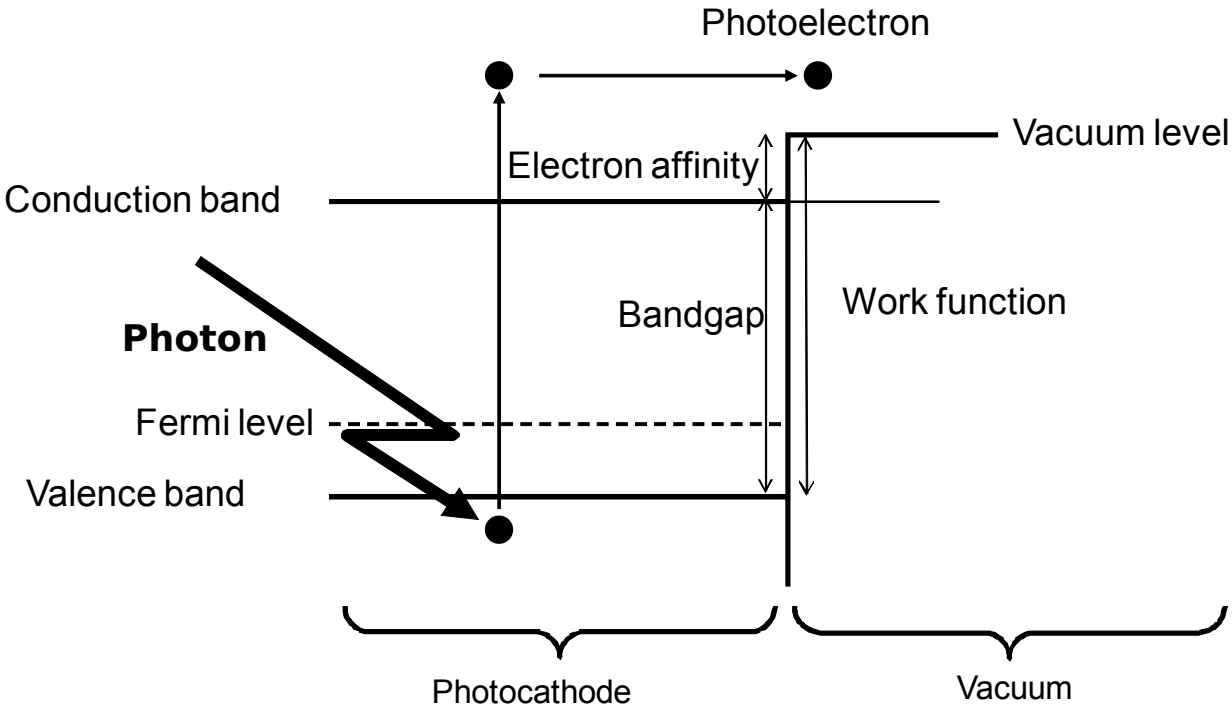

Figure 3.5: Band model for an alkali photocathode. Image credit: adapted from figure 2 in [37].

In order to maximise the sensitivity of an experiment, it follows that the choice of photocathode material is extremely important. In the wavelength regime relevant to *VERITAS* (*i.e.* UV-blue light, where most of the Cherenkov emission is), photocathodes are typically made from alkali metals which have low work functions (denoted φ), such as cesium ($\varphi =$ 1.95 eV [36, p. 12-124]). Bialkali photocathodes, which employ two alkali metals alloyed with cesium (e.g. Sb-Rb-Cs, Sb-K-Cs), are sensitive to UV and visible light and are hence desirable for the detection of Cherenkov light.

Some materials, such as GaAs (Gallium Arsenide, a semiconductor) have negative electron affinities, meaning that once an electron reaches the conduction band, it continues unimpeded (it is "motivated" to leave the conduction band). This means that the photocathodes can be made thick, which increases the probability of a photon undergoing the photoelectric effect upon entering the photocathode material. Photocathodes of this type degrade quickly when exposed to intense light and must be cooled as when operating at room temperature, they produce large amounts of dark current, an irreducible background described later in Section 3.2.2. Thus, they are impractical for use in telescopes like those used in *VERITAS*.

3.2.1.2 Charge Collection Efficiency

The next important parameter in a PMT is the charge collection efficiency, denoted ϵ, which depicts the PMT's ability to collect the ejected electron from the photocathode onto the first electrode of the PMT (called the first dynode). Together with the quantum efficiency, these numbers form the photon detection efficiency (PDE) which is the important value when discussing the sensitivity of a PMT (a PMT with high QE but poor charge collection efficiency can be less sensitive than a PMT with moderate QE but a high charge collection efficiency).

3.2.1.3 The Dynode Chain

Charge collection onto the first dynode is done using a focusing electrode between the photocathode and the first dynode. When the photoelectron arrives at the first dynode, it has sufficient energy to liberate δ electrons from the surface. This is called secondary emission. The number of secondary electrons depends on the chemical composition of the dynode and the voltage difference which accelerated the photoelectron, shown in Figure 3.6. Dynodes are usually made of a metal such as nickel, stainless steel, or copper-beryllium alloy, and coated with a material with a large secondary emission coefficient such as alkali antimonide, beryllium oxide, magnesium oxide, gallium phosphide, and gallium arsenide phosphide [35].

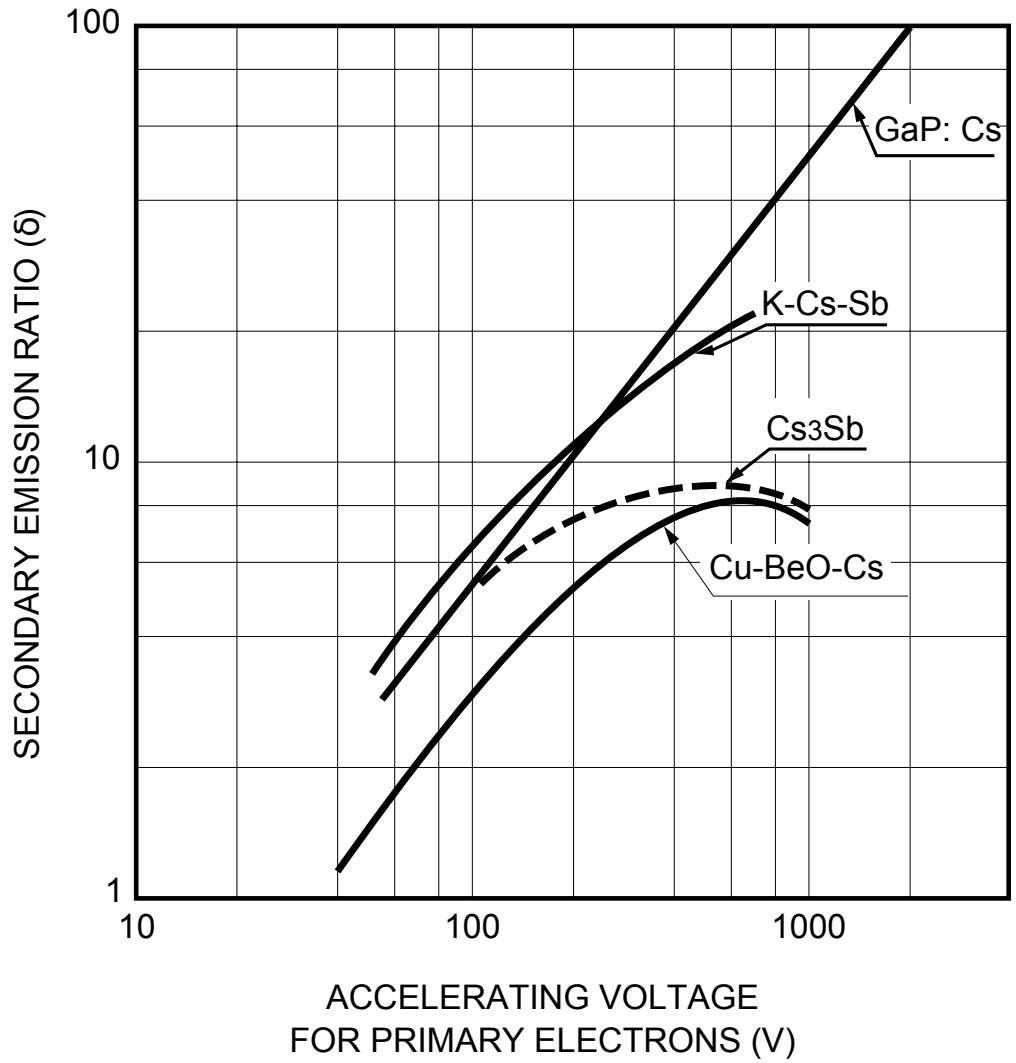

Figure 3.6: Secondary emission ratios for different dynode materials. Image credit: Figure 2-7 in [35].

The amount of secondary emission (*i.e.* δ), can be expressed as a function of the accelerating voltage V_{acc}:

$$\delta = \alpha V_{acc}^{k} \tag{3.2}$$

where α is a constant and k is determined by the dynode material. The secondary emission at the first dynode (δ_1) can also be expressed as the ratio of the current leaving the photocathode (I_{PC}) to the current leaving the first dynode (I_{D1})

$$\delta_1 = \frac{I_{\mathrm{D1}}}{I_{\mathrm{PC}}}. \tag{3.3}$$

By means of a large voltage gradient, these electrons are accelerated to a second dynode, where more electrons are emitted. This cascade continues through the rest of the dynode

chain (the *VERITAS* PMTs have 8). The secondary emission ratio δ_N of the N^{th} dynode stage is

$$\delta_N = \frac{I_{\text{DN}}}{I_{\text{D(N-1)}}}. \tag{3.4}$$

Thus, the dynodes serve to multiply the charge to make the signal from a single photon large enough to be easily measured. After the last dynode, the electron cascade is collected onto an anode, which has a current I, which can be expressed as

$$I = (\epsilon \cdot I_{\text{PC}})\delta_1\delta_2\delta_3\cdots\delta_{\text{N}-1}\delta_{\text{N}}. \tag{3.5}$$

A new quantity, the gain (denoted G), can thus be expressed as

$$G = \frac{I}{I_{\text{PC}}} = \epsilon\delta_1\delta_2\delta_3\cdots\delta_{\text{N}-1}\delta_{\text{N}} \tag{3.6}$$

A PMT is typically supplied with $V \sim 1000$ V which is then divided among the various dynodes using a voltage divider circuit to produce the desired inter-dynode voltage gradient. A circuit diagram for a PMT in such a configuration is shown in Figure 3.7. In the case of a simple voltage divider configuration where all dynodes are the same, and all inter-dynode voltage steps (V_{acc}) are the same, the PMT gain can be rewritten as

$$\begin{aligned} G &= \epsilon(\alpha V_{acc}^k)^N \\ &= \epsilon\alpha^N \left(\frac{V}{N+1}\right)^{kN} \\ &= \eta \cdot V^{kN} \\ &= \eta \cdot V^{\beta} \end{aligned} \tag{3.7}$$

where η and β are constants. Thus, the gain of a PMT is proportional to a power-law based on the applied voltage. A demonstration of this based on *VERITAS* data will be shown later in Section 8.1.1.

3.2.2 Dark Current

Dark current is the small amount of current that flows through a PMT even when there is no light incident on it. A discussion of the different components of dark current can be found in [35, section 4.3.6] which has been used as the reference for this review. While generally not an issue for *VERITAS*, the sources of dark current have been listed below for completeness.

3.2.2.1 Thermionic Emission

Thermionic emission refers to current produced due to the thermal energy of the photocathode and dynodes being greater than the work function of their respective materials. The amount of

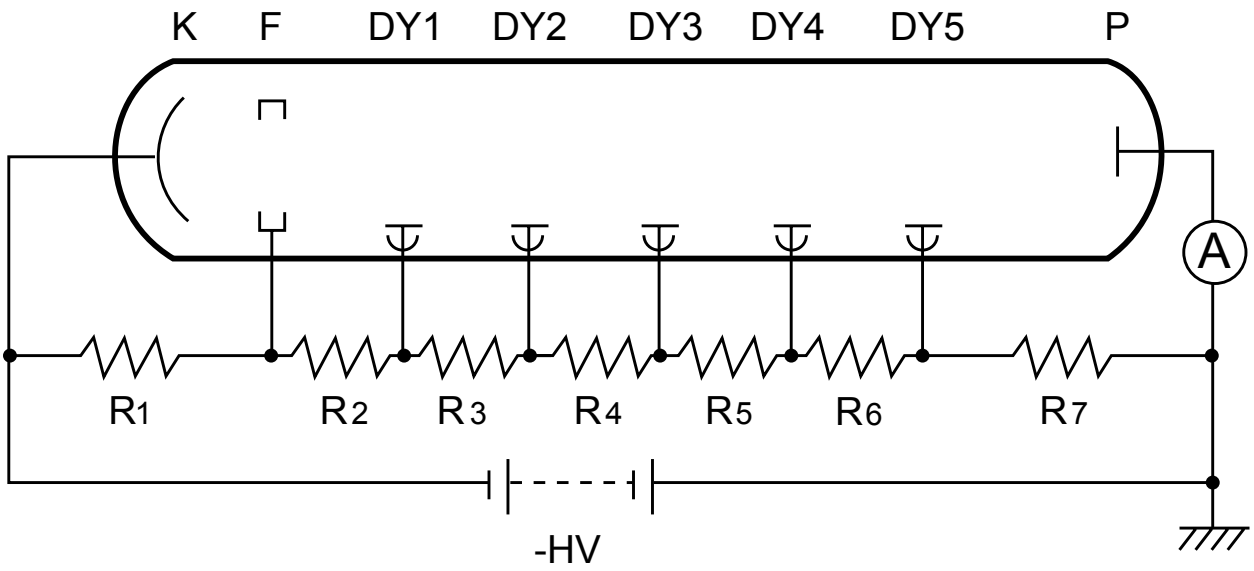

Figure 3.7: Schematic of a voltage divider circuit for a PMT. In this configuration, if each resistor is equal, there is a voltage of $V/(\mathrm{N}+2)$ between each dynode. This is slightly different from the treatment derived in Equation 3.7 wherein the voltage step of the focusing electrode (F) was not considered. It is still possible to regain the power law described there, however, by taking $R_1 = R_2 = R_3/2$ (with all other resistors equal to R_3), which makes the voltage step between the photocathode (K) and first dynode ($DY1$) the same as the voltage step between dynodes $DY1$ and $DY2$. The last step in the PMT for the electrons to be collected onto the anode (P). Image credit: adapted from figure 5-5 in [35]

thermionic emission from the photocathode can be expressed using the Richardson-Dushman equation (see [38]):

$$I_T = A\, T^2 e^{-\varphi/k_B T} \tag{3.8}$$

where T is the temperature (in Kelvin), q_e is the charge of an electron, k_B is the Boltzmann constant, and A is a constant (for temperatures relevant to *VERITAS*) given by

$$A = \frac{4\pi m_e q_e k_B^2}{h^3} \approx 120 \text{ A/cm}^2/\text{K}^2. \tag{3.9}$$

3.2.2.2 Leakage Current

Leakage current is the current flowing through the PMT components due to imperfections in the insulation between the PMT dynodes and anode. It can be quantified using Ohm's law:

$$I_L = \frac{V}{R_{\text{PMT}}} \tag{3.10}$$

where V is the PMT supply voltage, and R_{PMT} is the internal resistance of the PMT, for which a typical valus is $\sim 10^{12}$ Ω. For a PMT operated at 1000 V, this corresponds to

nanoamperes of current. This form of dark current dominates at low temperatures when thermionic emission is small.

3.2.2.3 Field Emission

Field emission occurs when a PMT is operated at a very high voltage. Conceptually, this can be thought of electrons being torn off the dynodes by the strong electric fields within the PMT. This can substantially shorten the life of the PMT and thus must be avoided.

3.2.2.4 Ion Feedback

Ion feedback current is current caused by residual atoms in the PMT (which is held at high vacuum) traveling back through the PMT after having been ionized by electrons traveling down the dynode chain. The ions that arrive at the photocathode (or at the first few dynodes) can liberate many electrons (which then make their way down the dynode chain) resulting in what is known as an afterpulse. To avoid this, PMT dynode structures are typically designed to prevent ions from propagating backwards towards the front face of the PMT.

3.2.2.5 Scintillation

Scintillation can occur in the PMT's glass casing when electrons from the photocathode or dynodes deviate from their normal trajectories and impact the glass.

3.2.2.6 Radiation Noise

Dark current can be produced by particles such as muons producing Cherenkov light as they pass through the glass of the PMT. Furthermore, radioisotopes in the glass itself, such as ^{40}K, can emit β rays (*i.e.* high energy electrons or positrons), producing spurious pulses.

3.2.3 Effects of Exposure to Bright Light

Usually after being exposed to "bright" light (e.g. room illumination), the PMT dark current will be high; dark current can be increased by several orders of magnitude in this way [39], and the time required to settle back to the normal level can be several hours to several days [39, 35]. It *is* possible to destroy the photocathode by exposing it to very bright light ($> 10^4$ lux) [35]. To put this in perspective, daylight is between 10^4 and 10^5 lux depending on the specific conditions. In comparison, moonlight (the main focus of this work) is about 10^6 times dimmer than daylight. Thus, photocathode damage is not a large concern when considering *VERITAS* observations under moonlight.

3.2.4 Dynode Ageing

Due to the constant bombardment of electrons, the material that makes up the dynode tends to degrade over time, in particular the cesium. This has an effect of reducing the secondary emission ratio and hence the gain of the PMT. This can be corrected for by increasing the PMT's HV.

Season-to-season, the *VERITAS* PMT gains are typically boosted by $\sim 5\%$ in order to take the change in PMT response into account. This must be done so that new detector simulations (using the degraded absolute gains) are not required. Using simulations with a mis-matched absolute gain after PMT degradation would result in a systematic shift in reconstructed gamma-ray energies to lower energies, since less light is being registered in the PMTs for a shower of a given energy.

3.2.5 The *VERITAS* Camera

Each telescope is instrumented with 499 PMTs arranged in a close-packed hexagonal configuration. A picture of a camera with only some of the PMTs installed is shown in Figure 3.8. Originally, the four telescopes were equipped with Photonis XP 2970/02 PMTs, but during an upgrade in 2012 they were replaced with Hammamatsu R10560-100-20MOD PMTs. Both the PMT types are shown in Figure 3.9. The new PMTs have "Super" Bialkali photocathodes with a peak quantum efficiency of $\sim 35\%$ at 350 nm and charge collection efficiency of $\approx 90\%$. The new QE translates to a roughly 50% higher peak quantum efficiency than the old tubes; a comparison of the two QE curves is shown in in Figure 3.10. The dynode configuration for the new tubes is 4-1-1-1-1-1-1-1, meaning that the voltage step between the photocathode and the first dynode is 4 times that of the other inter-dynode steps. This is to increase the photon collection efficiency onto the first dynode.

The centre-to-centre spacing of each PMT is 31.4 mm and the Hammamatsu PMTs have a diameter of (25.4 ± 0.5) mm [40]. The nominal plate scale (*i.e.* the relation between physical distance in the focal plane and angular size on the sky) is 0.148°/PMT [41]. This gives the each camera a total field of view of 3.5°. During the day, the camera is covered by a remote controlled shutter that prevents light from arriving at (and potentially damaging) the phototubes.

Folding the R10560 PDE with the Cherenkov light spectrum in the focal plane of a *VERITAS* telescope, one expects to detect 23% of the Chrenkov photons from an air shower; this is a 35% higher yield than with the old tubes [42]. The *VERITAS* PMTs (both pre- and post-upgrade) are run at a total gain $G = 2 \times 10^5$, thus a single photoelectron generates, on average, $2 \times 10^5 \times q_e$ C ≈ 0.03 pC of charge at the PMT anode.

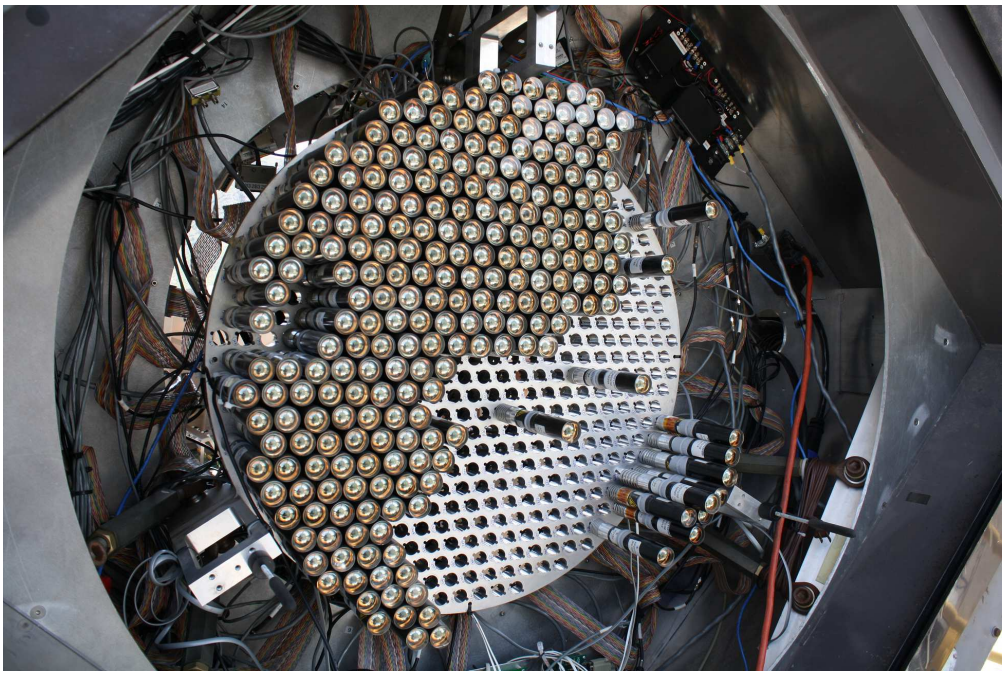

Figure 3.8: The camera of T4 during the camera upgrade. This photo was taken during the removal of the Photonis PMTs. The support structure which holds the PMTs in place can be seen.

The pulse width for the new PMTs is also narrower than the old ones (see Figure 3.11). This is due in part because the Hammamatsu tubes are physically shorter (there is less transit time for secondary electrons) and have fewer dynodes than the Photonis tubes (8 versus 10). This means that when extracting the signal from the raw data, less noise is integrated since the signal region is smaller. This improves signal-to-noise which affects various aspects of the data analysis.

It follows that a larger light yield and better signal-to-noise lowers the minimum detectable amount of light from an air shower. By extension, this decreases the energy threshold (*i.e.* the lowest detectable energy gamma ray) of the experiment. This has had the effect of opening *VERITAS* to new science goals, such as searching for pulsed emission from pulsars, probing lower dark matter particle masses, and closing the gap in energy between *VERITAS* and space-based instruments such as *Fermi*, which allows for investigations into absolute energy scales and systematic errors of the different instruments.

The *VERITAS* PMTs are combined with a preamplifier to form what is referred to as a camera pixel. The preamplifier magnifies the PMT pulse by a factor of 6.6; its purpose is to increase the size of the signal pulse before it traverses 45 m of signal cable from the telescope camera to the electronics trailer such that the effects of any noise acquired in the signal cable are small compared to the pulse size. Each pixel has a HV input cable, signal

Figure 3.9: **Front**: Hammamatsu R10560-100-20 MOD PMT used since September 2012. **Back**: Photonis XP 2970/02 PMT used on *VERITAS* prior to the upgrade. Image credit: Figure 1 in [42].

out cable, a cable which is run to the PMT current monitors (a set of sensors which measure the instantaneous PMT current, see Section 3.7.2), and an input cable for charge injection (a calibration subsystem for testing the data acquisition chain).

3.2.6 Light Cones

In front of every PMT is a modified Winston light cone [44] which serves to reduce the dead space between PMTs and reject stray light not from the telescope reflector. The *VERITAS* cones are not true Winston cones (which have a cylindrical symmetry); the *VERITAS* cones are *hybrid* cones which have a hexagonal entry aperture which morphs into a standard Winston cone. This allows the the PMTs to be close-packed, minimising dead space.

A Winston cone is an example of a non-imaging optical element and works by trading angular acceptance and resolution for area concentration. A detailed description of the geometry of a light cone is given in Appendix A. The cutoff angle of the light cones is described by two parameters:

$$\frac{d}{D} = \sin\theta_c \tag{3.11}$$

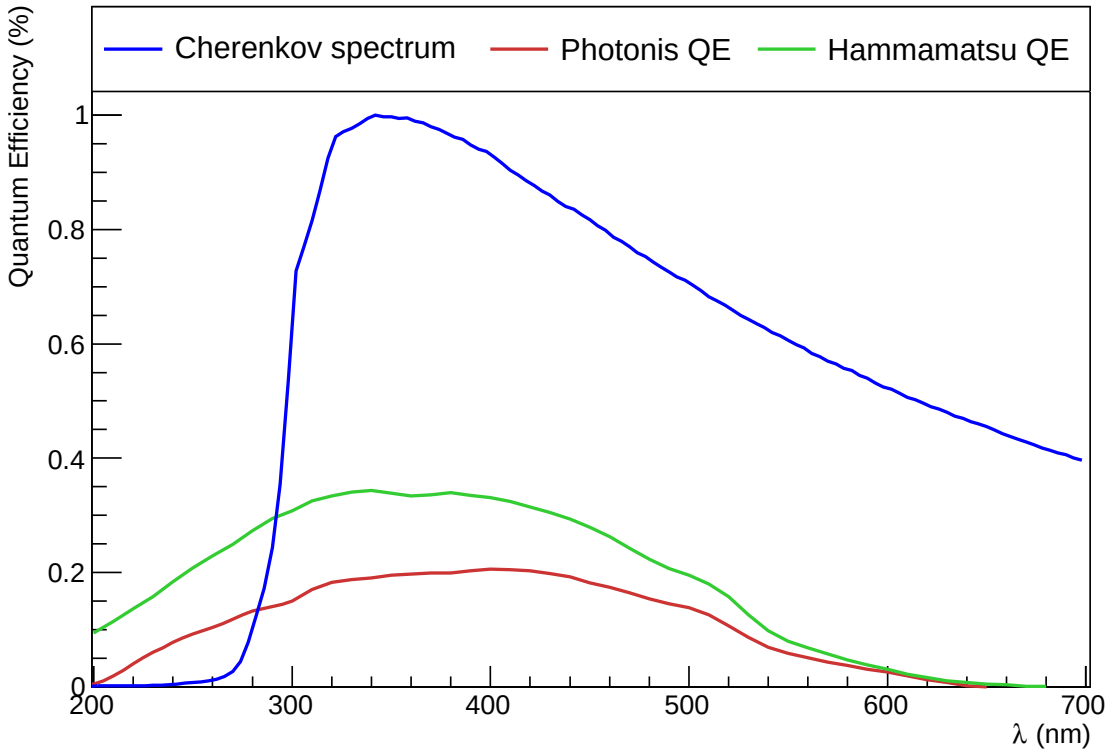

Figure 3.10: The quantum efficiency of the Photonis PMTs and the Hammamatsu PMTs, with the Cherenkov spectrum (at ground level) for a simulated 500 GeV gamma ray. The cutoff at low wavelengths is due to absorption of UV photons by ozone and Rayleigh and Mie scattering. The information in this figure was obtained from the detector simulations used in the analysis of *VERITAS* data.

where d/D is the ratio of the entrance to exit diameter of the cone and θ_c is the cutoff angle ($\sim 35°$ for *VERITAS*[2]). Note that the height of the cone h can also be described in terms of these values:

$$\tan\theta_c = \frac{D+d}{2h}. \tag{3.12}$$

Thus, the entire geometry of a light cone can be described by exactly two parameters.

Any light which reflects off the surface of the cone will exit the cone with an angle different from which it entered, so angular (or directional) information of the incoming photons (and hence the source) is lost. This limit is a direct consequence of Liouville's theorem which states that the phase-space volume of the system (in this case, the optical *entendue*) must be conserved.

[2]Assuming an ideal light cone.

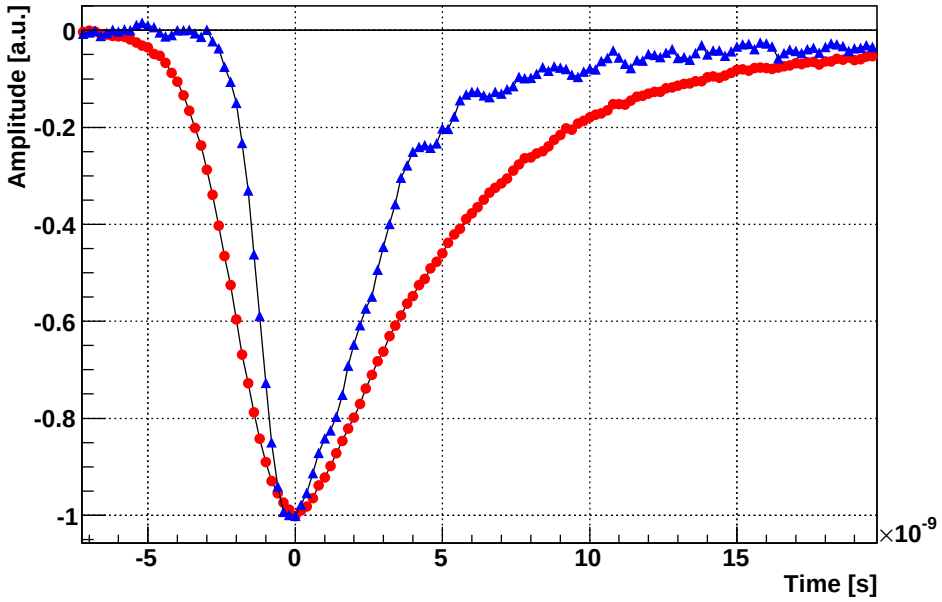

Figure 3.11: Red: Pulse shape for the old PMTs. Blue: pulse shape for the new PMTs. The new pulses are about 40% narrower than the old ones. Image credit: Figure 2 in [42].

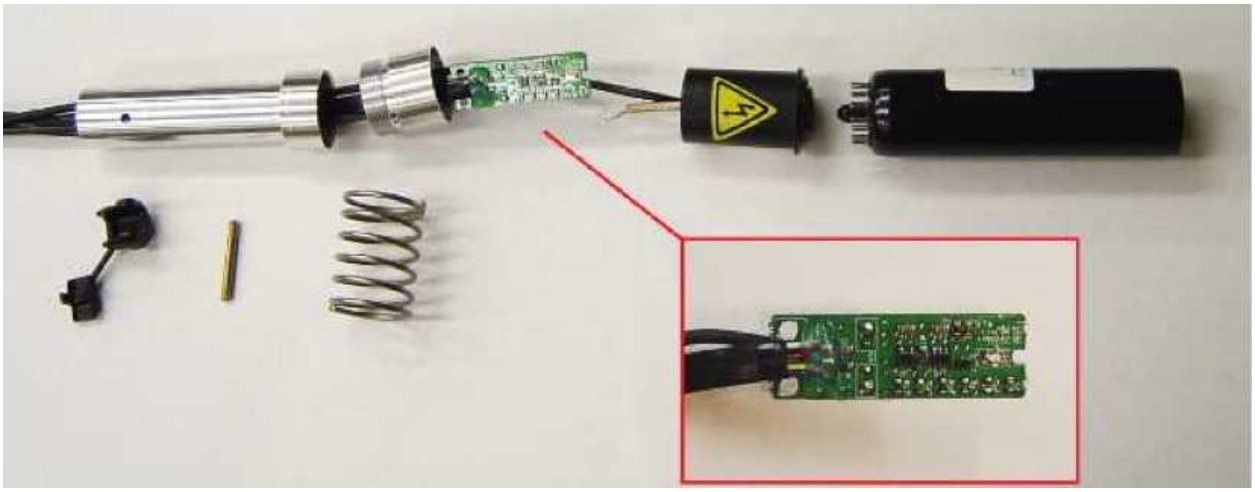

Figure 3.12: A *VERITAS* camera pixel. The main components are the PMT, preamplifier and the aluminium housing which provides shielding. When assembled, the assembly slides into a support structure inside the camera box. Image source: Figure 2 in [43].

The inner surface of each cone is coated with evaporated aluminium, giving it a reflectivity $> 85\%$ at relevant wavelengths. They increase the light collection efficiency (the ratio of light arriving at the photocathodes to light arriving at the camera focal plane) by $\sim 65\%$ by effectively decreasing the dead space between PMTs by 25% (this can be thought of as increasing the effective area of the photocathodes). The individual light cones are each installed on a plastic plate, which is then mounted on the camera, as shown in Figure 3.13.

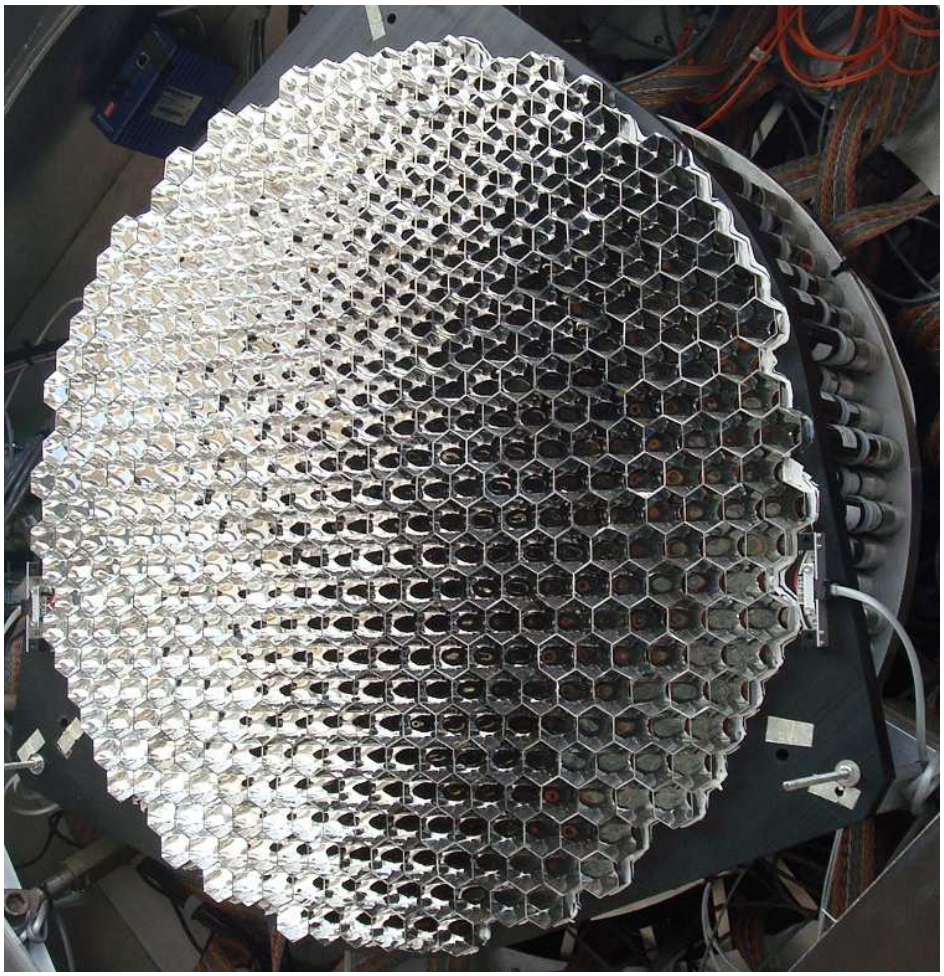

Figure 3.13: Light cones mounted on a *VERITAS* camera. The front of the light cones are in the focal plane of the telescope. Image credit: Figure 2.12 in [45].

3.3 The Reflector

The *VERITAS* telescopes are based on the solar furnace design from [46] (so-called "Davies-Cotton" optics). By using multiple spherical mirrors to approximate a large spherical reflector, one can produce a reflector with a large collecting area without encountering the manufacturing

issues associated with producing large mirrors. Furthermore, by approximating a spherical dish rather than a parabolic one, identical mirror segments can be used (as opposed to many different mirror segments, each constituting a different part of a parabolic reflector); this further simplifies manufacturing. This does, however, come at the cost of causing spherical aberrations (called coma). Of the three current-generation IACT arrays, the *MAGIC* and *H.E.S.S.*-II [47] telescopes use parabolic reflectors.

Each *VERITAS* reflector consists of ~ 350 identical hexagonal mirrors of width (60.96 ± 0.30) cm flat-to-flat, (11.5 ± 1.0) mm thick, and has a radius of curvature of 24 m $\pm$ 1%. The individual mirror facets are not "optical-quality" mirrors: the mean spot size for the individual facets is (6.0 ± 0.5) mm at the telescope focus [48]. Given that this is less than the physical size of an individual PMT, the spot size (which is large compared to that of an optical telescope mirror) has no effect on the Cherenkov telescope's performance. Each facet is attached to a 3-point mirror mount that allows for each facet to be oriented (Figure 3.14).

Figure 3.14: A *VERITAS* mirror mount. Each of the three points of the mount is a combination of a mounting bolt (so the mirror facet can be fixed to the mount) and a fine-alignment screw connected to a gimbal which allows for the facet to be adjusted.

VERITAS has an on-site mirror (re)coating facility and 120 spare facets which means that every telescope can have its mirrors replaced roughly every four years. This is because the telescopes are continuously exposed to the elements; the reflectivity of the mirrors degrade with time as small scratches due to dust occur over time. Mirror replacement is done in

batches of $\sim 1/3$ (about 120 facets) at a time so that no telescope ever has a particularly bad set of mirrors. A picture of a telescope with fresh mirrors is shown in Figure 3.15.

Figure 3.15: *VERITAS* Telescope 2 after a fresh batch of mirrors were installed on the bottom third of the dish. They appear to be darker because they are not coated with dust and small scratches due to being exposed to the elements, so there is less diffuse reflection. Image credit: *VERITAS* collaboration.

3.4 Telescope Pointing

Each telescope is pointed by an Azimuth-Elevation (Az-El) positioner which is capable of slewing the telescopes at 1°/s. The pointing accuracy, based on the telescope encoders, is approximately 50-100 arcseconds, and is dependent on the T-point model, which is a model which converts telescope encoder values to a pointing location in right ascension and declination.

The *VERITAS* pointing monitors (VPMs) are a set of two CCD cameras (two per telescope) used in a number of calibrations such as identifying the telescope pointing direction (with greater accuracy and precision than the encoders) or measuring the telescope's optical point spread function (*i.e.* the size of the image of a point source as seen by the telescope,

measured in the focal plane). The two cameras are mounted such that one views the PMTs in the camera box and the other views the sky in the direction that the telescope is pointing.

During normal observing, the VPMs image the sky at a rate of 0.5 Hz. The images are then analysed offline. Simply put, the sky camera images are compared to a star catalogue which allows the telescope's pointing direction to be identified. The results are written to a database and then used later in data analysis. In the event that VPM information is unavailable (e.g. in the case that the weather was poor or a camera was offline), the *VERITAS* analysis packages default to using the telescope positioner encoder values. The pointing residuals as determined by the VPMs are shown in Figure 3.16; the overall systematic error in the pointing is reduced to ~ 25 arcseconds.

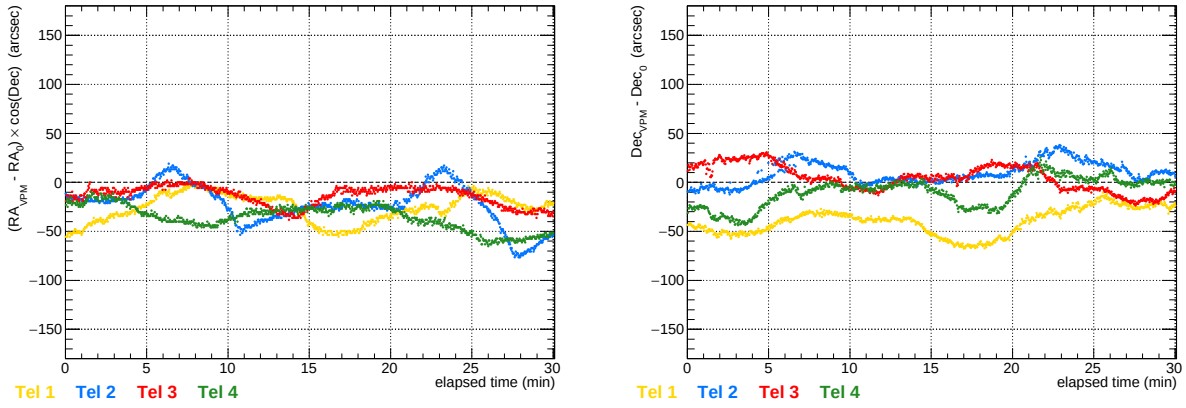

Figure 3.16: **Left**: Pointing residuals for right ascension. The oscillations are due to the limited resolution and step size of the telescope pointing encoders. **Right**: Like the left hand plot, but for declination.

3.5 The VERITAS Data Acquisition System

3.5.1 Signal Digitisation

The signals from each PMT are fed into custom-built 8-bit, 500 MSamples/s flash analog-to-digital converters (FADCs). Each FADC continuously digitises the signal from each camera pixel and stores the values (an 8-bit number representing a measured voltage and having units of digital counts (d.c.)) in a 65 μs buffer. The FADC dynamic range is extended by a factor of six by use of two different signal pathways. In the first pathway, the signal is amplified by a factor of three and in the other the signal is divided by a factor of two and delayed. The purpose of the delayed signal is to allow the FADC system to detect saturation:

if a pulse is determined to be saturating the FADC, a bit in the data acquisition chain is set (the so-called Hi-Lo bit) and the delayed pulse is injected into the FADC. A different FADC readout window, one that has been shifted such that it encompasses the delayed low-gain pulse, is then used to ensure that the low-gain pulse is then read out.

3.5.2 The Trigger

The night sky background (NSB) is the rain of photons arriving at the detector from the night sky. The constituents of the NSB will be described at-length later in this thesis in Chapter 5. The NSB continuously bombards the cameras with photons and is of the order of a few 10^{12} photons m^{-2} s^{-1} sr^{-1}. Without a way of identifying random NSB events from Cherenkov events in order to reject them in real time, data rates would be too high for any computer system to handle[3]. The way around this is to implement a trigger system which effectively steps down the amount of data by performing on-line rejection of signals which are not believed to be Cherenkov pulses. *VERITAS* employs a three-level trigger system, described below.

3.5.2.1 L1

The L1, or pixel-level trigger, is a trigger based on the number of photoelectrons a PMT has received. Signals from the PMTs are split: the first goes into the FADC memory and the second enters a discriminator. In the case of a threshold discriminator (TD), which triggers once its threshold has been reached, pulses of different sizes trigger at different times. This makes looking for coincidences between different pixels (which is the principle of the next level of trigger) difficult, since wider coincidence windows must be used. Thus, a system wherein the timing information of the pulse is taken into account is required. A constant fraction discriminator (CFD) accomplishes this. A CFD triggers at some fraction of the maximum pulse height. This is demonstrated in Figure 3.17.

The way a CFD works is by combining a TD and a zero crossing discriminator (ZCD). A block diagram is given in Figure 3.18. The threshold discriminator component is simple: for an input pulse above a certain threshold the TD is "high" while the pulse is above threshold. The *VERITAS* trigger is usually[4] set to 45 mV (about five photoelectrons).

[3] A back of the envelope calculation based upon the 4 *VERITAS* telescopes digitising the sky with the current hardware puts the raw data rate at $\sim$ one TB/s. To put this in perspective, a single Cherenkov event is $\sim$ 30 kB of data and the reconstructed gamma-ray rate after a typical analysis is at most a few gamma-rays per *minute*.

[4] There are some observing conditions for which is not the case (see Section 7.1).

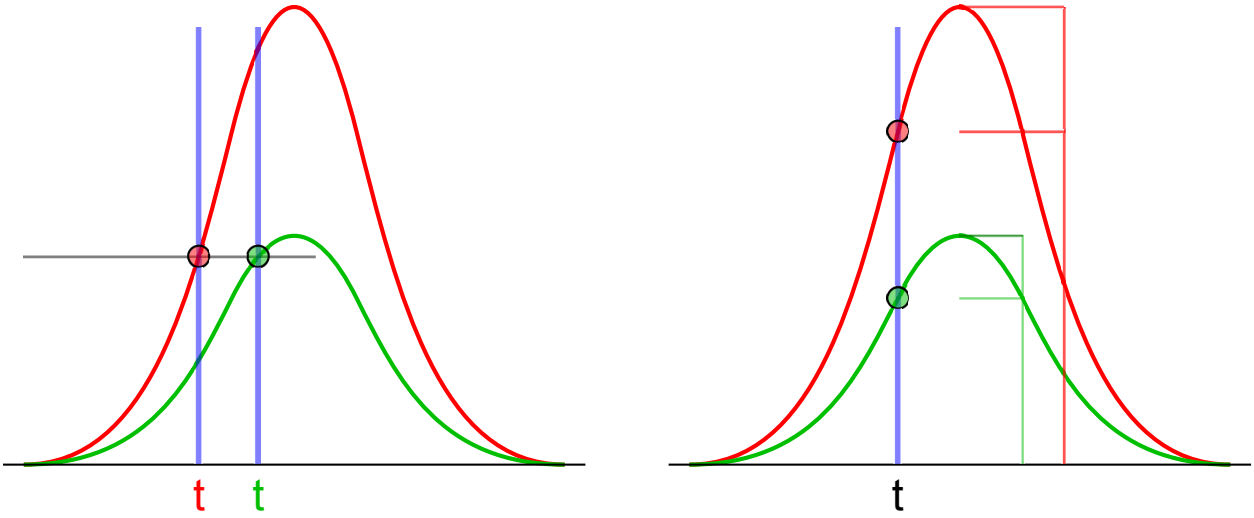

Figure 3.17: **Left**: Two pulses of different heights trigger at different times in a standard threshold discriminator. **Right**: For a CFD, the two pulses trigger at the same fraction of their maximum (in this case, roughly 75%) at the same time t. Image credit: "Constant fraction 1". Licensed under CC BY-SA 2.5 via Wikimedia Commons.

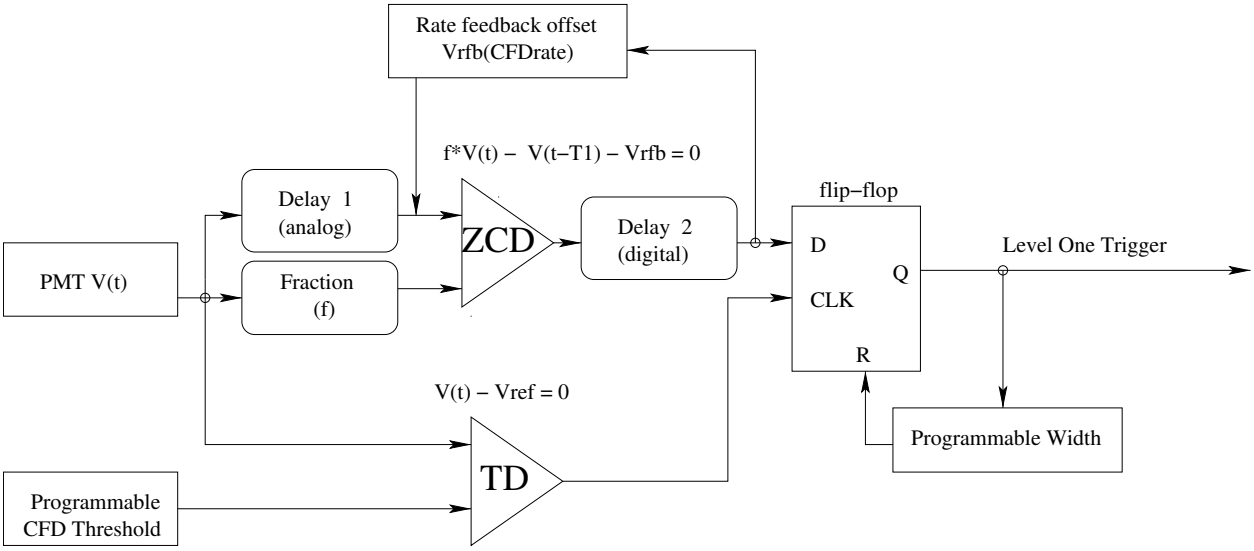

Figure 3.18: Block diagram of the *VERITAS* CFDs. The PMT signal $V(t)$ is split three ways: one enters the TD, and the other two are directed to the ZCD. One is delayed and inverted and one is scaled by some fraction f. The output of the ZCD output is fed into the rate feedback (V_{rfb}) which is then used to offset the ZCD trigger threshold. The outputs of the ZCD and TD are fed into a D-flip-flop, which triggers ($Q = 1$) if D is high and CLK is high. The D-flip-flop is then reset for a programmable amount of time. Image credit: Figure 1 in [49].

A ZCD functions by duplicating the input signal, delaying and inverting it, and then adding it back to the original signal. By triggering on the zero crossing, this ensures that pulses of all sizes trigger at the same time (the need for this will become apparent in the next section). This is demonstrated in Figure 3.19. An L1 trigger is produced if both the TD and ZCD are high at the same time.

The L1 trigger rates are highly susceptible to noise, such as the NSB or starlight. To counteract this, a rate feedback (RFB) is built into the L1 trigger system. The RFB mechanism effectively changes the trigger threshold by adding a voltage offset to the inverted pulse in the zero crossing discriminator. Every second, the RFB determines the L1 trigger rate and changes the voltage offset in the ZCD by 52 mV/MHz. For dark skies, typical L1 rates are on the order of $\sim$ a few MHz. Note that the L1 rates are not required anywhere in the analysis, so they are not stored as part of the data readout chain.

3.5.2.2 L2

The L2, or pattern trigger, takes the output of the L1 and looks for a coincidence between three neighbouring pixels (either a cluster of three, or three in a row). This is done using a sophisticated field programmable gate array (FPGA)-based system [50] which was installed on *VERITAS* in 2010. Prior to the FPGA-based L2, *VERITAS* used a pattern trigger that was effectively based on length-matched cables – this system, while adequate, was limited in that it was not programmable and had a fixed coincidence window of 8 ns. The L2 coincidence window is currently set to 5 ns; a narrow trigger coincidence window helps ensure that the 3-fold coincidences are not due to random NSB photons.

3.5.2.3 L3

The L3, or array trigger, looks for coincident L2 pulses from any two telescopes within 50 ns of each other. There is a caveat that there are pointing-dependant delays built into the L3. This is because depending on where the telescopes are pointing the array geometry as seen by the air shower is different, so propagation times of Cherenkov photons between telescopes are different. More details on the L3 can be found in [51]. During observing, typical L3 rates are $300 - 450$ Hz depending on elevation, sky illumination and CFD thresholds.

3.5.3 Data Readout

After the trigger criteria have been satisfied, the L3 computer (located in a dedicated computer room in the *VERITAS* array control building) instructs the individual telescopes to store

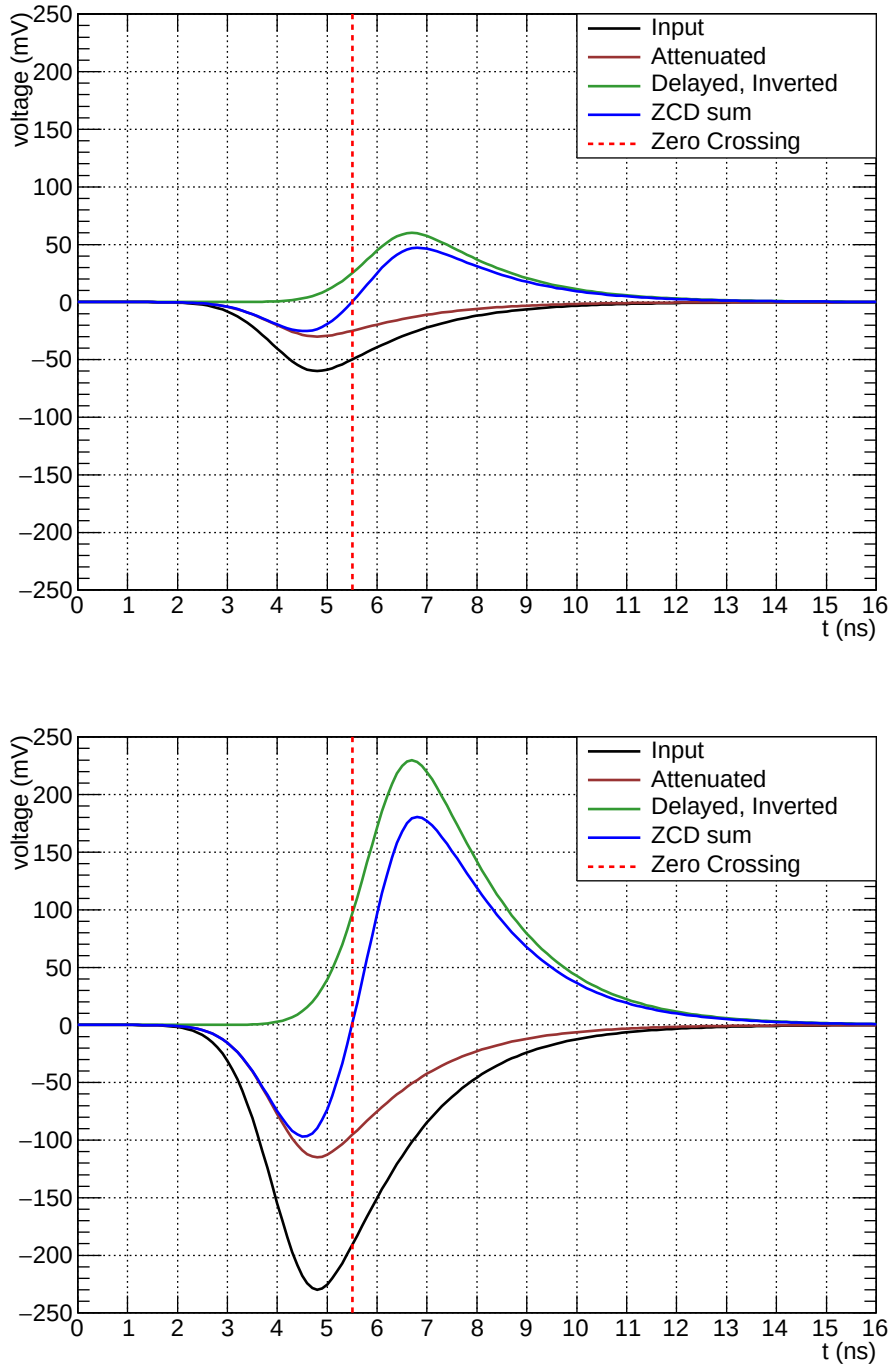

Figure 3.19: Operating principle of a ZCD. **Top**: A small pulse enters the CFD. The pulse in this example is only over the trigger threshold (50 mV) between $t \sim 4$ ns and $t \sim 5.5$ ns. The ZCD triggers at the zero crossing at 5.5 ns. **Bottom**: Same as above, but for a large pulse. The large pulse is roughly above the trigger threshold from ~ 3.5 ns to ~ 8 ns. but still triggers at 5.5 ns like the small pulse.

data to disk. Data corresponding to the event that produced the trigger are stored using Event Builders, which package the individual FADC traces into an event.

At the array level, the Harvester then retrieves the telescope-specific information from each Event Builder and combines it into the final data product. At the same time, the events are analysed in real time (see Section 3.7.1). The data are then compressed and stored in a custom file format called the *VERITAS* bank format. The resulting data rate is $\sim$ 25 GB/hr.

The typical length of a run is 30 minutes. This is chosen such that the individual data files are not too large (making them unwieldy) but long enough so that the additional overhead due to stopping and starting a run (order one minute) does not significantly reduce observing time.

3.6 Camera Calibrations with LED Flashers

The LED flashers, henceforth simply "the flashers", are a tool designed to allow for absolute and relative calibrations of the PMTs to be made. This information is required in order to model the detector response and analyse gamma-ray data. They were designed at McGill University to replace a laser that was used previously by *VERITAS*. The LED flashers replaced the laser in fall 2010[5]. Each is mounted 4 m from the camera on a cross bar which connects the quad arms (visible in Figure 3.3).

Each flasher (see Figure 3.20) contains seven Optek OVLGB0C6B9 LEDs [52] which are illuminated sequentially. This provides a brightness "ramp" of eight different light levels, starting with zero LEDs (a pedestal) and increasing sequentially to seven. Further technical specifications of the flashers can be found in [53]. The following discussion of PMT gain calculations are based off of the same text.

A so-called flasher run is a type of data run during which both the flasher and the *VERITAS* data acquisition system (DAQ) are simultaneously triggered (usually at a rate of 300 Hz) by an external source. Special delays in the DAQ ensure that the PMT pulses caused by the flasher are well-located in the FADC readout window. With each trigger, the number of lit LEDs increases by one in an infinite cycle from 0 to 7 LEDs. Flasher runs are taken nightly as they allow nightly variations in PMT response to be quantified (this is discussed in the next section). Furthermore, they provide a good real-time verification that the entire data acquisition chain is functioning correctly (from PMTs to digitized pulses).

[5]The author of this thesis assisted with the installation of the flashers on Telescopes 2, 3, and 4.

Figure 3.20: **Top**: An LED flasher. One is permanently installed on each telescope ~ 4 m from the camera. **Bottom**: Underneath a diffuser (not shown here), the 7 LEDs can be seen. Image credit: Figure 1 in [53].

3.6.1 PMT Absolute Gain Calibration

3.6.1.1 Single Photoelectron Measurements

A direct way to measure the gain (G) of a PMT is to measure the average amount of charge produced when a single photoelectron (SPE) is produced; this should be $G \cdot q_e$ Coulombs. This value of the gain does not include the collection efficiency of photoelectrons onto the first dynode; thus G is the multiplicative factor for p.e.s that have arrived at the first dynode.

In *VERITAS*, SPE measurements are made by covering the phototubes with a neutral density filter (in this case, a sheet of aluminium with small holes drilled over the centre of each photocathode; this is known as the "holey plate", Figure 3.21). In this configuration, flashing the camera will yield a charge distribution that contains mostly zero p.e.s (*i.e.* the pedestal), some events containing a single p.e. and a small fraction containing multiple p.e.s, following a Poisson distribution. The normalised charge distribution looks like Figure 3.22 and can fully described with a function with only five parameters:

$$Q(x, \mu_p, \sigma_p, \mu, \sigma, \lambda) = \\ \frac{\lambda^0 e^{-\lambda}}{0!} \frac{1}{\sigma_p \sqrt{2\pi}} e^{-\frac{(x-\mu_p)^2}{2\sigma_p^2}} + \sum_{n=1}^{\infty} \frac{\lambda^n e^{-\lambda}}{n!} \frac{1}{\sigma\sqrt{2n\pi}} e^{-\frac{(x-n\mu)^2}{2n\sigma^2}} \tag{3.13}$$

The first term corresponds to the pedestal (a Gaussian with mean μ_p and width σ_p weighted by the probability of counting zero p.e.s given a Poisson distribution with mean number of p.e.s λ) and the second term corresponds to the p.e.s (mean μ and width σ) weighted by the corresponding Poisson prefactor. The value of the absolute gain is the mean of the photoelectron term μ.

3.6.1.2 Photostatistics Method

While the absolute gains can be accurately determined using the SPE method, for the purposes of tracking PMT stability, the measurement is too time consuming to be performed every night. The photostatistics method takes only 2 minutes to perform (*i.e.* the length of a flasher run). Thus, every night the PMT gains can be calculated and the stability of the system can be traced.

For N photons arriving at the first dynode, one expects an amount of charge $\mu = GN$. For Poisson fluctuations, the spread in the number of photoelectrons is $\sigma_N = \sqrt{N}$. The corresponding spread in the charge is

$$\sigma = G\sigma_N = G\sqrt{N}. \tag{3.14}$$

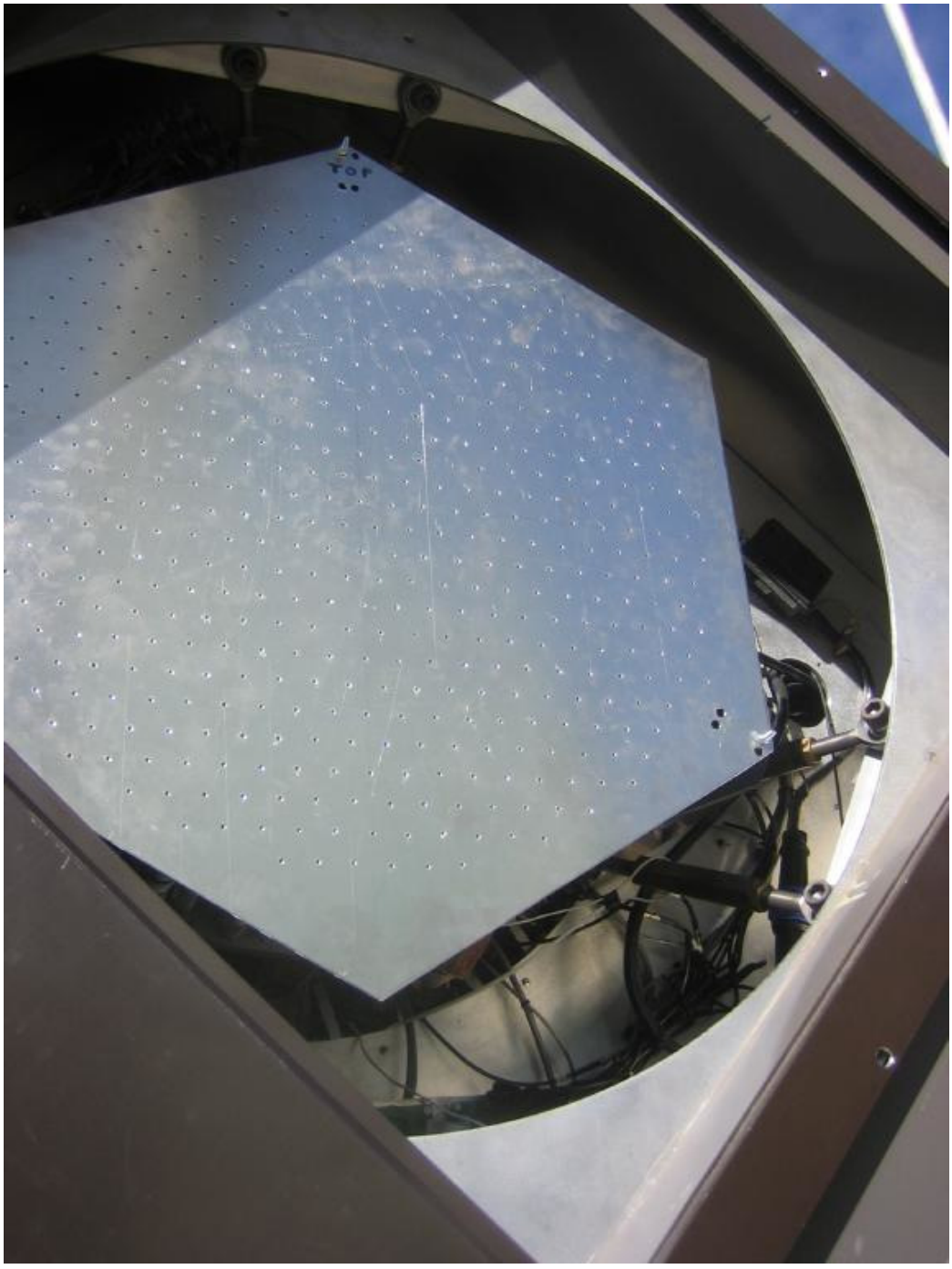

Figure 3.21: The "holy plate" neutral density filter. A small hole is drilled in the spot corresponding to the center of each PMT. This reduces the NSB to a negligible level. Hence, only a tiny fraction of photons (between 0 and a few) incident on the cameras make it to the PMT. This makes it possible to work at the low light levels required to see the SPE peak.

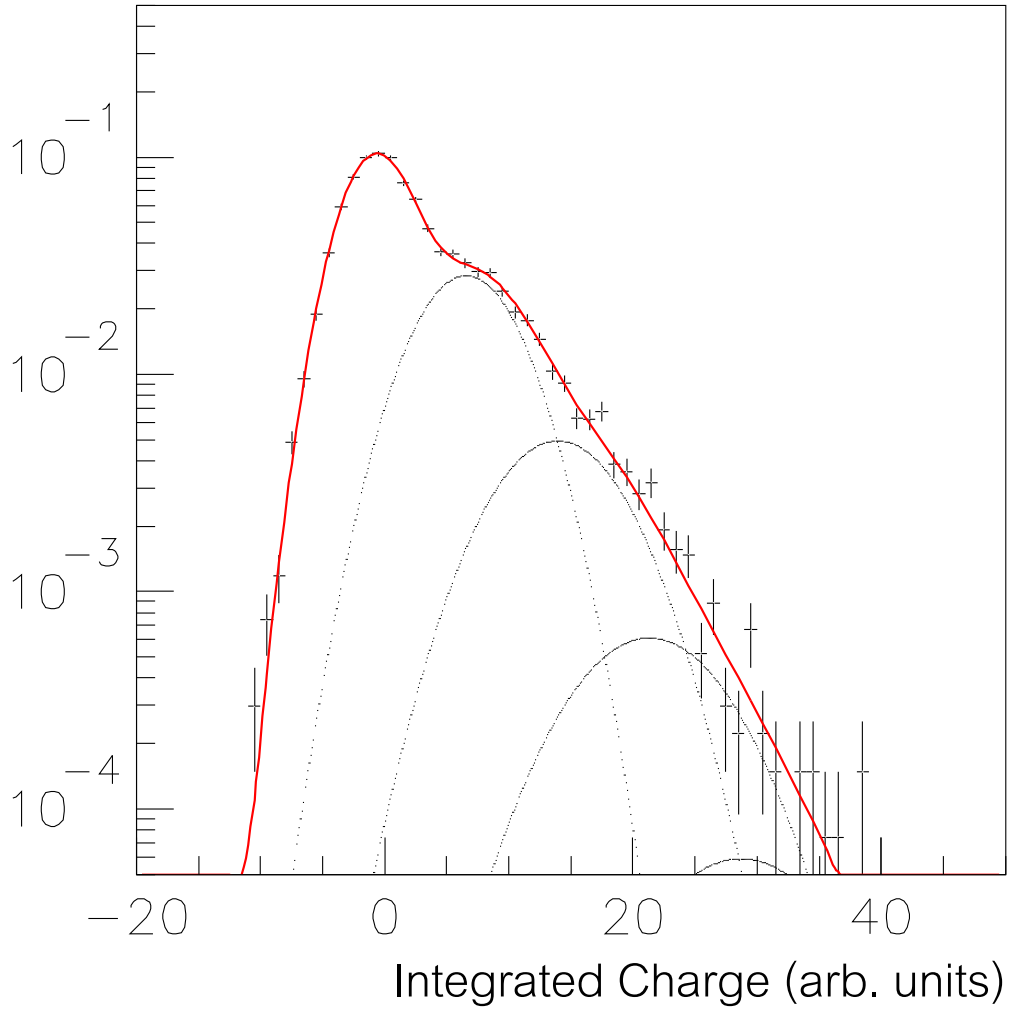

Figure 3.22: Single photoelectron charge distribution data with the corresponding fit. The different Gaussians corresponding to the number of photoelectrons are also shown. A similar distribution exists for every PMT in the *VERITAS* array. Image credit: adapted from Figure 13 in [53].

Thus, it is possible to construct a relation between the variance in the charge and the mean amount of charge from which the PMT absolute gain can be extracted:

$$\sigma^2 = G^2 N = G\mu. \tag{3.15}$$

There is one caveat to this method that must be mentioned. In this model, the statistical fluctuations at the other dynodes have not been considered. These follow a Polya distribution [54]. The corrected equation for the gain is

$$G = \frac{1}{1+\alpha^2}\left(\frac{\sigma^2}{\mu}\right). \tag{3.16}$$

where α is called the Polya factor, defined as

$$\alpha = \frac{\sigma_{spe}}{\mu_{spe}} \tag{3.17}$$

where σ_{spe} and μ_{spe} are the single photoelectron width and mean determined from from Equation 3.13. Polya factors differ PMT to PMT (see Figure 3.23) and change with time. Thus, it is not enough to track the absolute gains using the photostatistics method; dedicated SPE measurement runs must also be taken such that the Polya factors can be tracked and the nightly absolute gains can be corrected. To this effect, dedicated SPE measurements are made once a month.

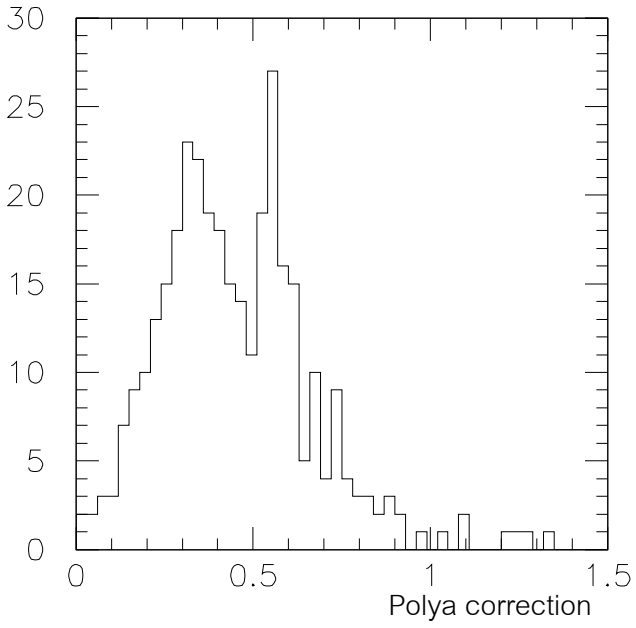

Figure 3.23: Distribution of Polya corrections $1/(1+\alpha^2)$ determined from SPE calibrations. Image credit: adapted from Figure 16 in [53].

3.6.2 PMT Relative Gain Calibration

The relative gain of a PMT is a measure of how much charge a PMT produces for a given amount of light compared to the average response of all the PMTs. The *VERITAS* cameras are "flatfielded" based on the relative gains of the PMTs, a process which ensures that for a given amount of light, all the PMTs produce the same signal. Due to nonuniformity in the PMT response, there can be night-to-night variations which require tracking such that they can be corrected for in the analysis (hence the reason for a nightly flasher run). The details of the relative gain calculation can be found in [53].

The relative PMT gains and gain distributions are calculated nightly and verified as part of the next-day data quality monitoring in order to track the stability of the PMTs. An example of the PMT relative gain distributions for each telescope is given in Figure 3.24. When the distributions are deemed to be too wide (due to changes in the absolute gains caused by the ageing of the PMTs), the cameras are re-flatfielded to tighten the distribution. Usually, the absolute gains are also increased to ensure that the detector configuration is stable over long periods of time. This is usually only done once a year, at the beginning of the observing season.

3.7 On-line Monitoring Tools

3.7.1 Quicklook

Quicklook is a near-real-time analysis tool that reads data as it is being sent to the Harvester. Using a simplified analysis, Quicklook is used to gain a preliminary understanding of the results of the data currently being taken. This is useful as it is a measure of the overall health of the experiment at any given time but also has science applications. Some objects are known to flare with minute-timescales. Hence, if one waits for the data to be analysed (say) the following day as part of a standard analysis, it would be entirely possible to miss the fact that an object was flaring and perhaps some interesting science. Furthermore, triggers from instruments such as the *Fermi*-GBM can have error boxes (the region within the 1σ errors on a position measurement) larger than the *VERITAS* field of view. Thus, it is likely that when taking data after one such trigger, the object in question is not at the originally quoted position. Thus, the ability to search the field-of-view for significance "hotspots" is required so observations can be adjusted accordingly.

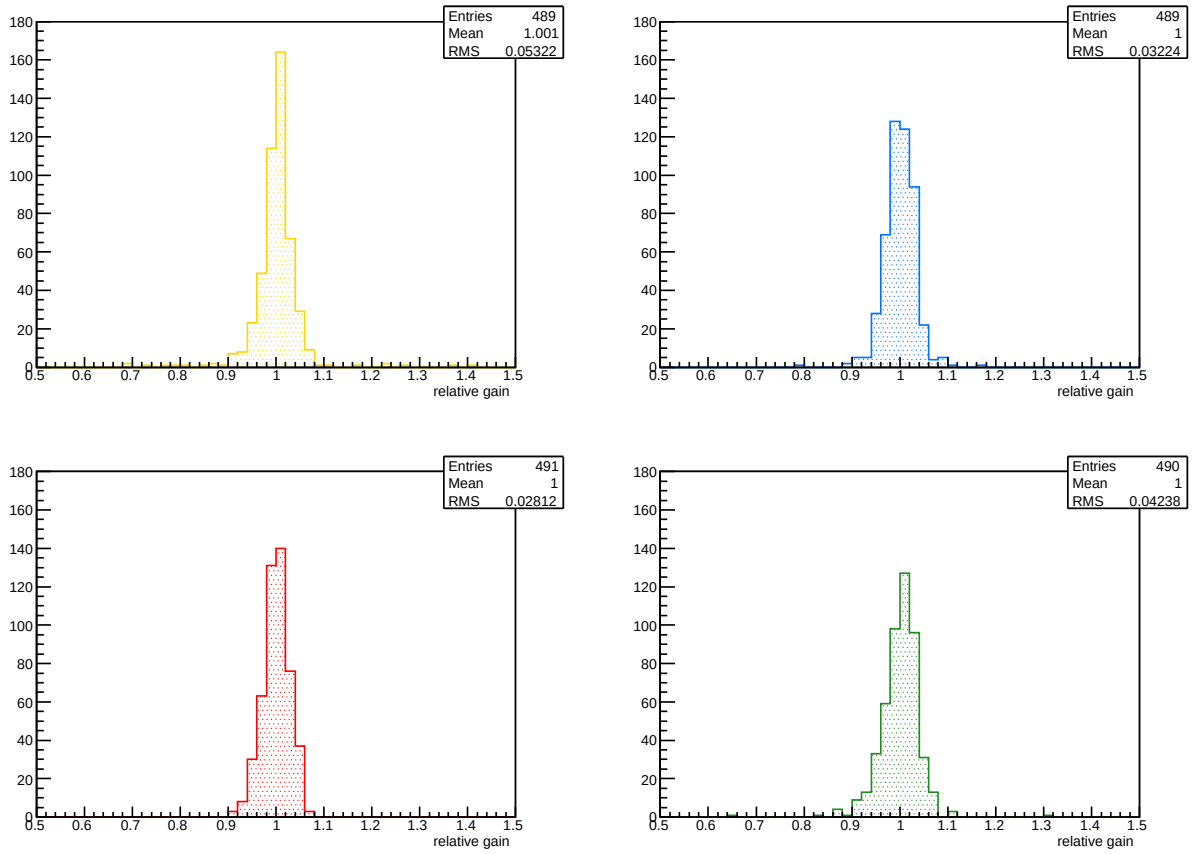

Figure 3.24: Relative gain distributions for the 4 telescopes, ordered Telescope 1 - Telescope 4 from top left to bottom right.

3.7.2 Current Monitors

Simply put, the current monitors are a a set of sensors installed in the cameras (one per PMT) which measure the instantaneous current of the PMT and relay it to software running in the *VERITAS* control room. The current monitors have an absolute resolution of 0.5 μA and the measurements are stored in the *VERITAS* database once a minute. They are read out and displayed at $\sim$ 1 Hz for monitoring purposes during observing.

The PMT currents are overlaid on a display and allow for the instantaneous state of the camera to be measured. The current monitors also relay information to the software which controls the PMT high voltage, which can disable a PMT if its current is too high, such as when a bright star is in the field of view. The auto-suppress threshold is set at 40 μA. The current monitors also act as a safety mechanism in the event of a car approaching the observatory with its lights on, or the beam from an errant flashlight. An example distribution of PMT currents for each of the four telescopes is given in Figure 3.25.

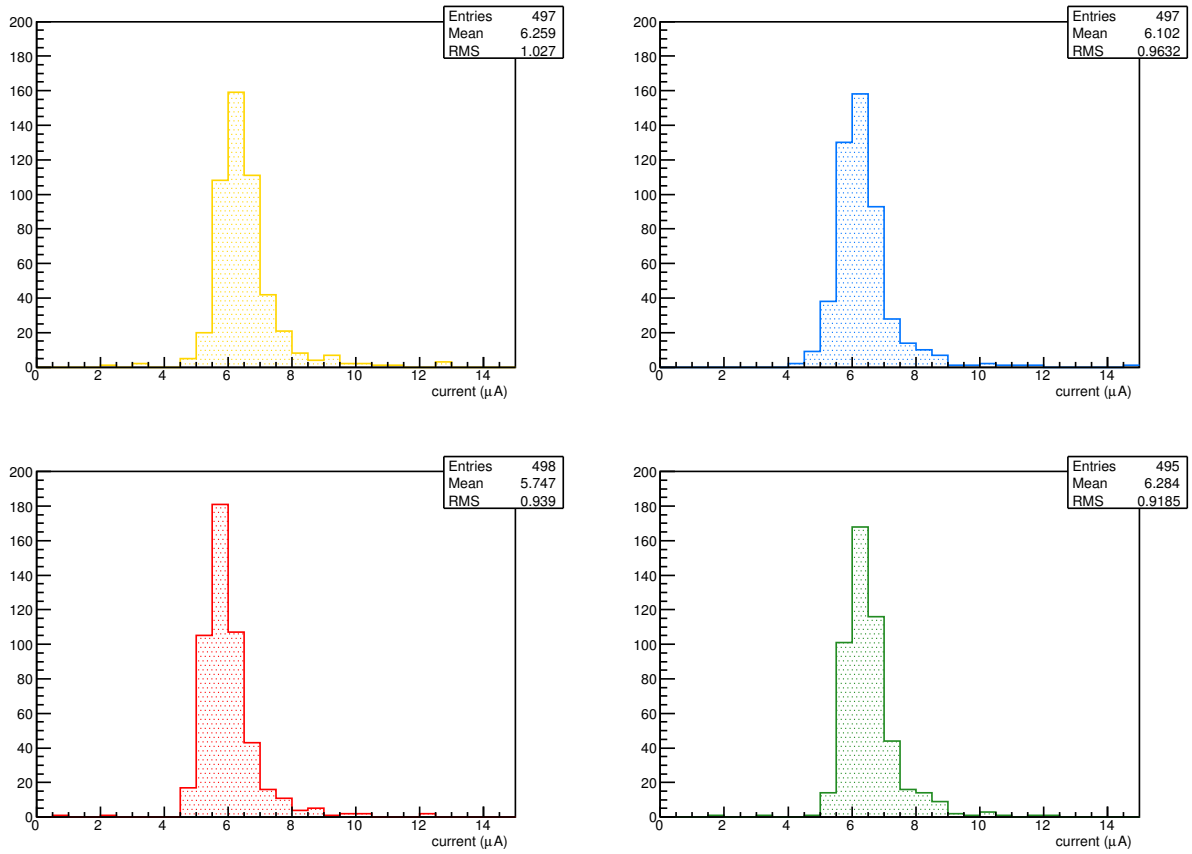

Figure 3.25: PMT current distributions during a typical observing run. The plots are ordered Telescope 1 to Telescope 4 from the top-left to bottom-right.

3.7.3 Miscellaneous

The following is a short list and description of several of the other monitoring tools used during observing to verify the operation of the array.

- Temperature sensors: Temperature sensors are installed in the telescope trailers, cameras, and FADCs to ensure that they are not too hot; given that the FADCs represent the bulk of the cost of a telescope, if they were to overheat (due to a failure in their cooling system, for example) the damage could be catastrophic and permanently disable a telescope.

- Weather station: A weather station is set up at the *VERITAS* site in order to monitor the wind speed and relative humidity. A reflector dish is effectively a giant sail; high wind speeds result in strong forces on the telescope which affect telescope pointing accuracy and could possibly damage the positioners. The threshold for discontinuing

observations is 20 mph constant wind, or gusts above 25 mph. High humidity ($\gtrsim 75\%$) can cause arcing in the telescope cameras (recall that PMTs are operated at a high voltage), so in such cases the cameras are powered down and observing is postponed until the humidity drops.

- LIDAR: A LIDAR is installed at the basecamp to measure the transparency of the atmosphere. At the time of writing, this information is not used in data analysis, but other collaborations have shown that it can be used to reduce the systematic errors induced in an analysis by changes in the atmosphere [55].

3.8 Summary

In this chapter, details of the *VERITAS* experiment and a description of the data acquisition system have been presented. The operating principles of PMTs (which are used to detect the Cherenkov photons from air showers) has been presented and discussed in detail. PMTs are extremely sensitive to light and can be damaged if exposed to high light levels. Thus, when operating it is important to ensure that both the amount of light reaching the PMTs and the currents flowing through them are not too high. This demonstrates the need for new observing modes such that *VERITAS* can operate under moonlight.

Chapter 4

VHE Gamma-Ray Data Analysis

Data, I think, is one of the most powerful mechanisms for telling stories. I take a huge pile of data and I try to get it to tell stories.

Steven Levitt (Economist)

4.1 Outline

The analysis of very high energy (VHE) gamma-ray data begins with a data file containing the information pertaining to the N events in the data run. This amounts to $N \times 4 \times 499$ FADC traces like those shown in Figure 4.1. There are also auxiliary data such as time stamps, and various words identifying, for example, which channels had an L1 trigger, and which telescopes contributed to the L3 trigger. From this, the following steps are performed:

1. Pedestal calculation and subtraction: The baseline for each event is removed such that the Cherenkov signal (if any) can be extracted.

2. Image identification: The PMTs which constitute the image are identified. This is known as "image cleaning".

3. Charge integration: The region in each FADC trace containing the signal is identified and the corresponding charge in each channel is integrated.

4. Flatfielding: The charges are scaled by the inverse of the PMT relative gain to reduce any pixel-to-pixel inhomogeneity in the PMT response.

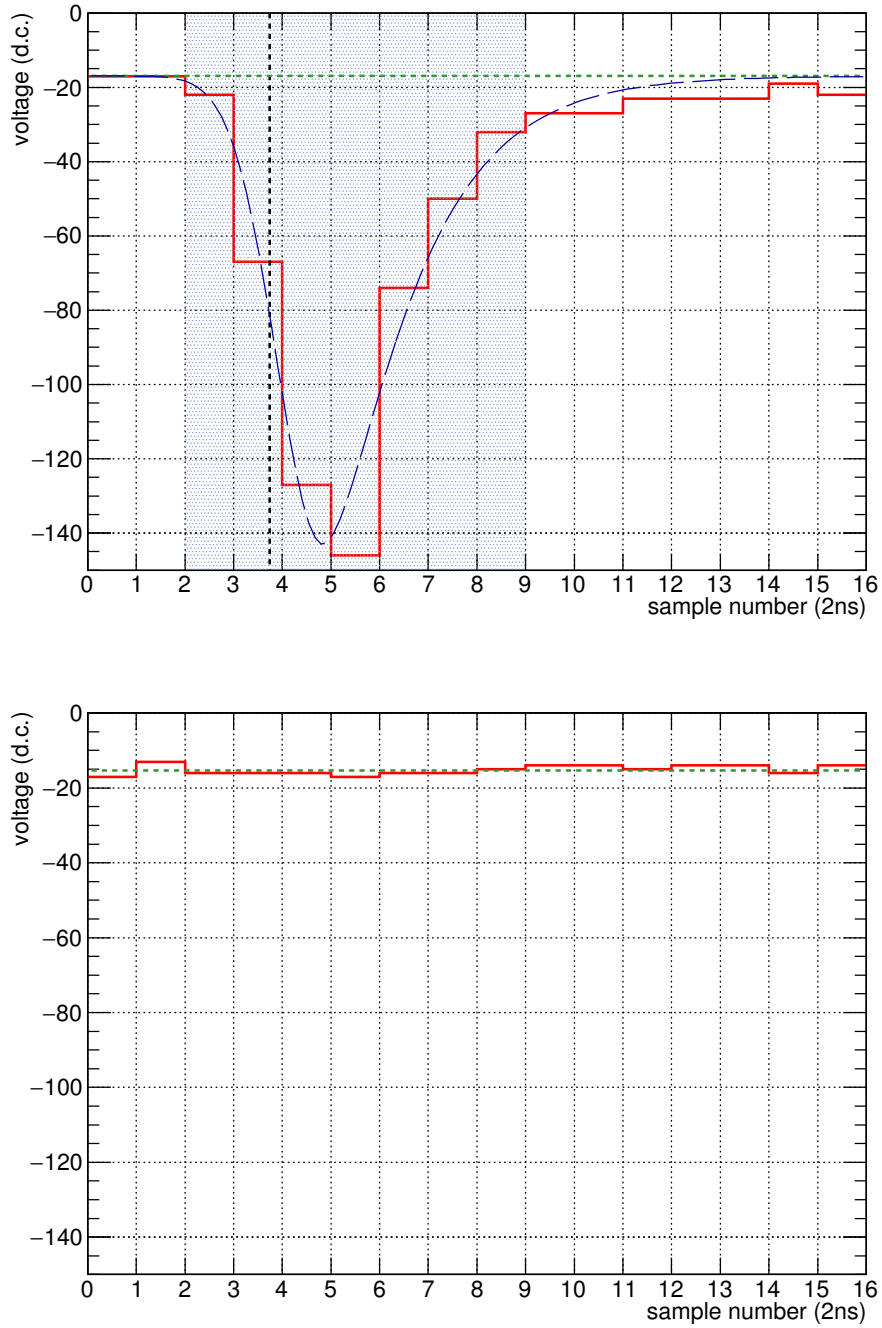

Figure 4.1: **Top**: An example FADC trace containing a Cherenkov pulse. The scale on the ordinate is digital counts (d.c.). The vertical line is the time at which the pulse reaches 50% of its maximum value. The dashed horizontal line is the baseline, or pedestal. A fit to the pulse shape is also shown. Pulse fitting allows for a more accurate measure of the charge, but requires ~ 90 times as long as simply summing the voltages within the integration window (the shaded region), so it is not used in a typical analysis. **Bottom**: An FADC trace containing only the pedestal.

5. Image parametrisation: Shower images are parametrised such that they can be compared to simulated gamma rays.

6. Direction reconstruction: The direction from where the gamma ray came is determined via the geometry of the various shower axes.

7. Distance reconstruction: The point on the ground where the air shower would have arrived (had it not been absorbed by the atmosphere) is determined.

8. Shower energy reconstruction. The parametrised shower is compared to simulated gamma rays in order to reconstruct the energy of the primary which initiated the air shower.

The above steps are repeated for every event. From here, source and background regions are identified and fluxes can be calculated.

In the next section, the specifics of the previously mentioned steps are presented and the details of one of the *VERITAS* analysis tools are discussed. The author did not make any modifications to the software packages in order to produce this thesis, thus only an overview of the methodology is provided. For an in-depth description of the analysis procedure, see [56].

4.2 General Description of the Analysis

4.2.1 Pedestals

The first step in signal extraction is the pedestal calculation, which allows the baseline of the signal in each PMT to be measured. Pedestal events are events that were not triggered by Cherenkov showers or large night sky background fluctuations. They are used to provide a measure of the baseline on which Cherenkov pulses from air showers sit. These "empty" FADC traces are read out when the *VERITAS* DAQ is triggered externally at a rate of 1 Hz. The pedestals (ρ) are calculated by taking FADC traces (on a per-channel basis) and computing the average over a number of FADC samples (e.g. 7 samples). Then, in the analysis, the pedestal values are removed from the FADC values, providing a baseline-subtracted FADC trace containing charge $Q_k = q_k - \bar{\rho}_k$ for PMT k.

On nights where the moon is illuminating the sky, the magnitude of the fluctuations in the pedestals, which contain only random noise due to night sky background photons (and the occasional truncated Cherenkov pulse) will change in accordance with how much light is in the sky. It is empirically true that the pedestal variance (or simply pedvar, denoted σ^2)

scales linearly with the brightness of the sky and is hence a good proxy for the amount of noise in the data (see Figure 4.2). In a typical *VERITAS* analysis, the pedestals and pedvars are computed in three minute time windows to track any changes over time.

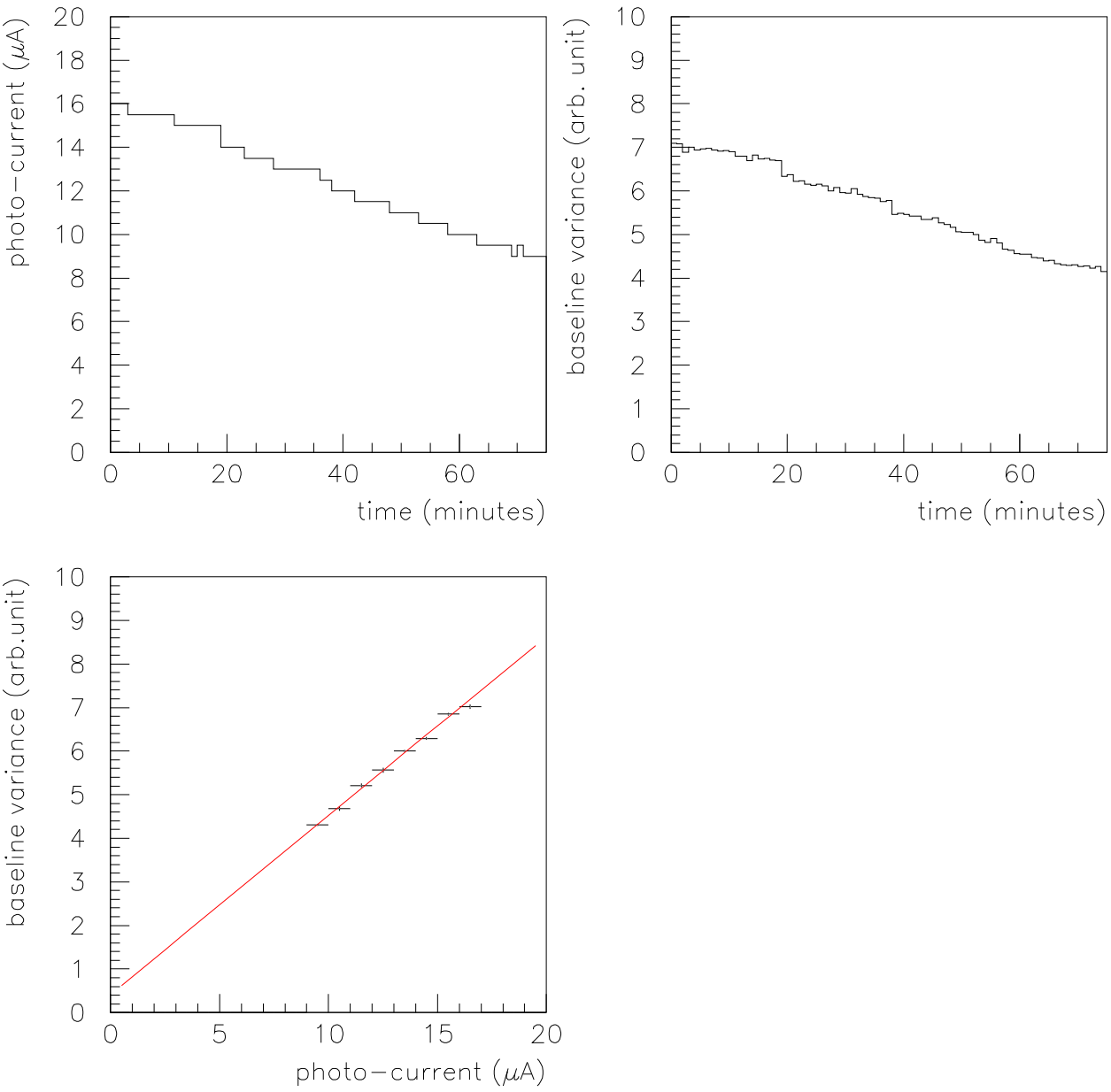

Figure 4.2: **Top left**: Current versus time for a single PMT as measured by the *VERITAS* current monitors on a night where the Moon was setting. **Top right**: σ^2 versus PMT current for that PMT calculated from pedestal events. **Bottom left**: Correlation between σ^2 and PMT current with a fit indicated. Image credit: Figure 2 in [57]

4.2.2 Image Cleaning

Image cleaning is the process of identifying Cherenkov shower images by comparing the amount of charge in a given channel to the RMS of the pedestal for that channel. This is a signal-to-noise (S/N) calculation; to be considered a "picture" pixel, the S/N

$$(S/N)_k = \frac{Q_k}{\sigma_k} \tag{4.1}$$

must be greater than 5. "Border" pixels (*i.e.* pixels on the edge of a picture pixel) must have a S/N of 2.5, and must be adjacent to at least one picture pixel. The second criteria has the effect of removing isolated pixels in the camera which contained a large fluctuation. An example of the cleaning procedure is given in Figures 4.3 to 4.5. Cuts can also be made to take into account bright stars which would contaminate images with large amounts of light; using star catalogues it is possible to identify pixels containing bright stars and remove them from the analysis procedure. The information can be "recovered" later in the analysis by (e.g.) using the average signal in adjacent PMTs as a proxy.

4.2.3 Flatfielding

To account for night-to-night differences in the PMT gains, the charge in an image is divided by the relative gain of the PMT in that channel:

$$Q'_j = \frac{Q_j}{g_j} \tag{4.2}$$

where the relative gain g_j has been determined using the method described in Section 3.6.2. This has the effect that if a PMT has a relative gain that is lower than the average, the charge for that channel is boosted accordingly (and vice-versa for PMTs with high relative gains).

4.2.4 Image Parametrisation

An image of a gamma-ray-induced air shower will be a 2D projection of the air shower, resembling an ellipse (Figure 4.6). Based on Monte Carlo simulations of gamma-ray and cosmic-ray air showers, A. M. Hillas proposed to quantify the image properties in terms of the parameters of an ellipse [58] and demonstrated that this would provide significant discriminating power between gamma-ray-like events and cosmic rays. These are historically known as the Hillas parameters, shown in Figure 4.7. They are defined as follows:

- Width (Length): The RMS width (length) of the ellipse's semi-minor (semi-major) axis, denoted w (l).

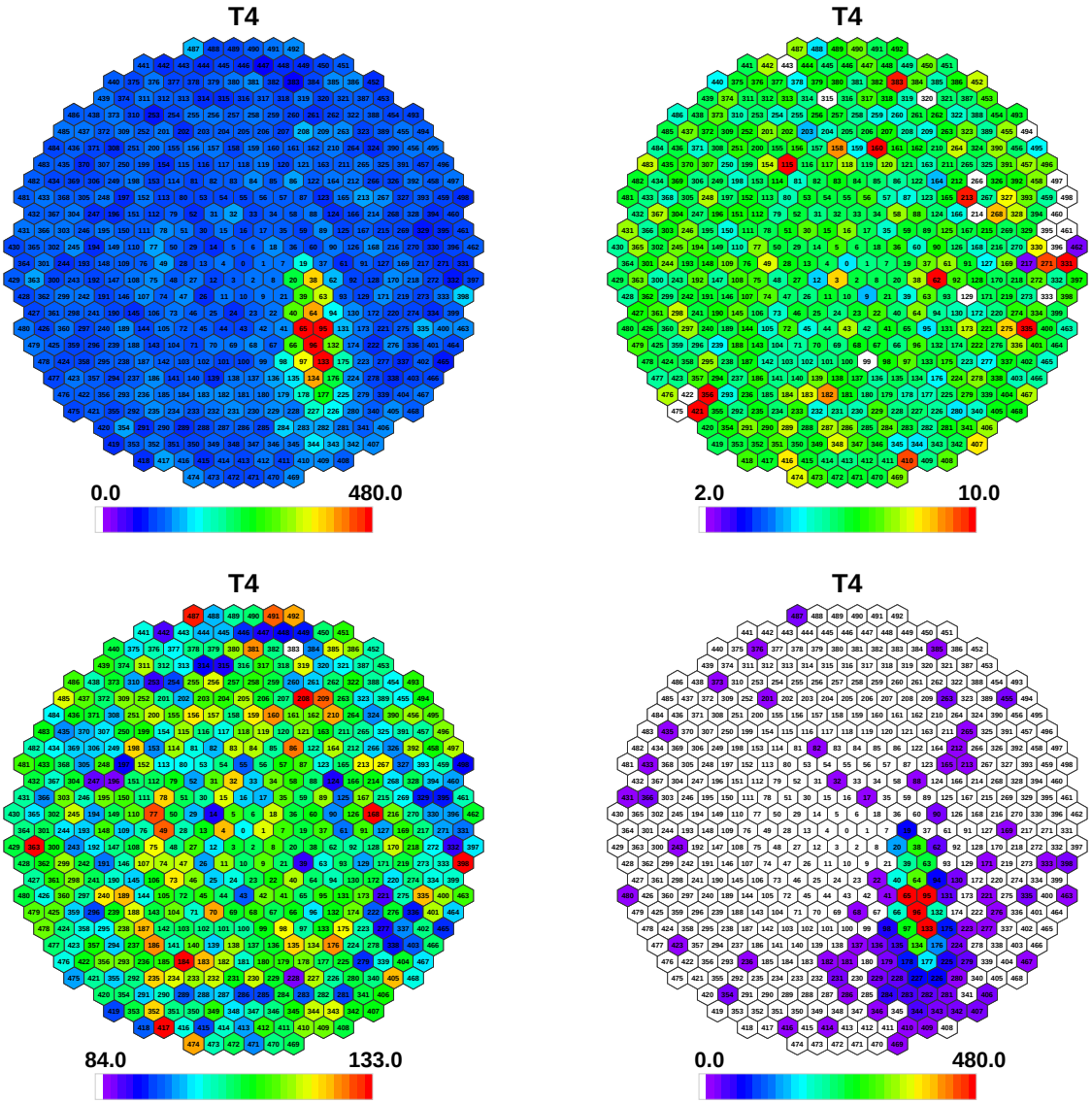

Figure 4.3: **Top left**: A raw image. **Top right**: The pedvars for the event. **Bottom left**: The pedestals for the event. **Bottom right**: The pedestal-subtracted image. The scale in each figure is digital counts. Image credit: A. McCann

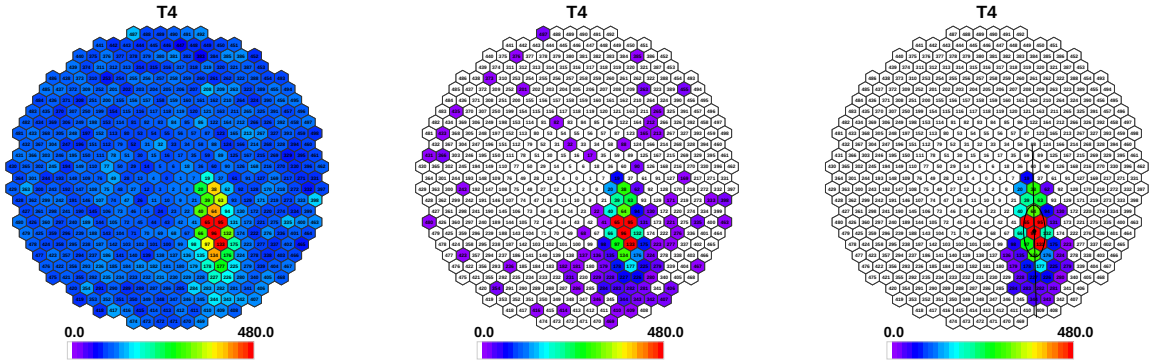

Figure 4.4: Side-by-side comparison of the different steps of image cleaning. **Left**: Raw image. **Centre**: Pedestal-subtracted image. **Right**: Cleaned image with the major axis of the image indicated along with a fit to the image centroid. Image credit: A. McCann

- Distance: The distance between the image centroid and the centre of the camera.
- FracN: The fraction of the total size contained in the N brightest PMTs. It is a measure of how concentrated the image is.

The following two Hillas parameters are not used in a stereo analysis, and hence are not used in this thesis. Note that these are valid when the telescope is pointing directly at the source. They have been included for completeness:

- Azwidth: The RMS spread of light along a line perpendicular to the line connecting the image centroid to the camera centre. It is a measure of the shape and orientation of an image.
- Miss: The perpendicular distance between the major axis of the image and the centre of the camera FOV. This contributes to measures of the orientation of the image.

The computation of the Hillas parameters is **not** a fit (although fitting algorithms for showers exist and are used in some cases, like when a large amount of the shower is truncated by the limited field of view of the camera), but a moment analysis. Fitting each event is time-intensive and makes data analysis prohibitively long for large data sets.

There are a number of other parameters which have been deemed to be useful in the study of air showers:

- Loss: The fraction of the image charge on the edge of the camera. It is a measure of how well contained the image is within the camera.
- Size: The integrated charge in a shower image, denoted s.

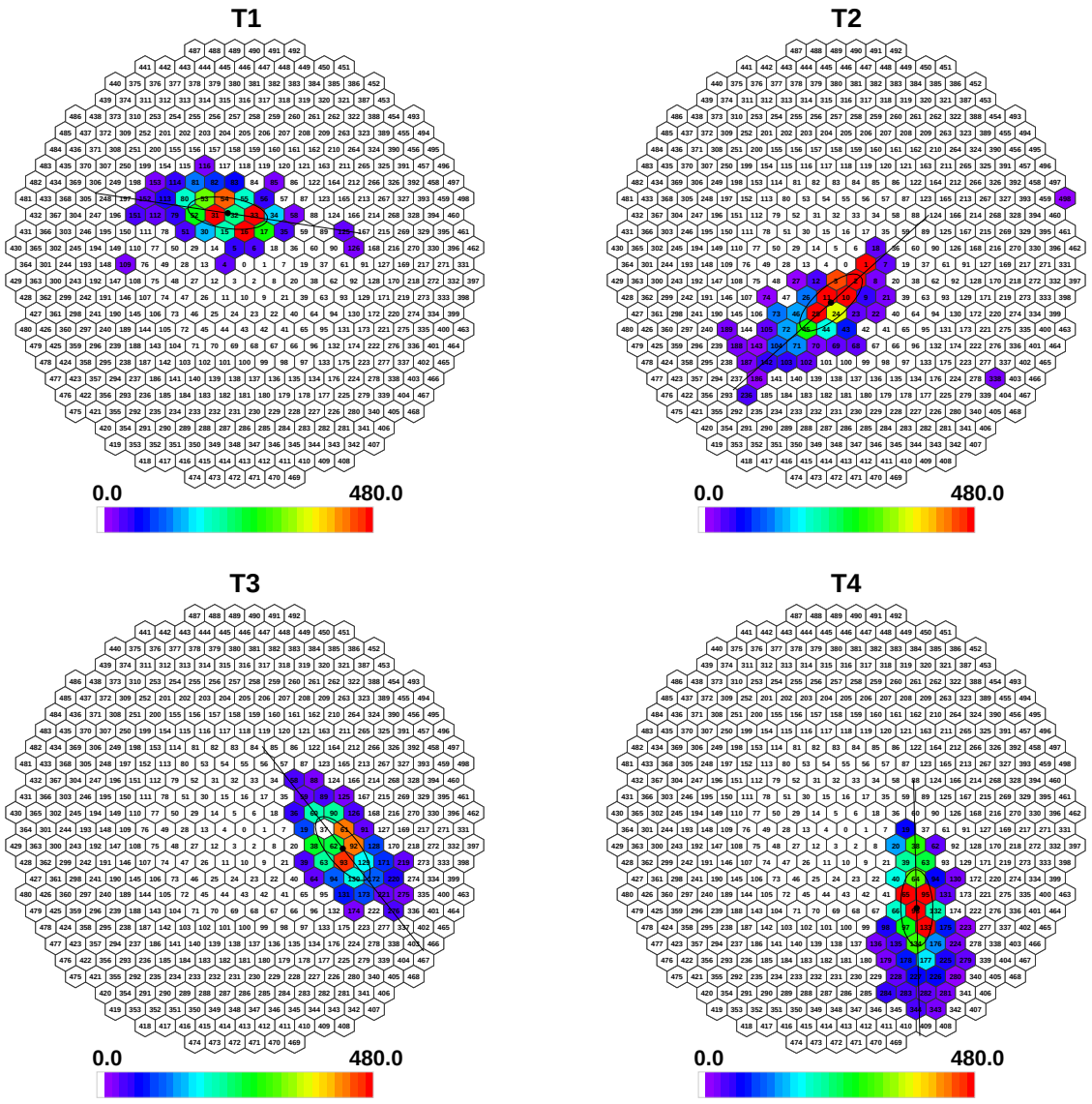

Figure 4.5: Cleaned images for an event for which each of the four telescopes contains an image. On each image the centroid and major axis resulting from a fit to the image is plotted. Image credit: A. McCann

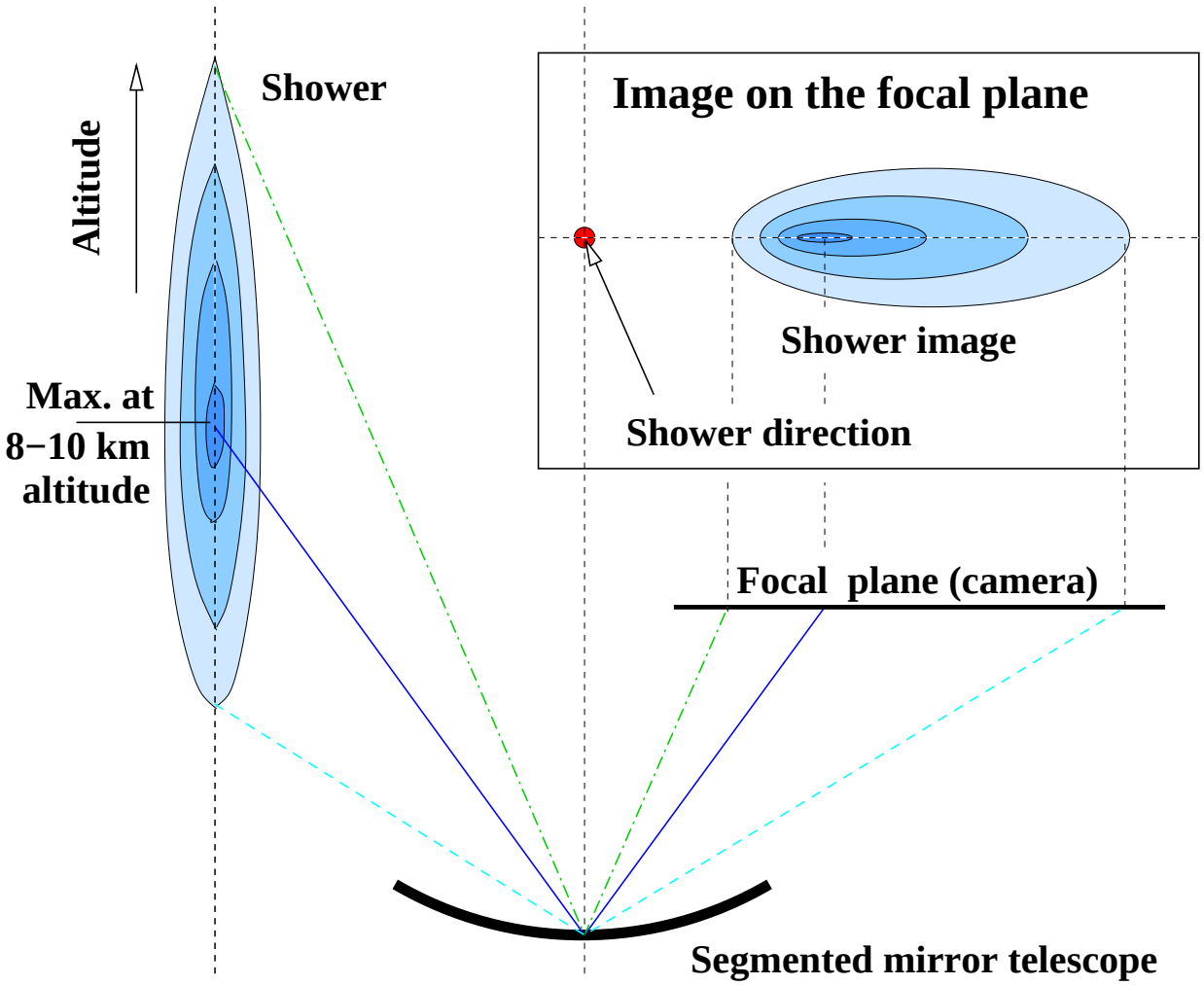

Figure 4.6: Geometry of how an air shower is projected onto the camera of a telescope. The axis of the shower is the major axis of the image, and points back to the origin location of the shower (*i.e.* the direction of the source). Figure 4.8 demonstrates how the direction is identified using this information in a stereoscopic analysis. Image credit: Figure 6 in [17].

- Alpha: The angle between the major axis of the image and a line connecting the image centroid to the centre of the FOV. This is a measure of the image orientation. Note that this parameter is only useful for monoscopic analyses and hence is not used in this work.

4.2.5 Direction

The direction of a gamma-ray-like event can be determined by overlaying the shower images and determining the intersection point of the major axes (Figure 4.8). A weighted average of the intersection points is then used to identify where in the sky the gamma ray originated.

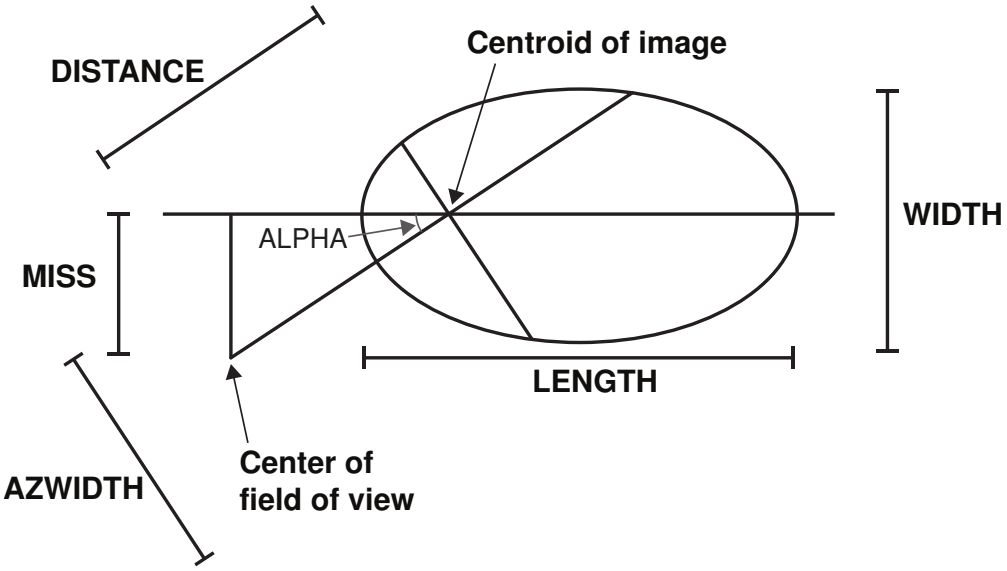

Figure 4.7: Cartoon of the historical Hillas parameters. Image credit: Figure 4.1 in [59].

This can be done both pairwise for each telescope pair (as is the case in the analysis presented in this work), or as a simultaneous fit to each image in an event.

An example of the weighting used in the direction reconstruction (and the previously mentioned core location reconstruction) is

$$W_{ij} = \left(\frac{1}{s_i} + \frac{1}{s_j}\right)^{-1} \times \left(\frac{w_i}{l_i} + \frac{w_j}{l_j}\right)^{-1} \times \sin\theta_{ij} \tag{4.3}$$

where i and j denote two telescopes of a pair, θ_{ij} is the angle between the image major axes, and the other parameters have previously been introduced. Thus, long, narrow pairs with large angles between them are weighted higher.

4.2.6 Shower Core Reconstruction

The observed properties of an air shower do not only depend on the energy of the primary which induced the air shower, but also the location of the shower relative to the telescope. In other words, showers will look different depending on where they fall with respect to the array. The shower core position is the physical location on the ground where the gamma ray would have landed had it not been absorbed by the Earth's atmosphere. It can be determined by placing the camera images at the locations of the telescopes and finding the weighted intersection point of the image major axes. This is shown in Figure 4.9.

The impact parameter (denoted r) is the distance between a telescope and the shower core in the plane perpendicular to the shower arrival direction. The impact parameter is an

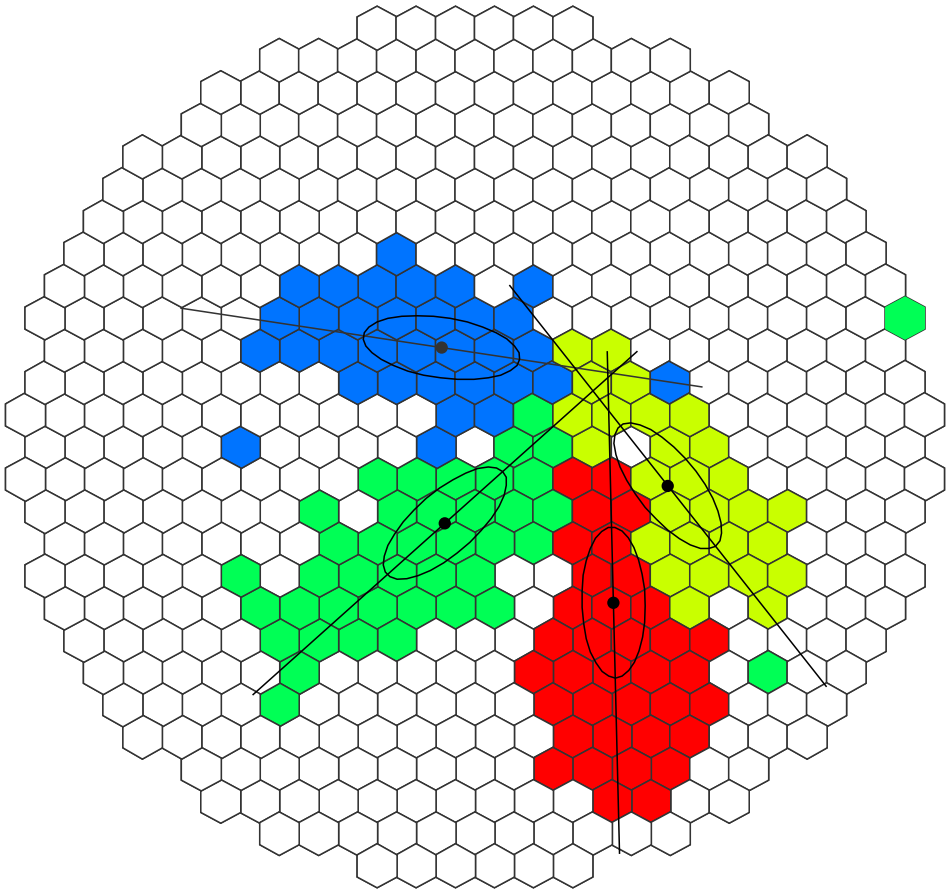

Figure 4.8: Schematic of the arrival direction reconstruction. Each of the four camera images has been superimposed, and the (weighted) intersection point between the four major axes of the images is the arrival direction of the gamma ray. Image credit: A. McCann

important parameter for the analysis; it is used when estimating the energy of the primary which caused the air shower (see Section 4.2.9).

4.2.7 Height of Shower Maximum

Geometrically, it can be shown that the plane of the camera images projects onto a plane perpendicular to the shower arrival direction and allows the height of shower maximum to be identified (see Figure 4.10 and [60]). The shower maximum is the point where the air shower contains the maximum number of particles and is consequently the brightest part of the shower. Its height can be calculated geometrically; for a telescope i, the height H_i can be determined via

$$H_i = \frac{r_i}{\tan \theta_i} \tag{4.4}$$

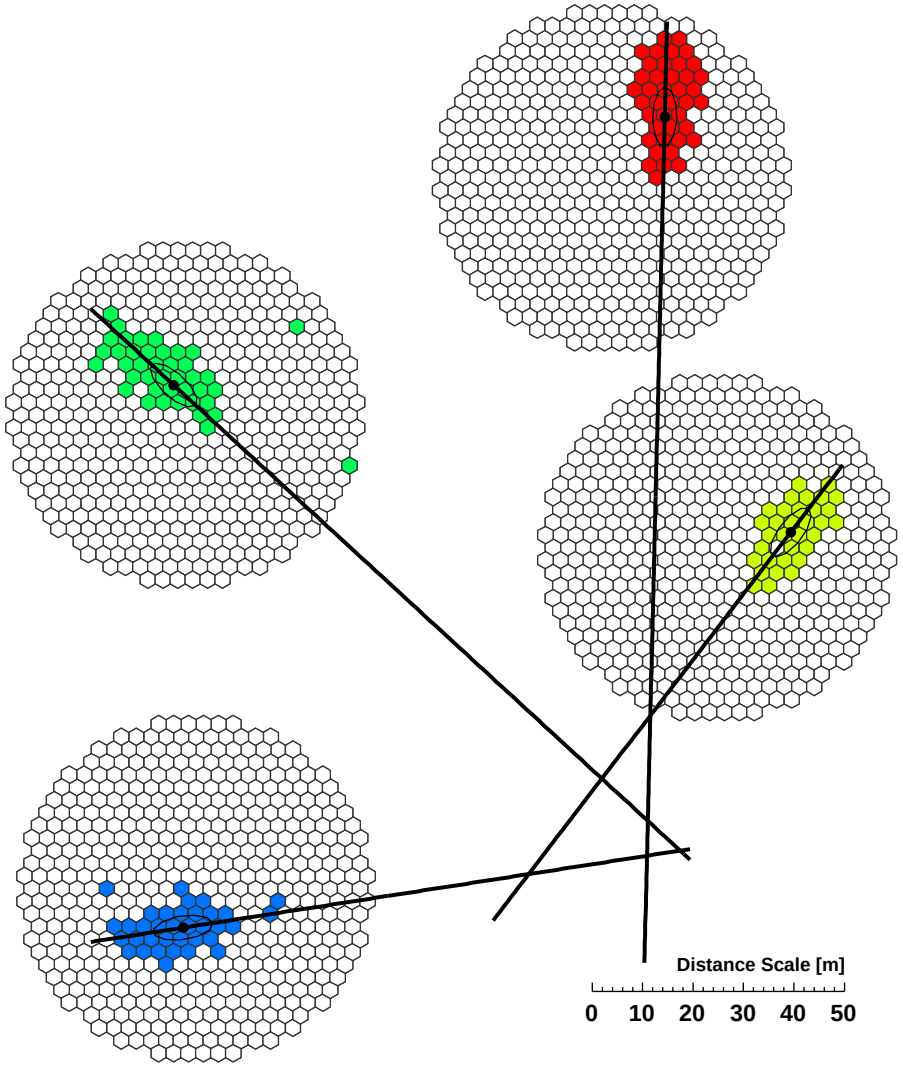

Figure 4.9: Schematic of core reconstruction. The telescope cameras are not drawn to scale. Each image is placed in the plane of the ground at the location of the telescope that recorded said image. The (weighted) intersection point of the shower major axes where each shower is the core position, which is the location on the ground where the gamma ray would have arrived had it not been absorbed by the Earth's atmosphere. Image credit: A. McCann

where H_i is the height of the shower maximum, r_i is the distance between the telescope and the shower core position, and θ_i is the angle between the image centroid and the reconstructed arrival direction in the camera of telescope i. This relation can be derived from the geometry in Figure 4.10.

For a given energy, air showers produced by charged cosmic rays penetrate deeper into the atmosphere than those produced by gamma rays. Thus, the height of the shower maximum is useful for rejecting background events.

4.2.8 Image Selection

Image selection is the process wherein cleaned images are selected for reconstruction using a set of image quality cuts. The specific cuts used in a standard *VERITAS* analysis are given later in Table 4.1.

4.2.9 Energy Reconstruction

The energy of the primary is determined by comparing the shower parameters from data to those from simulated gamma rays. Thus, energy reconstruction relies heavily on a solid understanding of shower physics. The ability to estimate shower energies comes from simulating millions of gamma-ray-induced showers and using the parametrised shower images to produce reference tables. These tables are multidimensional (functions of shower size, telescope pointing, etc.) in order to represent as large a subset of the vast observational parameter space as possible.

The weighted reconstructed energy is computed as follows:

$$E = \frac{\sum_{i=1}^{N_{Tel}} E_i/\sigma_i^2}{\sum_{i=1}^{N_{Tel}} 1/\sigma_i^2} \tag{4.5}$$

where E_i is the median entry in the table and σ_i is the 90% width of the size distribution. Note that the energy estimate (*i.e.* E) is a function of the image size (s_i), zenith angle (z), and impact parameter (r_i); this has not been explicitly written for clarity. An example of an energy reconstruction table is given in Figure 4.11. It is important to simulate a sufficiently large number of high energy photons; if a table bin has only a handful of entries, then the energy reconstruction will be limited by whatever fluctuations happened to occur in the simulated showers. To avoid this, *VERITAS* tables require at least five entries per bin for energy reconstruction. The distribution of the number of events that produced the tables in Figure 4.11 is given in Figure 4.12.

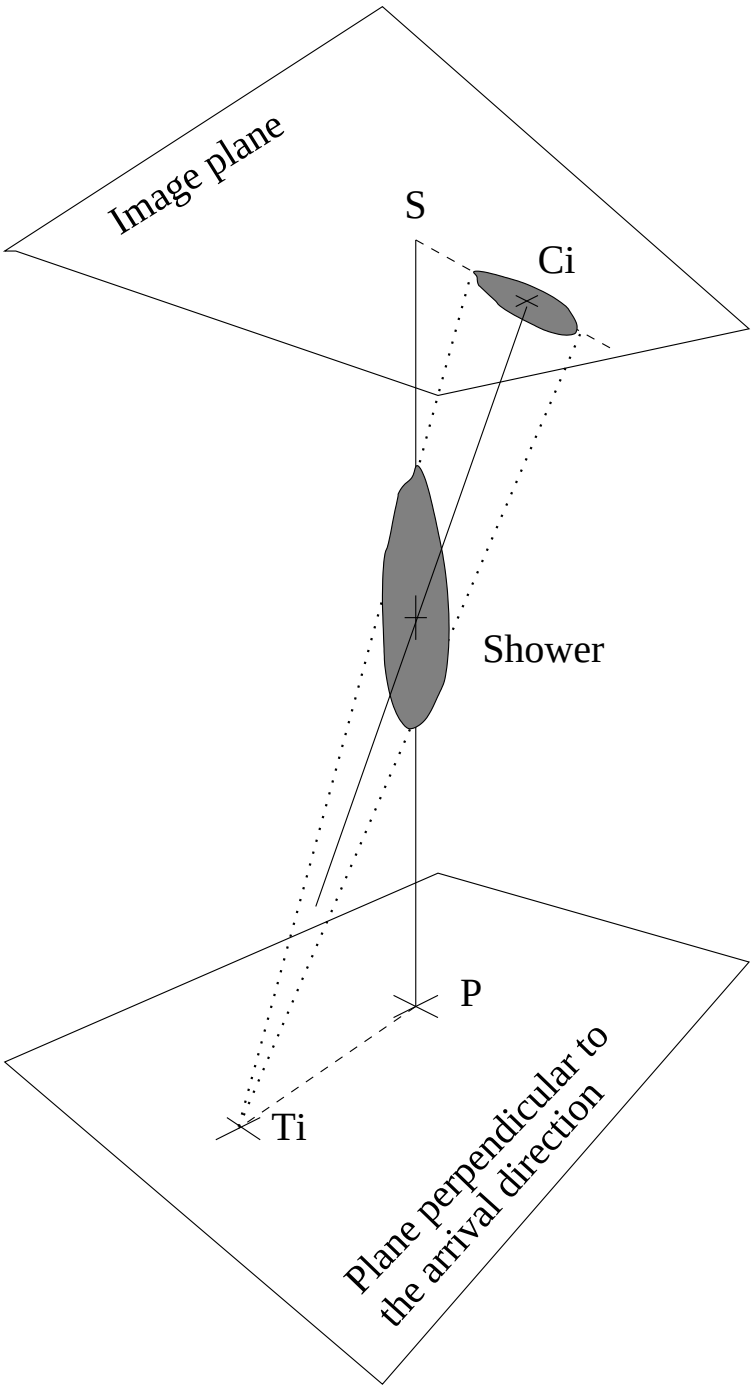

Figure 4.10: Schematic of how the shower is projected into the image plane. **P** is the core position, **S** is the source location, **Ti** is the telescope location, and **Ci** is the location of the image centroid in the image plane. The height of the shower maximum can be determined using the geometry shown here via Equation 4.4. Image credit: Figure 1 in [60].

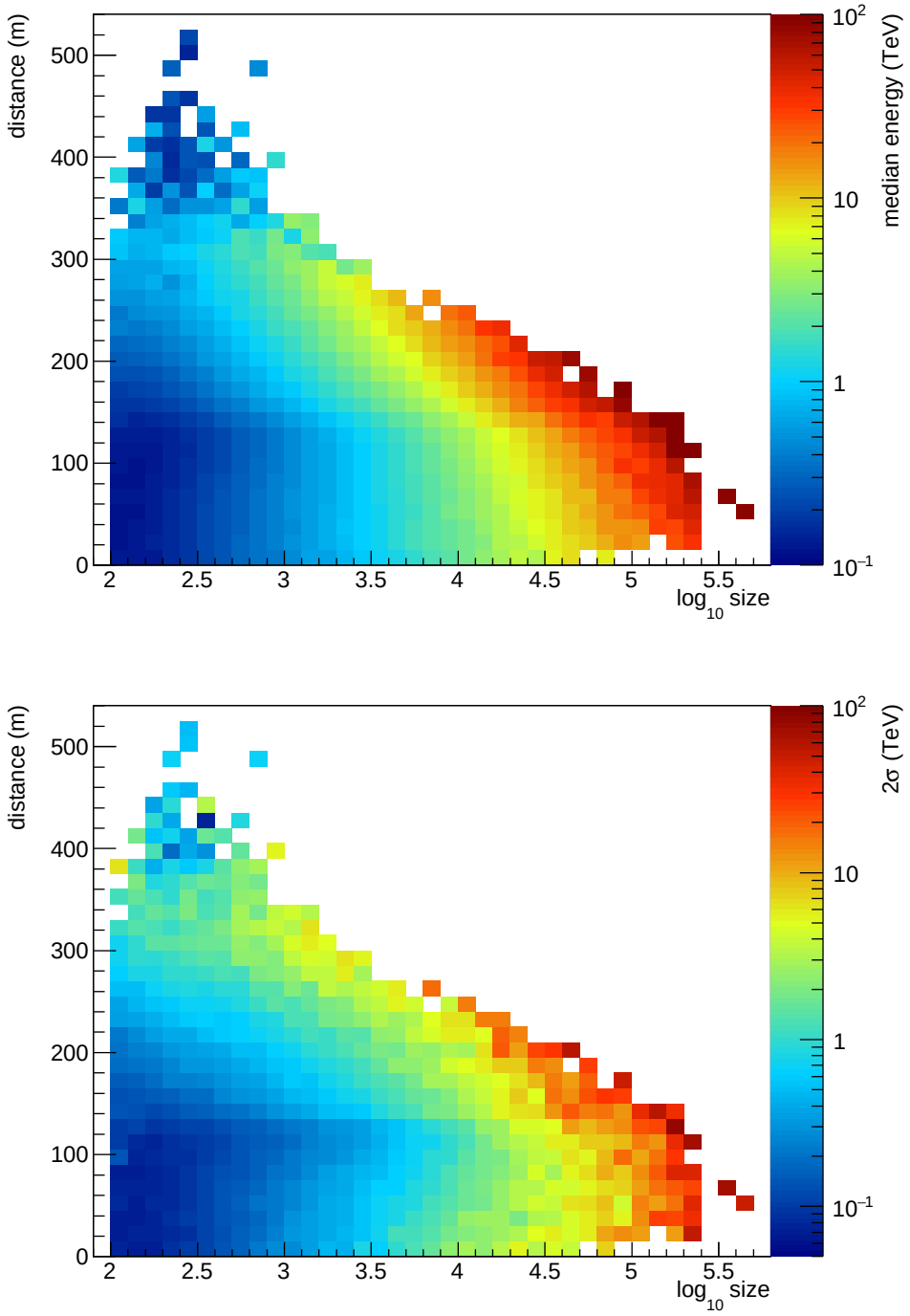

Figure 4.11: **Top**: An example of a gamma ray energy reconstruction table. The x-axis is the logarithm of the integrated shower size and the y-axis is the impact parameter. The z-axis is the median energy of the gamma-ray for a given size and impact parameter. **Bottom**: Distribution of widths for the above table. The x and y axes are the same, but the z-axis scale is twice the value of σ used in Equation 4.5.

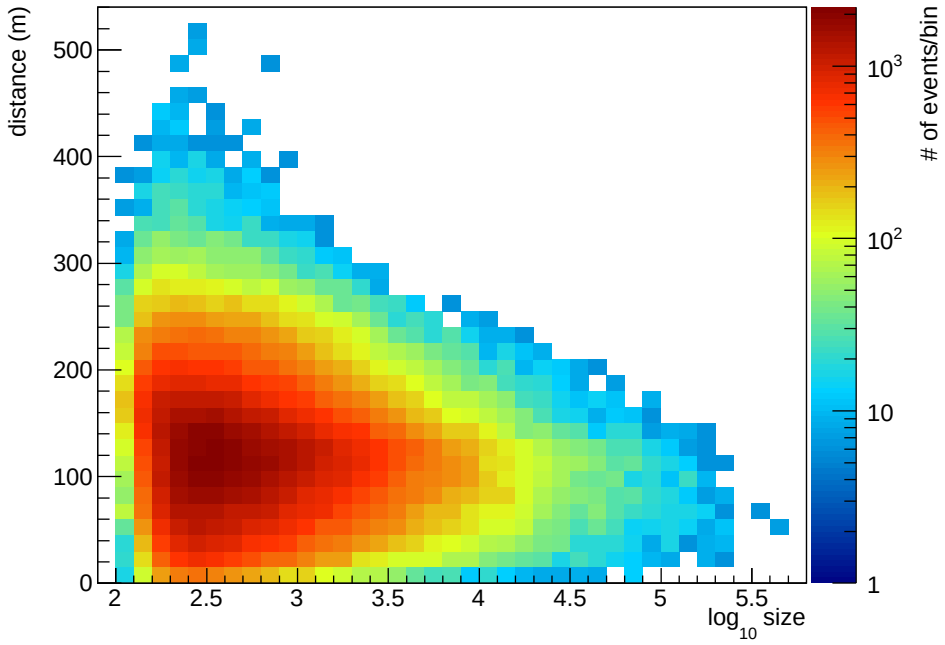

Figure 4.12: The number of events that went into each bin in Figure 4.11

4.2.10 Gamma/Hadron Separation

At this stage of an analysis, showers have now had directions and energies assigned to them, but the issue of separating gamma-ray-like events from hadronic events remains. A powerful discriminator for this is the so-called mean scaled parameter. Physically, the mean scaled parameters are a measure of how similar air shower images are to simulated gamma-ray induced air showers (for which the physical properties are well known). Thus, they can be used to discriminate between cosmic-ray induced images and gamma-ray-like images.

The mean scaled parameter is computed as follows:

$$\mathrm{MSP} = \frac{1}{N_{tel}} \sum_{i=1}^{N_{tel}} \frac{p_i}{\bar{p}_{sim}(z, s, r)} \tag{4.6}$$

where $\bar{p}$ is the mean value of the parameter (the image width or length, denoted w or l) for a simulated gamma ray observed at a zenith angle z, with size s, and impact parameter r. The mean *reduced* scaled parameter is defined somewhat differently:

$$\mathrm{MSCP} = \frac{1}{N_{tel}} \sum_{i=1}^{N_{tel}} \frac{p_i - \tilde{p}_{sim}(z, s, r)}{\sigma_p} \tag{4.7}$$

where $\tilde{p}$ is the median value of p in the simulations and σ_p is the standard deviation of p. This method is known to be more robust against outlier events. Using these definitions, it is

possible to calculate the two main quantities used in gamma-hadron separation: the mean scaled width and length (denoted MSW and MSL), and similarly the mean reduced scaled width and length (denoted MSCW and MSCL).

A plot of the mean reduced scaled width distributions for a signal region and background region is shown in Figure 4.13. There is an underlying assumption that the background region contains only cosmic rays. There *is* a diffuse gamma-ray component, but it is small[1]. It can be seen by eye that for MSCW > 1 the distributions are dominated by cosmic ray events.

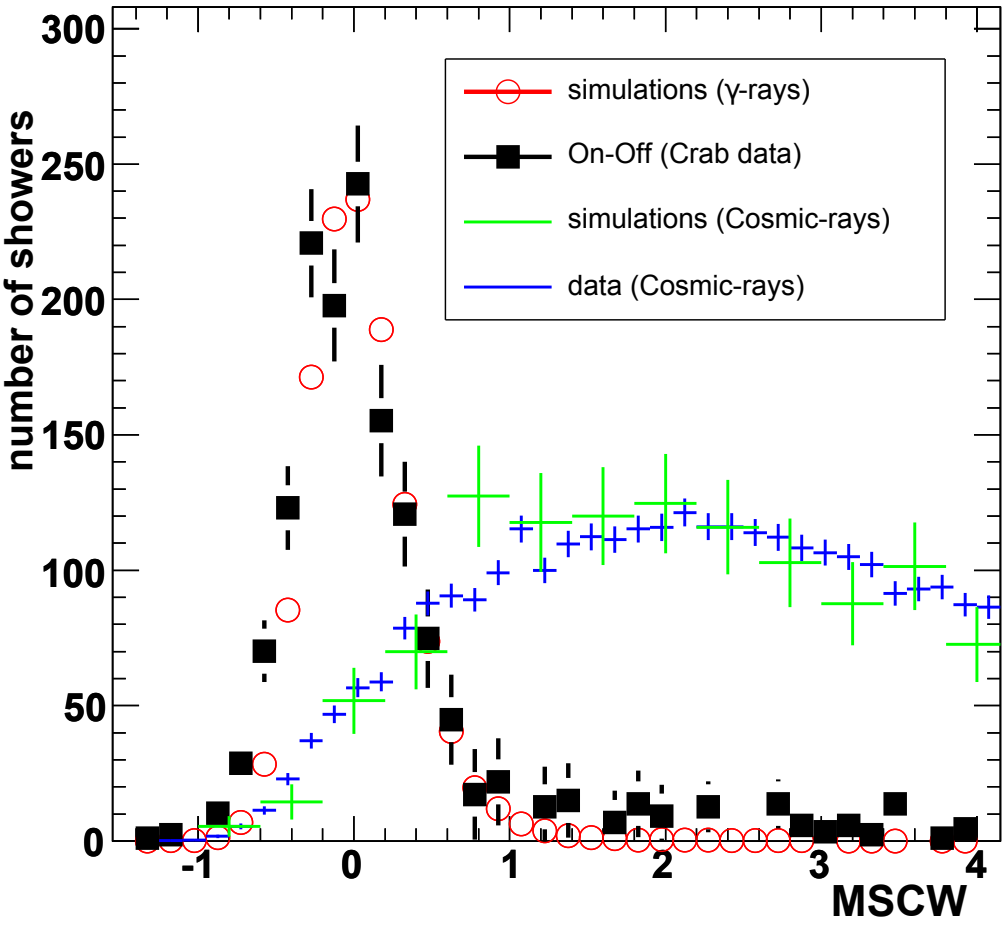

Figure 4.13: MSCW distributions for data and simulations of signal and background regions. It is clear that for MSCW > 1 the distribution is dominated by cosmic rays. "On-Off" refers to the difference in the events from the source and background regions; the determination of the On and Off regions is given formally in Section 4.3. Image credit: adapted from Figure 2 in [63].

[1]For example, the extragalactic gamma-ray background has an exponential cutoff at (279 ± 52) GeV [61]. *H.E.S.S.* has also demonstrated that there is weak, diffuse VHE emission in the galactic plane [62].

4.3 Background Determination

Even after using the aforementioned cuts to identify gamma-ray-like events, there will always be an irreducible background that must be considered (e.g. electron- and positron-induced air showers and cosmic-ray showers which look like gamma-ray showers). θ is defined to be the angle between the candidate source direction and reconstructed direction of the gamma-ray-like events. A cut on θ^2 is used to identify events from the candidate source. Between cuts on the mean scaled parameters and the θ^2 cut, typically 99% of hadronic showers can be rejected, while retaining 85% of the gamma-ray-induced showers [64]. A θ^2 distribution is given in Figure 4.14. The background-subtracted distribution can be used as a measure of the gamma-ray point spread function (PSF), but this was not required for this work so will not be discussed further. The gamma-ray PSF for *VERITAS* is $R_{68\%} \leq 0.1^\circ$ at 1 TeV.

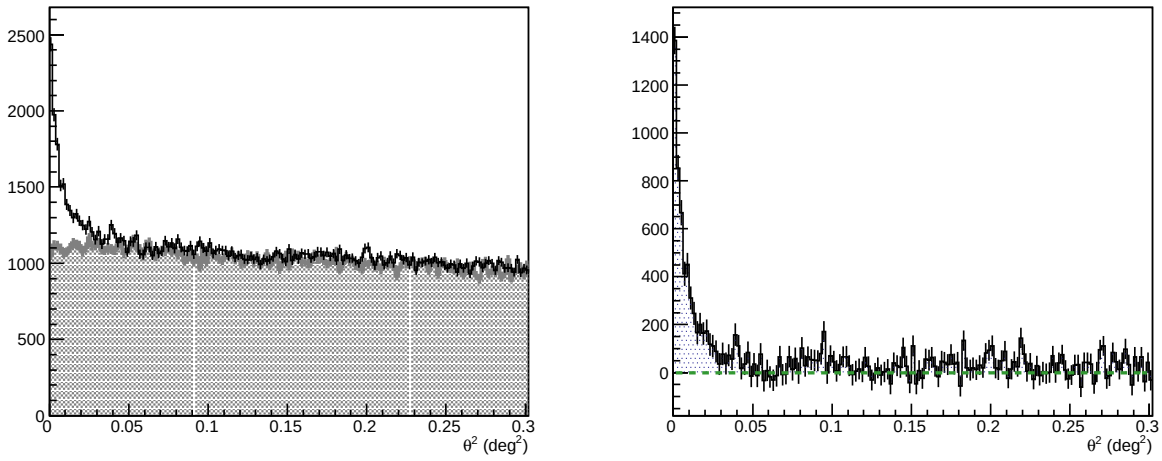

Figure 4.14: **Left**: θ^2 distribution for data taken on the Crab Nebula for the source (On) region and a background (Off) region. The Off region is shaded, the On region is not. **Right**: Residuals for the right hand plot. Below ~ 0.05 the signal due to the Crab can start to be seen.

Now, two regions can be defined: the On and Off regions. The On region corresponds to the region containing the candidate source and has a size that is the square root of the value of the θ^2 cut. The definition of the Off region is somewhat more involved. There are several different methods; the most common are described next.

Perhaps the simplest method of identifying a gamma-ray source is to identify a region of interest (ROI) in the sky and compare this region to a background sky pointing in a similar part of the sky (e.g. 30' away in right ascension) which is assumed to be devoid of gamma-ray

sources. This is known as the On/Off method, where observations are made of the source field (the On region) and then of a different (but similar) region of sky (the Off region). Then, the number of Excess events (*i.e.* how many more gamma-ray like events are coming from the source region than the background) is defined as

$$N_{\text{Excess}} = N_{\text{On}} - \alpha N_{\text{Off}} \tag{4.8}$$

where α is a normalisation parameter which allows for different sized On and Off regions (the need for this parameter will become apparent shortly). Note that both the On and Off counts must be corrected for the observing time spent on each field. Specifically, they must be corrected for livetime, which in this context is the time during which the data acquisition system is not busy storing data. Thus, to first order and assuming equal sized signal and background regions), α is the livetime ratio between observations of the On and Off fields. A major disadvantage of this method is that by definition it requires exposures of empty fields for extended periods of time (nominally an equal amount of time spent on both the On and Off regions, but not necessarily). Furthermore, it is highly susceptible to changes in observing conditions (e.g. zenith angle, sky brightness, bright stars in the field of view). Thus, other methods are often used instead.

There are several alternative methods for defining the Off region. The two most common are the ring background and reflected region models. They are described generally below, and an in-depth description can be found in [65], which is the canonical reference at the time of writing. Both of these models are designed such that dedicated background observations are not required; measurements of both the On and Off regions are made simultaneously. This is achieved through what is known as wobble-mode observations wherein the telescopes are deliberately pointed at a location offset from the candidate source location (often 0.5°, but not necessarily).

In the ring background method, the background region is defined to be a ring around the source region, as per the geometry shown in the left panel of Figure 4.15. In this case, α is the ratio of the solid angles subtended by the On and Off regions. The ring background method is useful because it provides a measure of the background closer to the candidate source position than the reflected region method, but the ring background method must account for any differences in the radial acceptance of the camera. The radial acceptance is the normalised likelihood of detecting an air shower in any given part of the camera as a function of distance from the centre (see Figure 4.16). Thus, the number of events from the On and Off regions must be corrected by scaling by the inverse of the radial acceptance. It is highest at the camera centre and ideally decreases monotonically outwards. The radial acceptance may also be energy and zenith-angle dependant [66]. Thus, when using the ring

background method special care must be taken to not introduce systematic errors into the background estimation.

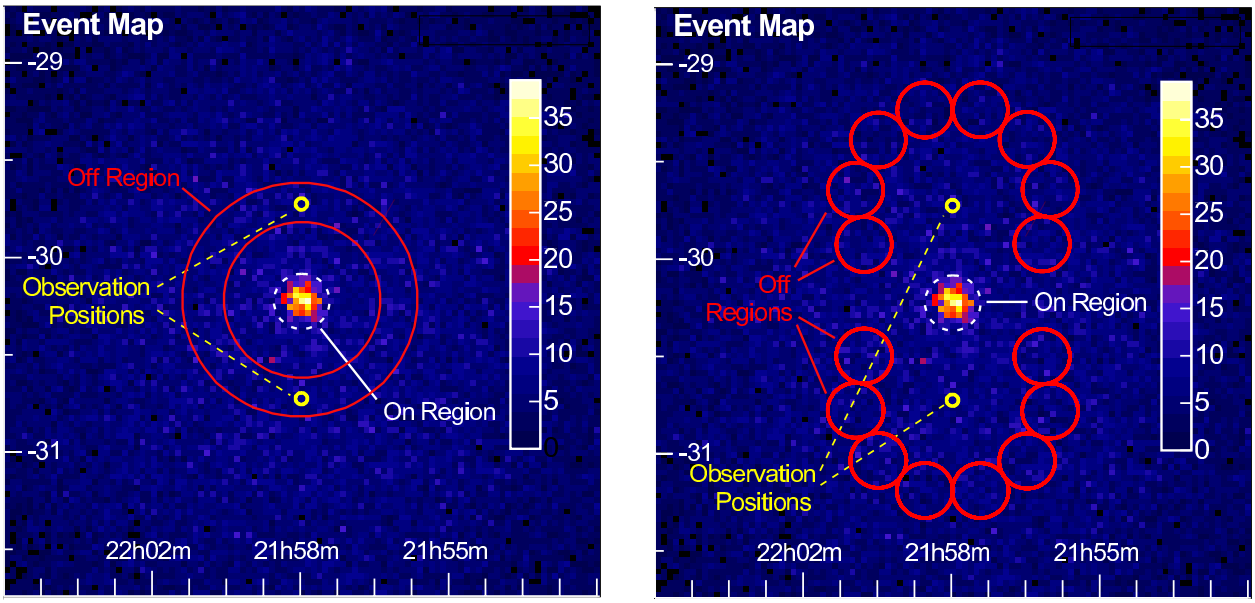

Figure 4.15: Excess counts maps based on 5 hours of HESS observations of the active galaxy *PKS 2155-304*. The data were taken with the telescopes wobbling ±0.5° in declination. The background regions used in each are indicated schematically. **Right**: Ring background method. **Left**: Reflected region model. Image credit: Figure 4 in [65].

The reflected region method uses a series of n_{Off} background regions of identical shape and size of the On region offset from the pointing direction by the distance between the candidate source location and the pointing direction (see Figure 4.15 (right)). For this method, it is assumed that the gamma-ray acceptance is the same for both the On and Off regions. Thus, there is no need for radial acceptance corrections[2]. In this case, $\alpha = 1/n_{\text{Off}}$. This is the background method used for the analysis of *VERITAS* data in this thesis. When taking wobble data, the telescopes are usually wobbled by 0.5° in one of the four cardinal directions in order to average out small differences in the data taken at different wobbles. The wobble angle and direction are not limited to the previously mentioned values; it is typical to chose larger wobble angles for extended sources.

[2]Note that the previous statements about the energy and zenith-angle dependence of the radial acceptance are still valid here, so the assumption may be introducing systematic uncertainties into the analysis. This is actively under investigation by members of the collaboration.

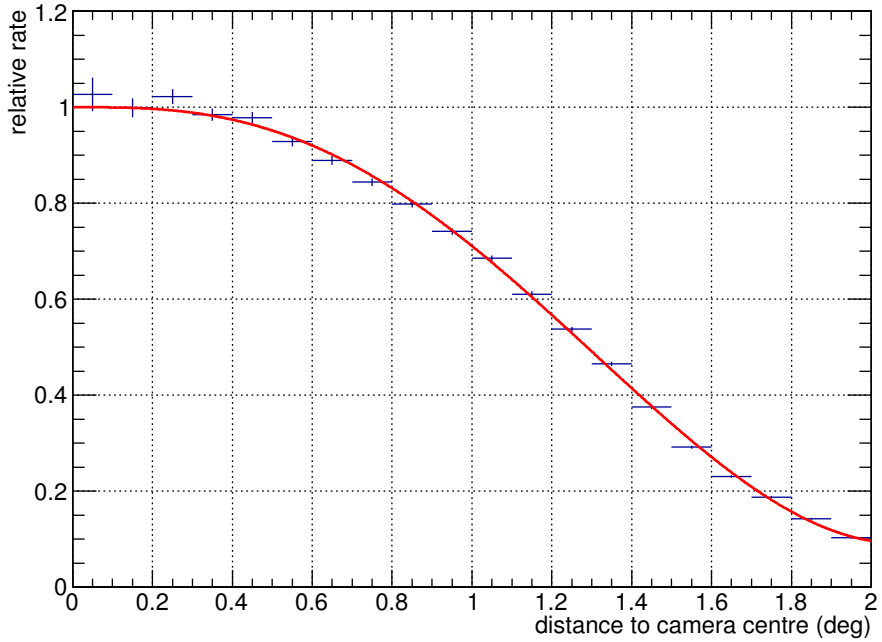

Figure 4.16: Example of radial acceptance. The points are data, and the red line is a 5$^{\text{th}}$ order polynomial, which is used in the analysis of *VERITAS* data. There is a higher probability of reconstructing an image to be arriving from near the centre of the camera than at the edges.

4.3.1 Detection Criteria

Calculating the significance of a detection with gamma-ray data is nontrivial and is discussed at length in [67] (subsequently referred to as Li & Ma). The standard calculation of the detection significance of a source is given by equation 17 in that paper, reproduced here:

$$S = \sqrt{2}\left[N_{\text{On}} \cdot \ln\left(\frac{1+\alpha}{\alpha} \cdot \frac{N_{\text{On}}}{N_{\text{On}} + N_{\text{Off}}}\right) + N_{\text{Off}} \cdot \ln\left((1+\alpha) \cdot \frac{N_{\text{Off}}}{N_{\text{On}} + N_{\text{Off}}}\right)\right]^{1/2}. \tag{4.9}$$

The commonly accepted threshold required to consider a source "detected" is a statistical significance of five standard deviations (*i.e.* $S \geq 5$). This is commonly written 5σ. In the absence of a signal, S can be described as a Gaussian function with width $\sigma = 1$ and mean $\mu = 0$. The probability of a detection with 5σ significance being due to background fluctuations is

$$P(5\sigma) = \text{erfc}\left(\frac{5}{\sqrt{2}}\right) \approx 5.7 \times 10^{-7}, \tag{4.10}$$

where erfc(x) is the complementary error function. Thus, a 5σ detection has a one in ≈ 1.8 million chance at being due to random fluctuations. The detection threshold is very high

because in the early days of the field, statistics were generally handled poorly and there were claims made about 3σ signals that turned out to be statistical fluctuations.

When calculating the significance of a detection, it is important to consider the random probability of having seen a fluctuation by simply by having looked. Simply put, if one looks at something often enough, the chances of detecting an upward fluctuation become non-negligible. The way this is handled is the use of a trials factor. Any time a given data set is analysed with a different set of criteria (e.g. changing the gamma/hadron separation cuts or target region), a trial penalty is incurred. The post-trials significance S' (which can be thought of as a "true" significance of a detection) of a detection with significance S and N trials can be calculated using the following procedure.

First, the probability corresponding to the significance S is computed:

$$P = \mathrm{erfc}\left(\frac{S}{\sqrt{2}}\right). \tag{4.11}$$

Then, the post-trials probability can be calculated:

$$P' = 1 - (1 - P)^N. \tag{4.12}$$

Finally, the post-trials probability is converted back into a significance:

$$S' = \sqrt{2} \cdot \mathrm{erfc}^{-1}\left(P'\right). \tag{4.13}$$

To demonstrate the importance of including trials factors, for a nominally 5σ detection of a source that incurred 1000 trials (by searching the entire field of view in a data set for a source, for example), the post-trials significance is only 3.4σ, which has a probability

$$P(3.4\sigma) = \mathrm{erfc}\left(\frac{3.4}{\sqrt{2}}\right) \approx 5.7 \times 10^{-4} \tag{4.14}$$

which corresponds to a roughly one in 1700 chance of a random occurrence, which is not very unlikely.

4.4 Instrument Characterisation

Instrument Response Functions (IRFs) are tools which allow data collected by the experiment to be converted from an experiment-specific result to physical units (e.g. a gamma-ray-like event with dimensions w, l and total camera charge Q to a gamma ray of energy E), described below. IRFs also allow for the detected number of events to be converted into fluxes.

Lookup Tables (LUTs) are tables that relate the observed characteristics of a shower to the energy of the gamma ray that produced it. They are mutli-dimensional tables, containing

values binned in (e.g.) noise, impact distance, and pointing direction. An example LUT was previously shown in Figure 4.11.

Effective Areas (EAs) are calculations of the effective collection area of the detectors and allow gamma-ray counts to be converted into physical fluxes. Conceptually, they can be thought of as a measurement of the relative probability of detecting a gamma ray at a given energy. Example effective areas are given in Figure 4.17.

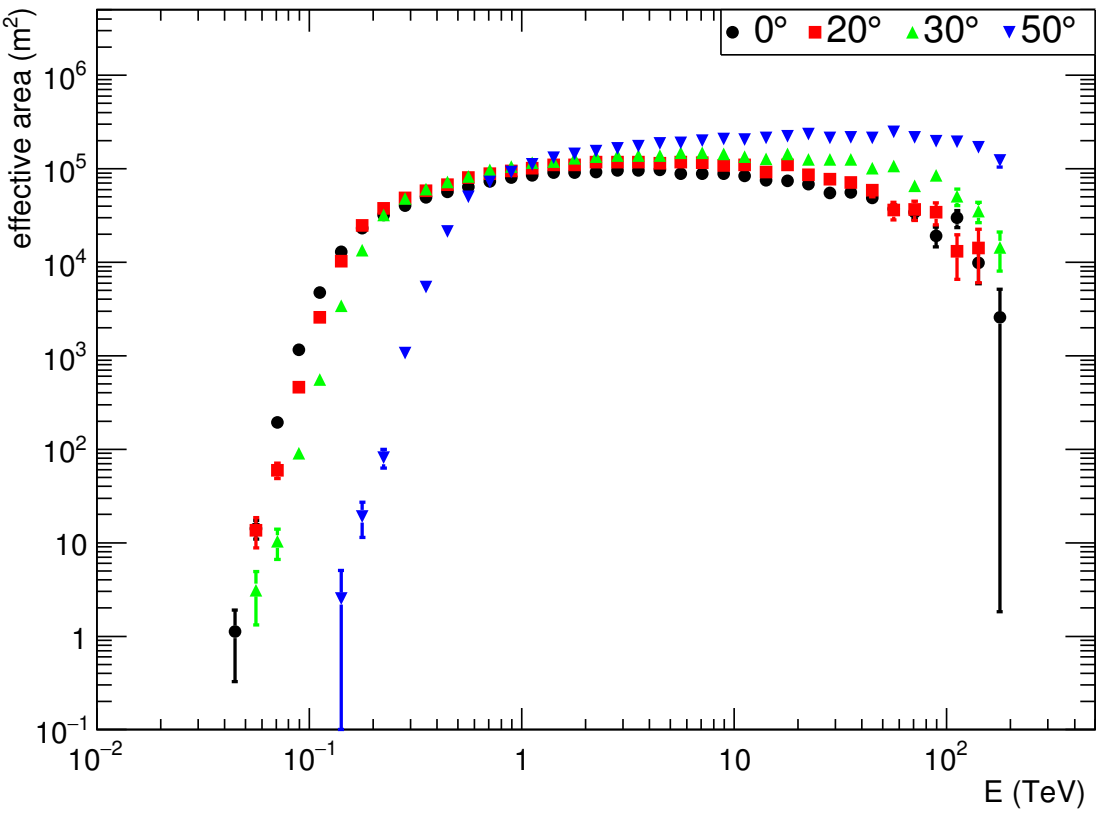

Figure 4.17: Example of four effective areas for four different zenith angles. For 0° and 20° the difference in effective area is minimal, but for larger zenith angles, the effective area is much smaller at lower energies (due to atmospheric extinction and the Cherenkov photons being spread out over a larger area, Cherenkov light from low-energy air showers may no longer trigger the array) but substantially larger at high energies (because the array sees a larger solid angle). This means in some cases, observations at large zenith angles are preferred over small zenith angles if the desired science is for a deeper exposure at the highest energies.

4.5 *VERITAS* Data Analysis Software

There are two analysis packages used for gamma-ray data analysis in *VERITAS*, `VEGAS` [68] and `eventdisplay` [69]. To produce the work presented in this thesis, the author used `eventdisplay` release `v470c`. There are three stages to performing an analysis with `eventdisplay`, the first of which has the same name as the analysis package. In this section, we refer to `eventdisplay` as the first stage of the analysis, and in subsequent sections `eventdisplay` refers to the analysis package as a whole.

4.5.1 `eventdisplay`

The first stage of the analysis involves four distinct steps, detailed below.

Relative Gain Calculation

Using the flasher run corresponding to that night's data, the relative gains of the PMTs are calculated as per the method described in Section 3.6.2. This produces a list of relative gain values used later in the analysis. Every data run has a flasher run assigned to it on a telescope-by-telescope basis. Usually, this is the same run for all telescopes, but occasionally the flasher on one telescope does not perform as expected and a flasher run from another night needs to be assigned.

Pedestal Calculation

Pedestals are calculated using events in the data stream that have been flagged by the DAQ as externally triggered pedestal events (recall that these are generated at a rate of 1 Hz). In `eventdisplay`, these are tracked in windows of 3 minutes in order to account for changing sky conditions.

Time-of-Arrival Calculation

The time-of-arrival (TOA) is the measure of when the pulse in any given PMT reaches 50% of its maximum value. It is used in placing the integration window (*i.e.* the interval over which the total charge in an FADC trace is calculated) used in the analysis. This is useful in the analysis since it allows for small integration windows to be placed. A small integration window around the pulse means that there is less random noise integrated in the trace. This improves the quality of the signal.

Image Parametrisation

This is the longest stage of the analysis as now every non-pedestal event is analysed, and using a set of pre-defined reconstruction cuts (see Table 4.1), events are cleaned and the Hillas parameters are calculated. A description of the different quality cuts is given in the following list.

- MINANGLE: The minimum angle between event axes required for events containing only two images. Less than this and there may not be enough difference between the two images to accurately reconstruct the event arrival direction.

- MINTUBES: The minimum number of PMTs required to constitute an image. This cut cleans away "images" caused by (e.g.) NSB fluctuations that happened to satisfy the L2 criteria.

- MINSIZE: The minimum amount of integrated charge in an image given in FADC digital counts (d.c.). The smaller an image is, the larger the relative errors in the reconstruction. Thus, this cut effectively limits the shower reconstruction error. Note that this also directly affects the lowest energy gamma rays that can be reconstructed.

- MAXLOSS: The maximum percent of an image's charge located on the edge of the camera (*i.e.* the outermost ring). This cut ensures that large amounts of the light in an image are not being truncated by the limited field of view of the camera; large errors in the shower reconstruction can occur otherwise. ‘

- MAXDIST: The maximum distance from the reconstructed shower centroid to the centre of the camera. This cut ensures that the images are well-localised on the camera and not truncated.

Quality Cut	Value
MINANGLE	10°
MINTUBES	5
MINSIZE	100 d.c.
MAXLOSS	20%
MAXDIST	1.75°

Table 4.1: List of image quality cuts used in a typical stereoscopic analysis. A description of the cuts is given in the main text.

4.5.2 `mscw_energy`

This stage of the analysis, also known as the lookup table (LUT) analysis, takes the quantities calculated in `eventdisplay` and uses the LUTs to reconstruct the event's energy and mean scaled parameters.

4.5.3 `anasum`

It is in the `anasum` stage that gamma-hadron separation cuts are applied to the output files from `mscw_energy` and all histograms pertaining to the final results are generated.

An example of gamma/hadron separation cuts used in a typical analysis is given in Table 4.2, where all cuts have previously been defined apart from the SizeSecondMax (SSM) cut, which is a cut on the size of the second largest image in the event. It is also referred to simply as the size cut. Note that this list is not exhaustive. Furthermore, cuts can be optimised to a specific analysis as long as the appropriate IRFs are generated.

The main difference between different sets of cuts is usually the size cut; a small value will lower the energy threshold (details of this are discussed later in Section 7.2.1) but due to the lower resolution for small showers, more background events can survive this cut, which would reduce overall sensitivity.

Cut Set	Soft	Moderate	Moderate/Extended
SSM	200 d.c.	600 d.c.	600 d.c.
ShowerMax	> 6 km	> 6 km	> 6 km
MSCW	< 0.5	< 0.5	< 0.5
MSCL	< 0.7	< 0.7	≤ 0.7
θ^2	0.008 deg^2	0.008 deg^2	0.050 deg^2

Table 4.2: An example of gamma/hadron separation cuts used in the version of `anasum` used in this analysis (the cuts can change release-to-release as the analysis is modified). Note that the main difference in the analysis of an extended source is the larger θ^2 cut (which makes sense, since gamma rays should not look any different coming from a slightly different part of the sky).

Gamma/hadron separation cuts must be chosen carefully with the candidate source in mind. For weak sources (*i.e.* the vast majority of VHE gamma-ray sources), if the VHE emission is expected to be at low energies it might be advantageous to use soft cuts to attain the lowest energy threshold. Alternatively, if a source is expected to emit gamma-rays at very high energies (say, above 1 TeV), but is very weak, it might be beneficial to use moderate cuts (or cuts with an even larger size cut), which would clean out much of the background at

the cost of having an increased energy threshold. Note that often the energy spectrum of a source is often not known, so multiple cuts are often used (each of which incurs a trial).

4.6 *VERITAS* IRF Generation

The vast majority of all *VERITAS* data was taken in one of three different epochs (or versions), defined here:

- V4 array: Pre-T1 move, Photonis PMTs, 2007-2009
- V5 array: Post-T1 move, Photonis PMTs, 2009-2012
- V6 array: Post-T1 move, Hammamatsu PMTs, 2012-present

Unless otherwise specified, the data presented in this thesis was taken with the V6 array. For each detector configuration, each of the following steps must be repeated to generate IRFs applicable to that epoch.

4.6.1 Detector Simulations & Simulated Data Acquisition

GrISUDet [70] and *CARE* [71] are two detector simulation codes used in the generation of simulations for *VERITAS*. For this work, the author worked heavily with simulations in order to produce instrument response functions for the new data type, hence both analysis packages are briefly described below; they are mentioned for the purposes of explaining how *VERITAS* IRFs are generated. IRF generation is relevant to this work as a substantial amount of time was spent producing and analysing simulations such that bright moonlight IRFs could be produced and released to the collaboration.

A large number of gamma-ray showers are simulated using *CORSIKA* [72], which models the interactions in the atmosphere, particle propagation and Cherenkov photon production. The energies of the gamma-ray primaries are generated using a power-law probability distribution with minimum energy 30 GeV and a power-law index of 2. The shape of the probability distribution is motivated by the desire to have a large amount of statistics where most gamma-ray signals are. Thus, there is no high energy limit; statistics at higher energies are limited by the overall number of showers produced. For 0° zenith angle, 10^7 showers are generated, for any other zenith angle 2.5×10^7 are generated.

For a given detector configuration, zenith angle z, wobble angle w, and background noise level (*i.e.* the arrival rate of photons at each PMT) N, and season (which affects the propagation of the air shower; the sky is more transparent during the winter when the air

is less humid; see [73] for more information on the effects of weather on air showers), the Cherenkov photons of each shower are passed to a simulation of the detector. If the simulated shower triggers the array readout, the shower information is written to disk in the same way that real data would be. The simulated components of the event (e.g. true energy, true arrival direction) are also stored to generate subsequent components of the IRF, described below. If an event does not trigger the array, an empty event is written (the number of events that did not trigger the array is required later on for IRF generation).

The *GrISUDet* package tracks individual Cherenkov photons through an array of Davies-Cotton telescopes and models the PMT pulses generated when said photons hit the PMTs before finally writing the FADC response to an output file. NSB noise is added to the output files afterward when generating the telescope IRFs. This means that only one set of simulations needs to be run, and then an arbitrary amount of noise can be added later on, which saves on computing time and disk space. However, since there is no noise in the simulations, the L1 trigger rate feedback (recall Section 3.5.2.1) is not modeled at all, meaning that an "effective" CFD trigger threshold must be chosen.

In addition to this shortcoming, *GrISUDet* currently does not correctly model the response of the high-low gain switch, which causes some issues in V6 data. Cherenkov pulses are now more peaked for a given number of photoelectrons and the high-low gain switch is being triggered more often than in the past. This has caused some issues, particularly in the reconstruction of showers above ~ 1 TeV. At the time of writing, *GrISUDet* is still being used for the generation of V4 and V5 array IRFs, with *CARE* being the analysis package used for the generation of most V6 array IRFs.

CARE is a more elaborate detector simulation which actually simulates the response of the telescope electronics. Features like the rate feedback are included in the detector simulation, as well as a correct model of the response of the high-low gain switch. As a result, it is a more accurate representation of the experiment but takes significantly longer to run as each noise level needs to be simulated individually (to account for the rate feedback). Thus for (say) 3 noise levels (e.g. a background photon rate per pixel of 100 MHz, 200 MHz, and 300 MHz), instead of generating a single batch of events and then overlaying three different amounts of noise, three different simulations must be run, requiring at least three times as much CPU time, plus any additional overhead. Noise photons are added to the simulated signal chain directly with arrival times determined by Poisson statistics.

4.6.2 Lookup Table Generation

The first step in generating IRFs is to analyse the simulated showers with `eventdisplay`. This produces parameters like the shower width and length, the pedvars, etc., which are required to compare real showers to the simulated ones. The simulated air shower parameters are used to fill multi-parameter LUTs using `mscw_energy`. Each LUT is binned in (e.g.) pointing direction, impact parameter, wobble angle, and noise.

Each step in this analysis is repeated for each zenith bin ($z \in \{0, 20, 30, 35\}$ degrees for small zenith angle simulations; 10° is omitted because between 0° and 20° zenith, the shower parameters do not change substantially), noise level (for a complete batch of simulations 8-10 steps are chosen with the uppermost noise level being "unphysically high" and the lowermost noise level being "unphysically low"), and wobble angle ($w \in \{0, 2.0\}$ in 0.5° steps). The issues pertaining to computing power become apparent at this point. Simulations must be finely spaced in order to reduce the amount of interpolation required, but coarse enough so that amount computing resources required is not overwhelmingly large.

4.6.3 Effective Area Generation

For `eventdisplay`, EA generation is done by analysing the simulated showers a second time using `mscw_energy`, but using the previously generated LUTs as a reference for the shower reconstruction. This amounts to analysing simulated showers with the LUTs that were generated using the same showers. This yields a list of reconstructed showers with their corresponding *reconstructed* and *true* properties which allows for systematic errors on, for example, the absolute energy scale and resolution, to be quantified.

The final step is to apply a set of gamma-hadron separation cuts to the analysed simulations and produce the effective areas. Conceptually, a simple calculation of the effective area is given by

$$A_{\text{eff}}(E) = A\left(\frac{N_{\text{accepted}}}{N_{\text{thrown}}}\right) \tag{4.15}$$

where A is the area over which the simulated gamma rays were generated (a circle with radius 750 m for *VERITAS*), and the second term is the fraction of the total number of gamma rays which actually triggered the array and made it through to the final stage of the analysis.

4.7 Summary

In summary, the major steps in an analysis are:

- Image cleaning and parametrisation.

- Direction reconstruction using shower geometry.
- Energy reconstruction using LUTs.
- Gamma/hadron separation.
- Flux reconstruction using EAs.

Following these steps it is possible to turn raw data into high-level science products which are ready for interpretation.

Chapter 5

The Brightness of the Night Sky

"The Hunter's Moon waxed round in the night sky, and put to flight all the lesser stars..."

J.R.R. Tolkien, The Lord of the Rings

The moonless sky is not entirely dark. The night sky background (NSB), by adding random noise to all images captured by Cherenkov telescopes, can have a large impact on the reconstruction of air showers. Conceptually, this can be seen as the NSB "washing out" showers by reducing signal-to-noise. The NSB has a number of components which contribute to it; the following is a mostly qualitative overview of the different contributing factors. A very thorough treatment of the different sources of background light from UV to IR wavelengths can be found in [74], which served as the basis for this review.

5.1 Conventions and Nomenclature

Many sources refer to the surface brightness at visible wavelengths (V-band) in units of $S_{10}(V)$, which corresponds to one magnitude 10 star per square degree, which is equal to 27.78 mag/arcsec^2. There is confusion in the literature over the S_{10} unit. Some authors quote results corresponding to a Sun-type star (G2 V -type, often identified with the subscript $\odot$, which is the standard when referring to a solar quantity), whereas others refer to Vega-type stars (A0 V -type), and others do not quote a reference at all. This is important since the emission spectrum of stars differs between stellar types. For example, Vega is hotter and has

more emission in blue light than the Sun. Thus, the stellar type used in the S_{10} system is important when comparing relative amounts of emission in different colour bands.

In this work, the author references the stellar type where available. Albeit the confusion surrounding S_{10}, it is used in this work since it is a standard in the literature, and is a convenient unit to use since only the brightest parts of the sky (or the Sun) require more than 3 digits (*i.e.* have S_{10} values greater than 999) and it is linear with brightness, unlike the magnitude system. Unless otherwise specified, it has been assumed that S_{10} is for an A0 star. This is a commonly-used convention (see, for example, [74]) and is a reasonable assumption: since A0 stars have the same magnitude at all wavelength bands, this removes the colour dependence of the unit.

There exist several astronomical magnitude systems. The Bessel photometric system, for historical reasons also known as the Johnson-Cousins photometric system (see [75, 76]), has been adopted for the following discussion. It is defined such that the fluxes in all colour bands, **U**ltraviolet, **B**lue, **V**isible, **R**ed and **I**nfrared, are normalised to Vega. A plot of the transmission curves for filters in the different colour bands is given in Figure 5.1. The convention when referring to the magnitude of an object in a certain colour band is to quote a value $X = a$, where X is the colour band in question (e.g. B or R) and a is the magnitude of the object. Vega is defined such that $U - B = B - V = V - R = R - I = 0.00$ and $V = 0.03$ [76, 77]. The colour index is a measure of how, for example, red or blue a star is; a colour index $B - V = -1.5$ means that there is more light in the B-band than the V-band.

For a number of colour bands, conversion factors to convert from S_{10} units to fluxes are given in Table 5.1. A value of $S_{10}(V)$ can also be converted to units of mag/arcsec^2 using the following relation:

$$I = (-2.5 \log_{10} S_{10}(V) + 27.78) \text{ mag/arcsec}^2. \tag{5.1}$$

The magnitude system, being nonlinear by design, is often used when quoting sky brightness. This can lead so some confusion – a flux increase of 0.1 mag/arcsec^2 on a baseline of 22 mag/arcsec^2 is very different than the same increase on a baseline of 10 mag/arcsec^2, since the change in magnitude is relative to the baseline. The linearity of S_{10} is more intuitive and therefore has been adopted in this work.

A photon flux

$$\frac{d^4N}{dA\ dt\ d\Omega\ d\lambda} \tag{5.2}$$

has units of photons per unit area, time, solid angle, and wavelength and is more relevant to gamma-ray astronomy due to the photon-counting nature of photomultiplier tubes. Using the conversion factors in Table 5.1 S_{10} values can be converted to flux values (at a given wavelength λ) by dividing a flux I_λ by the photon energy $E = hc/\lambda$.

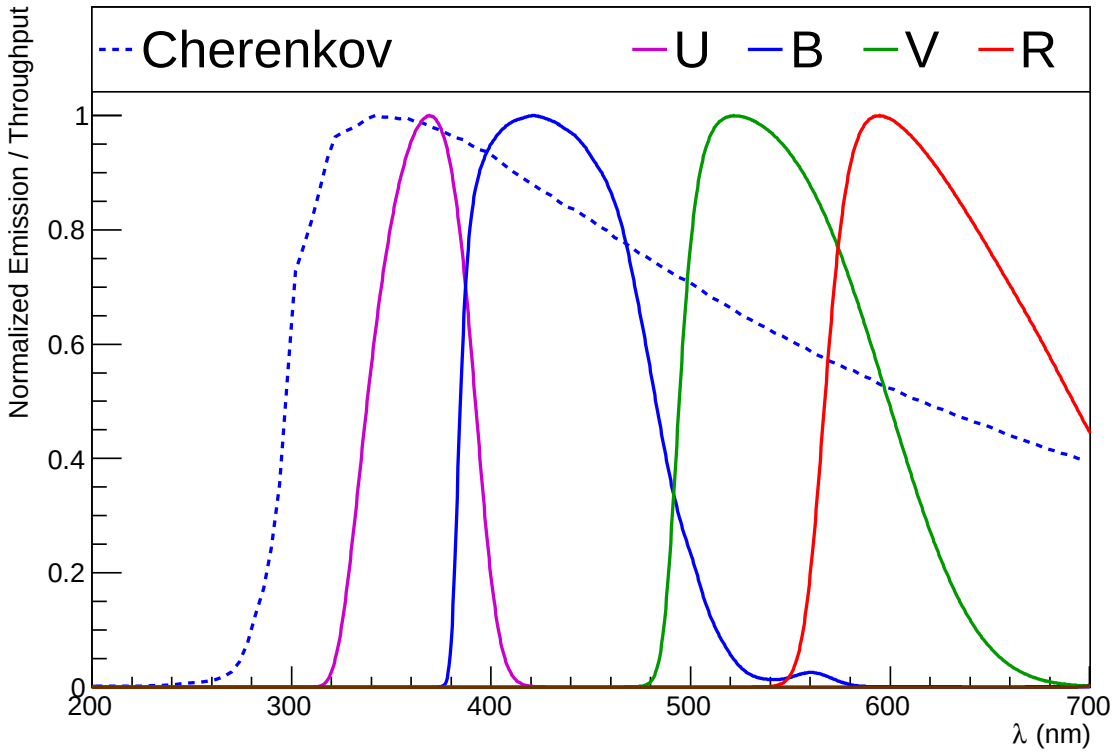

Figure 5.1: Transmission curves for typical Bessel filters. The Cherenkov spectrum for a 500 GeV gamma ray is also shown for comparison.

Wavelength	1 S_{10} unit corresponds to	1 $S_{10\odot}$ unit corresponds to	
(μm)	I_λ (10^{-8} W/m^{2}srμm)	I_λ (10^{-8} W/m^{2}srμm)	S_{10} units
0.36 (U)	1.37	0.670	0.488
0.44 (B)	2.17	1.19	0.550
0.55 (V)	1.18	1.18	1.0
0.70 (R)	0.570	0.921	1.61

Table 5.1: Conversion factors for S_{10} units for the Johnson U, B, V, and R-bands. Adapted from table 2 in [74].

5.2 Components of the Night Sky Background

5.2.1 Astrophysical Sources of Background Light

5.2.1.1 Galactic

Perhaps the most obvious contributing factor to the NSB is the presence of starlight. This is typically broken into two categories, integrated starlight from unresolved stars and diffuse Galactic light which is light reflected off interstellar dust particles. Figure 5.2 shows a measurement of the sky brightness as a function of Galactic latitude b. The contribution due to stars that cannot be seen with the naked eye is extremely well fit above 20° (where the contribution of starlight scattered by dust in the Galactic plane is small) by an exponential function:

$$S_{10}(V) = (230 \pm 10)e^{-(1.15\pm0.05)b/20^\circ} + (29 \pm 0.8) \tag{5.3}$$

Note that to produce this fit, data were extracted by hand from the source plot, and no error bars were provided, so the fit χ^2/NDF (1.1/6; $P \sim 98\%$) must not be over-interpreted.

To put this in perspective, [78] demonstrated that if all the light due to stars was spread evenly across the sky, it would be equivalent to 105 magnitude 10 stars (V-band) per square degree of sky. This is also equivalent to 51 stars as bright as Sirius, which is both nearby (8.8 light years) and intrinsically bright ($V = -1.58$).

The aforementioned values are made up mostly of stars with magnitude $6 < V < 16$; stars fainter than $V = 20$ contribute insignificantly to the brightness of the sky ($S_{10} \sim 5$ according to [78]). The component caused by light scattered off interstellar dust (I_{DGL} for "diffuse galactic light") can be estimated from a very rough fit to data in [78][1]:

$$S_{10}(V) \approx (120 \pm 8)e^{-(1.1\pm0.1)|b|/10^\circ}. \tag{5.4}$$

The numerical average of this function over the range $|b| \leq 90^\circ$ is 11.8 S_{10}; for simplicity this will be rounded to 10 S_{10} for this summary.

5.2.1.2 Extragalactic

Olbers' paradox, named after the German astronomer Heinrich Wilhelm Olbers (1758-1840), is a paradox that arises from the fact that if one assumes that the Universe is static, homogenous at large scales, and populated by an infinite number of stars, then any line of sight from the Earth would eventually intersect the surface of a star. Thus, the night sky would not be dark, but very bright.

[1] Specifically, figure 5-4 in [78].

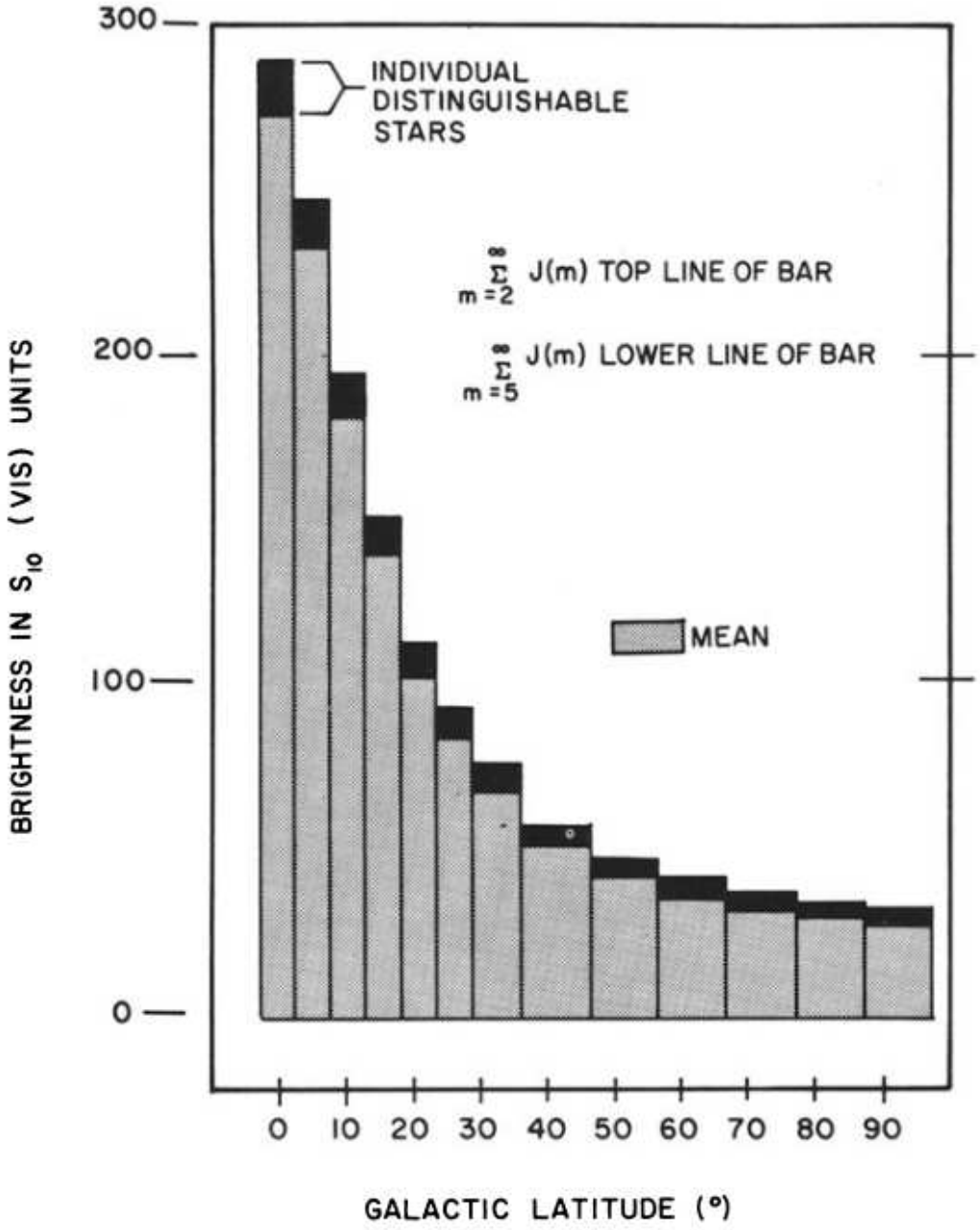

Figure 5.2: Integrated starlight versus Galactic latitude. The top portions of the rectangles represent the total integrated starlight to magnitude 2. The solid black portion is the contribution due to individual distinguishable stars between magnitude 2 and magnitude 5. The shaded region corresponds to the total integrated starlight from stars fainter than those discernible to the eye. Image credit: Figure 2-8 in [78].

Modern astronomy can resolve this paradox owing to two factors. First, the expansion of the Universe redshifts the light and increases the volume of the Universe (which for a static number of stars and galaxies means that the stellar density on large scales decreases). Second, due to the fact that galaxies have a finite age the number of photons they have produced is limited, which results in a low intergalactic radiation field. [79] has demonstrated that of these two contributing factors, the finite age of galaxies is the major contributing factor to the paradox's resolution.

The extragalactic background light (EBL) can be thought of as the bath of photons produced during star formation that permeates the Universe. Upper limits on the contribution can be made photometrically, whereas lower limits on the extragalactic contribution can be made via galaxy counts. Strong foregrounds from the Galaxy make direct measurements very difficult. For example, early measurements from the *Pioneer 10* spacecraft, between 3.27 and 5.15 A.U. from the Sun, and thus effectively free from a strong foreground (zodiacal light, see Section 5.2.2.2), set an upper limit of 3.9 $S_{10}(V)_{\odot}$ at 4400 Å [80] with 2σ confidence[2]. A more recent analysis using data from both *Pioneer 10* and *11* put that measurement at $S_{10}(V)_{\odot} \approx 1.5 \pm 0.8$ in the *Pioneer* B-band [81]. Due to the presence of strong foregrounds, direct measurements are difficult and this is largely the reason for the large errors on measurements.

Although its contribution is quite low (generally taken to be ~ 1 S_{10}) the EBL has been shown to contain substantial fluctuations on the scale of a few arcminutes to a few degrees [82]. This fact, however, would not have a large effect on gamma-ray observations since the optical resultion of an IACT is so poor (the anisotropies are smeared out by the telescope optics) and the EBL contribution is so low.

It is actually possible to make indirect measurements of the EBL using gamma-ray observations of extragalactic VHE sources. This is directly relevant to the Bright Moonlight Program as data at different energies probes different energy ranges of the EBL. This is described later in Section 10.3.2.

5.2.2 Effects of the Sun

5.2.2.1 Airglow

During the day, UV radiation emitted by the Sun is absorbed by the atmosphere. Airglow is light emitted from atoms and molecules due to this excitation. It is the brightest component of the night sky and is responsible for many atmospheric emission lines. The line emission is

[2]This confidence interval was chosen because the photometric measurement yielded a result consistent with zero: $(1.3 \pm 1.3) S_{10}(V)_{\odot}$.

driven by photo-ionisation, photo-dissociation, and photo-chemical reactions. Examples of possible reactions are given in Figure 5.3. A picture demonstrating airglow taken from the International Space Station is shown in Figure 5.4.

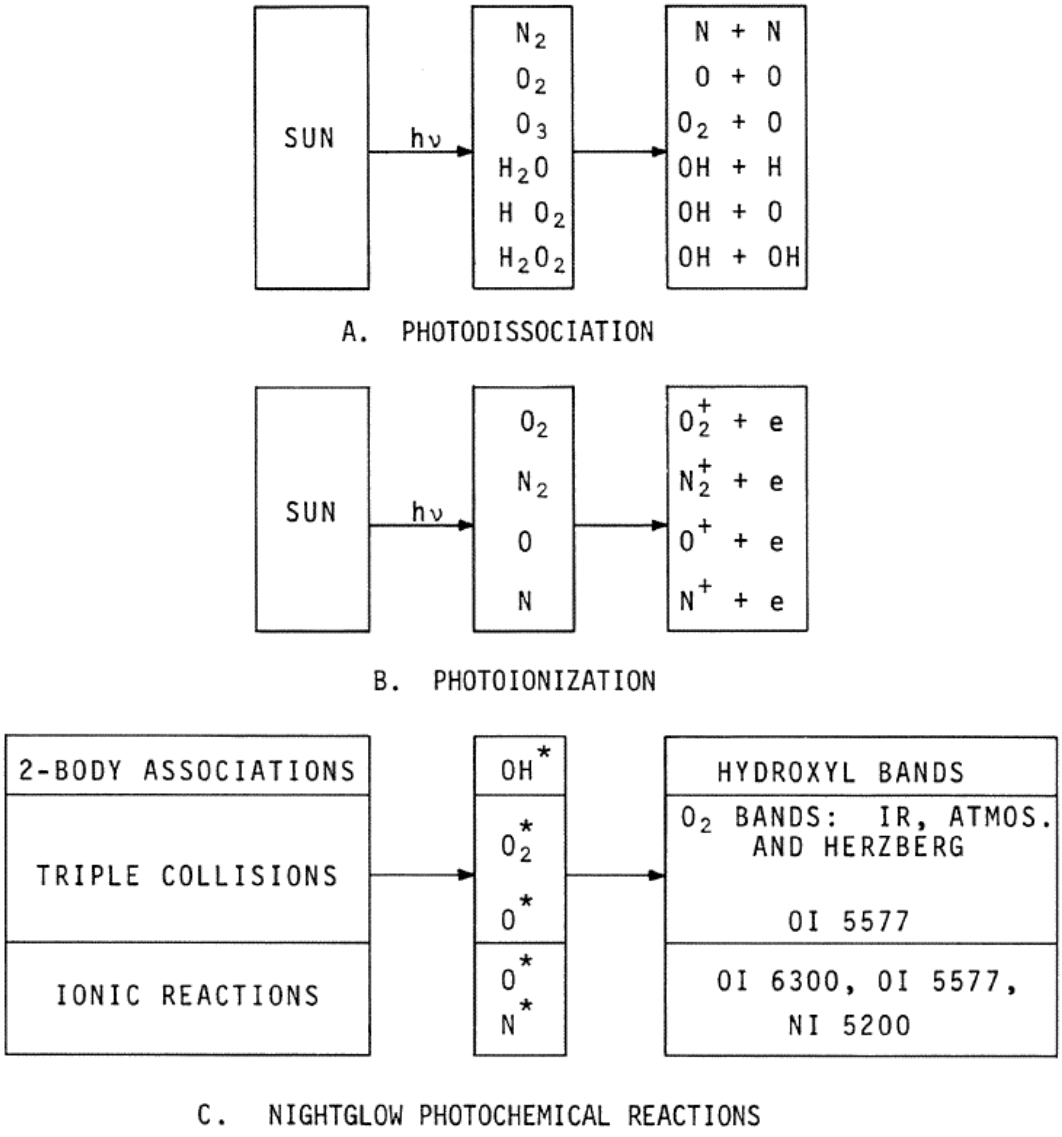

Figure 5.3: Example chemical reactions resulting in airglow. Image credit: Figure 4-2 in [78].

Airglow intensity depends on a number of variables. For example, it is a factor of 2 higher at 70° latitude than 20° latitude [83, page 34]. It also varies on short (minute) and long (year) timescales depending on changes in the atmosphere and solar activity. The solar UV flux (which is responsible for airglow due to photodissociation) is linearly proportional to the solar 10.7 cm radio-flux density [84]. This value is often denoted $S_{10.7\text{cm}}$ or $S_{10\text{cm}}$. It follows

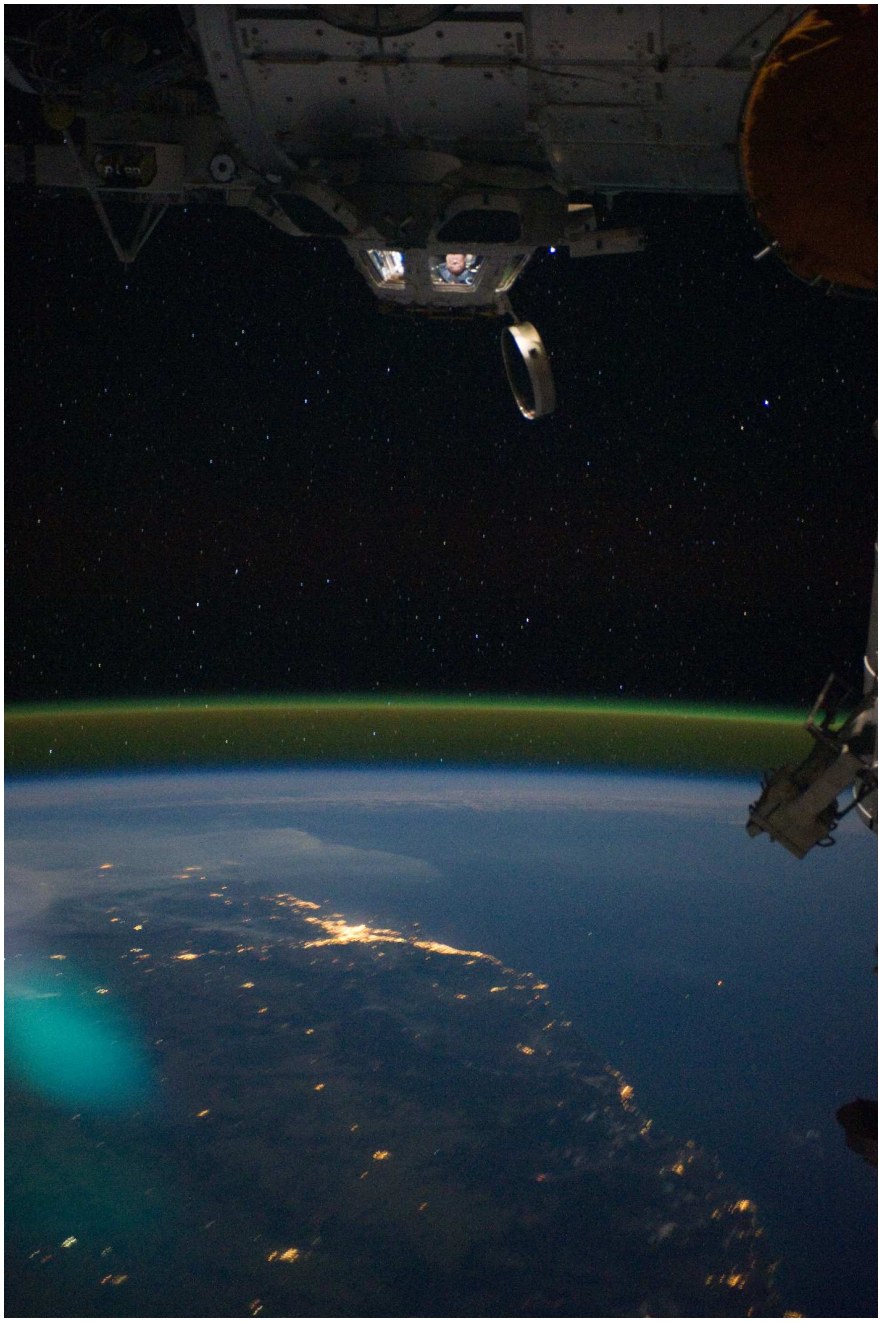

Figure 5.4: Picture taken of the Earth from the International Space Station by an Expedition 28 crew member. Airglow is clearly seen as a green (5577 Å oxygen line) emitting layer 90 km above the Earth's surface. There are also red emission lines from oxygen (6300 Å and 6364 Å) at 250-300 km and yellow sodium emission (the sodium 5890/5896 Å doublet) from atoms at $\approx$ 92 km (altitudes taken from table 13 in [74]). The turquoise spot in the lower left of the image is probably glare off a window. Image credit: "Cupola above the darkened Earth" by NASA - Licensed under Public Domain via Wikimedia Commons.

that $S_{10\text{cm}}$ can be used as a tracer for solar activity. $S_{10\text{cm}}$ varies roughly sinusoidally during the 11-year solar cycle, peaking at ~ 2 MJy and is minimal at 0.8 MJy. The most recent solar minimum was in January 2008. [85] identified the correlation between $S_{10\text{cm}}$ and sky brightness to be (0.14 ± 0.01) mag arcsec^{-2}/MJy.

Measurements of the night sky background made by [86] at the Kitt Peak Observatory (also in southern Arizona) are given in Figure 5.5. The results agree with the previous observation that there is a correlation between the sky brightness and solar activity; they determined that the sky is ~ 0.5 mag/arcsec^2 brighter at solar maximum. Note that this is slightly higher than the previously mentioned correlation predicts.

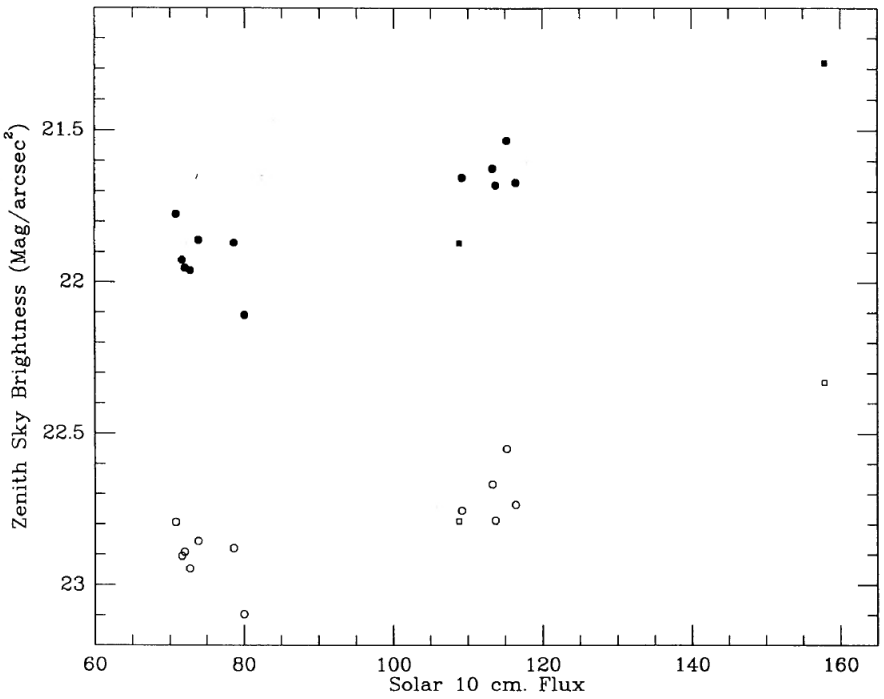

Figure 5.5: Night sky brightness versus solar flux in V-band (filled) and B-band (open) light. A correlation between solar activity and the sky brightness can be seen. Image credit: Figure 2 in [86]

The contribution due to airglow (I_A) will depend on zenith angle z and is greater at large zenith angles; there is more sky at large zenith angles to be emitting light. A thin emitting layer at height $h = 100$ km above the Earth's surface will have an airglow contribution of

$$I(z) = I(0)\frac{1}{\sqrt{1 - [R/(R+h)]^2 \sin^2 z}} \tag{5.5}$$

where $R = 6378$ km is the radius of the Earth. This is called the *van Rhijn function*, which is plotted in Figure 5.6.

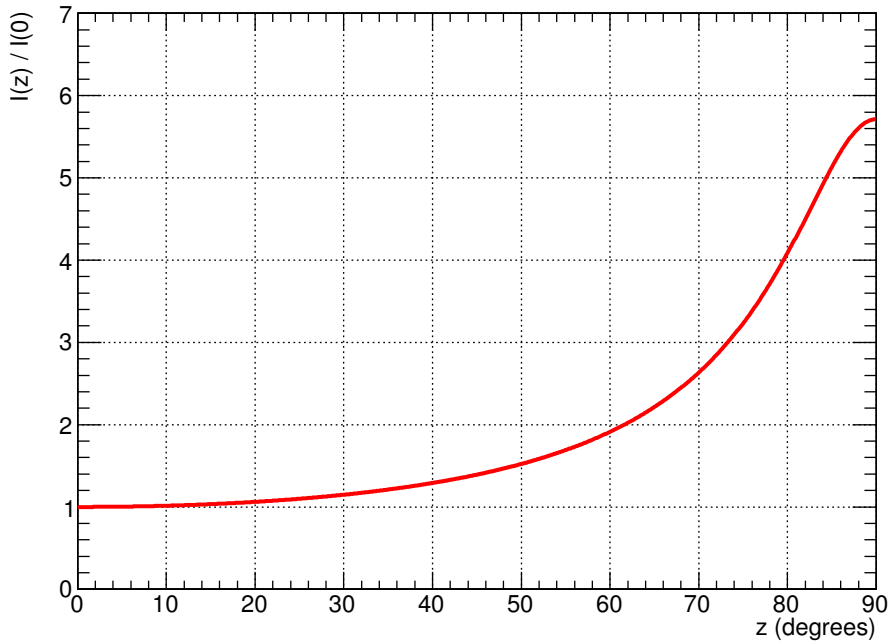

Figure 5.6: Zenith angle dependence of airglow intensity as described in Equation 5.5 with $R = 6378$ km and $h = 100$ km. At large zenith angles, the ratio quickly grows and reaches a maximum of ~ 5.7 at the horizon.

Based on observations from a number of sources, [87] determined that a typical value for I_A at zenith as a function of solar activity is

$$I_A \sim 145 + 130(S_{10\text{cm}} - 0.8)/1.2. \tag{5.6}$$

This relation has been adopted in this work (see Table 5.4).

5.2.2.2 Zodiacal Light

Zodiacal light is sunlight scattered by interplanetary dust. Zodiacal light has been studied since the 1600s; a brief history is given in [88]. The first interpretations of zodiacal light were made by Jean-Dominique Cassini (1748-1845) [89], and it was Jean-Jacques Dortous de Mairan (1678-1771) in the mid-18th century who first suggested that the dust cloud extends further than the Earth's orbit [90]. A drawing of zodiacal light by Dortous de Mairan is shown in Figure 5.7. Figure 5.8 is an image of zodiacal light as seen by a satellite in orbit.

The brightness of the zodiacal light decreases with distance from the Sun; measurements made by *Pioneer 10* and *11* determined that at $R = 2.4$ A.U. it is $< 10\%$ of the observed brightness at 1 A.U. [92], falling off as $R^{-2.6}$ before becoming undetected at $R > 2.8$ A.U. [93, and references therein].

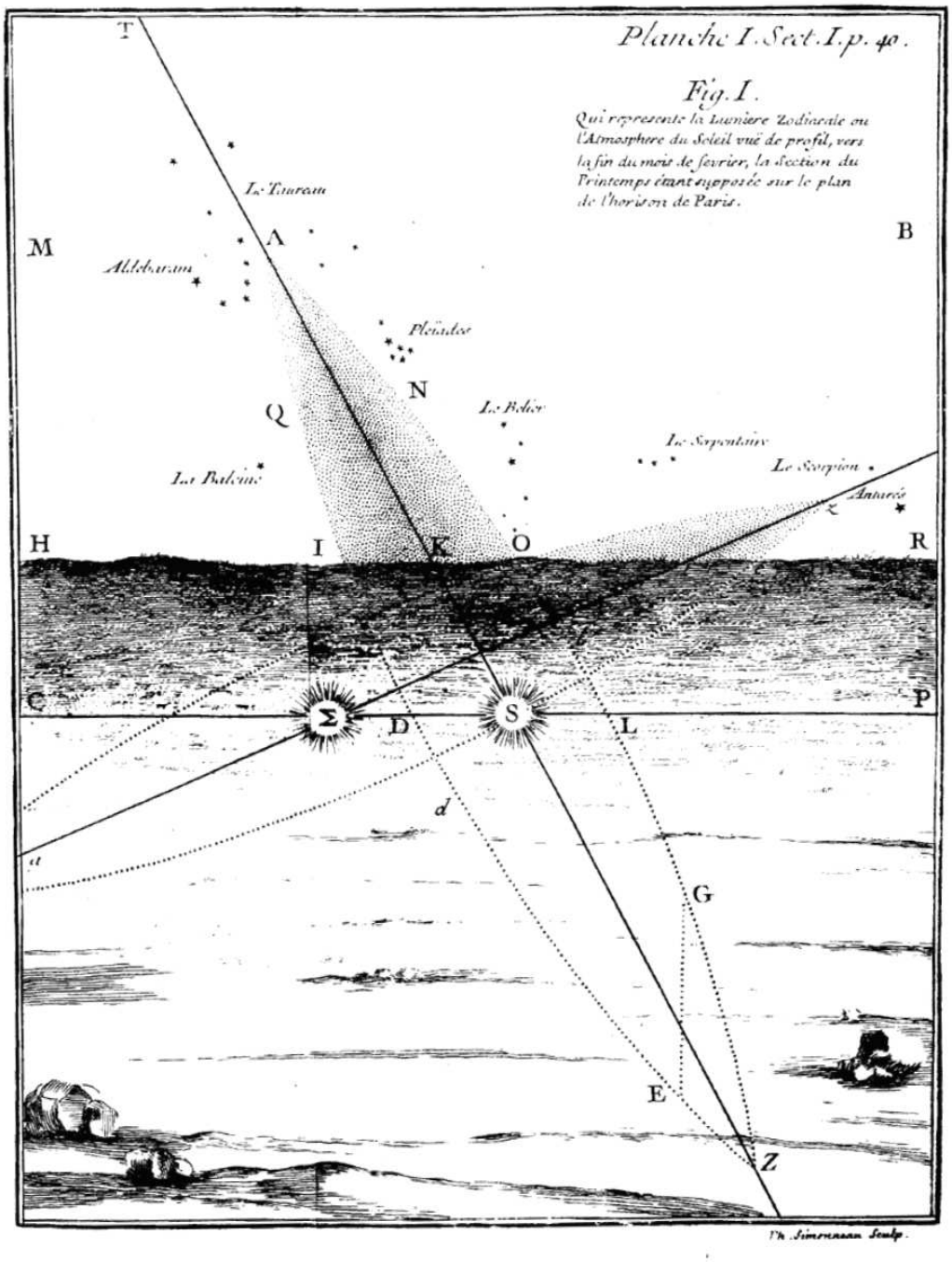

Figure 5.7: Drawing of zodiacal light. The shaded regions above the horizon are zodiacal light "cones"; the drawn ellipses below the horizon are presumably the inferred extent on the opposite side of the Sun. Several constellations are also indicated. The caption reads "Zodiacal light or the profile view of the atmosphere of the Sun, as seen at the end of the month of February, superimposed on the Paris horizon". Image credit: Figure 1 in [90].

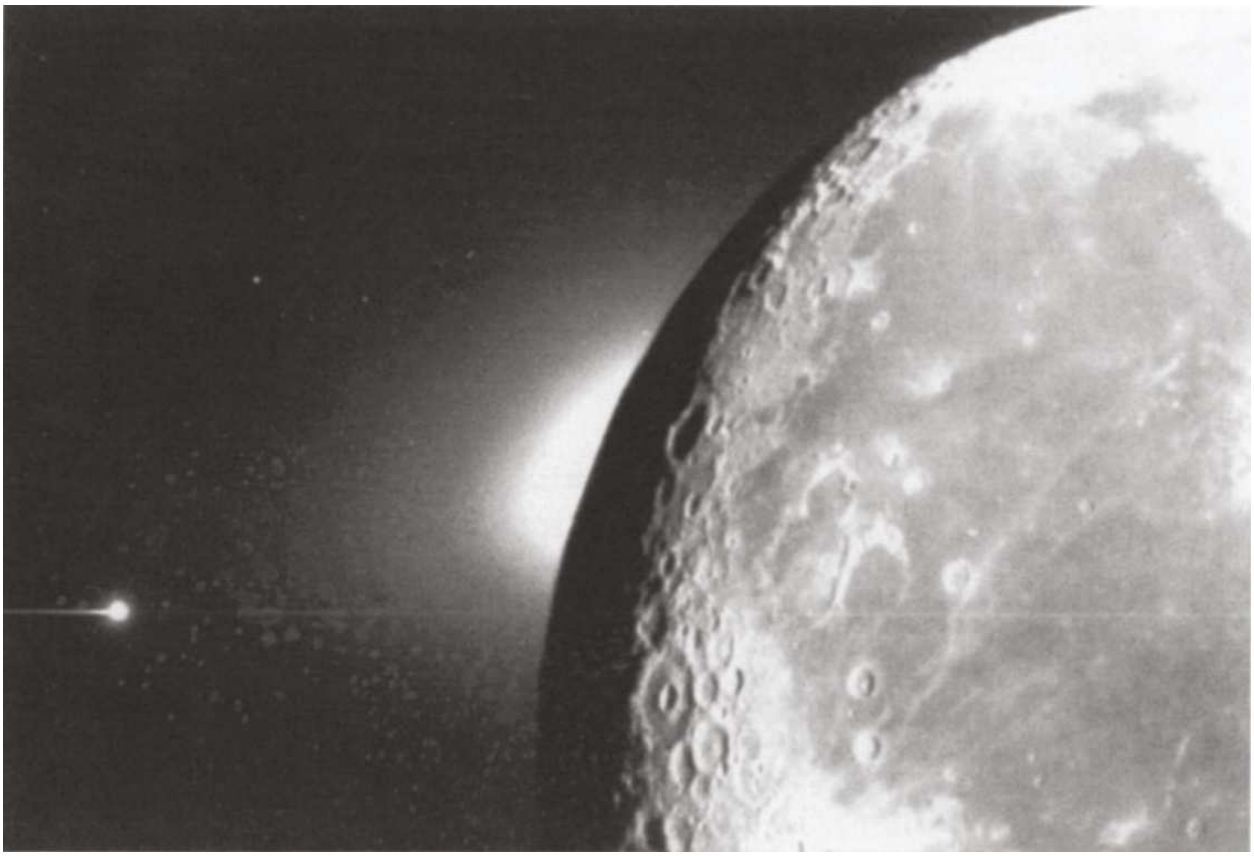

Figure 5.8: Inner zodiacal light extending over the lunar horizon. The Moon is illuminated by Earthshine. The bright object on the left is Venus. Image credit: Figure 5 in [88]; originally from [91].

As one would expect, the brightness of zodiacal light is largely dependent on the angular distance between the observing point (at ecliptic longitude λ) and the Sun (at ecliptic longitude $\lambda_\odot$). This is known as elongation, denoted ϵ or often simply $\lambda - \lambda_\odot$. At 1 A.U., zodiacal brightness is close to 2000 $S_{10}(V)$ at $\epsilon = 30°$ (brighter than the Milky Way) and is minimal near the ecliptic pole (the point where the celestial sphere meets the line perpendicular to the ecliptic plane), 60 $S_{10}(V)$.

The Gegenschein (literally "countershine" in German) is a part of the sky exactly opposite the position of the Sun which exhibits excess brightness compared to the rest of zodiacal light due to sunlight backscattering off interplanetary dust. An image is shown in Figure 5.9. It has an excess brightness of (40 ± 5) $S_{10}(V)$ very close to the anti-Sun position [94]. The maximum brightness in that region of the sky is ~ 200 $S_{10}(V)$ [95].

A brightness map of zodiacal light, as seen from the Earth, is given in Figure 5.10. Given that zodiacal light is scattered solar light, its spectrum is essentially that of the Sun, except for a slight reddening due to scattering off interplanetary dust. This spectral reddening is

Figure 5.9: Image of the Gegenschein, a bright spot in the anti-solar direction caused by a peak in back-scattered sunlight. Image credit: By ESO/Y. Beletsky (ESO) [CC BY 4.0 (licence)], via Wikimedia Commons.

unimportant for the purposes of this discussion.

The zodiacal brightness for $\epsilon = 150°$ as a function of ecliptic latitude β is roughly described by

$$S_{10}(V) = \begin{cases} (142.2 \pm 0.3) - (96.0 \pm 0.6) \sin|\beta| & ; \beta \leq 60° \\ 60 & ; \beta > 60° \end{cases} \tag{5.7}$$

This fit is based on data from table 1 in [88] and is similar to the one provided in [87].

5.2.3 Light Pollution

A growing concern in ground-based astronomy is man-made light pollution. Even at dark sites like the Whipple and Kitt Peak observatories, light due to the nearby cities of Tucson and Nogales is an issue. At the *VERITAS* site, the nearby town of Green Valley also contributes to the light pollution. Light pollution due to the cities can clearly be seen by eye

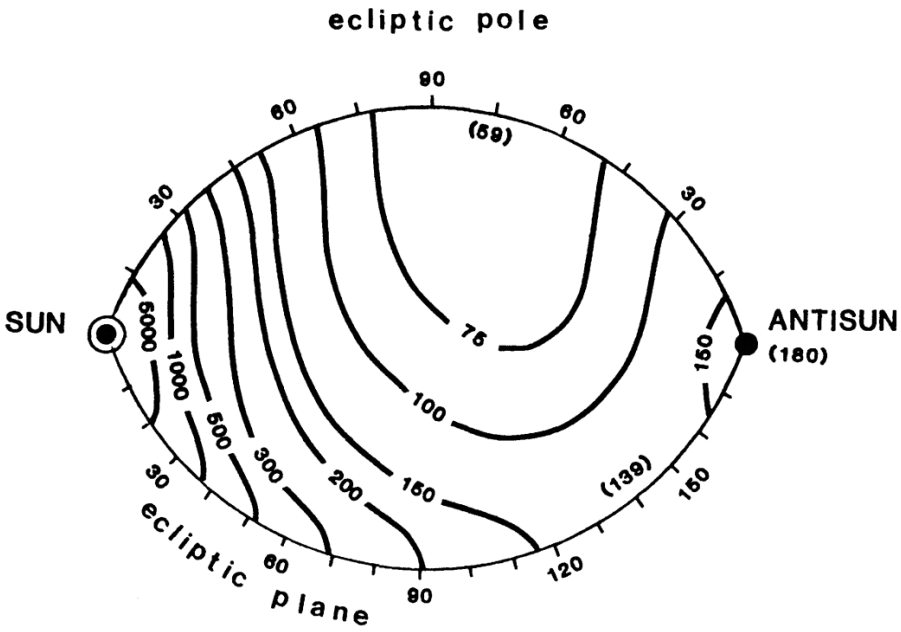

Figure 5.10: Map of zodiacal light. Image credit: Figure 4a in [88]; original source is indicated therein.

(e.g. Figure 5.11). The light from the city is easily visible in the PMT currents and trigger rates when the telescopes are pointing North and tracking a very low elevation source (e.g. a gamma-ray burst). Regulations exist for southern Arizona to limit the increase of light pollution and maintain the state's "dark sky" status [96]. Measurements by [97] at both Kitt Peak and Mount Hopkins over a 10 year time period determined that the increase in light pollution between 1988 and 1998 was more severe at Kitt Peak, with the blue-optical region increasing by $\approx 0.1 - 0.2$ mag/arcsec^2 at zenith, and as much as 0.5 mag/arcsec^2 near $z \sim 60°$ in the direction of Tucson.

A recent publication by [98] demonstrated that over the past 20 years, the sky brightness at Kitt Peak has increased by ~ 0.1 mag/arcsec^2 at zenith and ~ 0.3 mag/arcsec^2 in the direction of Tucson, but that lighting ordinances established by the city of Tucson and Pima County in the 2000s have been effective in maintaining the quality of the sky. In fact, [98] measured the sky to be ~ 0.1 mag/arcsec^2 darker toward Tucson than ten years prior.

The Kitt Peak and Whipple observatories are still considered to be dark sites. For this study, the contribution of the NSB due to light pollution is taken to be 0.1 mag/arcsec^2 which corresponds to ~ 20 S_{10} on a background of 250 S_{10} [99].

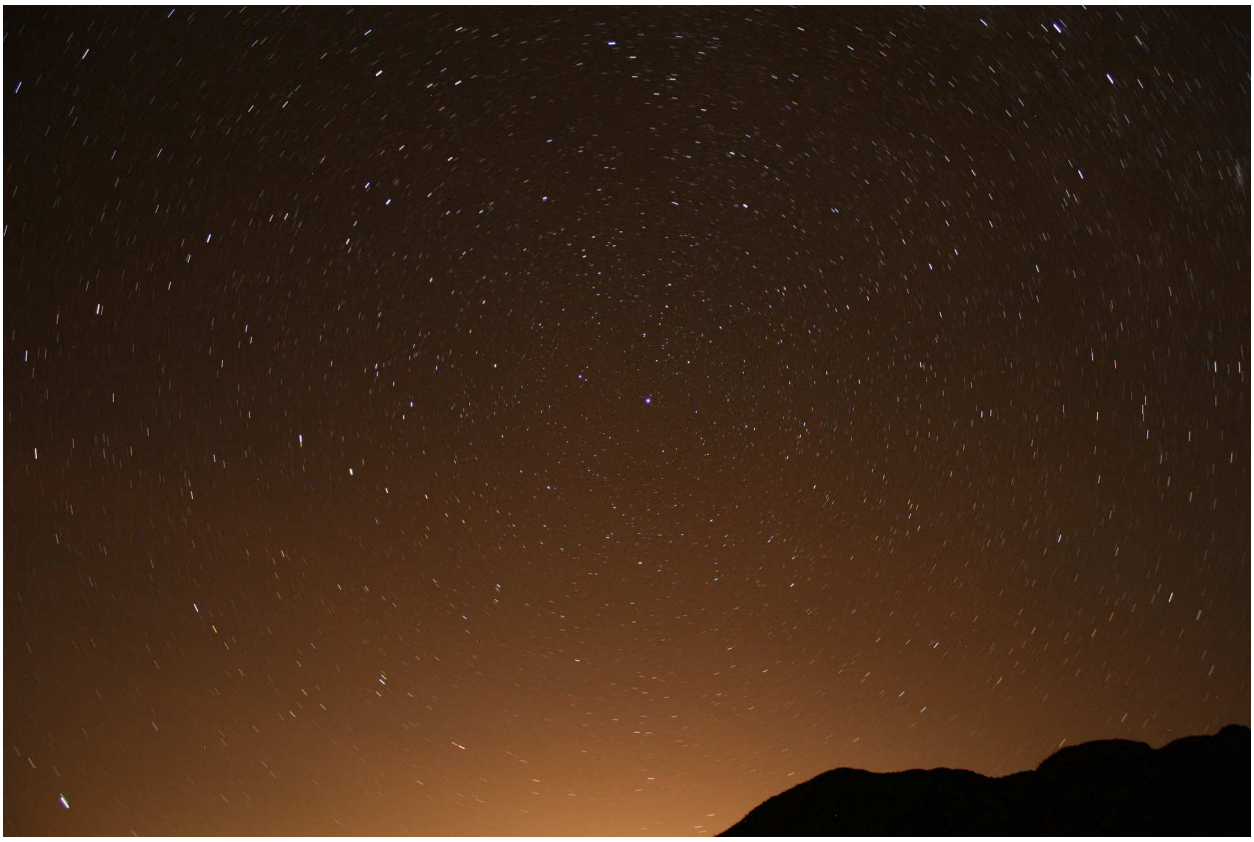

Figure 5.11: Picture of the horizon taken facing due North from the *VERITAS* site. The city of Tucson lies directly behind (at a distance of 70 km) the terrain which is silhouetted in the picture. Note that the effect of light pollution is made more clear by the fact that this is a long exposure; to the naked eye the effect is not as pronounced.

5.3 Effects of the Moon

The effects of moonlight on the brightness of the night sky are surprisingly poorly documented in the literature; many studies of the NSB (including the most of those referenced in this work) do not discuss the effects of moonlight at all. The vast majority of astronomers ideally want only the darkest skies for their measurements (which makes sense as this invariably increases signal-to-noise in any exposure) but do not have an easy way of quantifying the *actual* minimum required darkness for their measurements[3].

Moonlight is the light reflected from the lunar surface. It is mostly sunlight, with a smaller "Earthshine" component which can easily be seen with detectors on nights where the Moon is partially illuminated (see Figure 5.12). Given that moonlight is reflected sunlight, the spectrum of moonlight before entering the atmosphere is similar to the solar spectrum.

For a phase angle $g = 0°$ (*i.e.* the full moon), the lunar albedo at the site of the Apollo 11

[3]A tongue-in-cheek NOAO Newsletter was written "to help [astronomers] in this regard".

landing [100] is 0.0995, meaning that $< 10\%$ of light is reflected by the lunar surface. The albedo is also a function of the phase angle (see Figure 5.13). It is well documented that the Moon is much brighter near $g = 0°$, and after only a few days its brightness decreases substantially. This is due to an effect called opposition surge which is defined as a sudden surge in the brightness of an object as the phase angle of the observation approaches zero. In the case of the Moon, [101] demonstrated that this was a 10% increase between $g = 1°$ and $g = 0°$. The lunar mare, being more iron-rich than the lunar highlands are less reflective. Given that they have a complex distribution over the surface of the Moon the lunar albedo is largely variable as a function of position (varying up to 250% during the opposition surge, see [100]).

Figure 5.12: The Moon lit by Earthshine. Glare from the Sun is visible behind the Moon, and Saturn, Mars, and Mercury are visible as the three bright spots on the left. Image credit: "Plane of Ecliptic" by The Clementine Project, commissioned by NASA. Licensed under Public Domain via Wikimedia Commons.

The amount of light from the Moon entering the Earth's atmosphere can be calculated as

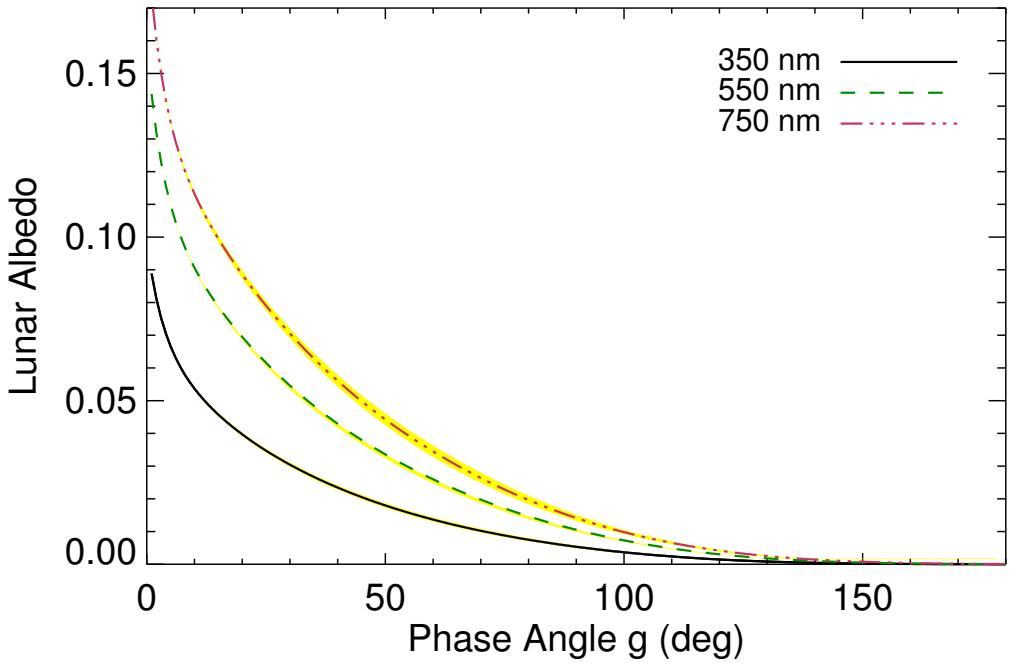

Figure 5.13: Lunar albedo as a function of phase angle g. The lines have been extrapolated for $g > 97°$. The albedo quickly decreases after the full Moon; this is consistent with opposition surge described in the main text. Image credit: Figure 3 in [102].

[103]

$$I^* = I_\odot \frac{\Omega_M}{\pi} A \left(\frac{D_{SM}}{1\ \text{AU}}\right)^2 \left(\frac{D}{\bar{D}}\right)^2 \tag{5.8}$$

where $I_\odot$ is the solar light intensity (*i.e.* the solar spectrum), $\Omega_M = 6.4177 \times 10^{-5}$ sr is the solid angle subtended by the Moon, D_{SM} is the Moon-Sun distance, D and $\bar{D}$ are the distance and mean distance from the Earth to the Moon (384,000 km), and A is the lunar albedo[4].

From here, the effects of attenuation due to airmass, Rayleigh scattering off atmospheric molecules, and Mie scattering off aerosols must be handled. Furthermore, the light can scatter multiple times (including off the ground) before finally reaching the detector. Describing this process is nontrivial and an exact model is difficult to attain. At the time of writing the only two models of moonlight brightness were found in the literature, and one of them is very recent [104, 102][5]. Since so many aspects of *VERITAS* observations are human-driven (e.g. observations start and stop when the sky is dark enough and not necessarily exactly at a given time) an exact treatment of the brightness of the sky is not required for operations.

It is common knowledge (not to mention intuitive) that the brightness of the Moon changes with its phase. This is quantified in Table 5.2. It also follows that when far below

[4]Note that there is a small discrepancy between this equation and the one used in the model in [102], which has inverted the $D/\bar{D}$ term and omitted the term containing D_{SM} entirely.

[5]Indeed, the lack of models has been noticed by other authors (e.g. [105])

the horizon, the contribution of the moon is zero. At full moon, the resulting increase in sky brightness depends strongly on wavelength. Spectra of the night sky at the Paranal Observatory in Chile, made during bright time and dark time are shown in Figure 5.14. The moonlit sky is more blue than the solar spectrum [105] and at long wavelengths the lunar contribution is smaller. This is consistent with the values in [106][6] which are shown in Table 5.3. These data indicate that even only a few days after the full moon the sky brightness has decreased substantially (e.g. after four days the brightness has decreased by a factor of four in the U-band), a result which is consistent with the strong change in lunar albedo.

g (°)	Before	After	g(°)	Before	After
0	1.000	1.000	80	0.120	0.111
10	0.787	0.759	90	0.0824	0.0780
20	0.603	0.586	100	0.0560	0.0581
30	0.466	0.453	110	0.0377	0.0405
40	0.356	0.350	120	0.0249	0.0261
50	0.275	0.273	130	0.0151	0.0158
60	0.211	0.211	140		0.0093
70	0.161	0.156	150		0.0046

Table 5.2: Relative illumination of the moon versus phase angle g. The columns labled "Before" and "After" correspond to data from before and after the full Moon. Data taken from Table 12.15 in [107], page 310.

Days from new Moon	Sky Brightness (mag/arcsec^2)				
	U	B	V	R	I
0	22.0	22.7	21.8	20.9	19.9
3	21.5	22.4	21.7	20.8	19.9
7	19.9	21.6	21.4	20.6	19.7
10	18.5	20.7	20.7	20.3	19.5
14	17.0	19.5	20.0	19.9	19.2
Brightness ratio	100	19.1	5.2	2.5	1.9

Table 5.3: Table of sky brightness values for different colour bands and different number of days from new Moon (14 is the full Moon). The last row is the ratio of the sky difference at full Moon compared to new Moon. Data taken from Table 1 in [108].

[6]The original source is indicated therein; at the time of writing it is not available online, thus they were taken from [105] which had reproduced them.

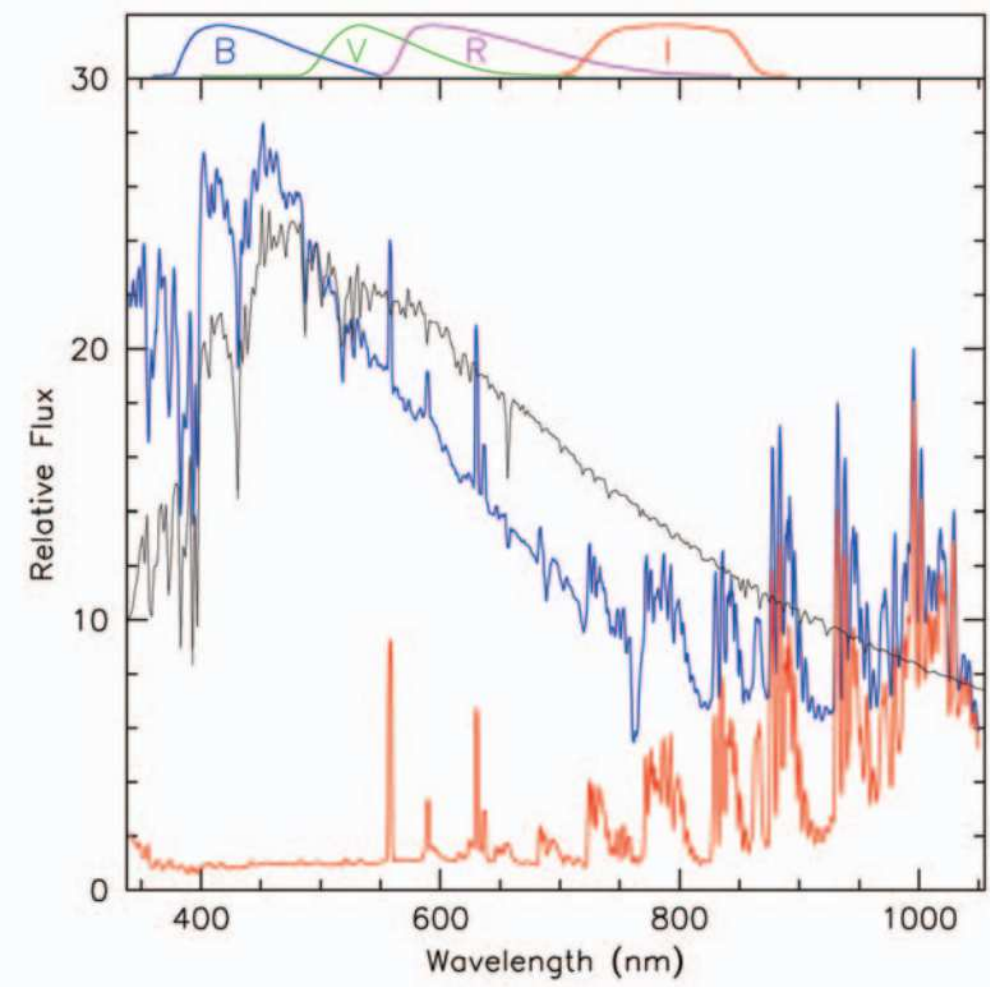

Figure 5.14: Comparison between the night sky spectrum during bright moonlight (blue) and dark time (red). The black line is the solar spectrum. The original source of this figure has stated that the region of the spectrum above 650 nm is contaminated by effects of the apparatus (this is beyond the regime relevant to *VERITAS*, so it is not a concern). Image credit: Figure 2 in [105].

5.4 Cumulative Effects

The cumulative sum of the different NSB components is given in Table 5.4. A typical value near solar minimum, taken away from the Galactic plane and away from the ecliptic, is 250 $S_{10}(V)$, or 21.8 mag/arcsec^2 for the V-band, with a lunar contribution that increases the sky brightness by a factor of five in that band. In the U-band, which is more relevant to *VERITAS*, the increase is a factor of 100. This value agrees well with the result of the 2009 zenith sky brightness at Kitt Peak ($V = 21.95$ mag/arcsec^2) reported by [98], and the $V = 21.9$ measurement at La Palma [87]. This is consistent with the night sky being similar around the world, which makes sense considering that NSB photons, aside from those from man-made light pollution, are of astrophysical origin.

Contributor	$S_{10}(V)$
Airglow (I_A)	$\sim 145 + (130)(S_{10\text{cm}} - 0.8)/1.2$
Zodiacal (I_Z)	$\sim 142 - 96 \sin \lvert\beta\rvert$; $\lvert\beta\rvert < 60°$
	~ 60 ; $\lvert\beta\rvert > 60°$
Stars (I_{SL})	< 5
Scattered starlight (I_{DGL})	$\sim 120 \exp(-1.1\lvert b\rvert/10°)$
EBL (I_{EBL})	~ 1
Light Pollution (I_{LP})	~ 20
Moonlight (I_M)	$\sim 0 - 1050$

Table 5.4: Numerical breakdown of the different contributions to the NSB. A typical value for the sky brightness at zenith is ~ 250 $S_{10}(V)$ near solar minimum. Note that the moonlight contribution is for the V-band; the maximum U-band contribution is over 2×10^4 $S_{10}(U)$.

The results of direct measurements of the NSB made using an apparatus built at McGill University and used at the *VERITAS* site were reported in [109]. The measured flux at 550 nm (the central wavelength in the V-band) was measured to be $\sim (1.0 \pm 0.1) \times 10^{10}$ ph/s/m^2/sr/nm [109, figure C.10]; the error is statistical only and conservatively interpreted from the results (there are a number of overlapping values). The author of [109] did not explicitly state the systematic uncertainties but based on the discussion within it is implied that they are likely more than 10%. These measurements were made at zenith while avoiding the Milky Way. In comparison, using the conversion values in Table 5.1, this work has predicted a NSB brightness of 250 $S_{10}(V) = 8.2 \times 10^9$ ph/s/m^2/sr/nm at 550 nm.

The value derived in this thesis assumes solar minimum, whereas the direct measurements were made between Fall 2005 and Spring 2006. The closest solar minimum (the start of Solar Cycle 24) was in January 2008. Assuming a sinusoidal variation from solar minimum to solar maximum over 11 years (which is approximately true), in January 2006 (2 years before solar

minimum, or 9 years after solar maximum), the Sun's $S_{10\text{cm}}$ flux was $\sim 43\%$ higher than the quiescent state. This has been determined using the expression

$$S_{10\text{cm}} = 0.6 \sin\left(2\pi \frac{t}{11 \text{ years}} - \pi/2\right) + 1.4 \tag{5.9}$$

assuming $S_{10\text{cm}}$ varies between 0.8 and 2.0 (as previously indicated) periodically. Using the relation for airglow given in Table 5.4, the airglow component was about 25% higher, roughly 38 S_{10}, which corresponds to a total sky brightness 288 $S_{10}(V) \sim 9.4 \times 10^9$ ph/s/m^2/sr/nm at 550 nm, which is closer to the measured value and within the systematic errors of the measurement in [109].

5.5 Summary

The different constituents of the NSB have been described and quantified, and estimates of the its total flux based on measurements of its different components have been shown to agree with direct measurements made at the *VERITAS* site. In the U and B colour bands the increase in the sky brightness due to moonlight is a factor of 100 and 19, respectively.

Based on this, it can be seen that non-standard observing modes are needed to prevent the *VERITAS* data acquisition system from being overwhelmed by noise and (arguably more importantly) prevent damage to the PMTs, since the experiment was designed with exposure to only low amounts of light in mind. Details on said observing modes will be given in Chapters 8 and 9.

Chapter 6

The *VERITAS* Observing Strategy

Typically, imaging atmospheric Cherenkov telescopes (IACTs) operate only during astronomical darkness (that is, when the sun is more than 18° below the horizon). There are two reasons for this: increased noise in the data limits sensitivity to gamma-ray signals, and increased light levels accelerate the ageing of the camera photomultiplier tubes (PMTs).

In this chapter, historical methods used to take VHE gamma-ray data under moonlight are presented, and some of the reasons why new observing modes are required are demonstrated. The observing strategy adopted by *VERITAS* is also presented. The main focus of this work is the implementation of the reduced high voltage (RHV) and UV filter (UVF) observing modes which will be compared to a standard, or nominal (NOM) analysis in the subsequent chapters.

The author has adopted the following naming convention when referring to various levels of moon illumination. Note that these levels are defined based on the mean PMT currents rather than a specific level of moonlight.

- Dark time: When the Moon is not in the sky and when the sky brightness is not being contaminated by moonlight being scattered through the atmosphere while the Moon is below the horizon. Typically, the averages of the PMT currents in each camera are below 10 μA in this case.

- Low/Moderate moonlight: When the near side of the Moon is $\lesssim 35\%$ illuminated. The average PMT currents are typically between 10 and 15 μA in this case.

- Bright moonlight: When the Moon is $\sim 35 - 65\%$ illuminated. In this case, reduced camera voltages are required. With reduced gains, the average PMT currents range from 5 to 15 μA.

- Very bright moonlight: When the Moon is $\gtrsim 65\%$ illuminated. In this case, the UV filters are required. The filters block out the vast majority of moonlight and NSB, placing mean PMT currents between 2 and 10 μA.

Both "bright" and "very bright" moonlight fall under the mandate of the Bright Moonlight Program.

6.1 Historical High-noise Observing

To circumvent the issues imposed by the night sky background on observing, the *Whipple* collaboration experimented with using a solar blind (*i.e.* UV-sensitive) camera on moonlit nights [110]. This resulted in the ability to detect gamma rays, albeit with a much higher energy threshold (1.2 TeV versus 0.4 TeV). It was also somewhat impractical as it required completely replacing the standard camera. The *ARTEMIS* experiment [111] used the *Whipple* telescope in an attempt to observe the shadowing of cosmic rays due to the Moon and required pointing the telescope $1-2^{\circ}$ away from the Moon. In the end, however, they were not sensitive enough to perform a measurement down to the percent level, which is required for the primary science goal of measuring the antimatter component of cosmic rays. The *Whipple* group also experimented with the use of filters to reduce the camera sensitivity at wavelengths greater than 360 nm [112].

Of the previous generation of IACTs, the *HEGRA* experiment was the first to operate regularly during moonlit nights using reduced camera gains [113]. It was demonstrated that the CT1 telescope could operate as soon as nautical twilight began (solar elevation $< 12^{\circ}$) depending on the pointing direction of the telescope. This yields an additional 40-80 minutes of observing a night depending on the telescope pointing direction. Conservatively, this implies an additional ~ 100 hours of observing a year. Note that twilight and moonlight observations were limited to CT1 only, and not the entire *HEGRA* array.

Unfortunately, owing mostly to limitations with the camera voltage control software, *VERITAS* cannot run under reduced high voltage during twilight, as the changeover between the RHV and NOM modes (or vice-versa) has a tendency to cause issues as the high voltage control software was not designed with the goal of quickly changing HV. Excluding time required for the PMTs to stabilize at the voltage, changing the HV level takes roughly one minute to do. Furthermore, the data acquisition system trigger settings must also be adjusted, which takes a few minutes to accomplish, barring any software issues. Thus, rather than risk losing "dark time" data to software problems, *VERITAS* sacrifices this time.

6.2 Current State of the Field

6.2.1 *H.E.S.S.*

The HESS collaboration is extremely conservative with their cameras and operates strictly under astronomical darkness during clear, moonless nights.

6.2.2 *MAGIC*

The *MAGIC* collaboration operates their PMTs at significantly lower gains than *VERITAS*. The cameras were designed with this in mind; the PMTs are run at a gain $\sim 3 \times 10^4$ to avoid high anode currents. Like *VERITAS*, the *MAGIC* PMT signals are amplified by a fast AC-coupled preamplifier before being sent to the digitizing electronics. The combined gain of the *MAGIC* PMTs and preamplifiers is $\sim 10^6$.

Running at a lower PMT gain allows them to operate under a large number of sky brightnesses without adjusting the camera voltages. This also allows *MAGIC* to operate in twilight. Thus, a single observing mode is used across a huge range of sky brightnesses. Details on the *MAGIC* observing strategy can be found in [114].

6.3 The *VERITAS* Observing Strategy

Prior to the inception of the Bright Moonlight Program, *VERITAS* observations took place strictly when the average PMT currents (with the PMTs operating at their nominal gains) were below 15 μA. This threshold was chosen to avoid unnecessarily ageing the PMTs, which is discussed in the next section. This limited observations to when the Moon was less than $\sim 35\%$ illuminated. This also cut into some of the available dark time: given the overhead in starting and shutting down the experiment (roughly 90 minutes for startup and 30 minutes for shutdown), on nights where the amount of available dark time was less than ≈ 1 hour, no data was taken at all.

The breakdown of current *VERITAS* observations is shown in Figure 6.1. Note that there are still a few nights around the full moon where *VERITAS* does not operate. There are several reasons for this: firstly, the sensitivity of *VERITAS* under the brightest moonlight is poor (this is elaborated upon later in Section 9) due to the high number of random triggers due to NSB photons. CFD thresholds must be raised to avoid spurious triggers overwhelming the DAQ, but increasing the CFD thresholds adversely affects the low-energy threshold of the detector. Furthermore, even with reduced PMT gains or UV filters, the mean PMT currents are high due to the sheer amount of light arriving at the phototubes; this is independent

of the issues with the DAQ when the L3 trigger rates are too high. Next, the aptly named "bright period" allows for telescope maintenance such as mirror replacement and alignment, or FADC replacement to be done without the risk of interfering with science observations. As any experimentalist will tell you, sometimes simply swapping out a piece of equipment with a spare can invite problems which can take a significant amount of time to rectify.

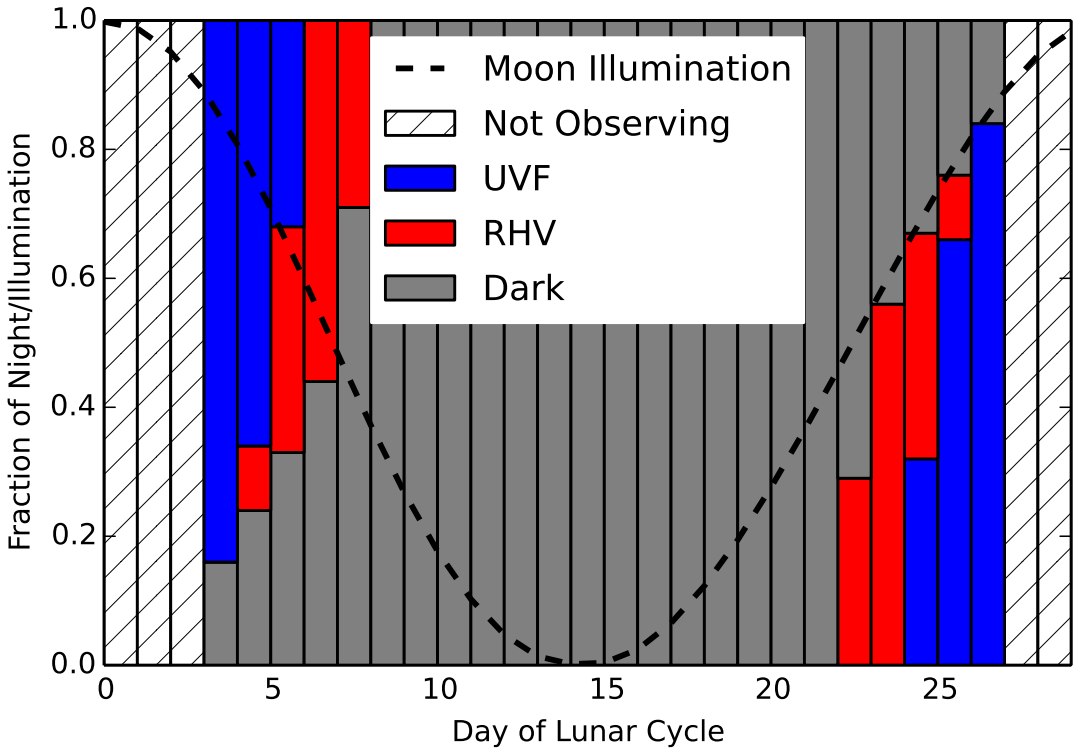

Figure 6.1: Breakdown of how much time is spent in each observing configuration as a function of days from the full Moon. Note that this is more of a guideline than a rule; the exact switchover between observing modes has always been at the discretion of the telescope operators and is based on PMT currents and not exact conditions (e.g. moon elevation). The observing pattern at the end of the lunar cycle is inverted with respect to the start; this is due to the fact that near the start, the Moon rises partway through the observing night. Conversely, near the end of the dark run, at the start of observing the Moon is above the horizon and subsequently sets as the night progresses. Note that on nights starting with NOM observations, there is a transition period where sources can be observed in the RHV mode. This feature is not indicated in this plot as the duration of observations during the transmission period is subjective and depends on the target list and specific observing conditions of that night.

6.4 Concerning Different Observing Modes

6.4.1 Spurious Triggers

In addition to ageing the PMTs due to increased light exposure, the presence of large amounts of NSB photons due to moonlight is a major concern for observers. Recall that in order to generate an L1 trigger, there must be ~ 5 photons that arrive close enough in time to each other such that their signals pile up and trigger the discriminator. Cherenkov pulses are large, as most of the Cherenkov photons arrive at the ground at the same time. However, the night sky background is random and obeys Poisson counting statistics. It is trivial to demonstrate that for a higher NSB rate, the probability of photon pileup increases. For an NSB rate Φ, the probability of detecting κ photons in a time window Δt is

$$P[N(\Delta t) = \kappa] = \frac{e^{-\Phi\Delta t}(\Phi\Delta t)^{\kappa}}{\kappa!} = P(\Phi, \Delta t, \kappa). \tag{6.1}$$

Note that this does not take into account the effects of the spectral distribution of NSB photons or the PMT photon detection efficiency, but these are second-order corrections in this demonstration. This approximation should be considered a lower limit since PMT pulses arriving at different times can add to the number of triggers (since a PMT pulse is not a δ-function), but modelling this would require Monte Carlo simulations and is overkill for the purposes of this demonstration.

Considering an elevated NSB rate $\Phi_\alpha = \alpha\Phi$ with α defined as a constant > 1, it is possible to calculate how much larger the probability of getting spurious triggers under a noisy sky for a given number of photons:

$$\frac{P(\Phi_\alpha, \Delta t, \kappa)}{P(\Phi, \Delta t, \kappa)} = e^{-(\alpha-1)\Phi\Delta t}\alpha^{\kappa}. \tag{6.2}$$

By taking the sum

$$\frac{\sum_{i=\kappa}^{\infty} P(\Phi_\alpha, \Delta t, i)}{\sum_{i=\kappa}^{\infty} P(\Phi, \Delta t, i)} \tag{6.3}$$

from a number of photons κ to ∞, it is possible to express the integrated difference in trigger probabilities. The shape of this integrated probability is demonstrated in Figure 6.2 for a number of values of α for a constant time window and base flux. For example, taking $\Phi = 170$ MHz and $\alpha = 1.5$ (very roughly the difference between standard observing runs taken on the Crab nebula and the observing limit for standard voltage observations), the probability of counting $\kappa \geq 5$ photons is ~ 8 times greater. For $\alpha = 3$ (putting the NSB in the regime requiring reduced PMT gain), the ratio is ~ 100. Thus, triggering rates are highly sensitive to the NSB rate over the noise levels typically observed during data taking.

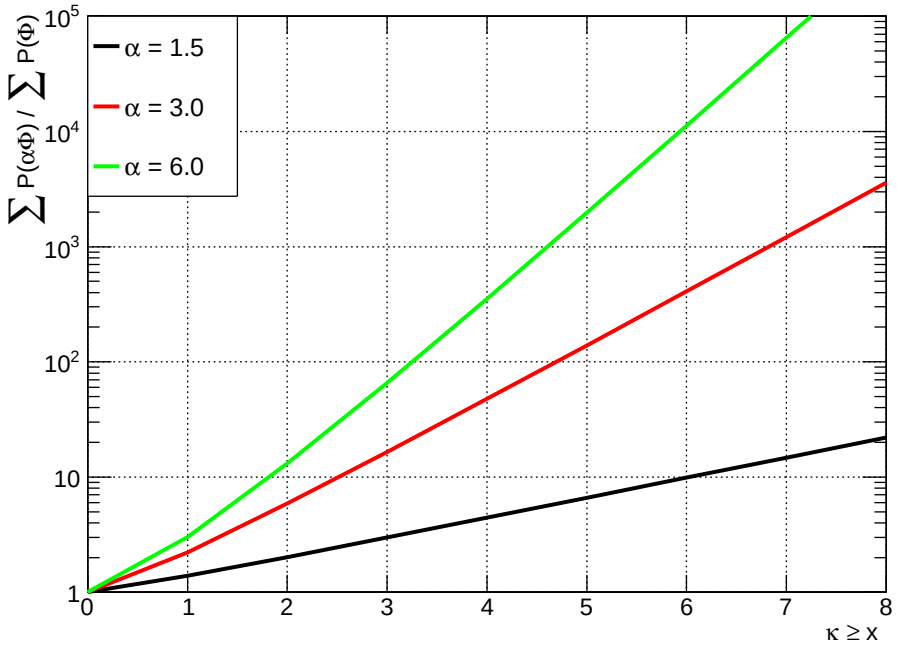

Figure 6.2: Integrated probability ratio (Equation 6.3) evaluated for a number of values of α.

6.4.2 Bias Curves & the Effects of the NSB on Trigger Rates

Based on this discussion, it is reasonable to assume that one way to avoid spurious triggers due to the NSB would be to simply raise the CFD thresholds to a level where the experiment triggers are again dominated by Cherenkov pulses due to cosmic rays (CRs) and not by NSB triggers (*i.e.* a threshold that requires a large k). In order to do this in a reasonable way the response of the detector as a function of CFD threshold must be quantified. This is done by means of a bias curve.

A bias curve is a plot of trigger rates versus CFD thresholds and can be produced for each of the telescopes individually (L2 rates) and the array trigger rate (L3 rate). In a bias curve, there are two clearly different regimes: a high-threshold component is due to triggers caused by cosmic rays, and a steeply falling component at very low thresholds is due to NSB triggers. The curves can be fit by a sum of two exponential functions:

$$R(x) = \left(e^{A+Bx} + e^{C+Dx}\right) \text{Hz}. \tag{6.4}$$

In this treatment, the first term corresponds to the size and shape of the NSB component and the second corresponds to the CR component. The value of x in the bias curve is the CFD threshold, which is proportional to the number of photoelectrons (the two are related by the PMT absolute gain). Two examples bias curves are depicted in Figure 6.3: one taken

on an extragalactic field and one taken on a Galactic field. Figure 6.4 contains only the L3 components of the bias curves on the same plot to emphasise the differences between the two.

One expects that for the Galactic field, where there is more light due to diffuse emission in the galactic plane, that the contribution due to NSB triggers to be shifted to higher thresholds. This changes the location of the inflection point where the NSB component of triggers dominates over the CR component. The fits for these bias curves are given in Table 6.1. While not strictly consistent, the fits to the CR component are quite close ($< 2\sigma$ for the normalisation), whereas the NSB component normalisation is significantly different (5σ) and the slope is significantly steeper in the bright field, which is to be expected. The solutions for the inflection point are $x \sim 36$ mV and $x \sim 33$ mV for the bright and dark bias curves, respectively.

	CR		NSB	
	A	B	C	D
Bright	7.17 ± 0.07	-0.023 ± 0.001	28.5 ± 0.1	-0.616 ± 0.004
Dark	7.35 ± 0.06	-0.025 ± 0.001	29.5 ± 0.2	-0.683 ± 0.007

Table 6.1: Fit values for the L3 bias curves in Figure 6.3. Each bias curve has been fit between 25 mV and 100 mV. The χ^2/NDF are 35.7/34 ($P \sim$ 0.388) and 45.1/34 ($P \sim$ 0.096) for the bright and dark curve, respectively.

The CFD thresholds will ultimately dictate the energy threshold for the data being taken. This means that in general the CFDs should be set as low as possible before the array becomes overwhelmed by NSB triggers and the array dead time becomes too severe (or the DAQ stops functioning all together). Thus, it is standard operating procedure to set the CFD thresholds near the inflection point (and on the CR-dominated side) in the bias curve.

6.4.3 PMT Ageing

It has been mentioned previously that over time PMTs age (due to radiation damage to the dynodes) as a function of how much current passes through them. Studies have been done on the *VERITAS* PMTs to quantify this. The details of these studies can be found in [42].

An example of the gain decrease as a function of amount of time the the PMT was exposed to light (which for a steady light source is proportional to how much integrated current the PMT produced) is given in Figure 6.5.

The shape of the curve is the sum of two exponential decay functions:

$$I = I_0 \left(A_1 \cdot e^{-t/\tau_1} + A_2 \cdot e^{-t/\tau_2} \right) \tag{6.5}$$

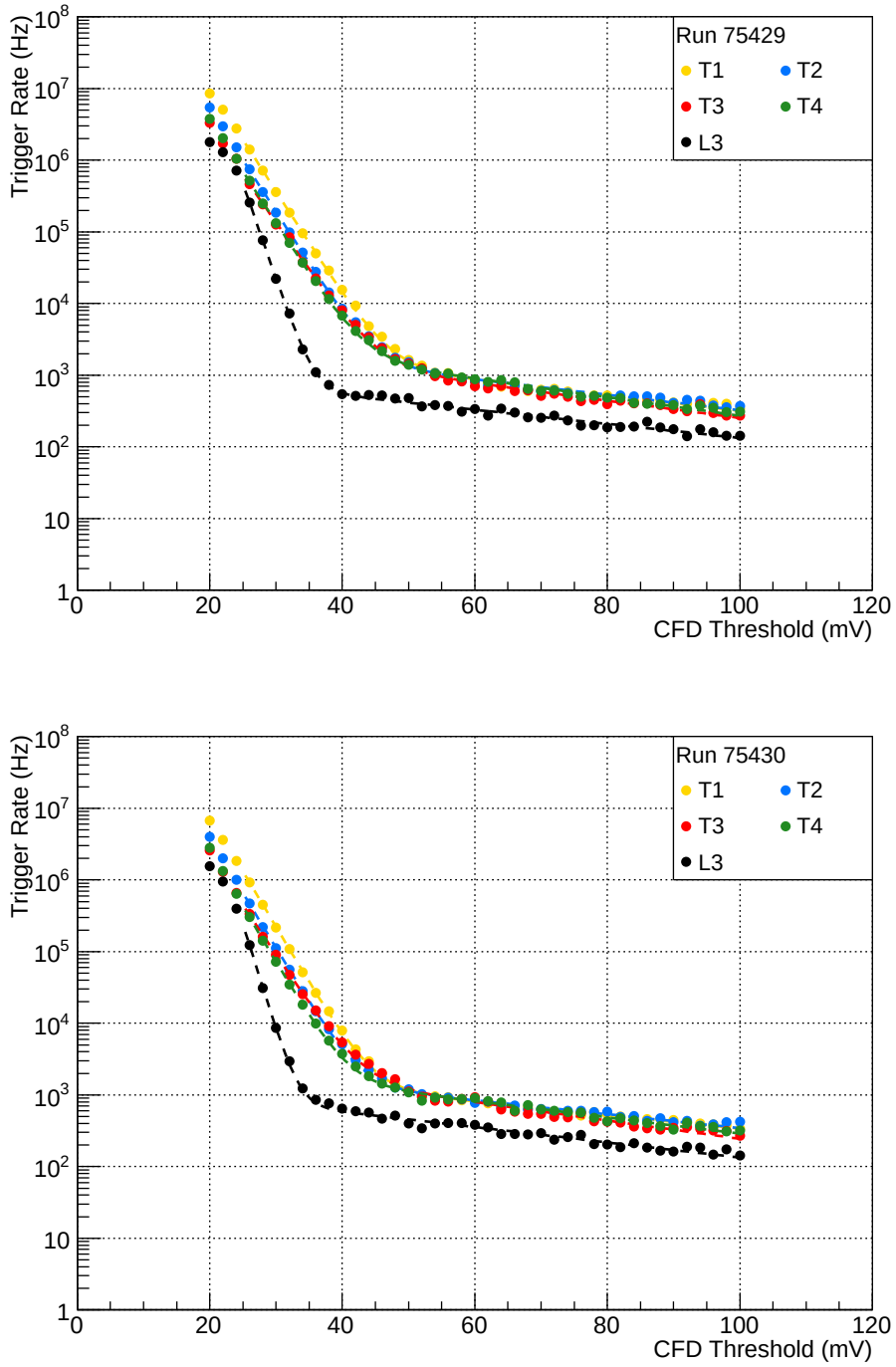

Figure 6.3: **Top:** Bright field (Galactic) bias curve. L2 rates for each telescope are given in addition to the L3 trigger rate. **Bottom:** Dark field (extragalactic) bias curve. The fit values for the L3 rates are listed in Table 6.1. By eye, the difference in the L2 rates can be seen (especially between 40 mV and 50 mV). The difference in the L3 rates between fields is more difficult to discern by eye on this scale (see Figure 6.4). This is because the L3 trigger is less sensitive to the NSB than the L2.

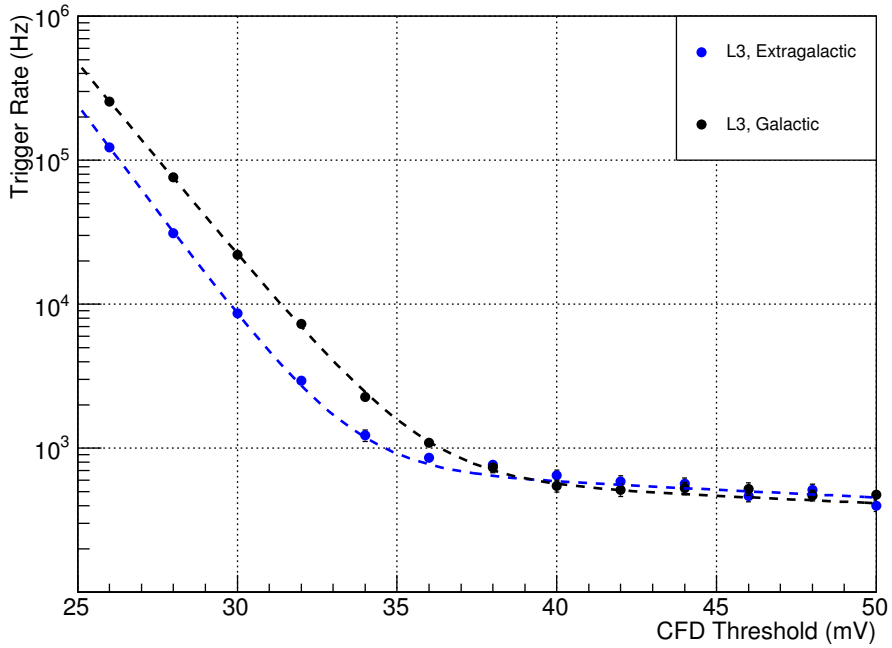

Figure 6.4: Galactic and extragalactic L3 bias curves. The inflection point for the galactic bias curve is slightly higher ($\sim$ 36 mV vs $\sim$ 33 mV).

where $I_0 = 45$ μA, $A_1 = 0.25$, $A_2 = 0.75$, $\tau_1 = 247$ hours, and $\tau_2 = 1300$ days. Note that [42] did not provide statistical uncertainties on these fit values due to the extremely high statistical precision of the measurement; the uncertainties are hence systematics dominated.

VERITAS typically has $\sim$ 1000 hours of observing in the standard mode a year, where the PMT currents are on average $\sim$ 8 μA. Thus, the integrated anode current for any given year is $\approx$ 29 C. The total integrated current resulting from Figure 6.5 is $\approx$ 96 C. Thus, the $\sim$ 25% gain drop shown corresponds to over 3 years of observing in the standard configuration. Based on this, it follows that operating the PMTs at their nominal HV during time that is considered RHV time (PMT currents in the range 15 μA $\leq I \lesssim$ 45 μA) would significantly contribute to the drop in PMT gain after a single year's observing and hence reduce the operational lifetime of the experiment.

6.5 Conventions

It is the convention in VHE gamma-ray astronomy to refer to the brightness of sources in "Crab Units", that is, fractions (or, very rarely, multiples) of the flux from the Crab Nebula. The Crab has long been used as the standard candle in the field; it is convenient as it is

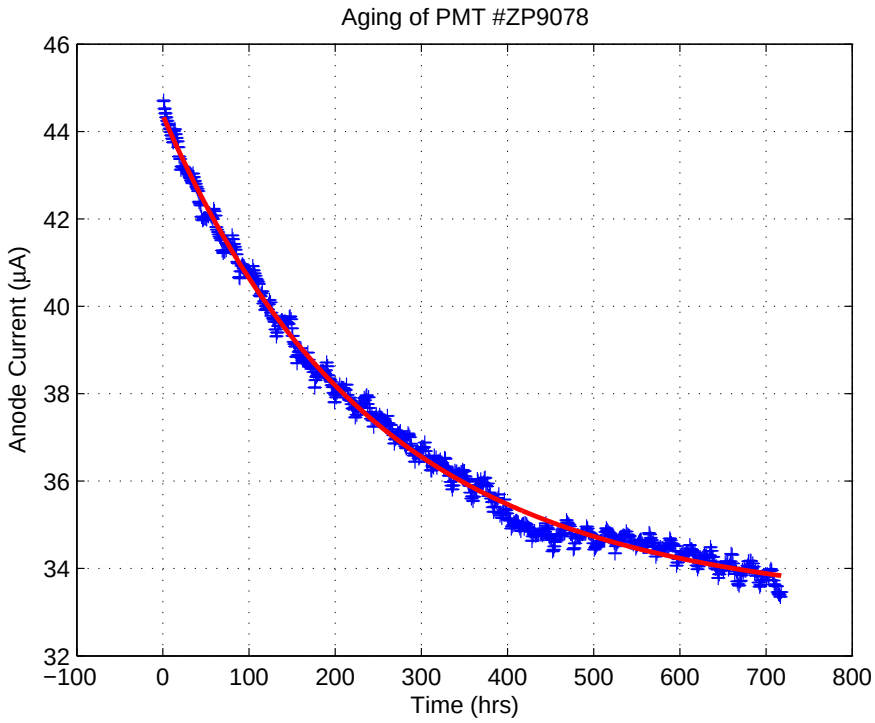

Figure 6.5: Change in PMT gain (manifesting as a reduction in anode current) versus time for a PMT exposed to a steady source of light. The initial current was 45 μA, which is $\sim$ six times higher than currents during a standard observing run. The red line is a fit to the data; the fit function is given in Equation 6.5. Image credit: Figure 4 in [42].

bright and steady at VHE energies (see e.g. [115]).

There are a number of measurements for the Crab spectrum by different experiments. Thus, there is no one value for the Crab spectrum (albeit most experiments tend to agree within errors, as one would expect). Hence, in this work, when quoting results from other experiments, their measured value of the Crab Nebula is the reference in such a case. Table 6.2 contains a list of Crab spectral fits from the following list of experiments.

- *Whipple* [116, 117] (W1998, W2007)
- *CAT* [118] (C2001)
- *HEGRA* [119] (HEG2004)
- *H.E.S.S.*[120] (HESS2006)
- *MAGIC*[121, 122] (MAG2008, MAG2015)
- *ARGO-YBJ* [123] (A2015)

- *VERITAS*[1] [115] (V2014)

The following acronyms for different spectral shapes have been used:

- Power Law (PL)

$$\frac{dN}{dE} = F_0 \left(\frac{E}{E_0}\right)^{-\Gamma} \tag{6.6}$$

- Power Law with Cutoff (PLWC)

$$\frac{dN}{dE} = F_0 \left(\frac{E}{E_0}\right)^{-\Gamma} \exp\left(-\frac{E}{E_c}\right) \tag{6.7}$$

- Curved Power Law (CPL)

$$\frac{dN}{dE} = F_0 \left(\frac{E}{E_0}\right)^{-\Gamma+\beta \log_{10}(E/E_0)} \tag{6.8}$$

These have been included explicitly so that there exists a single "clearing house" containing many of the measurements available at the time of writing. Furthermore, it demonstrates the differences in systematic uncertainties between different experiments, which tend to be of order 20% for experiments like *VERITAS*. This is important because the NOM, RHV, and UVF observing modes can be thought of as entirely different experiments. Thus, the scale of the differences in the final results of this thesis can be compared to the differences in Table 6.2 as a check on the validity of the measurements made in the different modes.

6.6 Summary

In this chapter, the reasons why new observing modes are required for observations under moonlight have been presented. The Crab Nebula, which will be the reference source in the analysis of data using the new observing modes, has been studied by a number of VHE observatories and their results have been included in this chapter to serve as a reference for the analyses presented in the next chapters.

[1] At the time of writing, the only published spectrum of the Crab Nebula is above 1 TeV. The systematic errors in this measurement are significantly higher than typical *VERITAS* measurements.

Experiment	Fit Form	F_0	E_0	Γ	β	E_c	E_{low}	E_{high}	χ^2/NDF	F ($E > 1$ TeV)
W1998	PL	3.20 ± 0.17	1	2.49 ± 0.06	-	-	0.5	5		2.1 ± 0.2
W1998	CPL	3.25 ± 0.14	1	2.44 ± 0.06	-0.151	-	0.5	5		
W2007	PL	3.19 ± 0.07	1	2.64 ± 0.03	-	-	0.49	8		
HEG2004	PL	2.83 ± 0.04	1	2.62 ± 0.02	-	-	0.5	80		1.75 ± 0.03
C2001	PL	2.20 ± 0.05	1	2.80 ± 0.03	-	-	0.3	15		1.22 ± 0.03
HESS2006	PL	3.45 ± 0.05	1	2.63 ± 0.02	-	-	0.41	40	104/10	2.11 ± 0.03
HESS2006	PLWC	3.76 ± 0.07	1	2.39 ± 0.03	-	14.3 ± 2.1	0.41	40	15.9/9	2.26 ± 0.08
MAG2008	PL	57 ± 2	0.3	2.48 ± 0.03	-	-	0.075	6.9	24 / 8	
MAG2008	CPL	60 ± 2	0.3	2.31 ± 0.06	-0.26 ± 0.07	-	0.077	6.9	8 / 7	
MAG2015	PLWC	3.80 ± 0.11	1	2.21 ± 0.02	-	6.0 ± 0.6	0.050	30	35/11	
MAG2015	CPL	3.23 ± 0.03	1	2.47 ± 0.01	-0.24 ± 0.01	-	0.050	30	20/11	
A2015	PL	0.52 ± 0.02	2	2.63 ± 0.05	-	-	0.34	17.7	5.8/7	1.97
A2015	PLWC	-	-	-	-	> 12	0.34	17.7		
V2014	PL	3.48 ± 0.14	1	2.65 ± 0.04	-	-	1.1	22.4	16.6/12	2.05 ± 0.07
V2014	PL	3.53 ± 0.15	1	2.72 ± 0.05	-	-	1.1	22.4	10.1/12	2.10 ± 0.06

Table 6.2: Selected Crab Nebula fit functions from a variety of experiments. Systematic errors for most values can be found in the respective papers. Acronyms for the fit forms and sources are given in the main text. Where no applicable range for the fit was explicitly stated, the values for the lowest and highest spectral points were used for E_{low} and E_{high}. The units for F_0 are 10^{-7} m^{-2} s^{-1} TeV^{-1}, F are 10^{-7} m^{-2} s^{-1}, and the units for E_0, E_c, E_{low}, and E_{high} are TeV.

Chapter 7

Observations in the Standard Configuration

In this chapter, the results of a standard *VERITAS* analysis of data taken in the nominal (NOM) configuration are presented. This NOM analysis will become the reference for the next two chapters, in which the two different observing modes, the reduced high voltage (RHV) and UV filter (UVF) modes, that allow *VERITAS* to observe during bright moonlight will be discussed.

7.1 Array Configuration

7.1.1 Typical Observing Constraints

When observing in its standard mode there are very few aspects of the detector configuration which must be fine tuned or altered due to observing conditions (this makes sense since in a moonless sky the NSB is effectively the same in all pointing directions, at least at the level *VERITAS* is concerned). However, there are still some observing constraints for the nominal configuration which must be adhered to in order to assure that the data quality is high.

Arguably the most important rule in *VERITAS* is that if the mean of the PMT currents is above 15 μA (due to e.g. sunrise, the presence of the Moon, or moonlight being reflected off clouds, etc.), observers must cease data taking and power off the cameras to preserve the PMTs. Note that the threshold is somewhat arbitrary and is not actually a physical limit of the PMTs. In fact, prior to the camera upgrade, the mean PMT current threshold was *also* 15 μA. The new PMTs, being more sensitive, have higher currents for a given light level, but

still have the same (conservative) maximum. Also, observers must take care to ensure that the data rates are not too high, as this increases dead time and reduces the sensitivity of the detector.

7.1.2 CFD Thresholds

Dead time is the time during which the experiment is "busy" reading out the data from the previously triggered event. During this time, if another event comes in that would otherwise trigger the array, the trigger is ignored and the event's information is lost. Thus, when taking data it is important to tread the line between maximising the trigger rate (*i.e.* the amount of data coming in) while keeping dead time at a manageable level. During standard operations, *VERITAS* dead time is approximately 15%.

During standard observations, one of two L1 trigger thresholds is used for data taking to limit dead time: in the event where the currents are above 10 μA, the constant fraction discriminator (CFD) thresholds are increased to 60 mV; otherwise they are set to 45 mV. This has an effect on both the low energy threshold and the detector's sensitivity to low-energy events (since lower energy showers may no longer trigger the array), so observing targets are chosen with this in mind.

7.2 Analysis Results

7.2.1 Performance Studies

In the end, the purpose of an analysis in the context of this work is to assign physical values (namely, the energy and arrival direction) to gamma rays based on observations of air showers detected by the experiment. The former is largely dependent on both simulations and the analysis tools used in the data reduction. In the following section, a discussion of how the detector performance can be quantified is presented.

It should be noted that the gamma/hadron separation cuts are an important part of generating the subsequent instrument response functions (IRFs) and in the data analysis shown in the next section. The cuts used in the NOM configuration analysis are standard "moderate" cuts which were presented earlier in Table 4.2. Note that changing any values used for gamma/hadron separation requires regenerating every IRF and reprocessing of data using the new IRFs. Thus, for brevity, only one part of the parameter space (*i.e.* the cuts previously mentioned) are presented.

7.2.1.1 Energy Threshold

An important quantity used when describing detector performance is the energy threshold. The energy threshold is the minimum energy of gamma ray to which the detector is sensitive and is typically broken up into two categories: *trigger* energy threshold and *analysis* energy threshold. The former refers to the minimum energy gamma ray capable of triggering the telescope array. The analysis energy threshold has several definitions. For example, in `eventdisplay` the default definition of the energy threshold is the energy at which the effective area falls to 10% of its maximum value. Recall that the effective area is used to convert a number of detected gamma rays at a given energy into a flux value (done by dividing the number of counts by the effective area and the dead-time-corrected observing time). At low energies the effective area is dominated by poor statistics, so errors are large and the results are no longer reliable.

Another definition takes the analysis energy threshold to be the energy above which the energy reconstruction bias and resolution (see below) are within acceptable limits (e.g. bias $< 20\%$). Once again, the motivation is to define an energy below which the errors intrinsic to the analysis become too large. Both these definitions depend on observing conditions (zenith angle, noise levels) and in the end represent a minimum energy to which the analysis can be trusted at some confidence level.

Note that the analysis energy threshold does *not* correspond to the lowest bin in an energy spectrum. The lowest energy bin in a spectrum usually has a lower edge that is above the analysis energy threshold. Thus, if the analysis energy threshold is 150 GeV a bin ranging from 100 to 200 GeV would not be used in the spectral analysis. This is because it would only have counts covering only half the energy range in the bin, and the effective area weighting would thus be wrong. Thus, binning is important when producing gamma-ray spectra; one must optimise the binning such that the bins are small enough to provide useful information on (for example) spectral shape but not so small that the statistical errors dominate and yield large fluctuations point-to-point. The energy resolution (described in the next section) must also be taken into account.

It is not unreasonable to ask "why not start the bins at the energy threshold?". It is surely possible, but an automatic rebinner is not currently implemented as part of `eventdisplay`. Thus, binning (both bin widths and bin centres) must be done by hand.

7.2.1.2 Energy Bias and Resolution

Two more important characteristics of the analysis are the shower reconstruction bias and resolution. The reconstruction bias is computed as the mean shift between the reconstructed

energy of a simulated gamma ray, as determined by the analysis software, and the true Monte Carlo energy. This allows the energy-dependent systematic error on the reconstructed energy of a real gamma ray to be estimated. The resolution is effectively the width of the distribution of reconstructed gamma ray energies for a given simulated gamma ray energy. Note that they are properties of the analysis and not physically motivated. MC simulations are used to estimate these parameters so that the errors inherent to the analysis of data can be quantified.

Figures 7.1 and 7.2 show the bias and resolution of the shower energy reconstruction for three different noise levels: the lowest and highest simulated levels and a third which is representative of the NOM data set presented in this thesis. The bias gets worse at low energies; this is expected because there are fewer Cherenkov photons and NSB fluctuations wash out some of the shower information. At low energies the reconstruction bias is driven towards positive values since the array is triggering only on upward going fluctuations in the air shower produced for a given gamma-ray energy. This means that in the generation of lookup table IRFs, only upward-fluctuating showers are being used to populate the bin. Hence, the gamma-ray energies are biased to higher values. At the other side of the energy spectrum (high energies), the limited field of view of the camera limits how much of an air shower can be seen. Hence, there is information lost preferentially in the case of higher-energy showers, and the IRFs reflect this.

The reconstruction bias and resolution are worse for higher noise levels, which is consistent with the signal-to-noise of shower images being lower for small (*i.e.* low energy) showers. The resolution is largely the same except at the very lowest energies, close to the trigger threshold, where errors are very large and analysis cuts would clean away the vast majority of those events.

7.2.2 Data

To provide a reference for the subsequent analyses of RHV and UVF Crab data, a subset of the *VERITAS* Crab data taken at roughly the same time of year was selected for comparison. Table 7.1 contains the list of runs and some corresponding observing details. These data were analysed using previously defined methods.

The analysis of the NOM data set yielded 3142 On events and 228.00 Off events (1368 total counts with the background normalization factor $\alpha = 1/6$). The resulting gamma-ray rate was 9.1 ± 0.2 photons/minute with a background rate of 0.71 ± 0.05 events/minute. Using the Li & Ma equation for significance calculation (Equation 4.9), the resulting detection significance is 84.3σ. The average analysis energy threshold in this data set was 144 GeV.

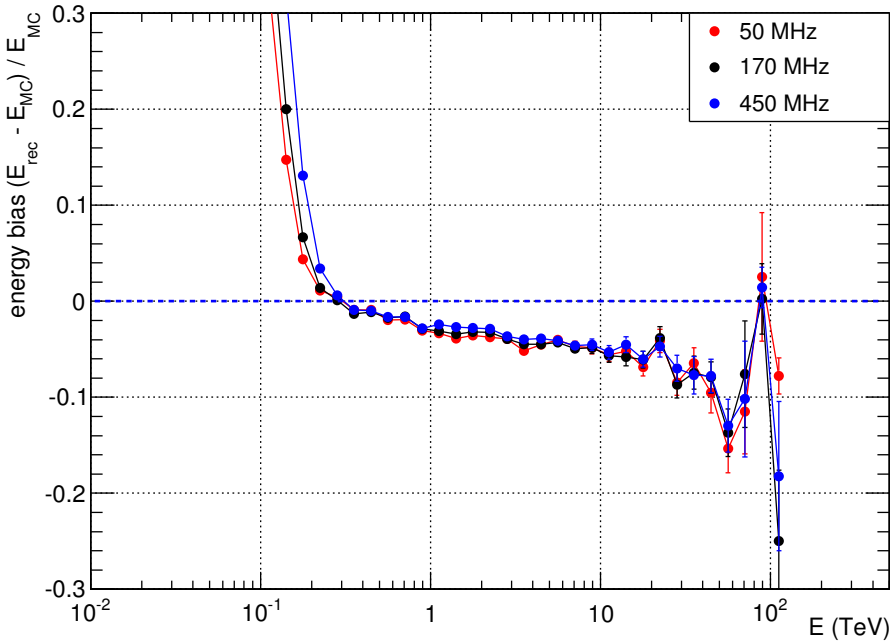

Figure 7.1: Energy reconstruction bias vs gamma-ray energy for simulated showers at 20 degrees zenith for three different noise levels for the V6 NOM detector. The blue dashed line indicates the ideal case of no energy reconstruction bias. The bias is large and positive at low energies due to the fact that the only showers which make it through to IRF production are showers for which there were upward fluctuations. The downturn at high energies is due to the fact that a large amount of the shower is truncated by the limited field of view of the camera and substantial information about the shower is being lost.

When proposing science targets, it is important to know how long it takes for the array to detect sources of different fluxes. By taking the gamma-ray and background rates for Crab data and scaling the gamma-ray event rates it is possible to determine how much time it would take to detect a source (based on a significance as determined by Li & Ma equation 17). The times required to detect a source for a number of flux fractions are given in Table 7.2. In later sections these values will be used to compare the sensitivity of the bright moonlight observing modes.

7.2.3 Spectral Reconstruction

The reconstructed energy spectrum based on the NOM data set is given in Figure 7.3. A power law and curved power law were fitted to the data. The fit values are presented in Table 7.3. The χ^2/NDF of the spectral points computed using the *MAGIC* curved power law is 65.3/9. This poor value is driven by the two lowest energy points which are $\sim 25\%$

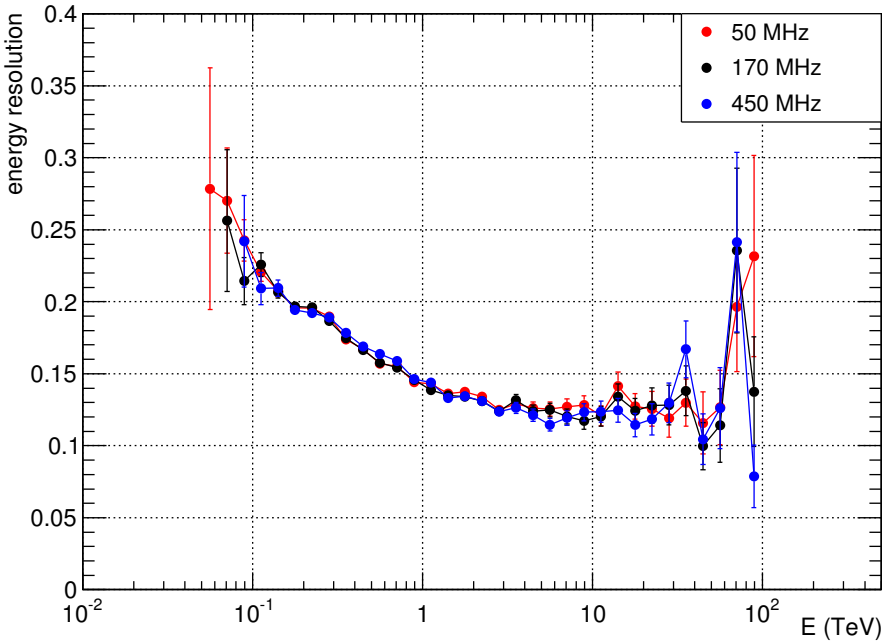

Figure 7.2: Energy resolution vs energy for simulated gamma-ray showers at 20 degrees zenith angle for three noise levels for the V6 NOM detector.

DATE	RUN	DUR (min)	WOB	SKY	EL (deg)	AZ (deg)	L3 (Hz)	NSB
20121206	65255	20	0.5N	A	75	124	435	8.9 (m)
20121208	65311	30	0.5E	A	74	125	437	7.2 (d)
20121208	65312	30	0.5W	A	79	154	438	7.0 (d)
20121210	65370	30	0.5N	A	73	119	425	7.6 (d)
20121210	65371	30	0.5S	A	77	142	428	7.6 (d)
20121211	65404	30	0.5E	A	79	148	449	8.0 (d)
20130105	65776	30	0.5E	A	64	105	433	7.4 (d)
20130105	65777	30	0.5W	A	71	117	438	6.9 (d)
20130105	65778	30	0.5N	A	76	130	442	6.8 (d)
20130105	65779	30	0.5S	A	79	163	443	6.8 (d)
20130113	66003	30	0.5S	A	77	141	460	6.9 (d)
Total:		320						

Table 7.1: NOM configuration Crab run list used in this thesis, with details pertaining to the observing conditions specific to the runs such as wobble angle (WOB), trigger rate (L3), and duration (DUR). Runs were selected such that they were high elevation (EL) and good weather (SKY) and generally close to the RHV and UVF runs analysed later in this work. The column titled "NSB" contains the average PMT current across the whole array during the data run. The letters in brackets are a coarse determination of the sky brightness (d = dark, m = moderate, l = high).

Crab Nebula Flux Fraction	Observing Time (minutes)
1	1.14
0.10	36.6
0.05	124
0.01	2670

Table 7.2: Time required to detect sources (requiring at least 5σ or 10 events) various values of the Crab Nebula flux under dark skies for V6 array using moderate cuts based on the Crab data set used in this thesis. These values assume a Crab-like spectrum.

above the flux predicted by the fit; excluding them from the calculation yields a χ^2/NDF of 9.8/7. The canonical systematic uncertainties on any standard *VERITAS* analysis are 20% in the flux normalisation and 0.2 in the spectral index.

Fit Form	F_0	Γ	β	χ^2/NDF
PL	3.26 ± 0.10	2.53 ± 0.03	-	17.4 / 7
CPL	3.51 ± 0.12	2.58 ± 0.04	-0.26 ± 0.04	5.5 / 6
MAGIC CPL	3.23 ± 0.03	2.47 ± 0.01	-0.24 ± 0.01	65.3 / 9

Table 7.3: Fit values for the Crab Nebula spectra shown in Figure 7.3. The values for the *MAGIC* curved power law are also given. The units of F_0 are 10^{-11} cm^{-2}s^{-1}TeV^{-1} and β is the curvature parameter at 1 TeV. Based on these results, the curved power law is the preferred spectral shape. The χ^2/NDF for the *MAGIC* CPL is the value computed with respect to the *VERITAS* data points; by excluding the two lowest spectral points from the computation the χ^2/NDF decreases to 9.8/7.

7.2.4 Data / MC Comparisons

Since the analysis relies heavily on simulations, it must be verified that the simulations being used match the data; it is not enough to verify that the results of an analysis of Crab data reproduce the canonical Crab spectrum. This is performed by producing data/MC comparisons between various distributions (e.g. mean scaled parameters, image size, number of PMTs in an image). The following data/MC comparisons are a subset of all possible comparisons. Several single-telescope distributions have been shown, as are several distributions that are used in gamma-hadron separation.

The following list indicates the quantity being compared and the corresponding figure. Note that in all subsequent data/MC comparisons, black points are data, red points are from simulations. Unless otherwise indicated, the vertical axis is in arbitrary units; each

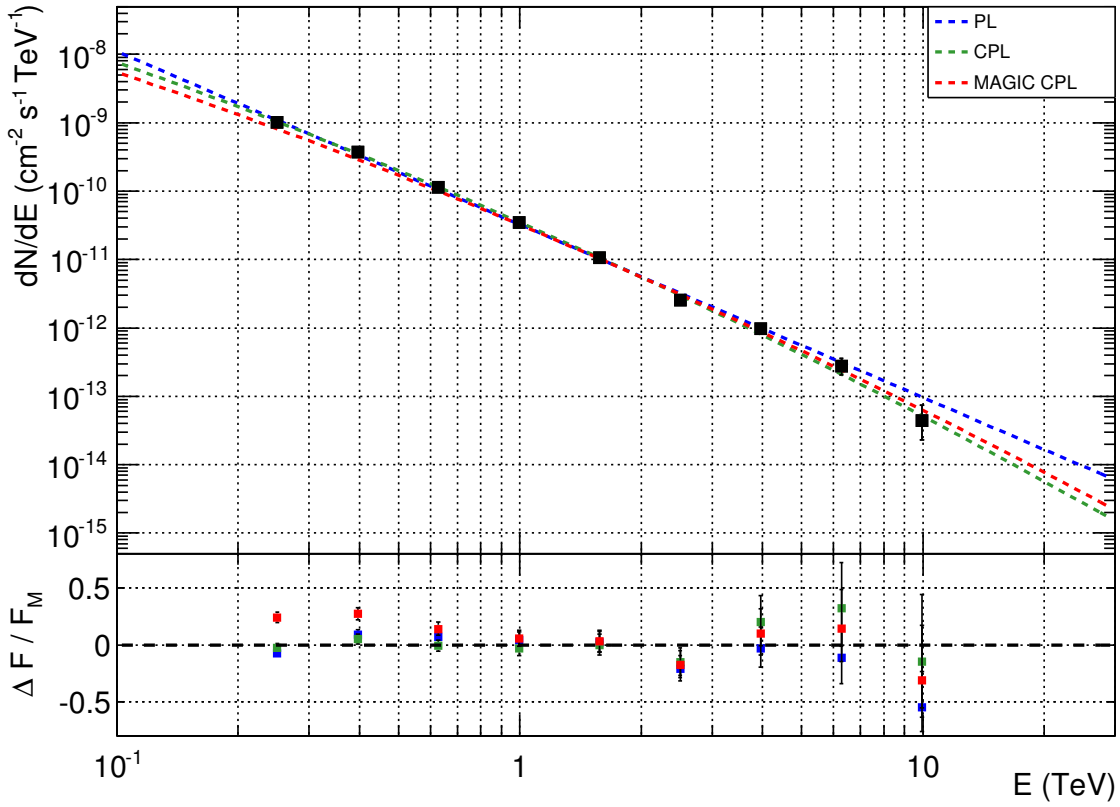

Figure 7.3: **Top**: Crab spectrum obtained from the analysis of the *VERITAS* NOM data set. **Bottom**: Fit residuals for the fit functions and a comparison spectrum. The fit values are given in Table 7.3. The two lowest spectral points differ from the *MAGIC* result by $\sim 25\%$.

distribution is a histogram scaled so that both the data and MC can be shown simultaneously. Single-telescope distributions are ordered T1-T4 from top-left to bottom-right.

- Mean Reduced Scaled Width and Length: Figures 7.4 and 7.5. Both these distributions have been broken into 6 energy ranges. Splitting the data into different energy ranges is useful because it could reveal differences in the reconstruction of air showers of different energies. For example, large showers tend to be truncated by the edge of the camera, and large images tend to contain more FADCs in low-gain mode. If either of these features is incorrectly modelled in the detector response functions these could (for example) manifest as misreconstructed mean-scaled parameters only above a certain energy. In the MSCW distributions plotted here, there is a systematic shift to lower MSCW values. There are two obvious reasons for this. Firstly, simulations are made at discrete noise levels and zenith angles, but real observations are not. Thus, when

comparing data and simulations it is entirely possible that the simulations are not an exact representation of the data set, which can cause small shifts like this one.

A much less likely reason would be that the effect is real and there is something wrong with the detector simulation. If this is the case, it does not significantly affect the analysis for a few reasons. Firstly, the shift is towards lower MSCW values. Thus, when gamma/hadron separation cuts are applied gamma-ray like events are not being cut out by the MSCW cut. Secondly, the shift is very small. Thus, for a typical cut of 0.5, only a small number of extra events are being included in the analysis since it is the tail of the MSCW distribution that is being included.

- Single-telescope Image Width and Length: Figures 7.6 and 7.7. These plots indicate whether or not the air showers are producing images that look like real gamma-ray-like events.

- Image Size: Figure 7.8. This distribution indicates whether the amount of light being detected in simulations agrees with the amount of light in real events.

- Image Length-over-size: Figure 7.9. This is a derived quantity (the ratio of the length l to the integrated charge in an image s). It provides a measure of whether or not the simulated air showers "look" like real air showers in terms of charge distribution within the image. It can be used as a discriminator for identifying muons, which have small l/s (see [124, Figure 5]).

- Number of PMTs in Image: Figure 7.10. The distribution of the number of PMTs in an image is another indicator that the air shower geometry being simulated matches that in real data.

- Number of Low-gain PMTs in Image: Figure 7.11. This distribution is important in verifying that the detector response is the same in both simulations and data.

- Shower Maximum Emission Height: Figure 7.12. This is the reconstructed height where the maximum amount of Cherenkov light was produced. This value provides insight as to whether or not the air shower physics are being correctly modeled.

7.3 Summary

In this chapter, the results of the analysis of a subset of the *VERITAS* Crab Nebula data set were presented and compared against results from the *MAGIC* collaboration. The analysis

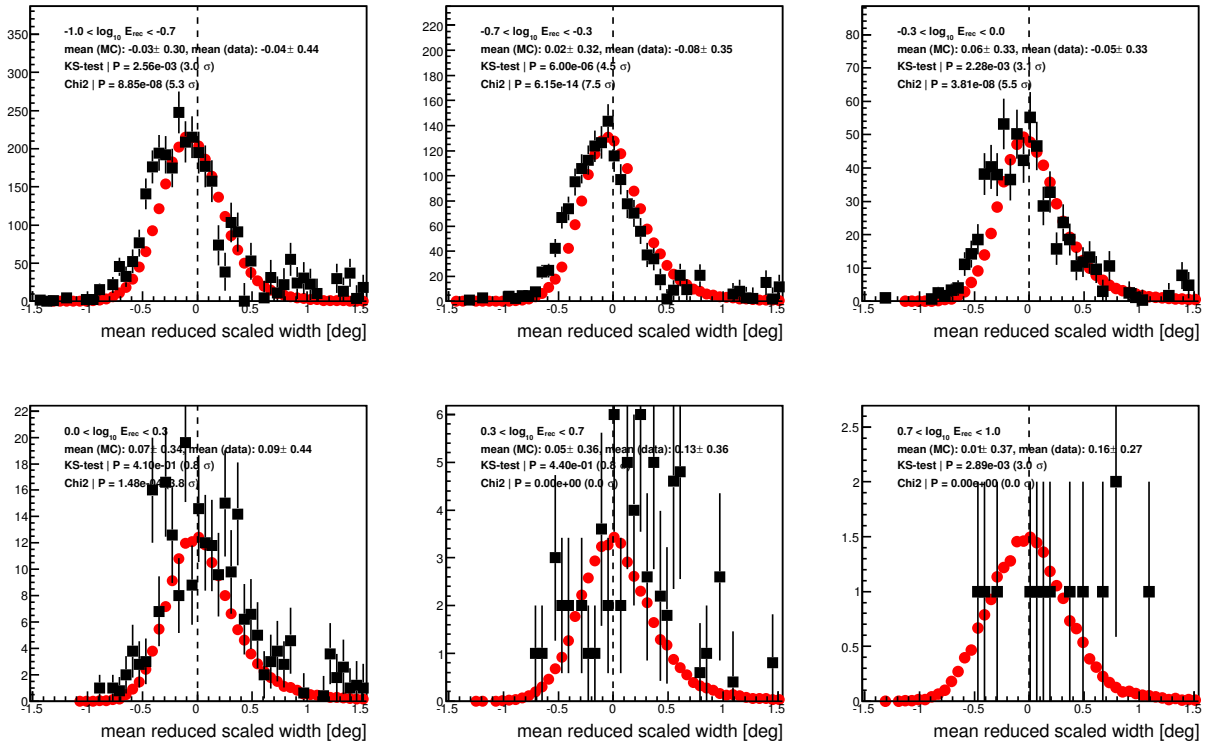

Figure 7.4: Mean reduced scaled width data/MC comparison separated into six energy ranges. There is a systematic shift in the MSCW distribution, but this was identified as an artefact of the NOM data set used in this comparison. A shift like this can arrive from the simulations not being perfectly matched to the data; a brief discussion of this is given in the main text. The low-statistics plots are shown for completeness and to indicate that there are no unexpected peaks in the data anywhere. Data are given in black and simulations are given in red.

results produced in this chapter will be used as the reference in the study of the bright moonlight observing modes which are described in Chapters 8 and 9.

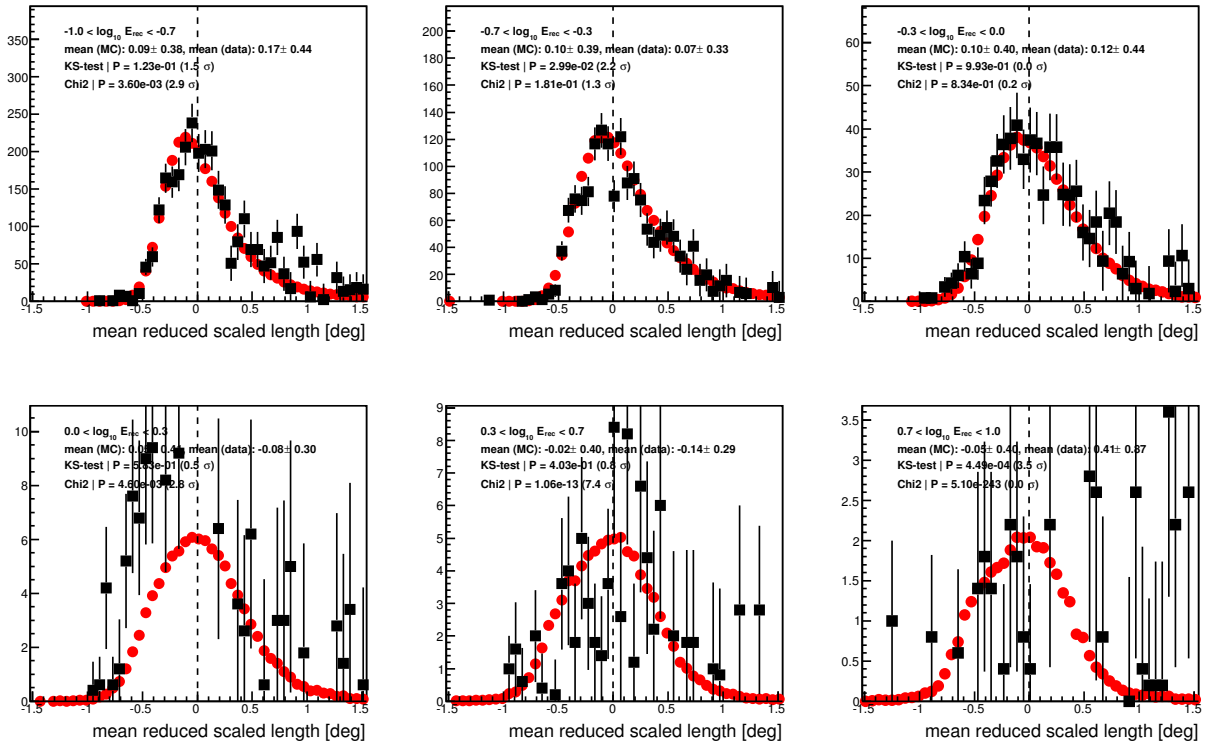

Figure 7.5: Mean reduced scaled length data/MC comparison for six energy ranges. The MSCL distributions agree quite well. Again, the low-statistics plots are shown for completeness and to indicate that there are no unexpected peaks in the data anywhere. Data are given in black and simulations are given in red.

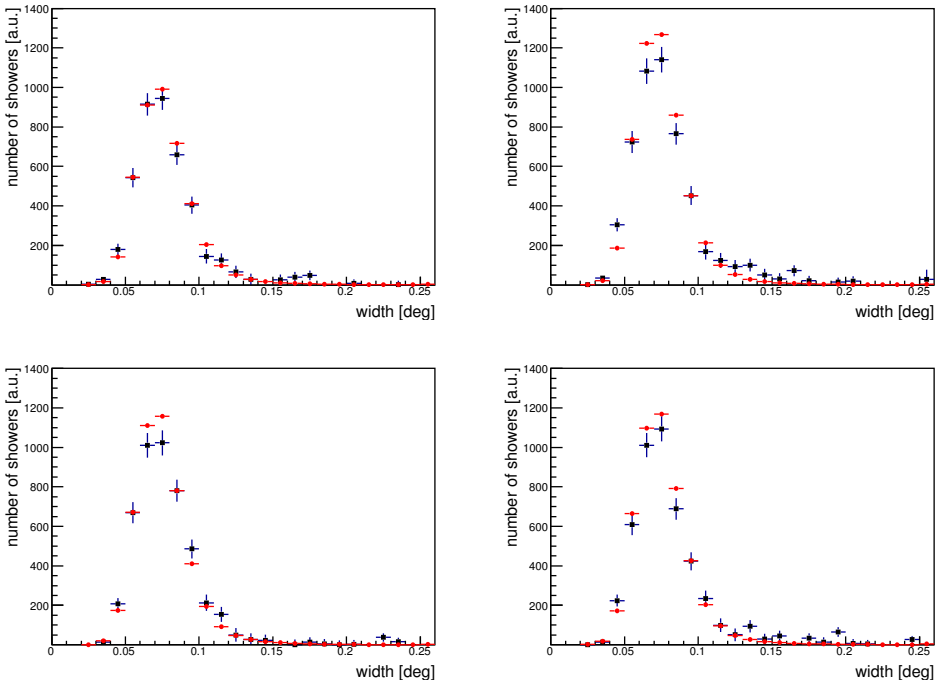

Figure 7.6: NOM configuration single telescope image width distributions. Data are given in black and simulations are given in red.

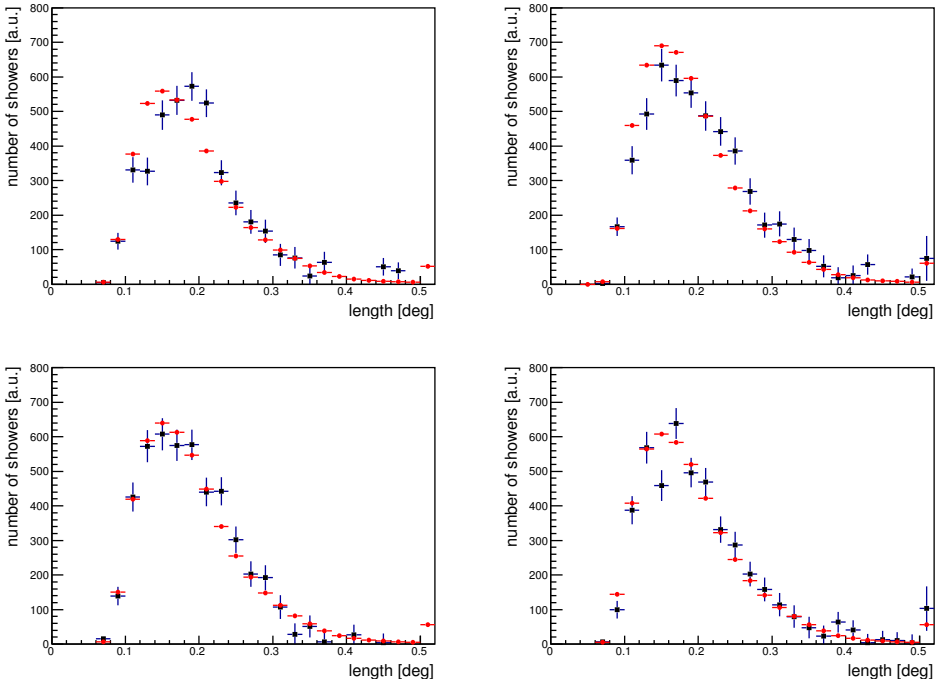

Figure 7.7: NOM configuration single telescope image length distributions. Data are given in black and simulations are given in red.

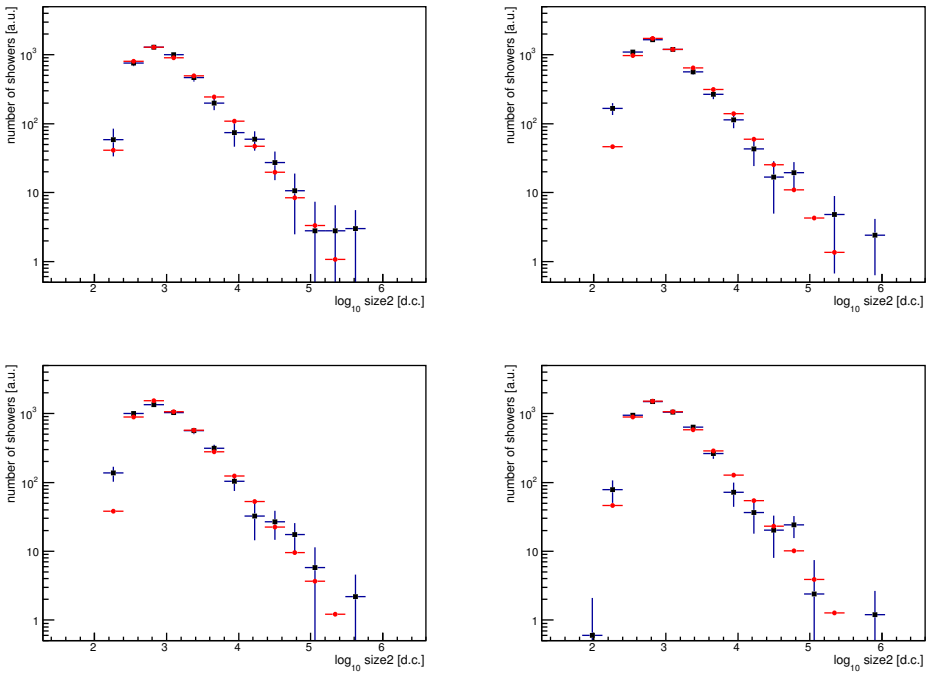

Figure 7.8: NOM configuration single telescope size distributions. Size is a measure of the total integrated charge in an image. Data are given in black and simulations are given in red.

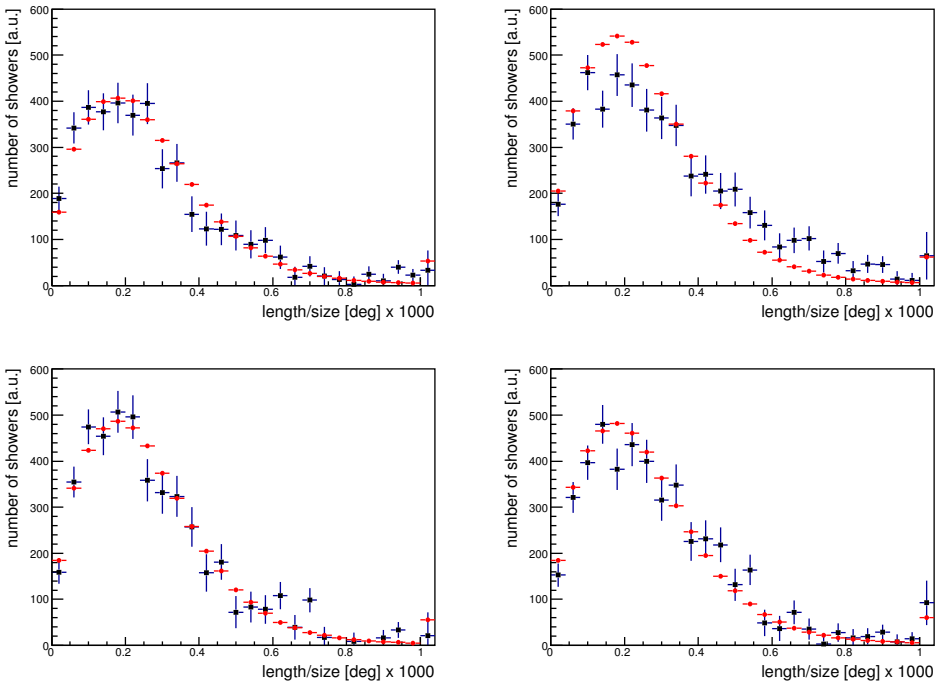

Figure 7.9: NOM configuration single telescope length-over-size (l/s) distributions. This is a derived parameter which is the ratio of the length to the integrated charge in an image. It provides a measurement of whether or not simulated showers "look" like real showers in terms of charge distribution in an image. This parameter can also be used to discriminate between images of air showers caused by local muons, which have a small l/s. Data are given in black and simulations are given in red.

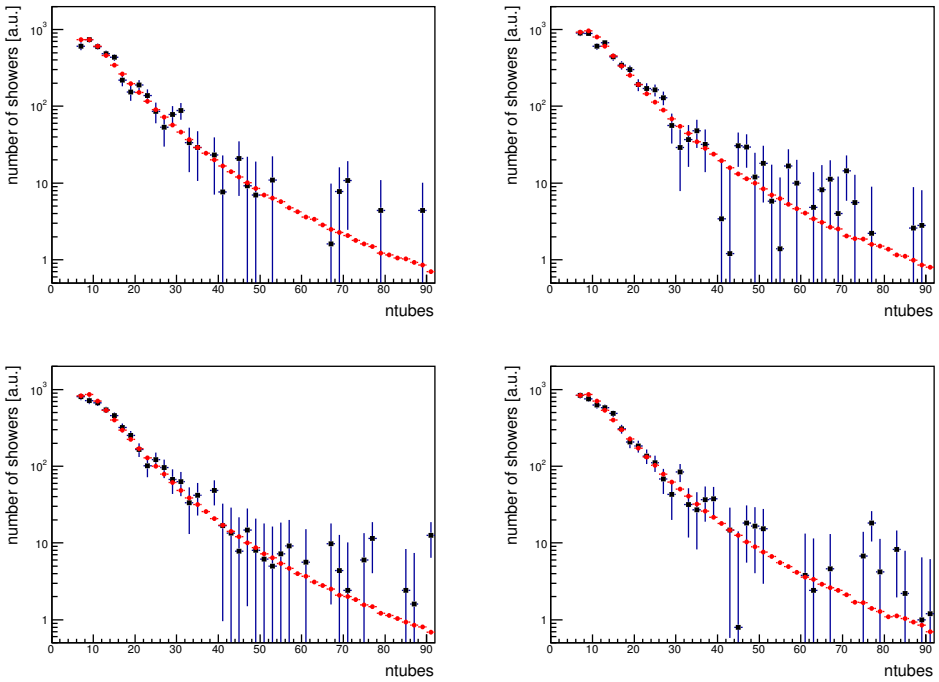

Figure 7.10: NOM configuration single telescope distributions of number of PMTs in an image. Data are given in black and simulations are given in red.

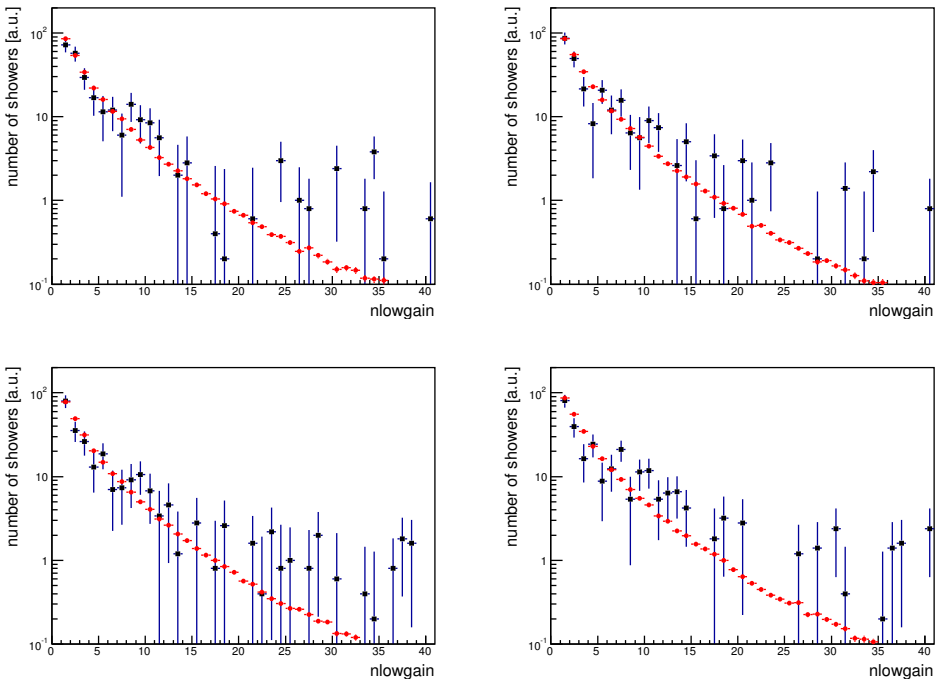

Figure 7.11: NOM configuration single telescope distributions of number of channels in an image that are in low-gain mode. Data are given in black and simulations are given in red.

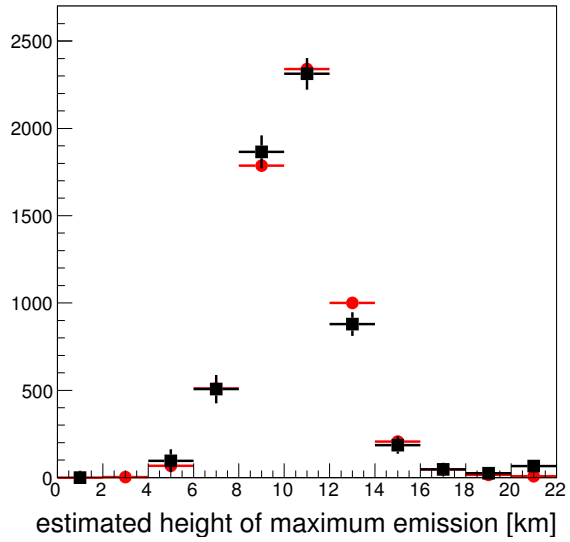

Figure 7.12: NOM configuration reconstructed shower maximum emission height. Data are given in black and simulations are given in red.

Chapter 8

Observations with Reduced High-Voltage

The first bright moonlight observing mode is the reduced high voltage (RHV) observing mode. The PMT gains can be reduced by reducing the voltage to the PMTs. This, in turn, reduces the wear on the PMT dynodes due to large currents. In this chapter, the details of the RHV observing mode are discussed following the same format as the standard analysis that was shown in Chapter 7.

8.1 Array Configuration

8.1.1 PMT Gain

As was shown in Section 3.2.1, a PMT's gain is proportional to a power of the voltage applied to it. To demonstrate this, a number of flasher runs were analysed, each with a different high voltage level: 80-100% of nominal HV, in increments of 5%. Using the method described in [53], absolute gains for each channel were calculated for each run. The distributions have not been separated by telescope as all the new PMTs were procured at the same time (*i.e.* the camera upgrade) and distributed randomly throughout the array. Figure 8.1 depicts two absolute gain distributions taken at two different high voltage levels (the NOM and RHV levels)[1]. The units of absolute gain used here are FADC digital counts (d.c.) per

[1]Both these distributions were generated using results from the `VEGAS` analysis package (see Section 4.5). `VEGAS` is an official *VERITAS* analysis package and this is the only time in this thesis for which `VEGAS` results will be presented; `eventdisplay` could not be used for the calculations as it does not include an absolute gain calculator.

photoelectron. The absolute gains shown here represent the gain of everything after the first dynode (PMT gain due to dynode chain, preamplifier gain, etc.). It is a value that is required in the detector simulations in order to convert the data (digital counts in an FADC trace) into something physical (photons on the PMT).

Taking the mean absolute gain (μ) and error on the mean ($\sigma/\sqrt{N}$) of each distribution and plotting it versus HV level yields Figure 8.2. From this, the power-law relation for the high voltage curve can be extracted. Figure 8.3 shows the same information but the gains for each telescope are separated. Recalling Equation 3.7, the power laws have the form

$$G(V) = G_0 \left(\frac{V}{V_0}\right)^{\beta}. \tag{8.1}$$

The fit to all the PMTs is

$$G(V) = (5.61 \pm 0.01) \left(\frac{V}{V_0}\right)^{6.03\pm0.02}. \tag{8.2}$$

Table 8.1 contains the fit values for the single-telescope fits. Given that all the PMTs were purchased at the same time and PMTs from different batches were distributed randomly throughout the array, one would expect them to be close but not necessarily identical, which is the case here. The values of G_0 are not expected to be the same since the mean absolute gain for each telescope is not required to be identical (any differences, however, must be mirrored in the detector model used when generating instrument response functions (IRFs)). Note that the fitted value for G_0 is higher than one would expect based on the mean absolute gain in the top panel of Figure 8.1. This is likely because two different analysis tools were used to analyse the two different data sets and could be related to the Polya correction factors (see Section 3.6.1.2), which can have $\sim 15\%$ effects on the scale of the absolute gain but do not affect relative differences. For this study this is unimportant as we are only interested in the relative differences in the gains between nominal and reduced HV.

	G_0	β
T1:	5.47 ± 0.02	5.95 ± 0.03
T2:	5.64 ± 0.02	6.13 ± 0.03
T3:	5.55 ± 0.02	5.89 ± 0.03
T4:	5.74 ± 0.02	6.06 ± 0.03

Table 8.1: Fit values for the absolute gain vs HV curves in Figure 8.3.

The PMT voltage used by *VERITAS* in the RHV configuration is 81% of nominal. This value was chosen somewhat arbitrarily; it is simply the result of reducing the PMT voltage by 10% twice ($0.81 = 1 \times 0.9 \times 0.9$). Realistically, on a PMT-by-PMT basis this will not be

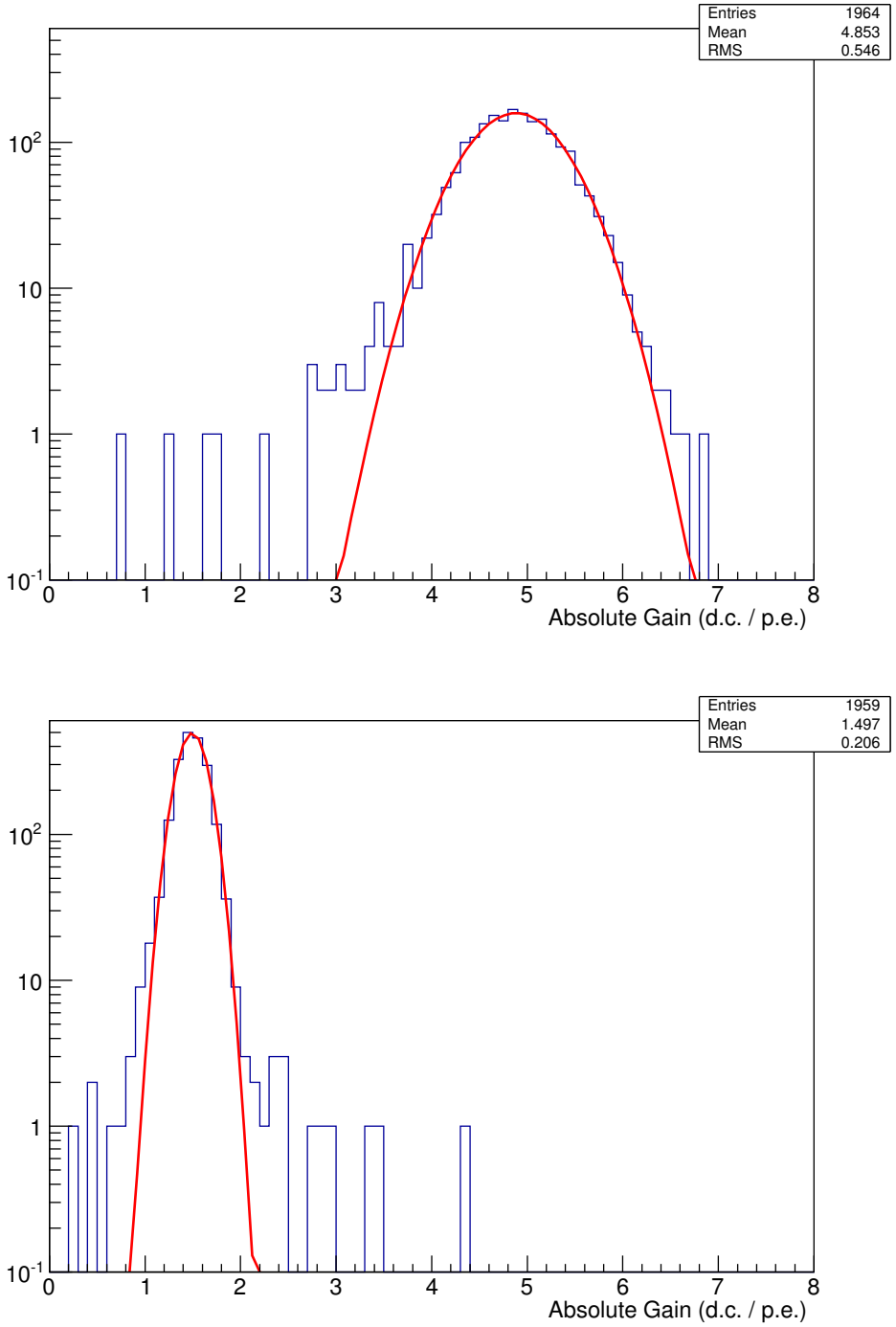

Figure 8.1: **Top:** Absolute gain distribution for all PMTs in the array for 100% HV. Note that there are not 4×499 entries in each histogram. This is due to a combination of bad PMTs, bad FADC channels, or the gain calculation algorithm failing for some other reason. Each distribution is approximately Gaussian, as demonstrated by the fit, which has $\chi^2/NDF = 48.1/43$ ($P \sim 0.275$). **Bottom:** Same as above, but for RHV (81% HV). The fit has $\chi^2/NDF = 42.6/24$ ($P \sim 0.011$).

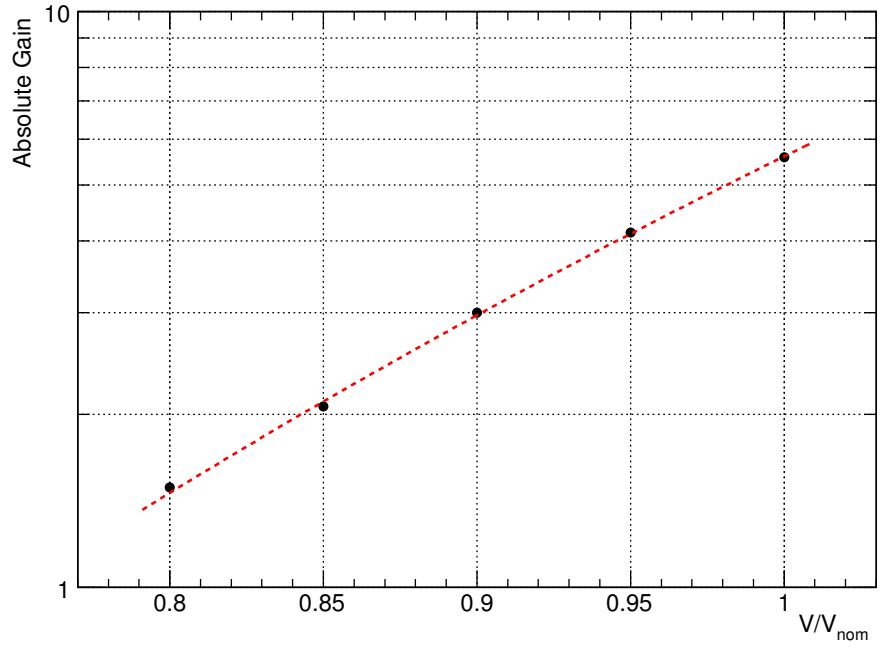

Figure 8.2: PMT absolute gain versus PMT voltage (in units of nominal operating voltage). The error bars are smaller than the data points.

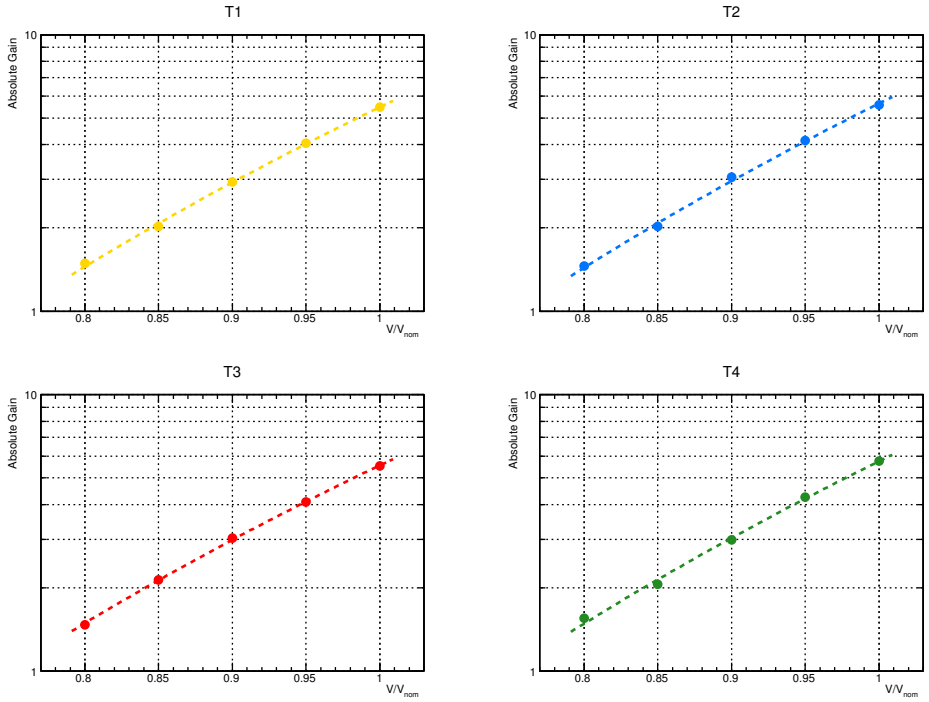

Figure 8.3: Like in Figure 8.2 but separated by telescope. As is expected, there are no large telescope-to-telescope differences.

exactly 81% since the PMTs must be flatfielded after the HV levels have been scaled. Since no two PMTs respond in exactly the same way (demonstrated in Figure 8.4), this means that the RHV voltage level on a PMT by PMT basis will be different.

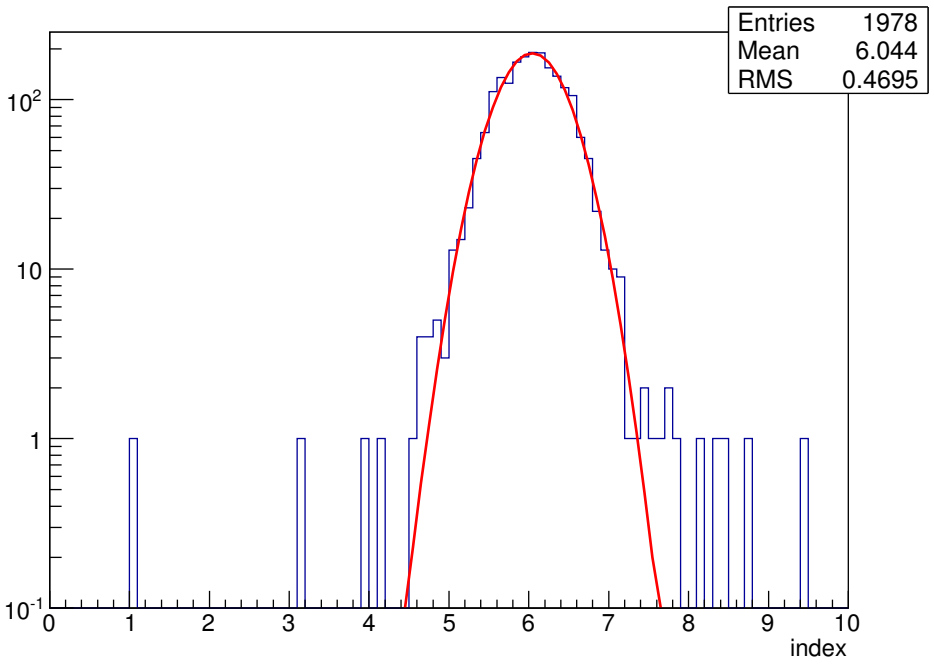

Figure 8.4: Histogram of the index in the power-law fits (β in Equation 8.1) for all PMTs. Each PMT has a slightly different response; if each PMT was identical there would be no spread in this distribution. Instead, it is well fit by a Gaussian ($\chi^2/NDF = 45.4/40$; $P \sim 0.256$).

The ratio of the absolute gain (as per Equation 8.2) is expected to be 0.282. The ratio of the absolute gains shown previously in Figure 8.1 is

$$\frac{G_{\mathrm{RHV}}}{G_{\mathrm{NOM}}} = 0.308 \pm 0.004 \tag{8.3}$$

where $\sigma/\sqrt{N}$ errors have been used for the errors on the gain values.

The difference is an 8% effect and can probably be explained by gain differences in the array between two consecutive seasons. The data from which Equation 8.2 was produced were taken in the 2012-2013 observing season and the data for Figure 8.1 were taken during the 2013-2014 season. Recall that PMTs age with time such that for a given HV level the absolute gain drops. Depending on when and by how much the gains were adjusted this effect is well within the tolerances of the analysis.

8.1.2 CFD Thresholds

Selecting constant fraction discriminator (CFD) thresholds for the RHV observing mode follows the same logic as standard observations. An example bias curve for RHV data is shown in Figure 8.5.

Given that the PMT gain (and by extension the pulse size) scales with HV, it should be able to determine the change in CFD threshold required to maintain a given trigger rate. It follows that the entire bias curve can be determined this way. To compare the trigger rates for RHV data to what they would be if the data were taken under bright skies with nominal HV, the CFD thresholds for the RHV data points have been scaled up by a factor of $(1/0.81)^{6.03} \approx 3.6$ (*i.e.* the nominal gain change) to account for the effect of the RHV pulse heights. The results are shown in Figure 8.6. Fit values for the RHV bias curves are given in Table 8.2. As is expected, the CR components agree well by eye and differences in the fits can likely be explained away by observing conditions, the gain ratio not being exactly the scale factor used, or systematic errors stemming from the fact that the detector configurations are not identical.

Note that the NSB components are *not* expected to agree with each other. The NSB rate during RHV is higher (due to the presence of moonlight), so the contribution of triggers due to the NSB is should be higher in the RHV mode, and in the scaled data set the inflection point should be at a higher threshold than for the NOM bias curve.

	CR		NSB	
	A	B	C	D
RHV	6.15 ± 0.22	-0.045 ± 0.006	23.7 ± 2.5	-1.000 ± 0.165
RHV scaled	6.12 ± 0.16	-0.013 ± 0.001	23.3 ± 0.1	-0.274 ± 0.002
NOM	7.35 ± 0.06	-0.025 ± 0.001	29.5 ± 0.2	-0.683 ± 0.007

Table 8.2: Fit values for the bias curves in Figures 8.5 and 8.6. The parameters are the same as in Equation 6.4. The RHV bias curve was fit between 15 mV and 50 mV and the scaled curve was fit over its entire range; a fit to the unscaled curve would not converge if the lowest point was included. This is likely an artefact of the fitter given that the fit to the scaled data converges and has a high probability. The χ^2/NDF are 7.954/4 ($P \sim 0.093$) and 7.995/5 ($P \sim 0.157$) for the RHV and scaled RHV curve, respectively.

The ratio of the fit slopes (recall that a bias curve is the sum of two exponential functions, Equation 6.4) for the scaled and unscaled CR and NSB components is expected to be the scaling factor, since adding a scale factor to the abscissa value is a simple scaling $x \to \beta x$. The ratio of the scaled RHV CR slope to the unscaled slope is $\beta = 0.045/0.013 \approx 3.5$ and the ratio of the scaled NSB slope to the unscaled slope is $\beta = 1.000/0.274 \approx 3.6$. Both these

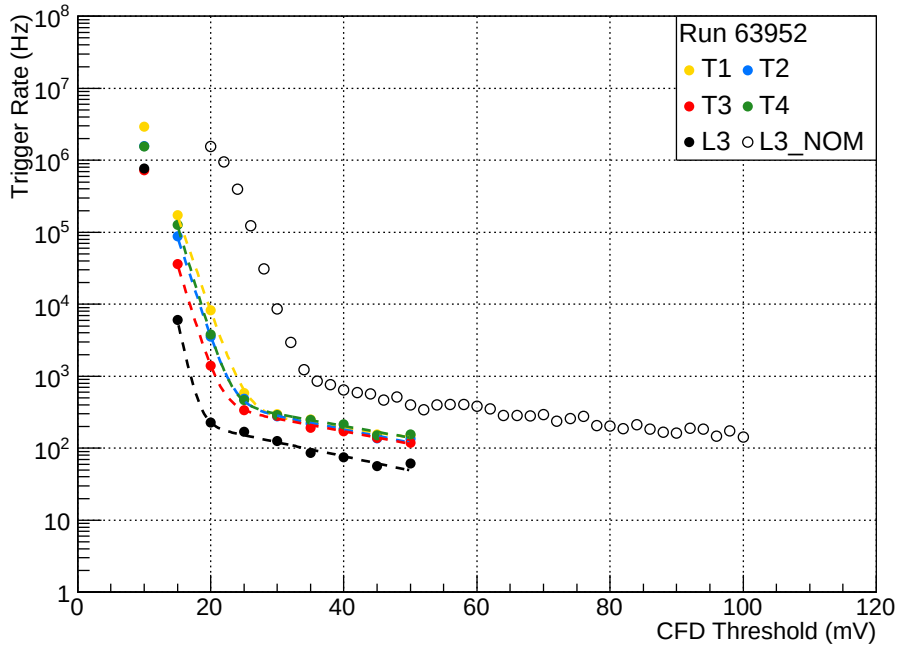

Figure 8.5: RHV bias curve. A nominal HV L3 bias curve is shown for comparison (the same as the extragalactic curve in Figure 6.3). Fit values for the L3 rates are given in Table 8.2. Each point has an error bar which is smaller than the marker. The turnover seen at very low thresholds is due to saturation in the DAQ.

values are close to the exact value of the scale factor and provides a good verification of the method.

Two sets of CFD settings, depending on the mean PMT currents, are used for RHV data taking. Below 10 μA, the CFDs are set to 25 mV. Above 10 μA the CFDs are set to 35 mV.

8.2 Analysis Results

For clarity, the following discussion of the RHV observing mode analysis is laid out in the same way as the previous section on the standard configuration. To avoid being redundant, descriptions of various topics have been omitted as they have already been described in the previous section.

8.2.1 Performance Studies

Figures 8.7 and 8.8 show the bias and resolution of the shower energy reconstruction for RHV data sets. For reference, results for a standard noise level in the NOM configuration is also

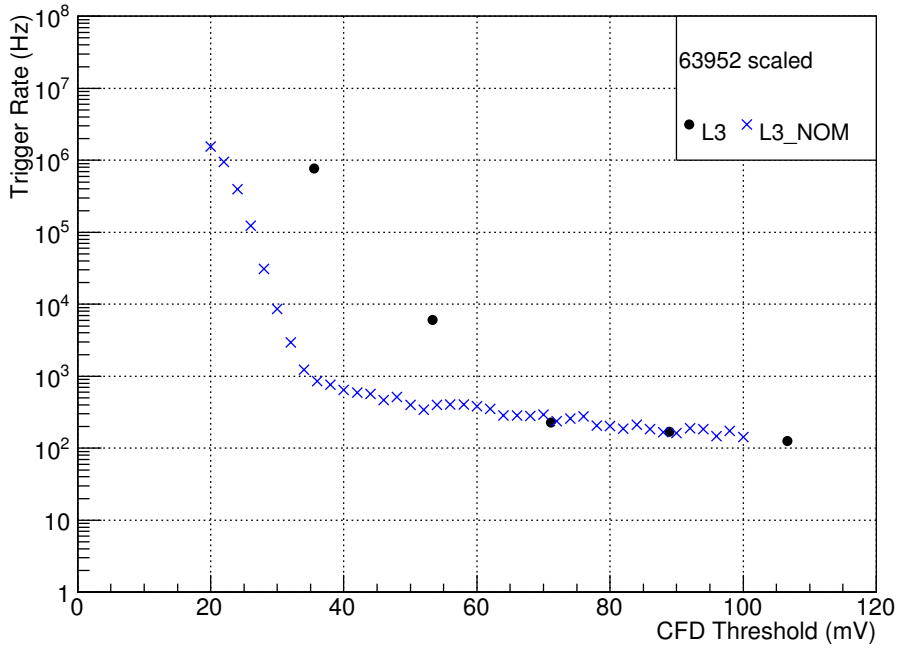

Figure 8.6: Scaled RHV L3 bias curve and a NOM bias curve (again, the same as the extragalactic curve in Figure 6.3). The scaled data was fit (see Table 8.2) but the line is intentionally not shown here to make it clear that the two CR components lie on top of each other.

plotted. The energy resolution is effectively the same in both configurations, but the bias becomes significantly worse about 50 GeV higher than for the NOM configuration. Once again, this is consistent with the performance being similar over a range where signal to noise is high.

8.2.2 Data

For the following analysis, the runs indicated in Table 8.3 were analysed in the exact same manner as those for the NOM data set with the exception of the gamma/hadron separation cuts. Cherenkov pulses in RHV data are smaller (by definition a factor of ~ 3 smaller due to the reduced PMT gain) for a given amount of light. Hence, the cut on shower size must be scaled accordingly. Standard "soft" cuts were used in this analysis (see Table 4.2).

The analysis of the RHV data set yielded 4249 On events and 243.50 Off events (1461 with $\alpha = 1/6$). The resulting gamma-ray rate was (8.5 ± 0.1) photons/minute with a background rate of (0.52 ± 0.03) events/minute. The detection significance is 102.4σ. The analysis energy threshold for the RHV data set is 160 GeV (average of all runs) and is fairly

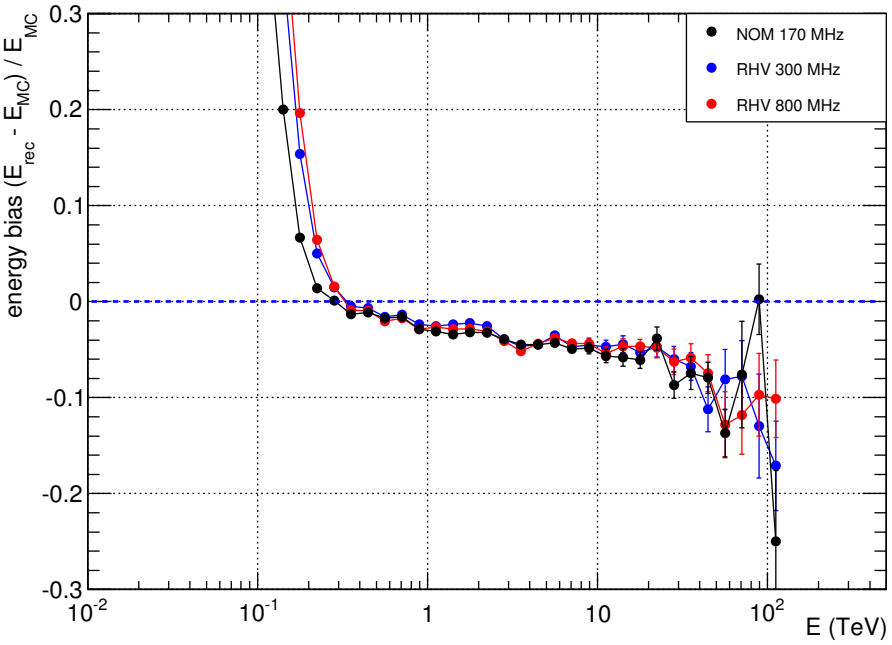

Figure 8.7: Energy reconstruction bias vs energy for simulated gamma-ray showers at 20 degrees zenith for two noise levels in the RHV configuration and one in the NOM configuration.

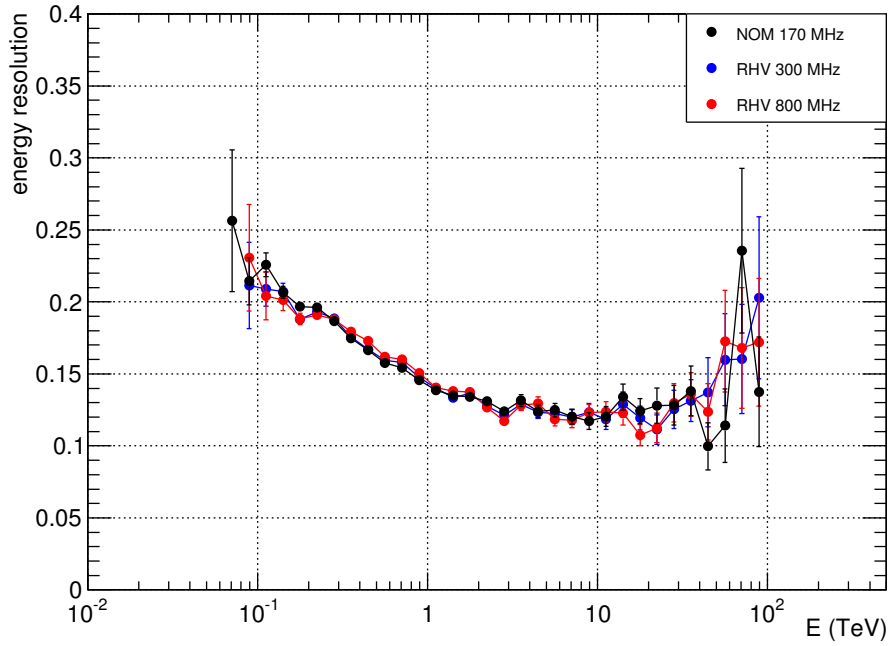

Figure 8.8: Energy resolution vs energy for simulated gamma-ray showers at 20 degrees zenith for several noise levels with the array in RHV mode.

DATE	RUN	DUR (min)	WOB	SKY	EL (deg)	AZ (deg)	L3 (Hz)	NSB
20130118	66169	30	0.5N	B	71	114	188	6.3
20130118	66175	30	0.5E	B	67	251	207	3.7
20130216	66858	30	0.5N	A	78	139	200	5.4
20130216	66859	30	0.5S	A	80	178	200	5.1
20130216	66860	30	0.5E	A	78	215	201	4.9
20130216	66861	30	0.5W	A	73	240	200	4.8
20130216	66862	30	0.5N	A	66	255	196	4.7
20130217	66893	30	0.5S	A	78	148	170	8.4
20130217	66894	30	0.5E	A	80	187	184	8.1
20130217	66895	30	0.5W	A	77	227	185	8.1
20130217	66896	30	0.5N	A	71	246	180	7.9
20130217	66897	30	0.5S	A	64	254	175	7.7
20131028	70322	30	0.5N	A	80	203	187	4.9
20131028	70323	30	0.5S	A	75	229	185	5.1
20131028	70324	30	0.5E	A	71	245	183	5.3
20131112	70690	25	0.5W	A	75	129	182	4.1
RHV subtotal:		475						

Table 8.3: Runlist for the RHV Crab data set used in this thesis with details pertaining to the observing conditions specific to the runs (see Table 7.1 for a description of each column).

constant across the zenith and sky brightness range covered by the data set. In comparison, recall from Section 7.2.2 that the NOM data set energy threshold is 144 GeV.

Serendipitously, the size cut in soft cuts is 1/3 that for moderate cuts, which is roughly the same as the RHV/NOM gain ratio. This is why the performance of the RHV configuration (see Table 8.4) is very similar to NOM; the size cut is restricting both modes to showers of roughly the same energy. Overall, the performance of the RHV configuration with soft cuts appears to be quite comparable to the performance of the standard data made with moderate cuts. This means that the RHV observing mode is well suited to a number of science tasks that do not require the absolute lowest energy threshold.

8.2.3 Spectral Reconstruction

As with the NOM analysis, an energy spectrum for the RHV Crab data set was produced and is shown in Figure 8.9. The fit values are given in Table 8.5. The NOM power law (PL) and RHV PL fits agree to within statistical uncertainties. The curved power law (CPL) fits have spectral indices that differ at the 2σ level, which is no cause for concern. As was the case with the NOM fits, the *MAGIC* CPL has a large χ^2/NDF which is driven by the lowest

Crab nebula Flux Fraction	Observing Time (minutes)	
	NOM	RHV
1	1.14	1.19
0.10	36.6	33
0.05	124	109
0.01	2670	2290

Table 8.4: Time required to detect sources having various fractions of the Crab nebula flux. Based on these numbers, it can be concluded that a RHV analysis with soft cuts is very similar to a NOM analysis using moderate cuts.

energy spectral points.

Fit Form	F_0	Γ	β	χ^2/NDF
PL	3.21 ± 0.08	2.52 ± 0.02	-	18.1 / 7
CPL	3.44 ± 0.10	2.70 ± 0.05	-0.22 ± 0.06	3.6 / 6
NOM PL	3.26 ± 0.10	2.53 ± 0.03	-	17.4 / 7
NOM CPL	3.51 ± 0.12	2.58 ± 0.04	-0.26 ± 0.04	5.5 / 6
MAGIC CPL	3.23 ± 0.03	2.47 ± 0.01	-0.24 ± 0.01	77.4 / 9

Table 8.5: Fit values for the Crab Nebula spectra shown in Figure 8.9. The values for the *MAGIC* curved power law are also given. The units of F_0 are 10^{-11} cm^{-2}s^{-1}TeV^{-1} and β is the curvature parameter at 1 TeV. Based on these results, the curved power law is the preferred spectral shape. The χ^2/NDF for the *MAGIC* CPL is the value computed with respect to the *VERITAS* data points.

8.2.4 Data/MC Comparisons

As was done with the NOM data set, the following is a list of quantities and the associated data/MC comparison plot. The binning is the same as the NOM analysis so that they can be directly compared.

- Mean Reduced Scaled Width and Length: Figures 8.10 and 8.11
- Single-telescope Image Width and Length: Figures 8.12 and 8.13
- Image Size: Figure 8.14
- Single-telescope Image Length-over-size: Figure 8.15
- Number of Tubes in Image: Figure 8.16

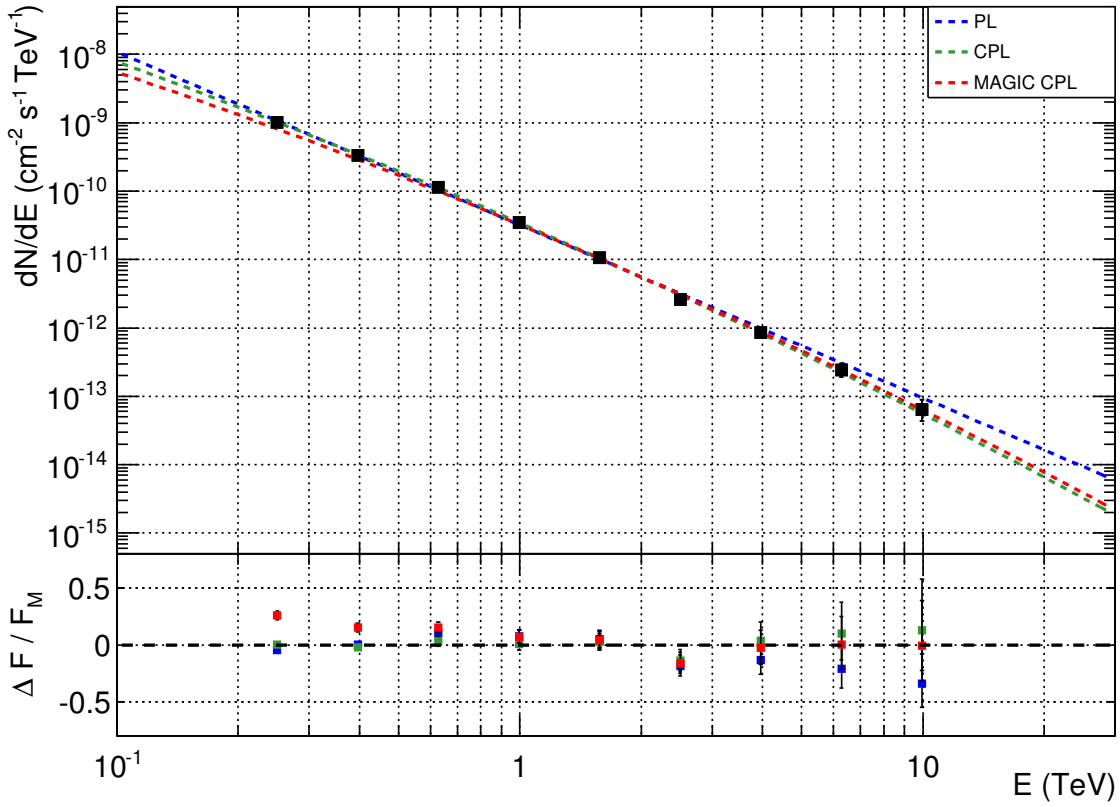

Figure 8.9: **Top**: Crab spectrum obtained from the analysis of the *VERITAS* RHV data set. **Bottom**: Fit residuals for the fit functions and a comparison spectrum. The fit values are given in Table 8.5. As was with the NOM results, the two lowest spectral points are considerably higher than the *MAGIC* result.

- Number of Low-gain Tubes in Image: Figure 8.17
- Shower Maximum Emission Height: Figure 8.18

8.3 Summary

It has been shown that for a standard analysis, RHV data has a similar energy threshold and sensitivity to that of NOM data. The systematic errors in the RHV mode are also largely the same as those in the NOM mode; the energy bias and resolution are similar, and any offsets in data/MC comparison plots are seen in both data sets. The difference in the spectral fits for the RHV and NOM analyses is both statistically insignificant and well within standard systematic errors.

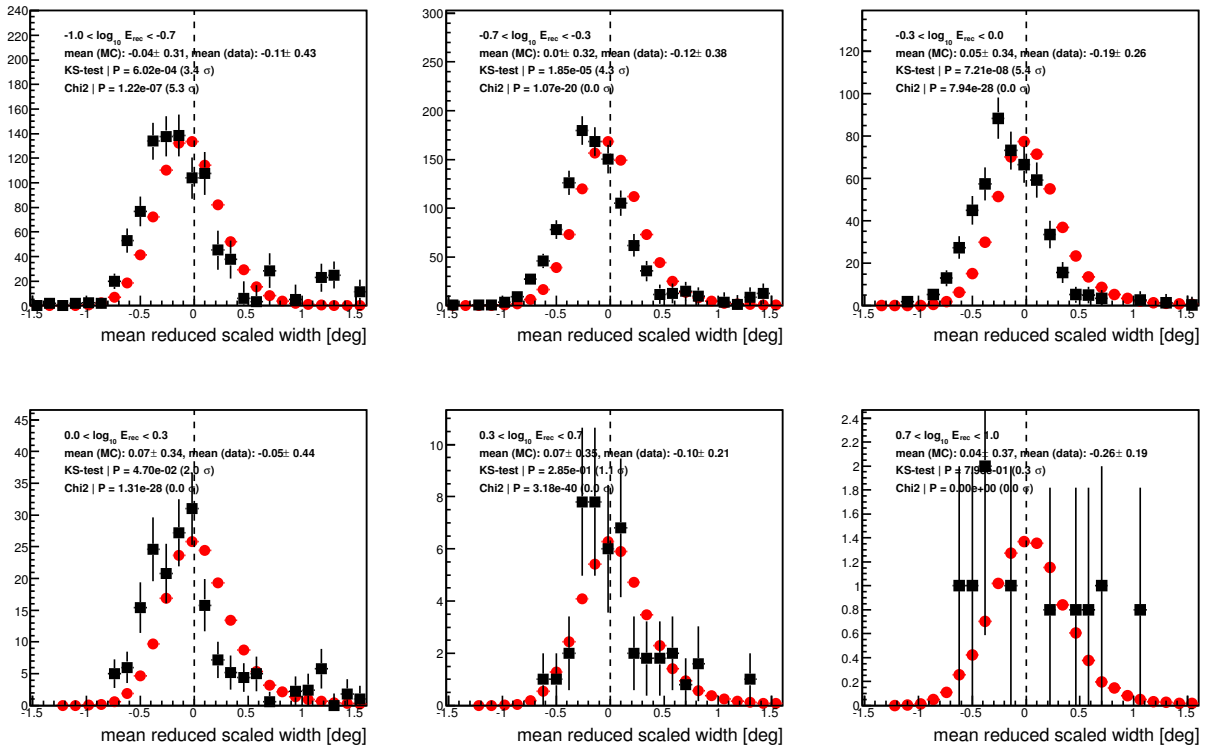

Figure 8.10: Mean scaled width data/MC comparison. There is a small systematic shift in the MSCW distribution, as is the case with the corresponding distribution in the NOM analysis. Data are given in black and simulations are given in red.

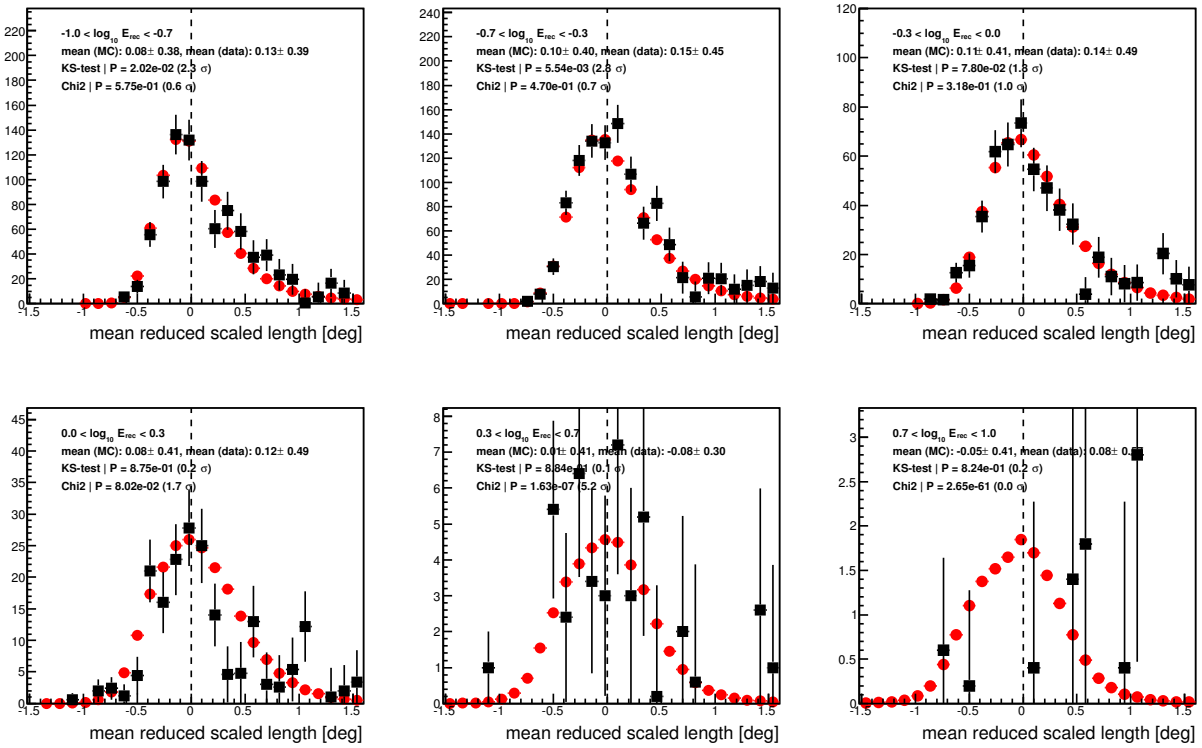

Figure 8.11: Mean reduced scaled length data/MC comparison, binned in energy. The MSCL distributions appear to agree well, but this data set is limited by low statistics. Data are given in black and simulations are given in red.

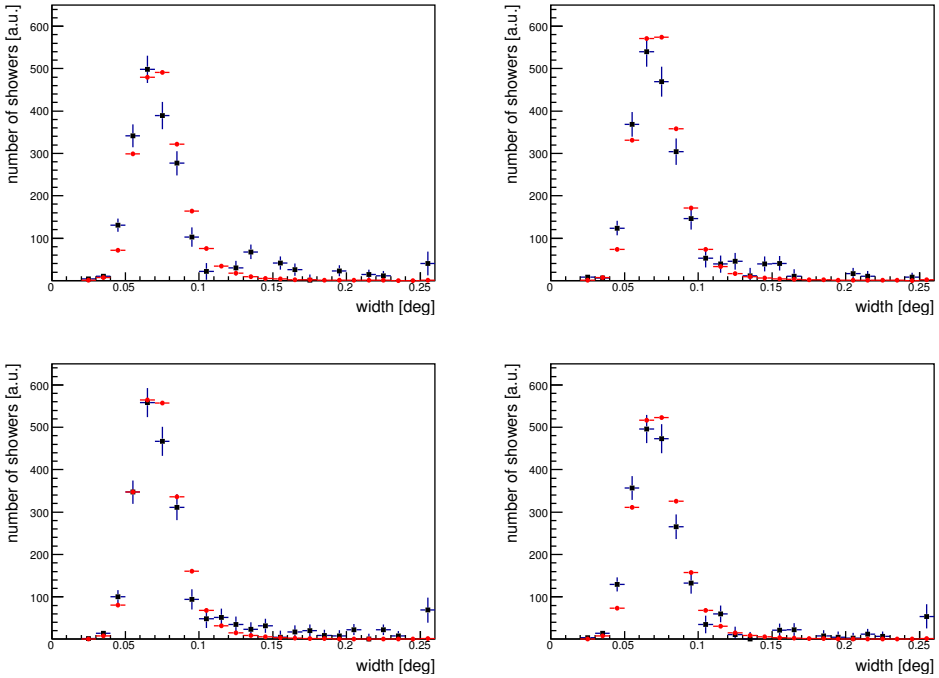

Figure 8.12: RHV configuration single telescope image width distributions. Data are given in black and simulations are given in red.

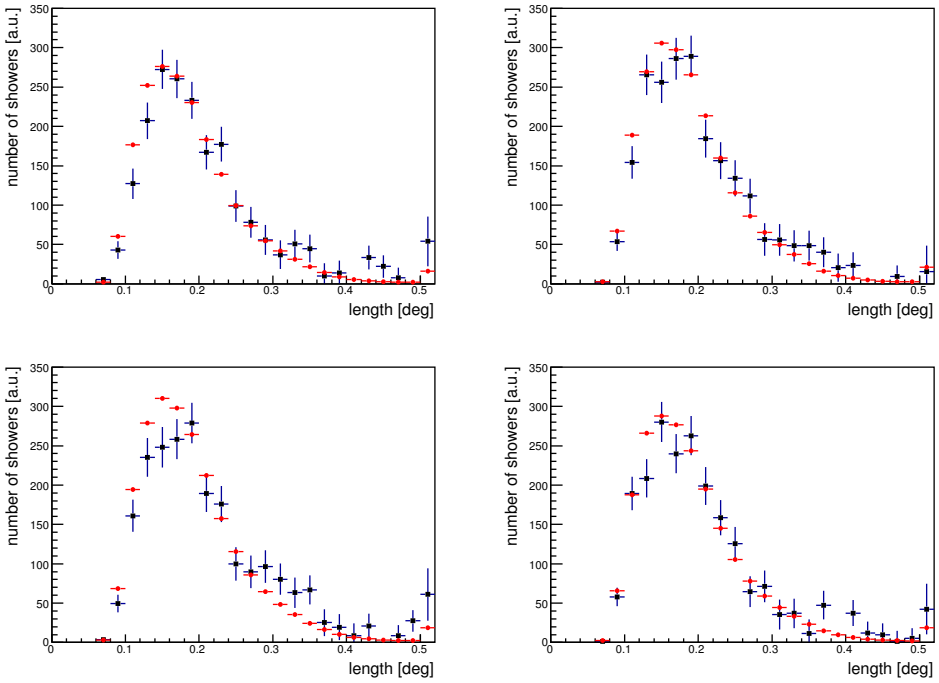

Figure 8.13: RHV configuration single telescope image length distributions. Data are given in black and simulations are given in red.

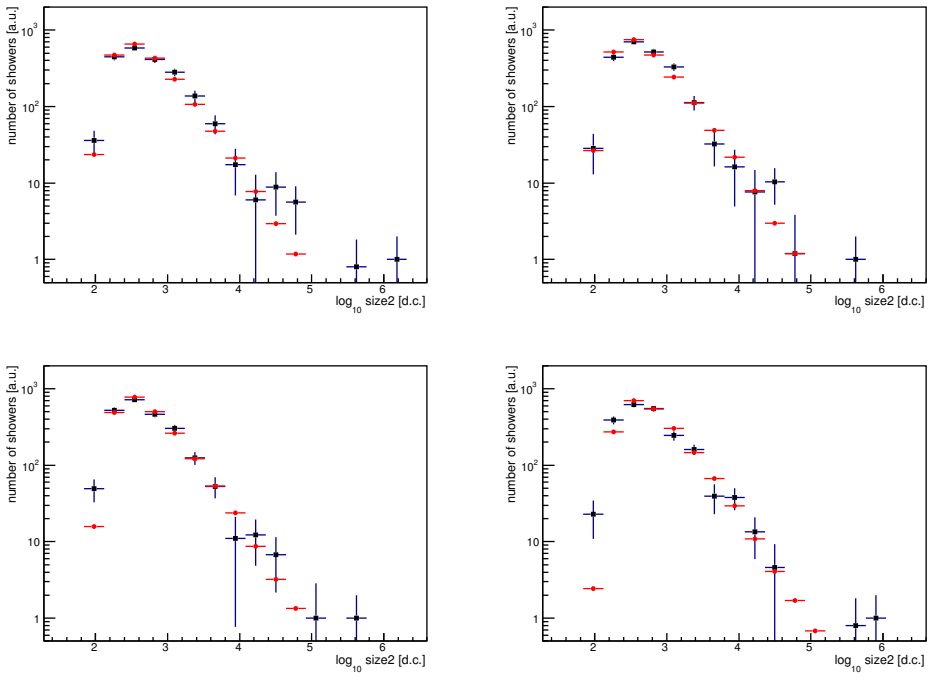

Figure 8.14: RHV configuration single telescope size distributions. Data are given in black and simulations are given in red.

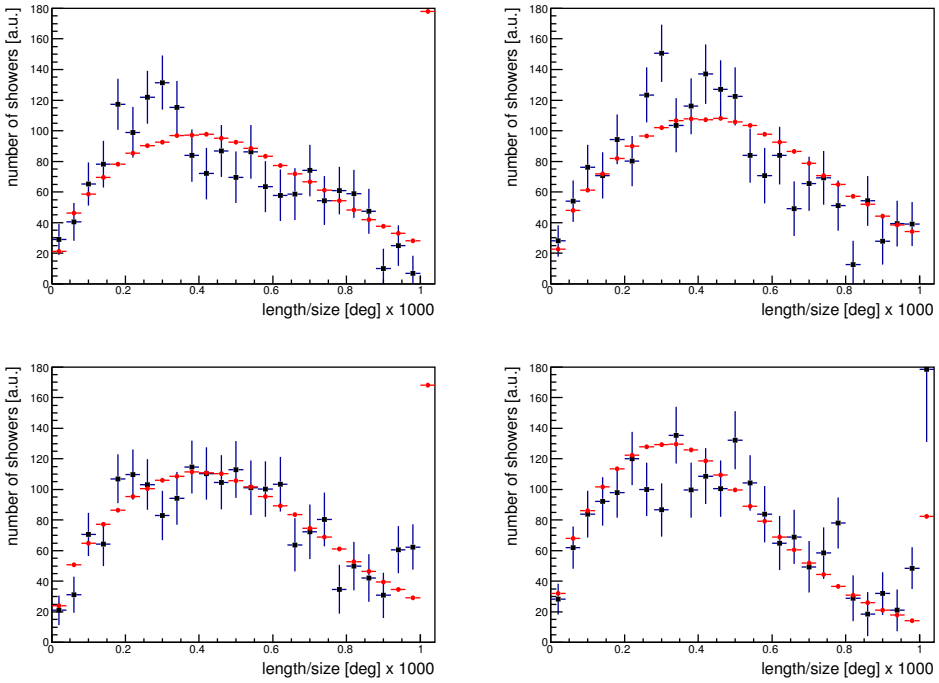

Figure 8.15: RHV configuration single telescope length-over-size distributions. Data are given in black and simulations are given in red.

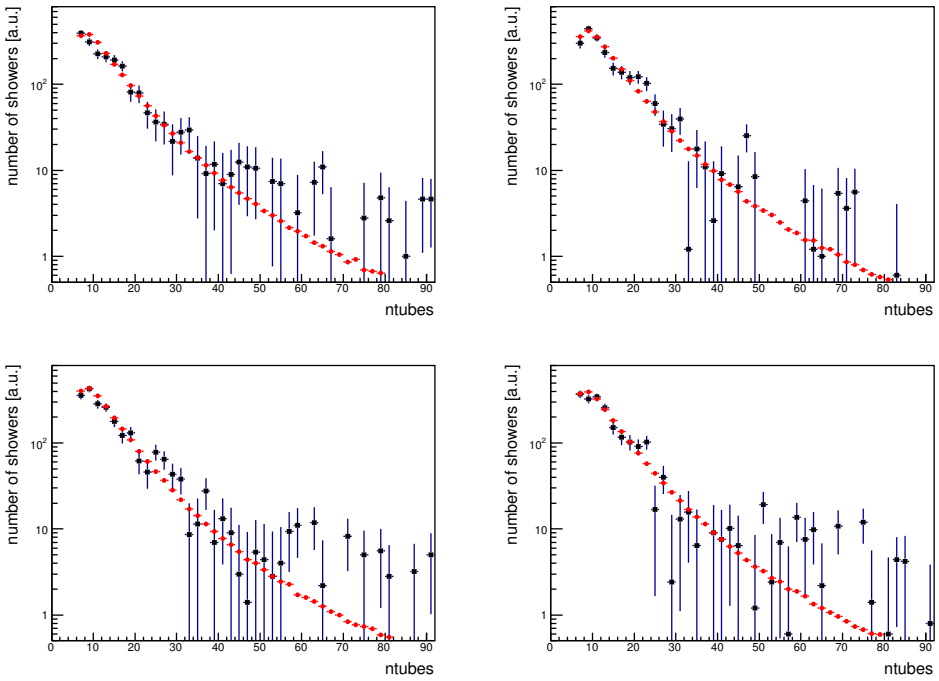

Figure 8.16: RHV configuration single telescope distributions of number of PMTs in an image. Data are given in black and simulations are given in red.

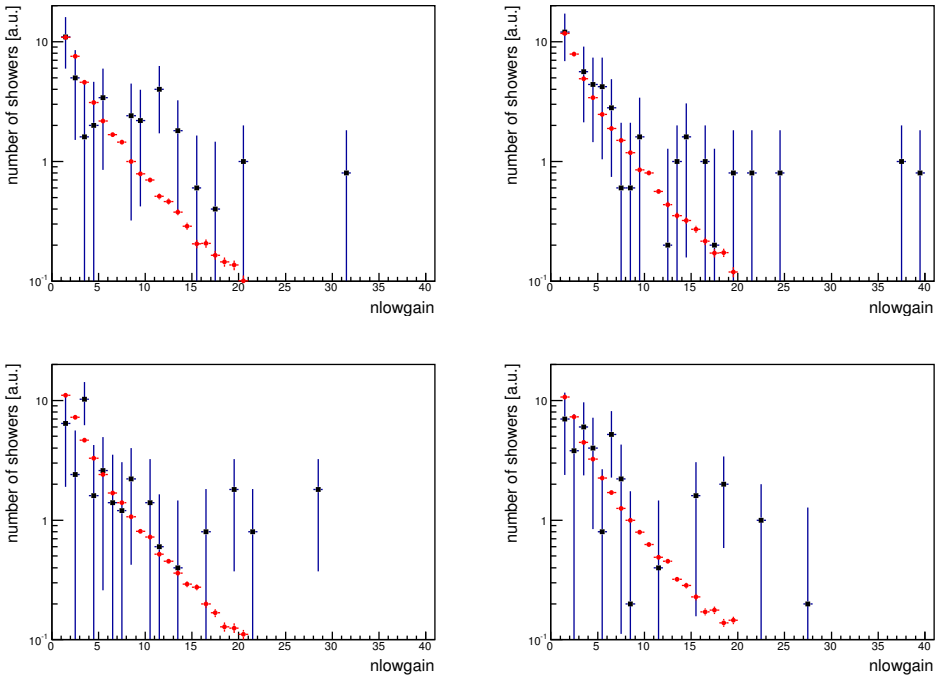

Figure 8.17: RHV configuration single telescope distributions of number of channels in an image that are in low-gain mode. As expected, there are substantially fewer low gain PMTs in RHV data due to the fact that the gain is a factor of three lower than for standard configuration data. The x-axis has intentionally been left the same as in this figure's NOM counterpart such that the two can be compared easily. Data are given in black and simulations are given in red.

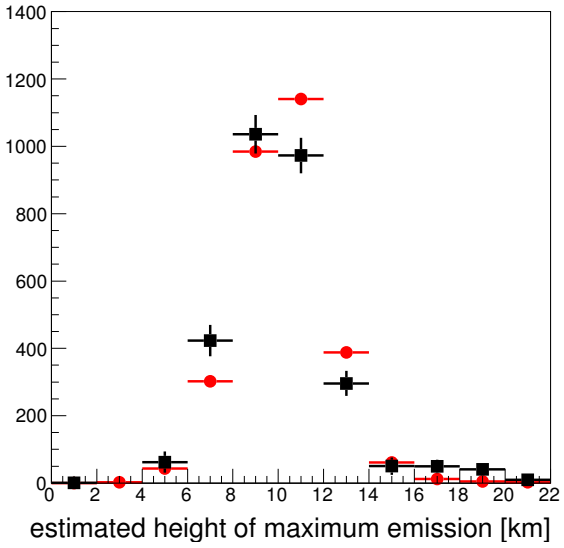

Figure 8.18: RHV configuration reconstructed shower maximum emission height. This is similar the corresponding distribution for the NOM configuration, which is expected, since air shower physics (which dictates the shape of this plot) has nothing to do with the PMT gains or ambient noise levels. Data are given in black and simulations are given in red.

Chapter 9

Observations with UV Filters

9.1 Array Configuration

While reduced high voltage (RHV) observations allow observing under bright moonlight without risking damage to the PMTs, once the moon is greater than approximately 65% illuminated, the mean PMT currents once again surpass the 15 μA safety threshold. Furthermore, at this point, while reducing the PMT gain would help protect the dynodes, it does nothing to protect the photocathode. Thus, in order to continue observing into the bright period, one must reduce the amount of light actually arriving at the PMTs. This is achieved using UV pass-band filters in what is called the UV filter (UVF) observing mode, implemented on *VERITAS* using SCHOTT UG-11 UV band-pass filters [125].

9.1.1 Physical Properties of the Filters

The amount of light transmitted by the filters is calculated from two components: light reflected via Fresnel reflection at the air-glass interfaces (the reflection factor, $\rho(\lambda)$) and internal absorption within the filter itself (the internal transmittance, $\tau_i(\lambda)$).

Reflection Factors

At an interface between two media with refractive indices n_1 and n_2, for a photon arriving at the interface with some angle θ_i, there will be some light that is transmitted through the interface and some light will be reflected. The fraction of the incident light that is reflected has two components, denoted R_s and R_p, which depend on the polarisation (s and p) of the incident light. These are the reflectivity terms. Similarly, the transmissivity, denoted T_s and

T_p, is the fraction of the incident light which is transmitted through the interface. The angle of the reflected light is $\theta_r = \theta_i$ and the angle of the transmitted light is θ_t, which is just the refracted angle determined via Snell's Law.

The equations for the reflectivity and transmissivity are

$$R_s = \left| \frac{n_1 \cos\theta_\mathrm{i} - n_2 \cos\theta_\mathrm{t}}{n_1 \cos\theta_\mathrm{i} + n_2 \cos\theta_\mathrm{t}} \right|^2 = \left| \frac{n_1 \cos\theta_\mathrm{i} - n_2 \sqrt{1 - \left(\frac{n_1}{n_2}\sin\theta_\mathrm{i}\right)^2}}{n_1 \cos\theta_\mathrm{i} + n_2 \sqrt{1 - \left(\frac{n_1}{n_2}\sin\theta_\mathrm{i}\right)^2}} \right|^2, \tag{9.1}$$

$$R_p = \left| \frac{n_1 \cos\theta_\mathrm{t} - n_2 \cos\theta_\mathrm{i}}{n_1 \cos\theta_\mathrm{t} + n_2 \cos\theta_\mathrm{i}} \right|^2 = \left| \frac{n_1 \sqrt{1 - \left(\frac{n_1}{n_2}\sin\theta_\mathrm{i}\right)^2} - n_2 \cos\theta_\mathrm{i}}{n_1 \sqrt{1 - \left(\frac{n_1}{n_2}\sin\theta_\mathrm{i}\right)^2} + n_2 \cos\theta_\mathrm{i}} \right|^2, \tag{9.2}$$

and

$$T_s = 1 - R_s, \tag{9.3}$$

$$T_p = 1 - R_p \tag{9.4}$$

where the last two originate from the conservation of energy (assuming no absorption at the interface). For unpolarised light, the total reflectivity and transmissivity are simply

$$R = \frac{R_s + R_p}{2} \tag{9.5}$$

and

$$T = 1 - R. \tag{9.6}$$

For a filter with an index of refraction $n(\lambda)$, assuming normal incidence and multiple reflections, the light transmitted through the filter will be reduced by an amount

$$\rho(\lambda) = \frac{2n(\lambda)}{n(\lambda)^2 + 1} \tag{9.7}$$

where $\rho(\lambda)$ is known as the reflection factor. This expression can be derived from Fresnel's equations and to first order applies independently of the thickness of the glass [126].

For a consistency check, one can calculate this for the UG-11 filters, for which $n(\lambda = 365\ \mathrm{nm}) = 1.585$. Thus, $\rho(\lambda = 365\ \mathrm{nm}) \approx 0.90$, which is close to the SCHOTT-specified value of $\rho = 0.91$. The SCHOTT value is taken to be constant across the transmission band of the filter (as per the specifications datasheet).

Transmittance in a Filter

There are two types of filters which work in different ways: dichroic filters and absorptive filters. The former is also known as an "interference filter" and works by constructing a filter

out of thin layers of material with thicknesses designed such that undesired wavelengths destructively interfere as they are reflected at the various interfaces, but desired wavelengths are not. By carefully choosing the thickness of the various coatings, it is possible to precisely control the wavelengths of light which are transmitted the filter. Note that this limits these filters to normal or near-normal incidence. This is the basic operating principle of a Fabry-Pérot interferometer.

In absorptive filters, like those used in *VERITAS*, light loses intensity as it passes through the filter due to scattering and absorption within the filters. Absorptive filters are typically made of glass which has been doped with different materials (e.g. transition-metal ions such as Cu^{2+}, Fe^{2+}, Cr^{3+}, or Co^{2+} [127]) depending on the desired optical properties of the filters. Doping will colour the glass; the colour has to do with the specific absorption characteristics of the doping materials. For example, the amber colour of beer bottles comes from iron sulphide and charcoal, and uranium doping provides fluorescent green or yellow colour. The most common process for absorption is the absorption of light between two energy levels. Contrary to interference filters, absorptive filters can be used at any incidence angle.

The internal transmittance depends on the thickness of the filters. The dependence of the total transmittance on filter thickness is given by

$$\tau_{ix}(\lambda) = \tau_{iy}(\lambda)^{x/y}, \tag{9.8}$$

where x and y are filter thicknesses, with y being the reference thickness, and x being the thickness of the filters in use.

The total transmittance (denoted τ) is defined as

$$\tau(\lambda) = \rho(\lambda)\tau_i(\lambda). \tag{9.9}$$

Figure 9.1 shows the total transmittance of the filters (assuming normal incidence) along with the Cherenkov emission spectrum for a simulated 500 GeV gamma ray, and the solar spectrum (recall that the lunar spectrum is basically the solar spectrum) at ground level. The transmittance has been calculated using the SCHOTT-specified reflection factor for normal incidence (0.91) and the specified transmittance for 1 mm thick filters, scaled to the thickness of the *VERITAS* filters (3 mm) using Equation 9.8.

9.1.2 The Filter Plates

The plates (referred to as the "filter plates") which hold the individual filters are made of a set of 9 interlocking plates in 3 layers: two 1/32" outer layers ($\approx$ 0.8 mm each) and one 1/8" inner layer ($\approx$ 3 mm), for a total thickness $<$ 5 mm. When installed on the camera, the

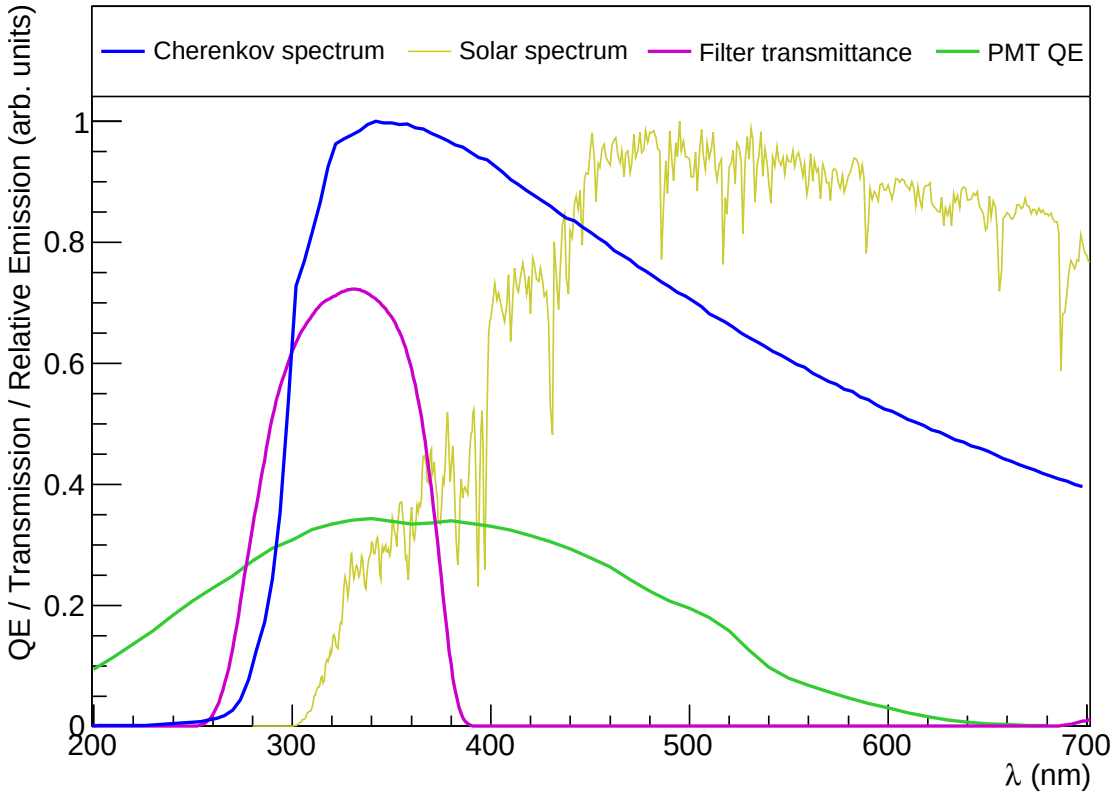

Figure 9.1: PMT quantum efficiency, filter transmittance, the Cherenkov spectrum of a 500 GeV gamma ray and the solar spectrum at ground level. The solar spectrum is the ASTM G173-03 reference spectrum [128]. The UV filters block out 96% of the moonlight photons but still transmit 17% of the Cherenkov spectrum.

filter plates are sandwiched between the light cones and the phototubes. The original design concept was for the filter plates to be as thin as possible such that the additional distance between the light cone plates and the PMTs would be minimized in order to minimize any effects on the telescope optical point spread function.

Large filters are difficult to manufacture due to (e.g.) uniformity issues and are exceptionally expensive. It was deemed to be more financially viable to use many small filters (one for each PMT) rather than one large one. Also, a filter is only needed over the photosensitive part of the PMT, so a large fraction of glass would be mostly wasted. Furthermore, in the case of an accident during installation of the filter assembly, it is far less expensive to replace individual small filters than one large one. Thus, the filter plates, shown in Figure 9.2, are made from 499 individual filters each with diameter 22 mm. The entire assembly is often referred to as simply “the filters”.

Figure 9.2: Picture of a UV filter plate. Each PMT has its own filter. The individual filters are larger than the exit aperture of the light cones. The bright points near the center of the image are daylight coming through the filter assemblies. Image credit: D. Hanna.

9.1.3 Telescope Optics and the Ideal Effective Filter Thickness

The specifications from SCHOTT assume normal incidence of light on the filters. This is not the case for the *VERITAS* filters, as light from different parts of the telescope reflector arrive at the focal plane at different angles depending on the orientation of the mirror at the point where the incident photon was collected. This is demonstrated in Figure 9.3.

In order to calculate the mean thickness of filter seen by light rays from the reflector, it is first necessary to determine the mirror-area-weighted distribution of photon arrival angles at the focal plane. Using the geometry of Figure 9.3, the following relation is true:

$$\frac{\sin\theta}{r} = \frac{\sin(\pi/2)}{f} \tag{9.10}$$

with $f = 12$ m is the focal length of the telescope (which is the same as the radius of curvature of the reflector), r is the radial distance from the optical axis of the telescope, and θ is the angle from the focal plane normal. Thus,

$$\sin\theta = r/f \tag{9.11}$$

Note that the maximum incidence angle $\theta_{\max} = 30^\circ$ occurs at $r = 6$ m. Each angle has a weight W which is proportional to the differential area of the dish at a given r,

$$W(r) \propto \frac{dA}{dr} = 2\pi r. \tag{9.12}$$

Using Equation 9.10 it is possible to convert $W(r)$ into $W(\theta)$ which yields

$$W(\theta) \propto \sin\theta \tag{9.13}$$

which is shown in Figure 9.4 to demonstrate the shape of the distribution over the range of valid angles.

The average of $W(\theta)$ over the range $0^\circ \leq \theta \leq 30^\circ$ occurs at $\theta \approx 14.8^\circ$. Including effects of refraction, the effective filter thickness x_{eff} seen by photons entering the filters at this angle is given by

$$x_{\text{eff}} = \frac{x}{\cos\theta'}, \tag{9.14}$$

where x is the thickness of the filters (3 mm) and θ' is the angle from the filter normal after the light has been refracted:

$$\sin\theta' = \frac{n_1}{n_2}\sin\theta. \tag{9.15}$$

The above equation is simply Snell's Law. For $n_1 \approx 1$ (the index of refraction of air) and $n_2 = 1.585$ (the index of refraction of the filters at 365.0 nm), $\theta' \approx 9.3^\circ$. Thus, $x_{\text{eff}} \approx 3.04$ mm. This would be a small effect on the overall filter transmission ($\sim 1\%$ at 365.0 nm, less at shorter wavelengths) but does not include additional effects due to the light cones, which is explained in the next section.

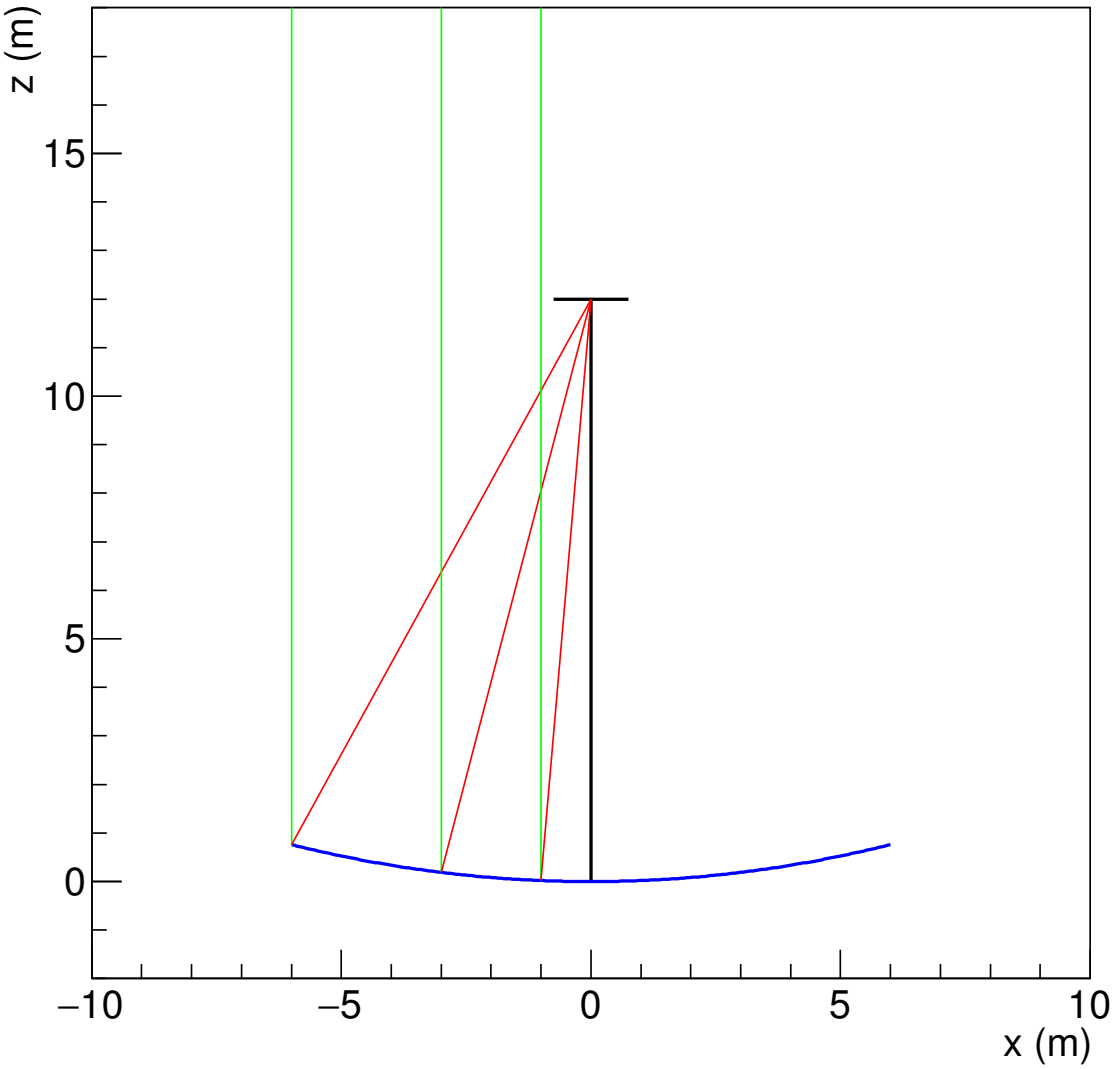

Figure 9.3: Example of an ideal spherical reflector with dimensions similar to a *VERITAS* telescope. The vertical black line at $x = 0$ represents the optical axis of the telescope, and the short horizontal line at $z = 12$ m is roughly the same size of a *VERITAS* camera. The green lines are incoming photons from infinity, and the red lines are the photons after they have reflected off of the dish. Light reflecting off different parts of the dish arrive at the focal plane at different angles. Note that the behaviour of the rays shown here are not representative of a perfectly spherical dish. Rather, they are representative of a Davies-Cotton reflector, which is minimizes spherical aberrations for on-axis rays.

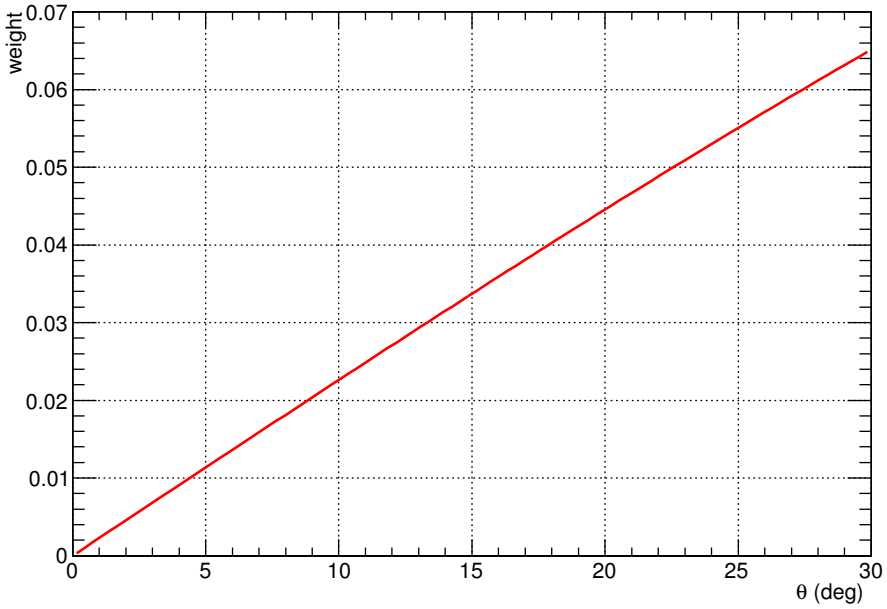

Figure 9.4: Weighting function for determining the angle of photons arriving at the focal plane. This is just $\sin(\theta)$ normalized such that the area under the curve for $0 < \theta < 30°$ is 1.

9.1.4 Effects of the Light Cones

One must also consider additional effects caused by the light cones; this is because much of light exiting the cones does so at large angles to the normal (see Figure 9.5) even if the incidence angle on the cone is small. This further complicates the issue of light not entering the filters at normal incidence.

9.1.4.1 Theory

In order to calculate the effective filter thickness seen by photons due to effects of the light cones on the optical system (and hence how much attenuation would be expected), a ray tracing program was implemented[1]. Ray tracing is the process of following photons as they interact with optical surfaces in order to characterise an optical system. The details of the ray tracing algorithm can be found in Appendix B and an example of a result from the ray tracing program is given in Figure 9.6.

The arrival angles with respect to the optical axis of the light cone were generated using the previously introduced weighting function $W(\theta)$ in the range of angles applicable to a *VERITAS* dish ($0° \leq \theta \leq 30°$). The arrival angle about the optical axis (which can be

[1]This is how Figure 9.5 was produced.

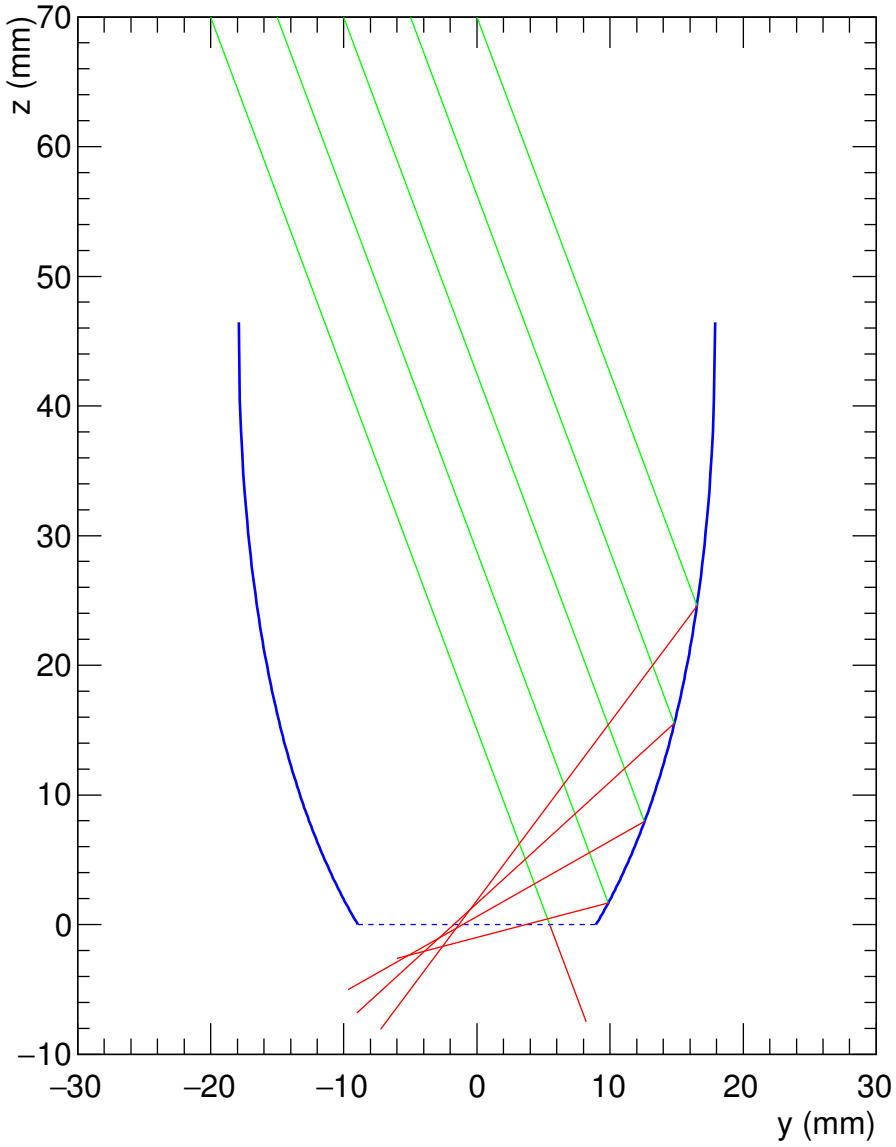

Figure 9.5: Example of parallel rays entering an ideal light cone at 20 degrees from the axis of the cone. All rays are in the same plane ($x = 0$), hence this is essentially an example of the "trivial" two dimensional case. The blue lines are the sides of the light cone and the blue dashed line at $y = 0$ is the exit aperture of the cone. The red lines represent the photon direction after its final intersection, or the path after it has exited the bottom of the cone without intersecting. Depending on the origin of the rays, the exit angles are greatly different even through their incoming angles are the same.

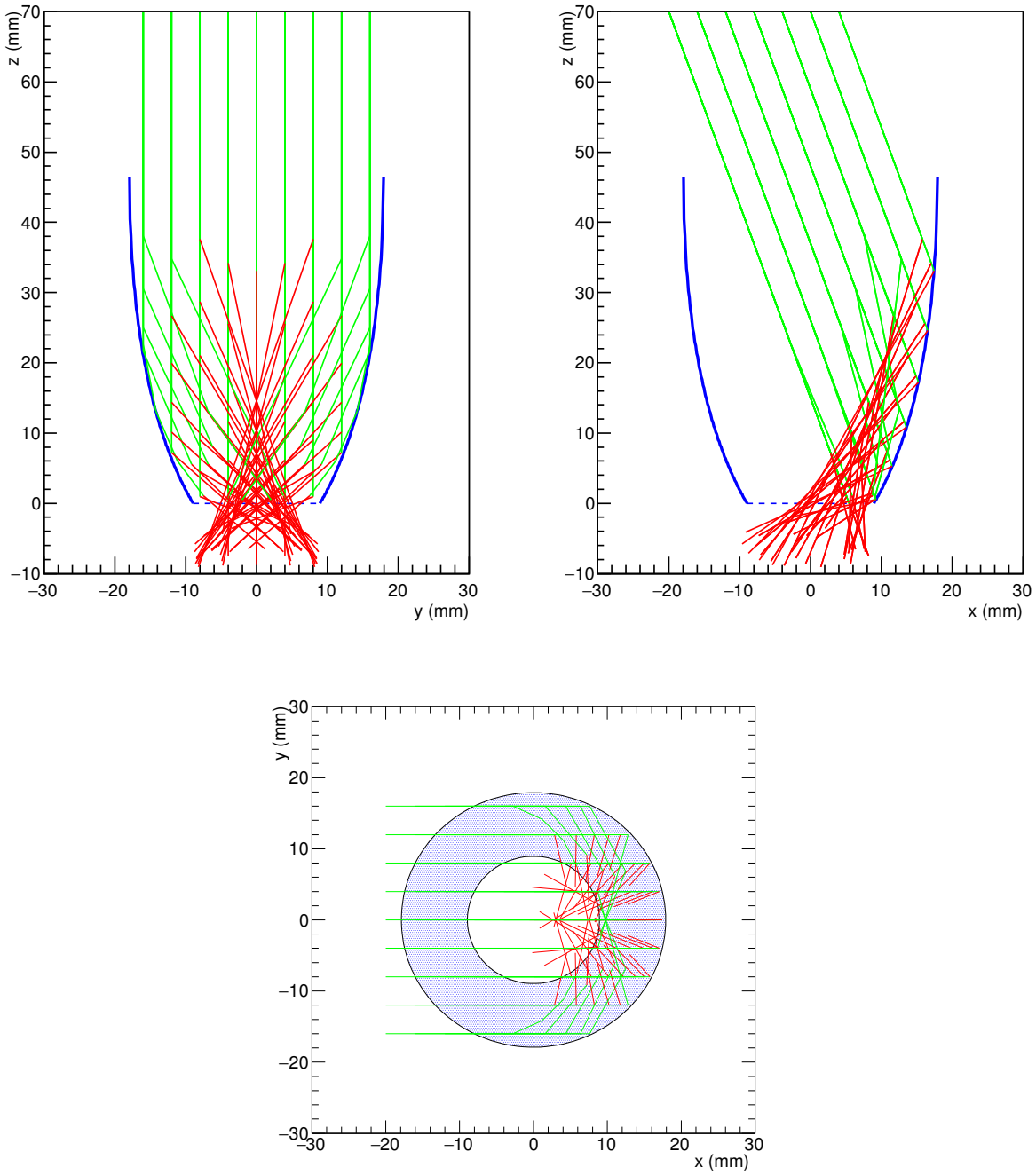

Figure 9.6: Example of parallel rays entering an ideal light cone at 20 degrees from the axis of the cone. The ray origins are a 20 mm by 20 mm grid with 4 mm spacing between adjacent rays. Only rays which enter the cones are drawn here. **Top**: Side projections. **Bottom**: View from directly above the cone. The blue shaded region is the interior of the cone and the circle in the centre is the exit aperture.

thought of as the azimuthal coordinate around the optical axis) was spread evenly about all angles, since in the ideal situation of a perfectly circular dish there is no preferred azimuthal angle.

The *VERITAS* light cones have an exit aperture $D_{out} = 17.9$ mm and entrance aperture $D_{in} = 31.4$ mm. This makes the cutoff angle of the light cones $\sim 35°$. The light cones simulated here have been tailored to have the same exit aperture as the *VERITAS* cones but a slightly larger input aperture. This has the effect of making the cutoff angle of the cones in the simulation equal to the maximum incoming angle from the reflector (30°). For simplicity, standard Winston cones have been simulated (as opposed to the *VERITAS* hybrid type which have a hexagonal entrance aperture and circular exit aperture, see Section 3.2.6).

Using Equation 9.13 as a probability distribution for arrival angles at the focal plane, 10^5 photons were generated with starting positions were distributed randomly and uniformly across the face of a simulated light cone. The uniform distribution is motivated by the fact that *VERITAS* images extended air showers with sizes that are at *least* $\sim 0.3°$ in diameter (which is dictated by the L2 trigger). Each photon was traced through the light cone system and its exit angle and position were stored. The distribution of angles away from normal for the photons exiting the light cones is given in Figure 9.7. This calculation assumes 100% reflectivity for the light cones, so $N_{in} = N_{out}$.

It is not enough to take this exit angle distribution and use it to calculate the amount of filter thickness seen by photons at each incidence angle. The reflection factor in Equation 9.7 is only valid for normal incidence. Thus, it must be recalculated for each incidence angle on the filter. In order to do this, Fresnel's equations must be utilized.

To first order, light entering the filters will be refracted once at the air-glass interface, and then again at the glass-air interface. Knowing this, $\rho(\lambda)$ can be calculated using Fresnel's equations and Snell's law at each interface. Now, all the information is available to calculate the total light yield through the filters including effects of the light cones.

In order to determine the distribution of photons exiting the bottom of the filters, a Monte Carlo simulation was produced wherein each photon was given a probability of being transmitted at the air-glass interface (determined by Fresnel's equations), surviving attenuation in the glass itself (determined by the filter internal transmittance $\tau_i(\theta_t)$), and then being transmitted at the glass-air interface (again determined by Fresnel's equations). The refractive index of the filters was taken to be 1.600 in the simulation (this is very close to the refractive index in the peak region of the filter transmission spectrum, 1.601 [125]). Note that the uncertainty on the refraction index is secondary to effects like the wavelength-dependence of the transmittance in the filter "plateau" region or the wavelength-dependent reflectivity of real-life light cones. The resulting distribution of exit angles for photons exiting the filters is

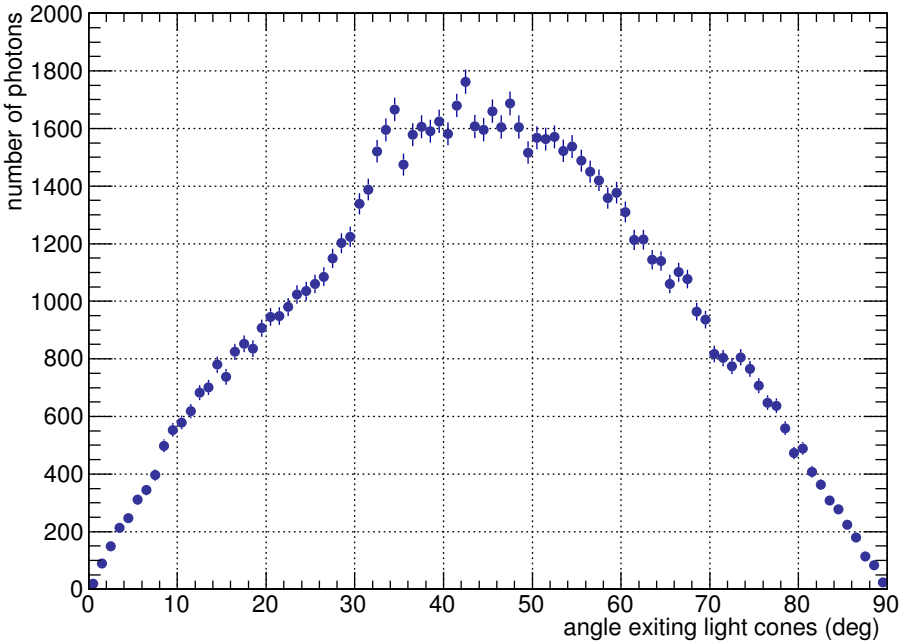

Figure 9.7: Distribution of angles for photons exiting the simulated light cones assuming a uniform distribution of arrival positions at the focal plane and arrival angles weighted by the mirror area.

given in the top panel of Figure 9.8. The ratio of the transmitted photons to the incident photons (as a function of incidence angle) is the total transmittance of the filters as a function of incidence angle, shown in the bottom panel of Figure 9.8.

The distribution of effective filter thicknesses seen by photons exiting the light cones with angles determined by the ray tracing is shown in Figure 9.9. The structure at the low end of the plot is due to photons passing straight through the light cones without reflecting off the walls, and the peak near 3.2 mm corresponds to the change in the slope seen at 33° in the top panel of Figure 9.8.

In the end, the total transmittance of the filters, weighted by the light cone optics, is simply the ratio of the number of photons exiting the filters to the number of photons arriving at the filters

$$\tau_{eff} = \frac{N_{transmitted}}{N_{incident}} = 0.631 \pm 0.003. \tag{9.16}$$

This value is simply the ratio of the integrated number of photons in each distribution in the top panel of Figure 9.8. At normal incidence, the filter total transmittance from the specifications, $\tau_{\perp}$, peaks at ≈ 0.72. The ratio

$$\frac{\tau_{eff}}{\tau_{\perp}} = 0.873 \pm 0.004. \tag{9.17}$$

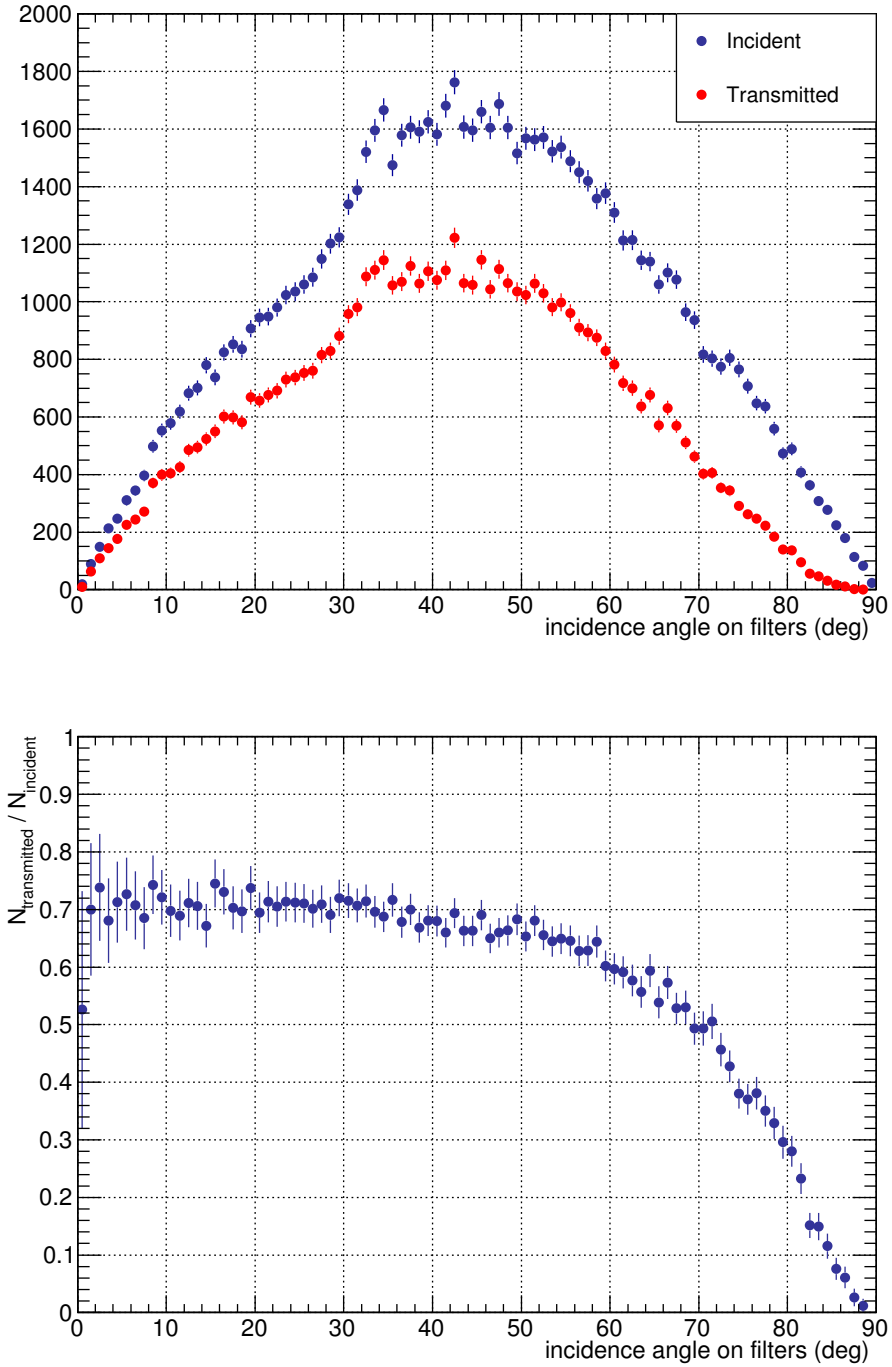

Figure 9.8: **Top**: Distributions of the number of photons incident on a filter and transmitted through it as a function of incidence angle. **Bottom**: The ratio of transmitted photons to incident photons (*i.e.* τ) as a function of incidence angle. In principle, the shape of this distribution can be derived analytically from Fresnel's equations and the internal transmittance of the filters. At small angles, the mean value for τ is ≈ 0.72, which is the value predicted for normal incidence according to the filter specifications.

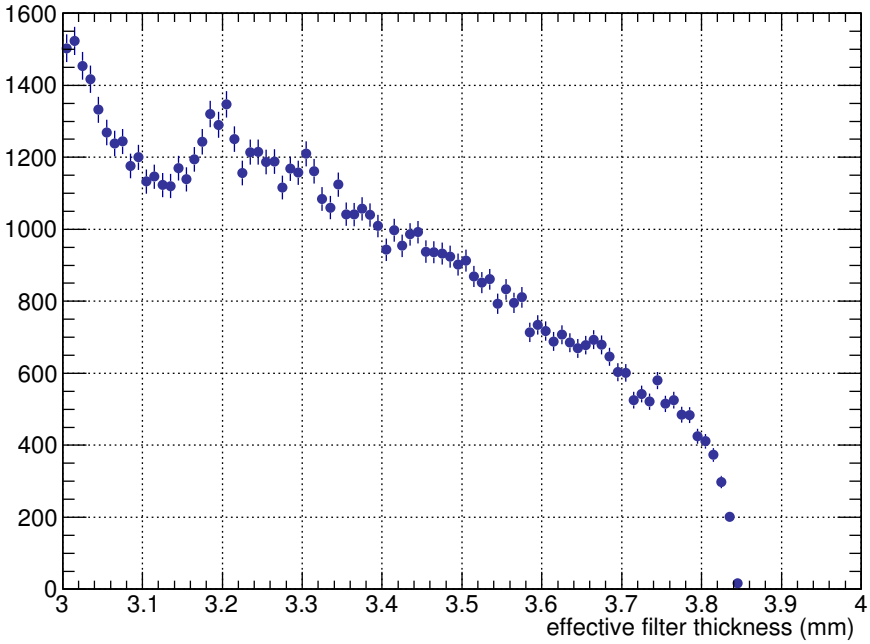

Figure 9.9: Distribution of effective filter thicknesses seen by photons exiting the light cones with angles as determined by the ray tracing. The peak at 3.2 mm corresponds to an incidence angle $\sim 33°$ on the filter; referring to Figure 9.8, there is a change in the slope of the distribution at this angle.

Thus, according to this simulation, the effective reduction in light yield is a factor of 1.15.

9.1.4.2 Direct Measurements

Simulating a system can usually provide good insight into a process, but in the end sometimes a direct measurement is required to quantify aspects of the detector[2]. This is usually because simulations can only take into account effects the programmer considered, but a direct measurement by definition encompasses any and all secondary effects which might contribute to an overall effect.

Direct measurements of the angular response of the light cone / filter combination were made using a test setup designed to measure the boost in light yield normally gained from using a light cone in front of the PMT. The following figures were produced using data provided by a collaborator, J. Eisch from Iowa State University. For simplicity, the following abbreviations are used:

[2]Also, by the time the ray tracing was done, it was concluded that there were too many secondary effects, such as the increase in path length through the photocathode (which increases the probability of a photoelectron being produced) that could not easily be accounted for.

- LC: Light cone +PMT
- FLC: Filter + light cone + PMT

The test setup consists of an LED positioned ~ 5 m in front of the light cone / PMT assembly, which is mounted on a computer-controlled platform which can rotate $\pm 45°$ with $0.5°$ precision. Measurements of the PMT current are made in steps of $1°$ over this range; the systematic uncertainty on the angle (*i.e.* the accuracy) is $\pm 1°$ at each point. The underlying assumption is that this setup produces rays that enter the light cones at only one angle (dictated by the orientation of the assembly).

At each pointing, the PMT current is measured 2500 times and averaged in the the data acquisition system before being saved to disk. Thus, the statistical errors on each current measurement are expected to be very small. The entire procedure was repeated using a second LED. The mean emission wavelengths for the LEDs are 340 nm for LED 1 and 370 nm for LED 2 (see Figure 9.10). The LEDs are Thorlabs models LED341W [129] and LED370E [130], respectively. The optical properties of both are given in Table 9.1.

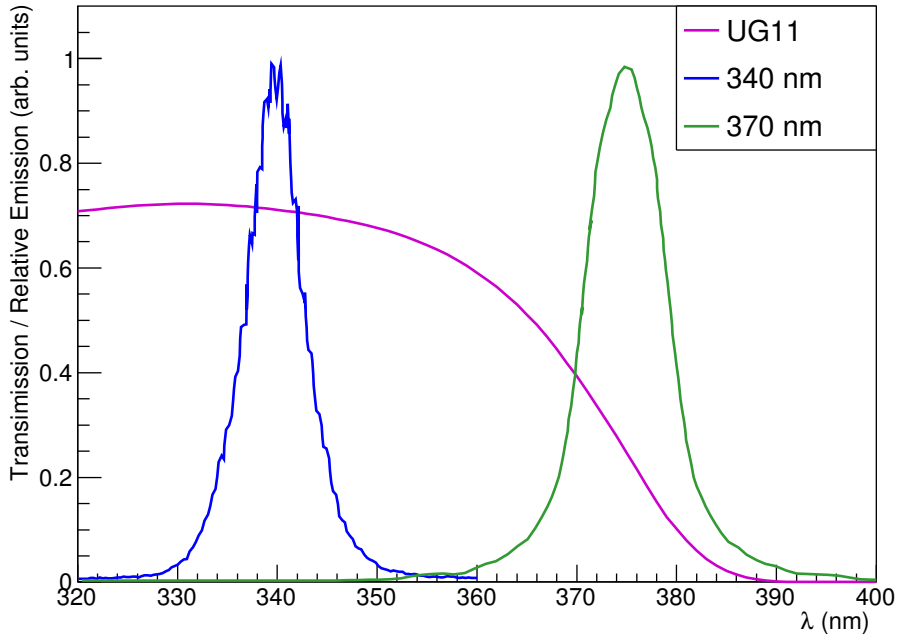

Figure 9.10: Emission spectra for the LEDs used in the test setup with the SCHOTT UG11 filter transmission spectrum for comparison. Note that the location of peak emission has a large uncertainty (± 15 nm for LED341W and ± 10 nm for LED370E).

By taking the ratio of a current measurement taken with and without a light cone, the boost in light yield due to the light cones (which effectively increase the effective collection

Characteristic	LED341W (nm)	LED370E (nm)
Centre Wavelength	340 ± 10	375 ± 10
FWHM	15	10

Table 9.1: Optical characteristics of the LEDs used in the test setup.

area of the PMTs) can be directly measured. Then, by weighting each point by the mirror collection area, and integrating over the range of angles incoming from the dish, the "boost factors" can be calculated. The results of the measurements of the light yield for the LC and FLC setups are given in Figures 9.11 and 9.12.

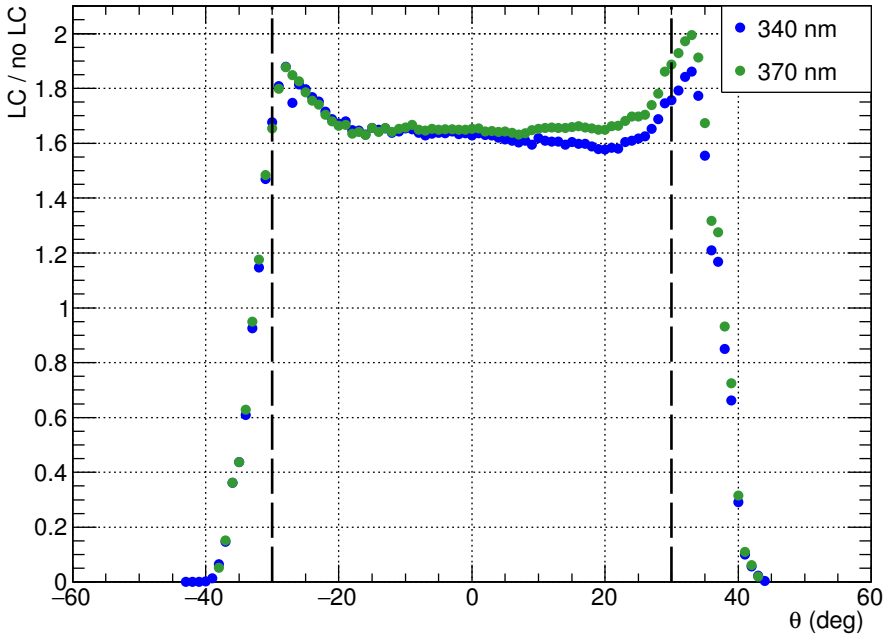

Figure 9.11: Results of LC light yield measurements. The curves are approximately the same, which is expected if the spectral response of the light cone is the same for both LEDs. The vertical lines at ±30° represent the maximum angles at which light from the *VERITAS* reflector arrives at the light cone.

There are a few features worth noting. Firstly, the results are not symmetric about $\theta = 0$. This is likely due to the light cone and PMT assembly being slightly angled (*i.e.* there is a systematic offset between the measured angle and true angle). This offset has been used to estimate the systematic error; when calculations are made in the following section, ±30° (*i.e.* the maximum angle for photons arriving from the *VERITAS* dish) was typically used for the integration limits over the data sets. The integrals have also been computed for ±27° and

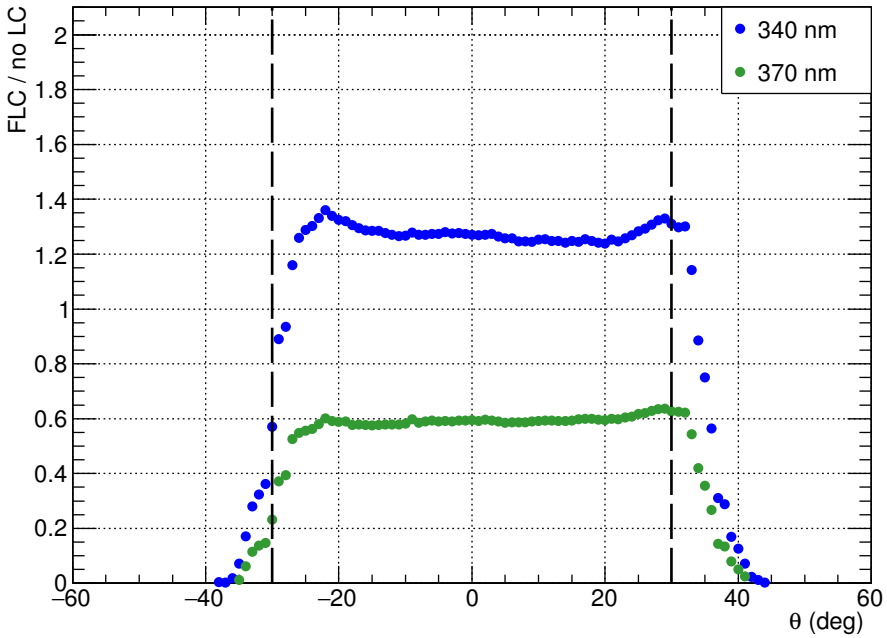

Figure 9.12: Like Figure 9.11 but for the FLC setup. The curves are not the same due to the spectral response of the filter being different for the two different LEDs. The vertical lines at ±30° represent the maximum angles at which light from the *VERITAS* reflector arrives at the light cone.

±33° (*i.e.* ±10%). The average difference between this value and the "nominal" value at 30° has been used a systematic error to take into account the accuracy of the apparatus (±1°) and the offset from zero ($O(5°)$).

Another feature is that there are "horns" at large angles. This is indicative of an increase in the light yield at large angles; this is possibly due to increased path length through the PMT photocathode which increases the probability of interaction. The horns are also less prominent in the FLC measurements.

For the LC setup, the boost in light yield, denoted Λ, due to the light cones is $\Lambda_1 = 1.67 \pm 0.02$ and $\Lambda_2 = 1.70 \pm 0.02$ for LED 1 and 2, respectively. For the FLC setup, the boost factors are $\Lambda_{F1} = 1.25 \pm 0.05$ and $\Lambda_{F2} = 0.58 \pm 0.02$. The FLC values are the convolution of the LC boost factor, any change in light yield due to the fact that the light cone exit aperture is separated from the PMT (due to the fact that the filters are 3 mm thick), and the wavelength-dependent filter transmission. As shown in the previous section, there are also reflection effects due to the fact that light will not be normally incident on the filter face.

Plotting the ratio of the FLC measurements to the LC measurements yields Figure 9.13. The mean ratio is a measurement of the transmission efficiency (ξ) of the filters: $\xi_1 = 0.78 \pm 0.02$

and $\xi_2 = 0.35 \pm 0.01$ for the LED 1 and 2, respectively. These values have been determined by taking the mean of the distribution of efficiency values in the "plateau" region of Figure 9.13 ($\pm 25°$). The systematic errors are also derived by shifting the integration limits by $\pm 3°$.

Note that ξ is *not* a measurement of the transmittance of the filters at that wavelength which was previously introduced as $\tau(\lambda)$. Instead, it is a measure of the total transmission integrated across the emission spectrum of the LED.

It is worth noting that the value at 370 nm is on the falling edge of the filter transmission spectrum, so errors here are large (a small change in wavelength corresponds to a large change in the light yield), but the 340 nm value is actually higher than the peak transmission value in the UG-11 transmission spectrum. The reasons for this are unclear; one possible explanation is that light is being refracted towards the center of the PMT photocathode, which is generally more sensitive than the edge.

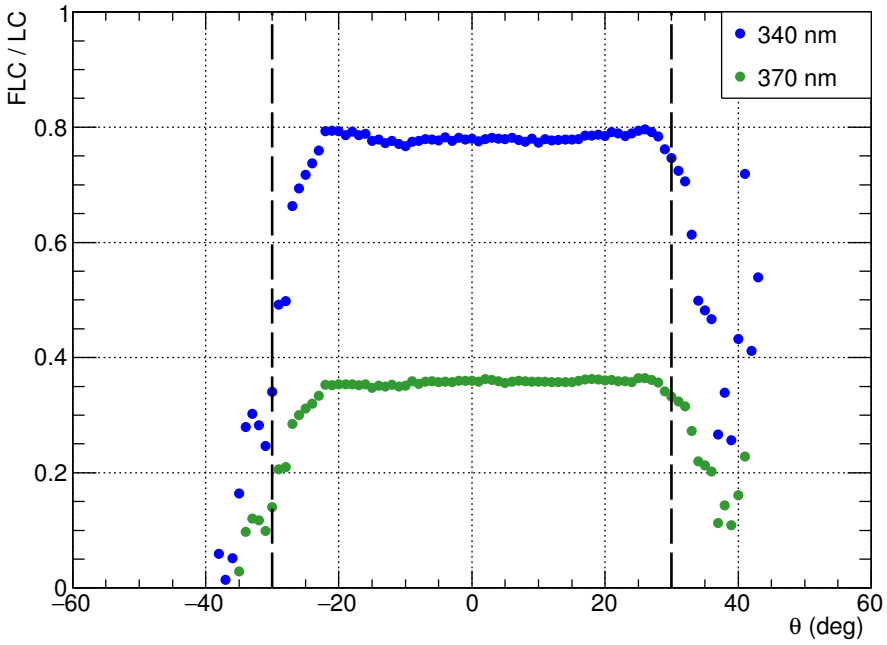

Figure 9.13: Ratio of the FLC measurements to the LC measurements. The mean value in the "plateau" area of both curves ($|\theta| < 25°$) is 0.78 and 0.36 for the LED 1 and 2, respectively. The vertical lines at $\pm 30°$ represent the maximum angles at which light from the *VERITAS* reflector arrives at the light cone.

The total transmission efficiency corrected boost factor for the filter + light cone combination is given by the ratio

$$\Lambda'_{\mathrm{F}} = \frac{\Lambda_{\mathrm{F}}}{\xi}.$$

The numeric values for the boost factors for both LC and FLC are given in Table 9.2. They are both $\sim 4\%$ less than their respective values for the setup without filters, which implies that the light yield on the PMTs is less than the nominal value when the filters are in use. The numeric values for the decrease in light yield are ~ 3.5 times smaller than what was predicted by the simulations, but this discrepancy should not be over-interpreted since the estimated systematic uncertainties (which admittedly are fairly rudimentary) of this measurement mean that the FLC values are consistent with the LC configuration.

The take-home message after both these studies is that a reduction in the light yield is to be expected but is difficult to directly measure; this will be discussed later in Section 9.2.

LED	Λ	Λ_F	ξ	Λ'_F
340 nm	1.67 ± 0.02	1.25 ± 0.05	0.78 ± 0.02	1.60 ± 0.07
370 nm	1.70 ± 0.02	0.58 ± 0.02	0.36 ± 0.01	1.63 ± 0.08

Table 9.2: Light cone boost factors (Λ) and transmission efficiency (ξ) values for the light cone and filter + light cone setups. The efficiency-corrected values (Λ'_F) are $\sim 4\%$ less than the values without the filters, but the systematic uncertainties are consistent with the values for Λ, so it is difficult to draw any conclusions. The uncertainties on Λ'_F are the errors resulting from standard error propagation.

9.1.5 CFD Thresholds

Two UVF bias curves taken under different amounts of moonlight ($\sim 90\%$ and $\sim 80\%$) are given in Figure 9.14 and the curve fit values are given in Table 9.3. Between these two observations, there is a large difference in the position of the inflection point: 41 mV for the brighter moon data set and 33 mV for the other. This is proof that the constant fraction discriminator (CFD) trigger rates are strongly dependent on the illumination of the Moon; even a 10% change in illumination has a strong influence on the NSB portion of the bias curve. They are also dependent on the position of the Moon and the angle between the Moon and the observing target, which institutes some logistical constraints.

As was previously mentioned, there is a limited amount of personnel and computing power available for producing simulations used in analysing data. For the UVF configuration, it was determined that a single, conservative set of CFD thresholds be used for the vast majority of observations called "science" thresholds (45 mV) and a second set of "discovery" thresholds used for going after potential sources where the low energy threshold is more of a concern (35 mV). All but a handful of data taken with the filters are taken with "science" thresholds. This considerably reduces the phase space required for simulations at the cost of sensitivity and energy threshold.

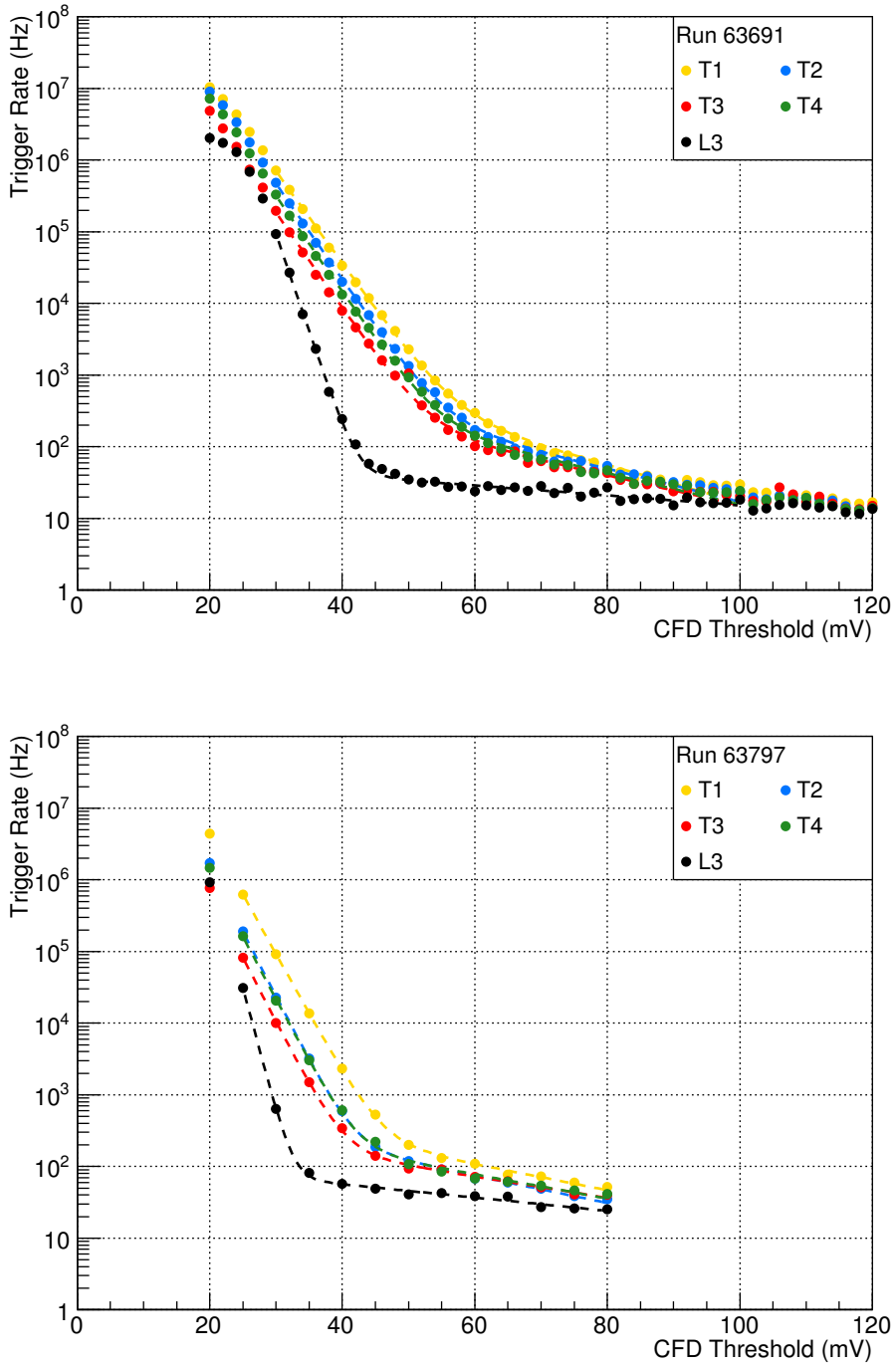

Figure 9.14: **Top**: Bias curves taken on a night where the Moon was $\sim 90\%$ illuminated. **Bottom**: Like above, but taken on a night where the Moon was $\sim 80\%$ illuminated. The inflection point is clearly at a higher threshold in the upper panel. The fit values for the L3 bias curves are given in Table 9.3. Note that for the bottom bias curve, the interval between data points is larger (this was a choice made by the observers) and the range over which the measurement was made is smaller. Hence, the error bars on the fits are larger.

	CR		NSB	
	A	B	C	D
UVF 90%	4.32 ± 0.09	-0.016 ± 0.001	30.1 ± 0.2	-0.624 ± 0.005
UVF 80%	4.89 ± 0.14	-0.021 ± 0.002	30.2 ± 0.6	-0.794 ± 0.023
NOM	7.35 ± 0.06	-0.025 ± 0.001	29.5 ± 0.2	-0.683 ± 0.007

Table 9.3: Fit values for the bias curves Figure 9.14. The parameters are the same as in Equation 6.4. The 90% bias curve was fit between 30 mV and 100 mV and the 80% bias curve was fit between 25 mV and 100 mV. The χ^2/NDF are 47.6/32 ($P \sim 0.038$) and 5.5/8 ($P \sim 0.701$), respectively.

9.2 Analysis Results

9.2.1 Details of the Detector Simulations

As was previously stated, there are very few bright, steady VHE gamma-ray emitters, and even fewer of them have been detected in UVF data. Thus, it is difficult to determine what corrections need to be made to a detector configuration in order to make the analysis results agree with measured values, without fine-tuning the analysis to work on only the data set in question. Prior to the *VERITAS* camera upgrade (*i.e.* the V5 configuration), there were a number of observations made of the Crab Nebula with filters installed to test the functionality of the filters (e.g. testing to see if *VERITAS* could detect sources under the full moon). These data were effectively used to help calibrate the V6 Crab data, by testing how changing the light yield in the simulations affects the shape of a reconstructed spectrum.

In the end, to produce the results in this section, the light yield on the cameras had to be reduced by a factor of 1.15 in order to produce a Crab spectrum with the UVF data set that was within standard uncertainties of a canonical value. It was chosen based on the results from the ray tracing, direct measurements, and taking into consideration what was learned through various iterations of different V5 light yield configurations, and not as a result of fine-tuning the V6 detector configuration.

9.2.2 Performance Studies

Figures 9.15 and 9.16 show the bias and resolution of the shower energy reconstruction for UVF simulations. For reference, results for a standard noise level in the nominal (NOM) configuration are also plotted (the same as were used for reference for the corresponding RHV plots).

Unlike the other observing modes for which the detector sensitivity is minimally affected by sky brightness, the sensitivity of *VERITAS* in the UVF mode has a strong dependence on

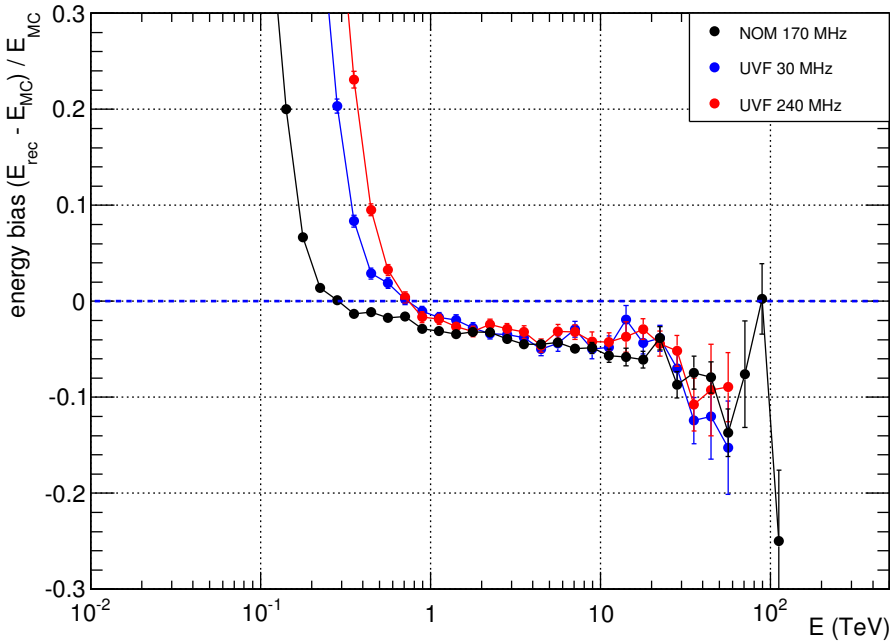

Figure 9.15: Energy reconstruction bias vs energy for simulated gamma-ray showers at 20 degrees zenith angle for two noise levels in the UVF configuration and one in the NOM configuration. The blue dotted line represents the ideal case (no energy reconstruction bias). The UVF bias traces the NOM bias above $\sim$ 800 GeV. Below this, it diverges and the energy reconstruction bias becomes large.

the observing conditions. This is demonstrated in Figure 9.17 which depicts the run-by-run Li & Ma sensitivity versus mean PMT currents (*i.e.* sky brightness). The same information for the NOM and RHV data sets is shown for comparison. There is a strong anti-correlation between the sky brightness for UVF data that is not evident in the NOM data (although the lever arm here is probably too small to say this definitively). The RHV data set has only a slight anti-correlation. The correlation coefficients are -0.3, and -0.70 for RHV and UVF, respectively. The time required for *VERITAS* to detect sources at various flux fractions in the UVF configuration is given in Table 9.4. These values are based on the numbers attained from the entire UVF data set (*i.e.* both "dark" and "bright" UVF observing conditions), so they can be interpreted as average values.

Based on these observations, the UVF configuration is best suited for bright, hard-spectrum sources, or science targets where additional exposure at high energies is desired.

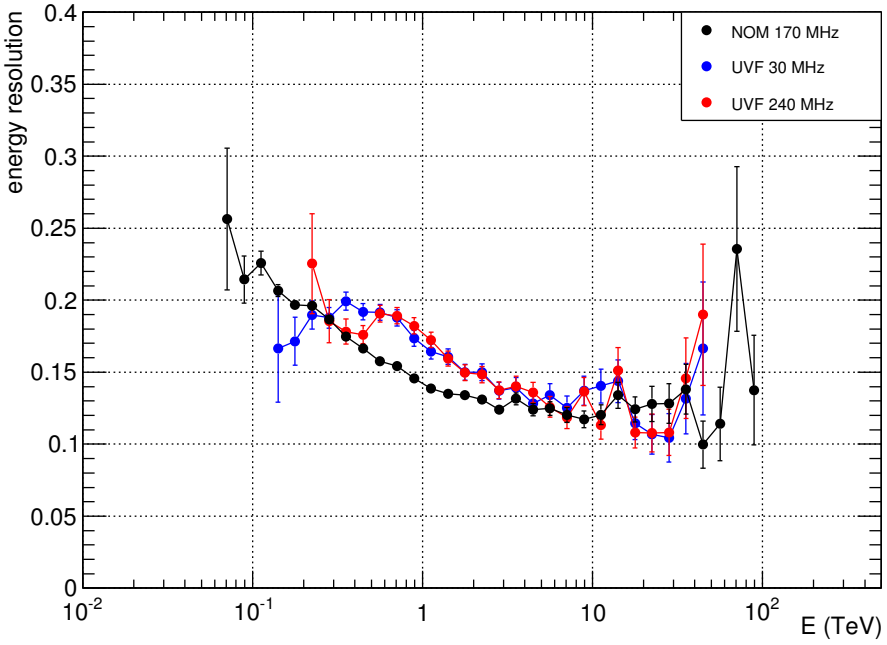

Figure 9.16: Energy resolution versus energy for simulated gamma-ray showers at 20 degrees zenith angle for several noise levels with the array in UVF mode. Below $\sim$ 20 TeV the energy resolution is systematically poorer than the energy resolution for NOM data. This is consistent with there being less information from which to reconstruct the shower. The maximum difference is a $\sim$ 20% effect. The two lowest energy points of the 30 MHz UVF data are lower than the NOM points, but this is completely driven by statistics.

Crab Nebula Flux Fraction	Observing Time (minutes)		
	NOM	UVF (Soft)	UVF (Moderate)
1	1.14	4.89	6.17
0.1	36.6	229	188
0.05	124	842	638
0.01	2670	19500	13400

Table 9.4: Time required to detect sources at various fractions of the Crab Nebula flux based on the numbers from the results from the entire UVF data set. The same data were also analysed with slightly harder cuts (the same cuts used in the NOM analysis). Note that with harder cuts, the sensitivity to small flux fractions increases significantly. This is because the cosmic ray spectrum is steeper than the Crab Nebula spectrum (*i.e.* the ratio of cosmic-ray events to gamma-ray-like events changes favourably). With the larger size cut, the energy threshold is also increased (520 GeV versus 320 GeV). This demonstrates that if one is willing to sacrifice energy threshold for sensitivity (as would generally be the case when using UVF data) a $\sim$ 25% boost in sensitivity for weak sources can be obtained at the cost of a moderate increase in energy threshold.

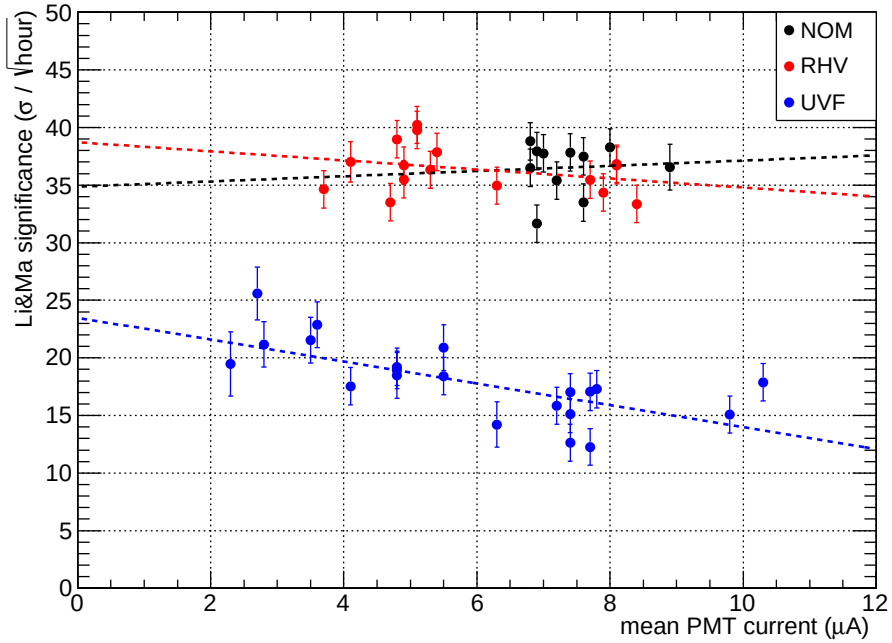

Figure 9.17: Sensitivity to the Crab vs mean PMT currents for the NOM, RHV, and UVF configurations. Each point corresponds to the sensitivity of a different data run. The lines are fits to indicate the trend and should not be used quantitatively. The UVF fit is the only line that does not have a slope statistically consistent with zero.

9.2.3 Data

The runs used for the UVF analysis are indicated in Table 9.5. Note that there is a factor of approximately four difference in sky brightness between the darkest and brightest runs used in this analysis. This is relevant to the sensitivity discussion that was mentioned in the previous section.

As was the case with RHV, these runs were analysed in the exact same manner as those for the NOM data set with the exception of the gamma/hadron separation cuts. Given that a large amount of the Cherenkov light is cut out by the filters, "soft, open" cuts were used in this analysis. These cuts were identical to those used in the RHV analysis except for the cut on the mean scaled parameters. The cut on the mean scaled parameter was "opened" to include all values < 1 for MSCW and MSCL (which are usually cut off at 0.5 and 0.7, respectively). The motivation for this is the presence of a shift seen in the data/MC comparisons, and will be discussed later.

Note that since UVF substantially changes the amount of Cherenkov light seen by the PMTs (as opposed to simply reducing the pulse height as is the case in RHV), it is reasonable

to assume that the source and background distributions are different enough compared to NOM data such that standardised gamma/hadron separation cuts are not as efficient as they could otherwise be. This is currently under investigation, and would only make the analysis better, but is not included in this thesis.

DATE	RUN	DUR (min)	WOB	SKY	EL (deg)	AZ (deg)	L3 (Hz)	NSB
20121026	64437	20	0.5N	A	71	114	53	3.6 (l)
20121026	64438	20	0.5S	A	74	126	55	2.8 (l)
20121026	64439	10	0.5S	A	76	136	57	2.3 (l)
20121027	64468	20	0.5W	A	72	119	51	6.3 (l)
20121027	64469	20	0.5N	A	76	128	52	5.5 (l)
20121027	64470	20	0.5S	A	78	148	54	4.8 (l)
20121027	64473	20	0.5E	A	80	180	56	3.5 (l)
20121027	64474	15	0.5W	A	79	210	57	2.7 (l)
20121124	65067	30	0.5N	A	74	121	46	4.8 (l)
20121125	65086	30	0.5S	A	63	106	42	7.7 (h)
20121125	65087	30	0.5E	A	70	113	41	7.2 (h)
20130122	66296	30	0.5W	A	72	243	69	10.3 (m)
20130122	66297	30	0.5N	A	66	254	56	9.8 (m)
20130923	69663	30	0.5W	A	65	107	41	7.4 (m)
20131114	70750	30	0.5W	A	74	123	36	5.5 (l)
20131114	70751	30	0.5N	A	78	142	38	4.8 (l)
20131114	70752	30	0.5S	A	80	180	38	4.1 (l)
20140111	71606	30	0.5N	A	65	105	42	7.8 (m)
20140312	72491	30	0.5E	A	73	240	44	7.4 (m)
20140312	72492	30	0.5W	A	66	253	42	7.4 (m)
20140312	72493	30	0.5N	A	60	261	40	7.7 (m)
Total:		535						

Table 9.5: UVF configuration Crab run list used in this thesis, with details pertaining to the observing conditions specific to the runs (see Table 7.1 for a description of each column).

The analysis of the UVF data set yielded 1920 On events and 312.17 Off events (1873 with $\alpha = 1/6$). The resulting gamma-ray rate was 3.00 ± 0.08 photons/min with a background rate of 0.58 ± 0.03 events/min. The resulting detection significance is 52.8σ. The average analysis energy threshold in this data set was 320 GeV. Note that the energy threshold is strongly dependent on observing conditions (both sky brightness and elevation); the run with the lowest (highest) analysis energy threshold was run 64439 (72493) with a threshold of 266 GeV (422 GeV). Note that the run with the highest energy threshold was also taken at fairly low elevation (60 degree mean elevation). The energy threshold at similar elevations but under brighter skies is 335 GeV (e.g. run 66296).

9.2.4 Spectral Reconstruction

As with the NOM and RHV analyses, an energy spectrum for the UVF Crab data set was produced and is shown in Figure 9.18; the fit values are given in Table 9.6. For the UVF data set, the curvature parameter in the curved power law fit is nearly consistent with zero and the other parameters are consistent with the power law values. This implies that the data set does not have enough statistical power to see the curvature. The NOM and UVF power law normalisations are consistent to within 2σ. The power law indexes are not statistically compatible but this is likely driven by the poor statistics at high energies.

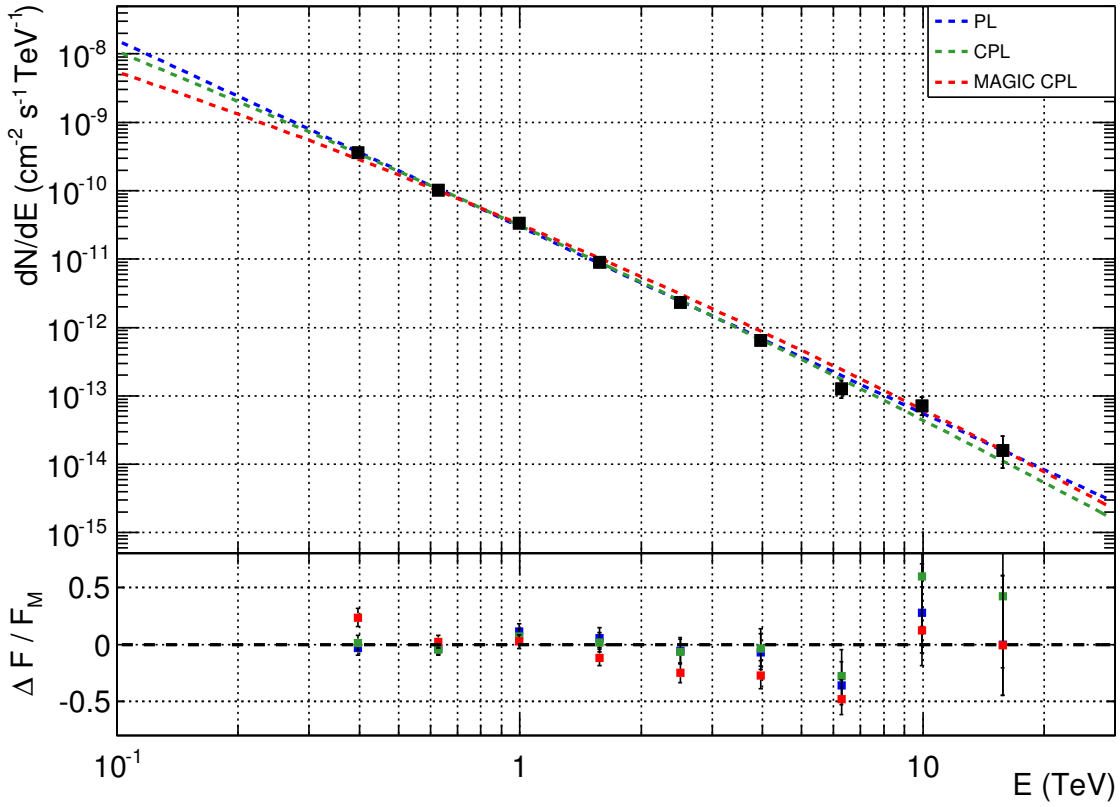

Figure 9.18: **Top**: Crab spectrum obtained from the analysis of the *VERITAS* UVF data set. **Bottom**: Fit residuals for the fit functions and a comparison spectrum. The fit values are given in Table 9.6.

It should be noted that there are a few outlying points in the UVF Crab spectrum. For this example, consider the lowest energy spectral point. In the previously presented NOM and RHV spectra, the lowest energy points were consistently higher than the *MAGIC* spectrum at the 25% level. The energy bias at those energies is small for those observing modes, so the

Fit Form	F_0	Γ	β	χ^2/NDF
PL	2.97 ± 0.09	2.72 ± 0.04	-	8.3 / 7
CPL	3.08 ± 0.12	2.70 ± 0.05	-0.14 ± 0.11	6.3 / 6
NOM PL	3.26 ± 0.10	2.53 ± 0.03	-	17.4 / 7
NOM CPL	3.51 ± 0.12	2.58 ± 0.04	-0.26 ± 0.04	5.5 / 6
MAGIC CPL	3.23 ± 0.03	2.47 ± 0.01	-0.24 ± 0.01	32.3 / 9

Table 9.6: Fit values for the Crab Nebula spectra shown in Figure 9.18. The values for the *MAGIC* curved power law are also given. The units of F_0 are 10^{-11} cm^{-2}s^{-1}TeV^{-1} and β is the curvature parameter at 1 TeV. The χ^2/NDF for the *MAGIC* CPL is the value computed with respect to the *VERITAS* data points. Note that the curvature parameter in the UVF CPL is almost consistent with zero; this is consistent with the energy range in this analysis not being large enough to see the curvature in the spectrum, which only becomes apparent for fits over several energy decades with low-uncertainty spectral points.

reasons for this are difficult to explain. However, this is not the case for UVF, which has a roughly 10% energy reconstruction bias at 400 GeV.

Assuming a power law spectrum, for a given energy bias ϵ and spectral slope Γ, it is possible to estimate the effect this has on the location of the spectral point using the following equation:

$$\frac{E_{true}}{E_{biased}} = \left(\frac{1}{1+\epsilon}\right)^{\Gamma}. \tag{9.18}$$

For a bias $\epsilon = 0.1$ (taken from Figure 9.15) and spectral slope $\Gamma = -2.72$ (taken from Table 9.6), the ratio in Equation 9.18 is ≈ 1.3. The 400 GeV energy spectral point is roughly 24% higher than the spectral fit from *MAGIC*, so to first order, the energy bias can explain some of the discrepancies between the UVF spectrum and canonical values. A similar approach can be applied to the other spectral points. This process is known as spectral unfolding, which is a nontrivial process. At the time of writing, methods of correctly accounting for the energy bias are actively under investigation.

9.2.5 Data/MC Comparisons

As with the NOM and RHV analyses, a number of data/MC comparisons have been produced to verify the validity of the UVF detector model; the figures are listed below. Recall that red corresponds to simulations and black corresponds to data.

- Mean Reduced Scaled Width and Length: Figures 9.19 and 9.20. There is a large, energy dependent shift in the mean scaled width distribution. The reasons for this are unknown and difficult to trace. This is not an artefact isolated to the UVF simulations;

current versions of the NOM detector model (newer than the NOM detector model used in this thesis) also show signs of this feature which is actively under investigation.

The shift is towards larger values; this means that showers look wider than they do in simulations. To account for this, in the analysis of the Crab Nebula data, a wider cut on the mean scaled width was used so that gamma rays, particularly those at higher energies, would not be removed by the analysis.

- Single-telescope Image Width and Length: Figures 9.21 and 9.22
- Image Size: Figure 9.23
- Single-telescope Image Length-over-size: Figure 9.24
- Number of Tubes in Image: Figure 9.25
- Number of Low-gain Tubes in Image: Figure 9.26
- Shower Emission Height: Figure 9.27

9.3 Additional Discussion

During the development of this work, it was discussed at length whether or not dedicated simulations for UVF instrument response functions were required. The primary use of simulations in the analysis is to determine the energy of the gamma-ray primary. Conceptually, for similar zenith angles and azimuths, the cosmic ray showers seen by the experiment with and without UV filters are exactly the same. In the case of two identical cosmic ray events (one observed using the filters, one without), the only difference is the amount of light reaching the PMT due to attenuation in the filters. Since it is impossible to identify two identical showers in the data, one can use the size distribution of cosmic rays to directly measure the throughput of the filters. Thus, it may be possible to correct the energy scale of the showers, at least for larger showers where triggering is not an issue. This method experimentally calibrates the UVF data with observables rather than relying on simulations.

Even with this correction to the energy scale, however, there are still issues with the analysis. For example, the effective areas would still be wrong, especially at the low energy end (near the trigger threshold) of any spectrum. Herein lies a challenge with VHE gamma-ray astronomy. There is only one standard candle (the Crab) and the results correcting the effective areas by "training" an analysis such that it reproduces the Crab would be unverifiable since there is no other steady source to compare with. There are other sources

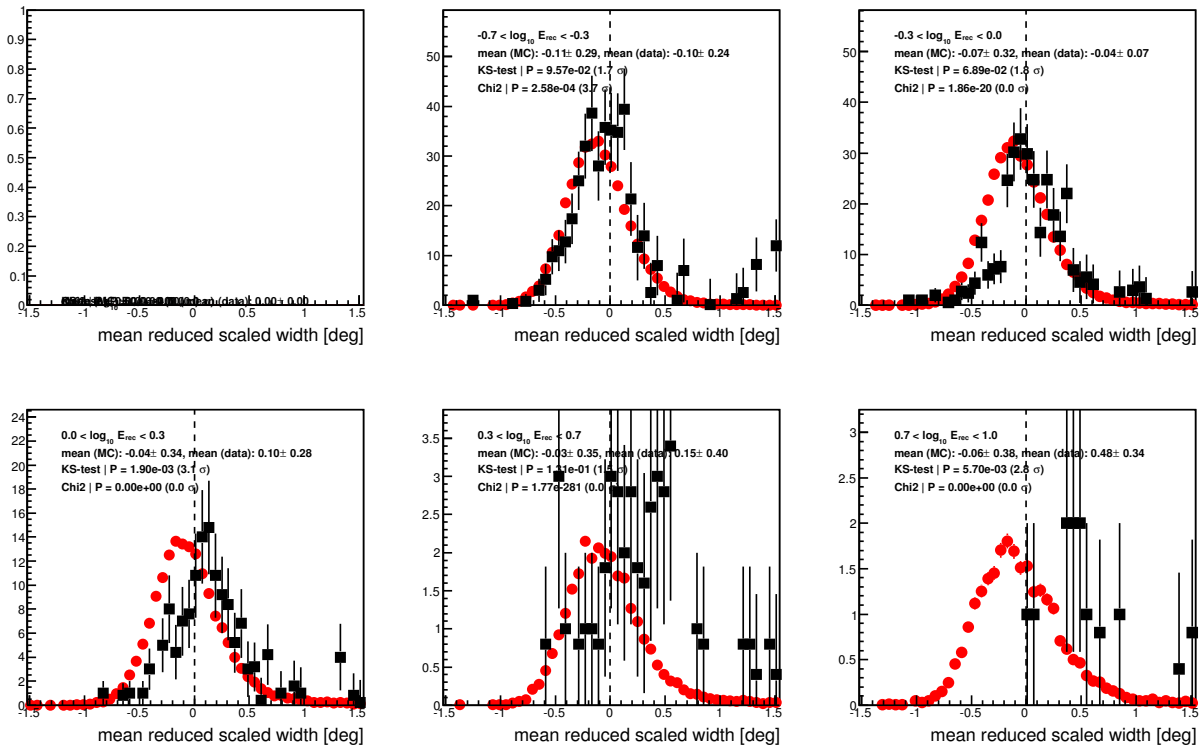

Figure 9.19: UVF mean reduced scaled width data/MC comparison. The first plot is empty since the energy range is below the energy threshold of the UVF analysis. It has been included so that this plot is consistent with the corresponding plots in the NOM and RHV sections. There is a large, energy dependent shift in the mean scaled width distribution. The shift is difficult to quantify due to poor statistics but is most pronounced above 1 TeV. Data are given in black and simulations are given in red.

which undergo massive flaring (e.g. *Markarian 421*, an extragalactic source) but their flux *and* spectral shape is typically highly variable [131, 132, 133], so it would be difficult to determine if the reconstructed flux using modified effective areas would be correct. A source under consideration is the supernova remnant *Cassiopeia A*, which has a relatively hard spectral index ($\Gamma = 2.62 \pm 0.24_{\text{stat}} \pm 0.2_{\text{sys}}$), but is very weak (3% of the Crab nebula flux above 200 GeV), and thus would require extensive observations to detect with enough significance to perform any sort of investigation of spectral correction factors.

9.4 Summary

To produce this chapter, the optical effects of the filters have been studied at length in order to correctly produce values for the UVF detector model. Based on this, a 15% reduction in

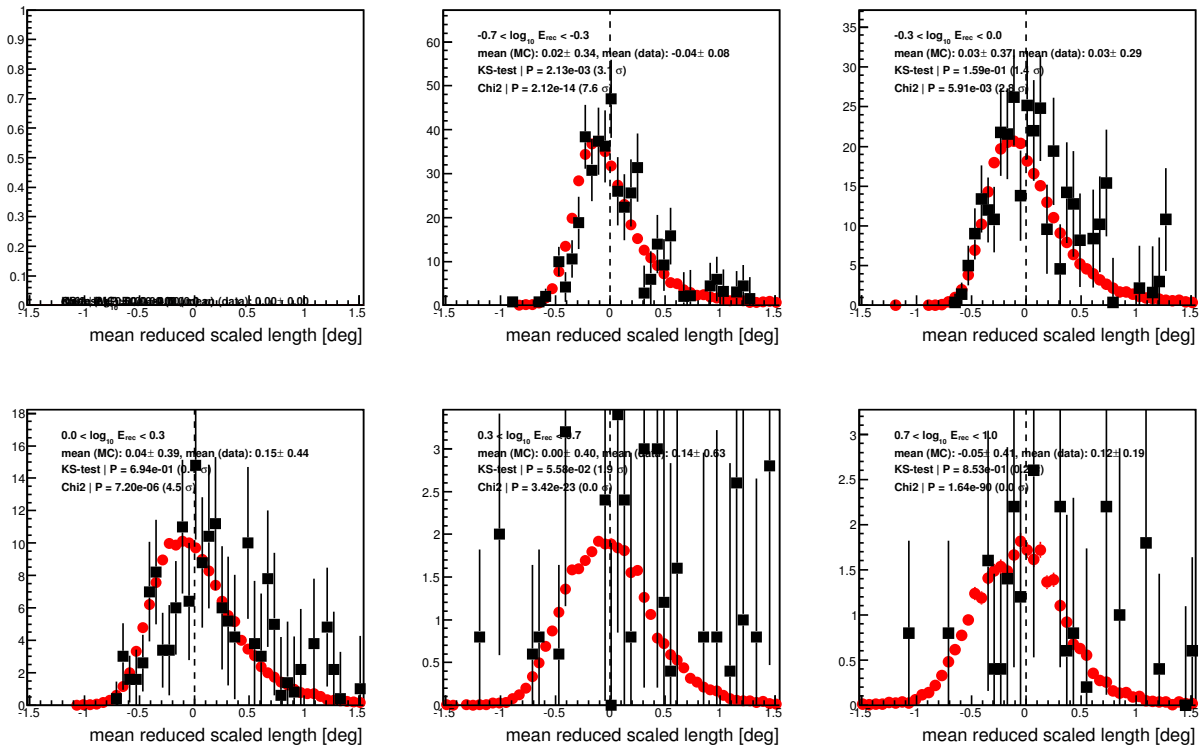

Figure 9.20: UVF mean reduced scaled length data/MC comparison, binned in energy. The MSCL distributions appear to agree well, but this data set is again limited by low statistics. Data are given in black and simulations are given in red.

the camera light yield was introduced into the UVF detector model, which made it possible to reconstruct the Crab Nebula spectrum to within standard systematic errors. UVF data has been shown to be significantly less sensitive than the NOM and RHV modes, but is still the only observing mode that allows for observing under the brightest skies. There is a significant energy bias below $\sim$ 500 GeV that must be understood for future analyses; the reasons for this are not yet clear. Despite the decreased sensitivity and increased energy threshold the additional observing time gained can benefit a number of science goals which are described in the next chapter.

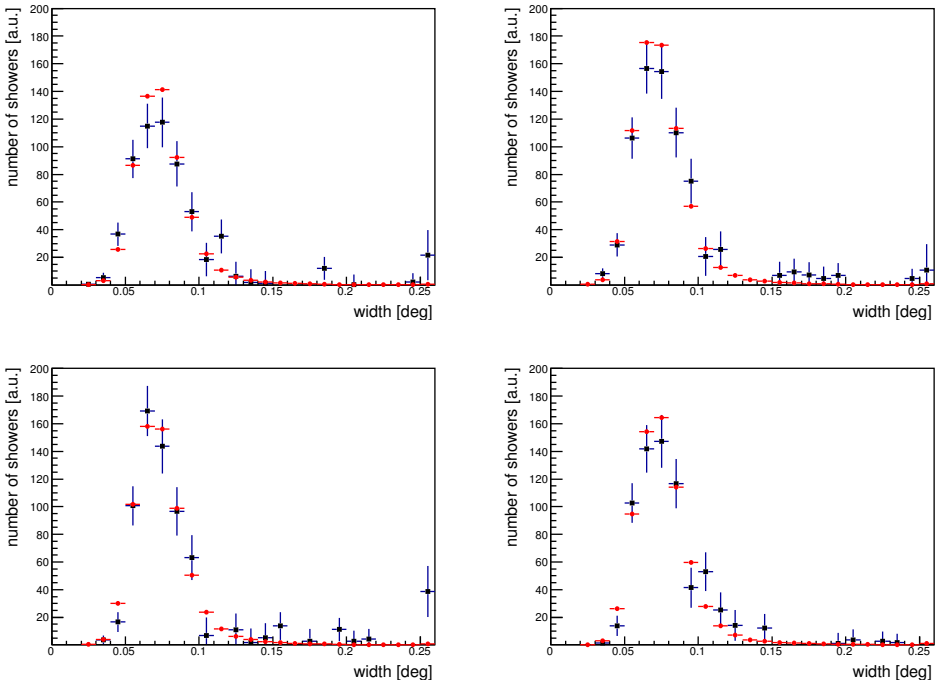

Figure 9.21: UVF configuration single telescope image width distributions. Data are given in black and simulations are given in red.

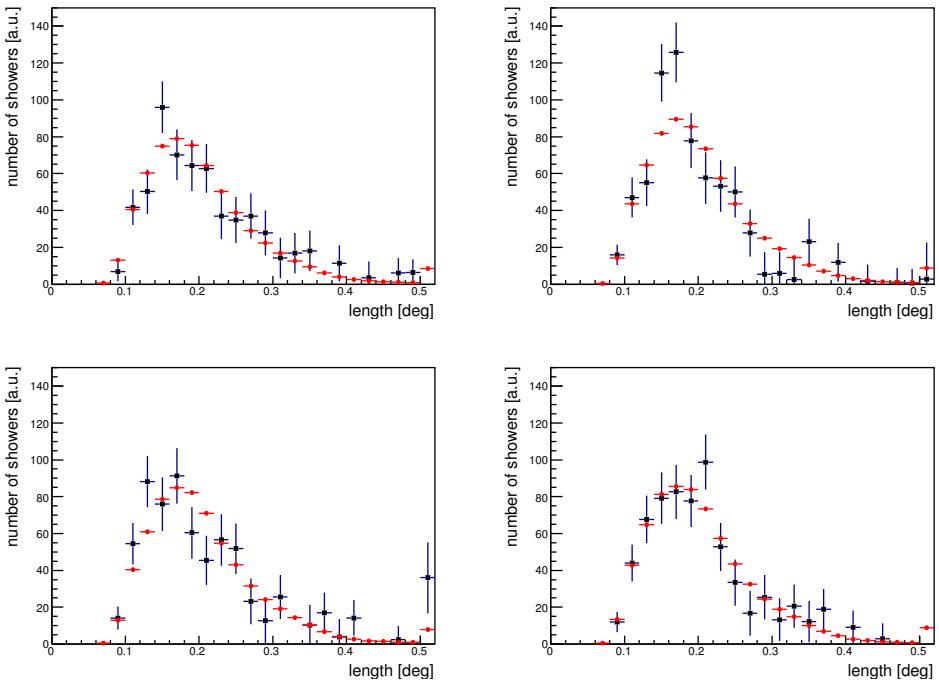

Figure 9.22: UVF configuration single telescope image length distributions. Data are given in black and simulations are given in red.

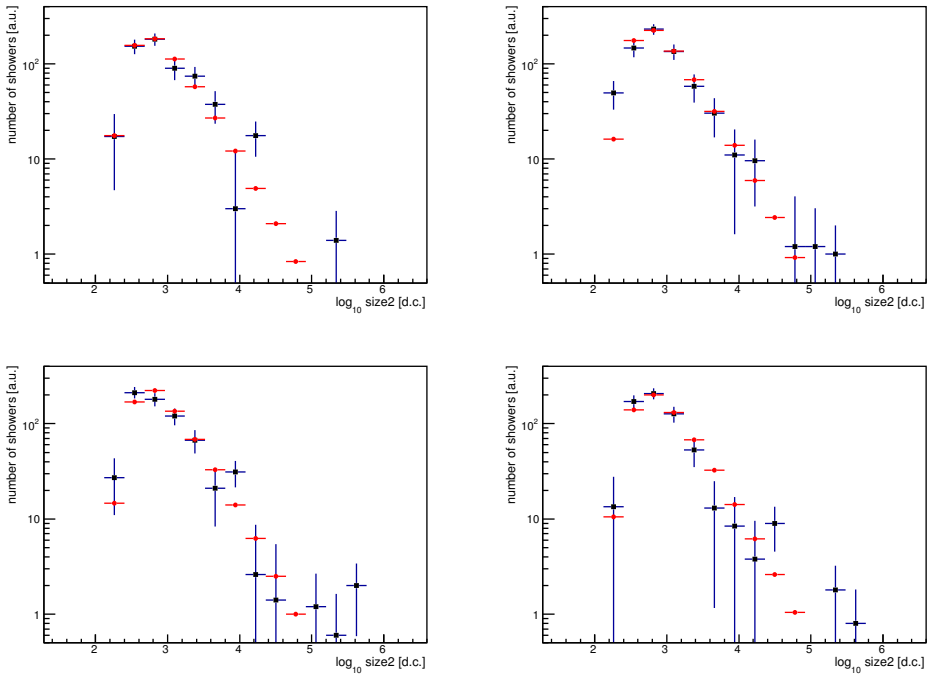

Figure 9.23: UVF configuration single telescope size distributions. Data are given in black and simulations are given in red.

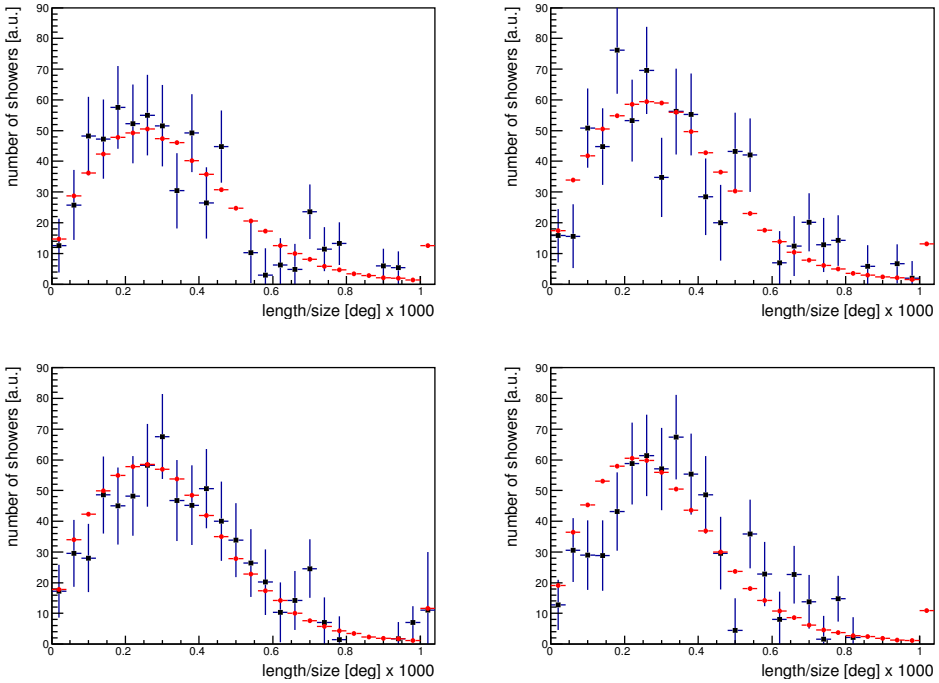

Figure 9.24: UVF configuration single telescope length-over-size distributions. Data are given in black and simulations are given in red.

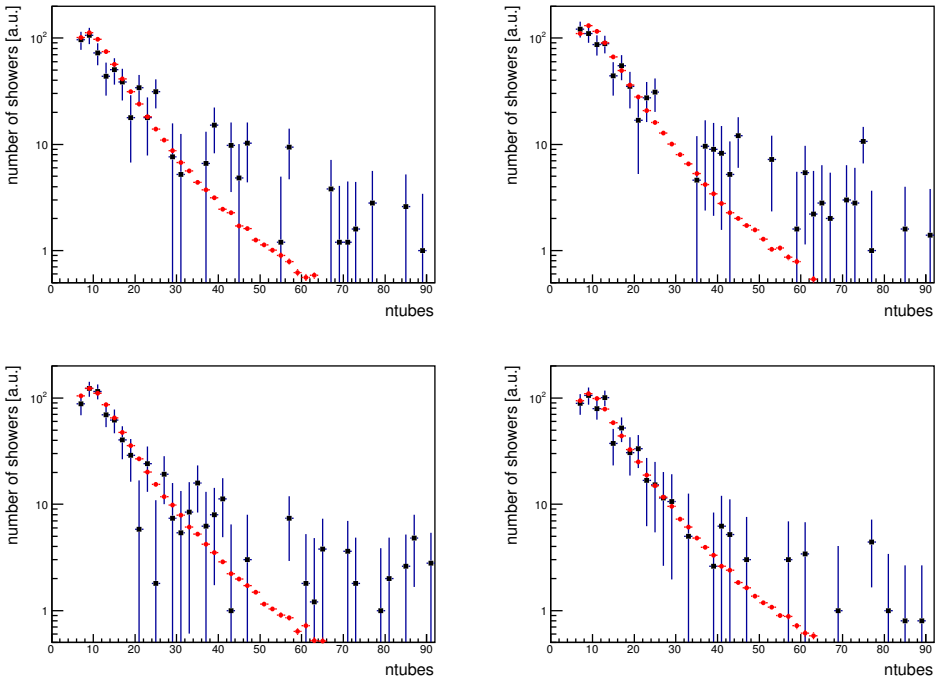

Figure 9.25: UVF configuration single telescope distributions of number of PMTs in an image. Data are given in black and simulations are given in red.

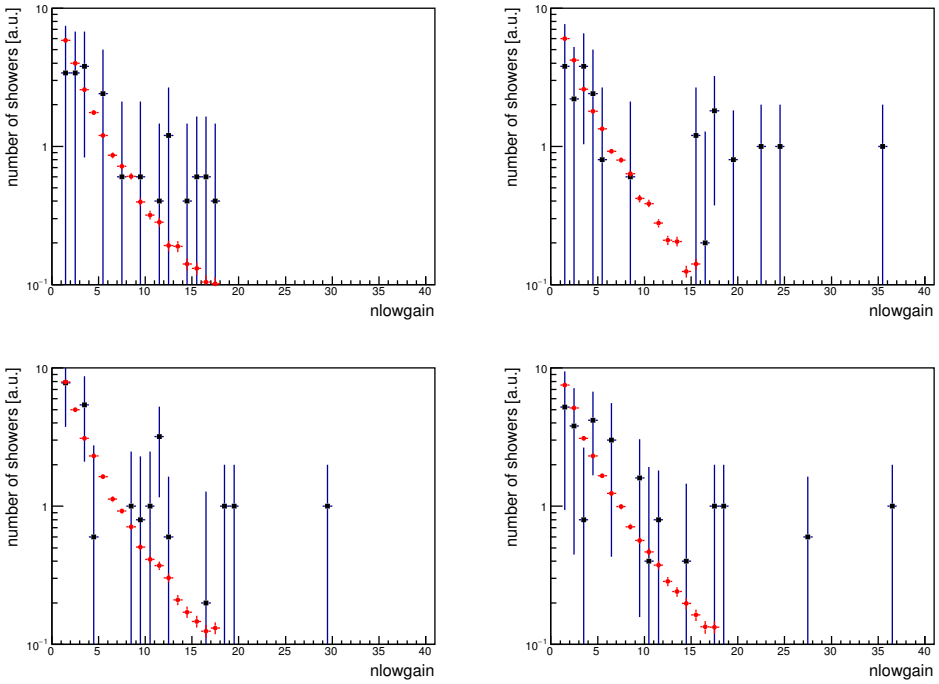

Figure 9.26: UVF configuration single telescope distributions of number of channels in an image that are in low-gain mode. Again, there are substantially fewer low gain PMTs in UVF data due to the fact that there is much less light reaching the PMT face than for standard configuration data. Data are given in black and simulations are given in red.

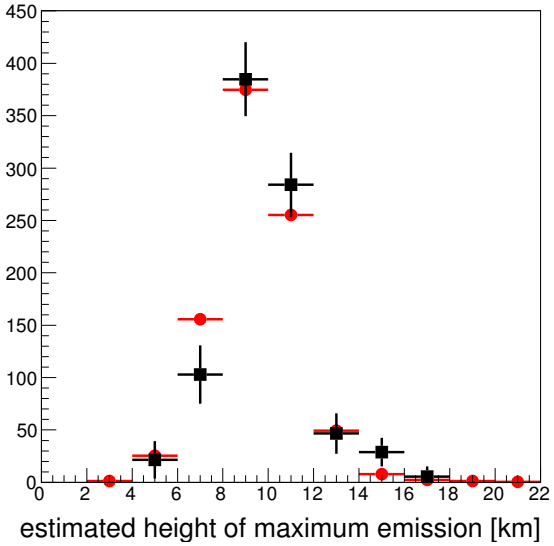

Figure 9.27: UVF configuration reconstructed maximum shower emission height. Data are given in black and simulations are given in red.

Chapter 10

Science Applications

"But the reason I call myself by my childhood name is to remind myself that a scientist must also be absolutely like a child. If he sees a thing, he must say that he sees it, whether it was what he thought he was going to see or not. See first, think later, then test. But always see first. Otherwise you will only see what you were expecting."

Douglas Adams, *So Long, and Thanks for All the Fish*

10.1 Motivation

Arguably the most important reason for bright moonlight observations is the question of observing time. Additional observing time allows for deeper exposures and also increases the ability of the experiment to observe transient events. In fact, due entirely to the Bright Moonlight Program, *VERITAS* was able to detect large-scale variability (*i.e.* a flare) from a known extragalactic source (the details of this are given in Section 10.4). This was the first detection of variability from the source, and it is important to note that this flare would have gone undetected had the observatory not been operating under moonlight. The following is a subset of the various motivations for increasing the livetime of the experiment by pursuing observations under bright moonlight.

10.1.1 Observations of Sources with Hard Spectra

Over the energy range relevant to VHE astronomy, the vast majority of VHE sources have energy spectra that obey a power law:

$$F(E) = F_0 \left(\frac{E}{E_0}\right)^{-\Gamma}. \tag{10.1}$$

The naming convention for the spectral characteristics of VHE sources is such that a *soft* source has a large spectral index Γ (resulting from steeply falling spectrum), and a *hard* source has a small spectral index (resulting from a flatter spectral shape). Note that this is completely different from *weak* and *strong* sources, where the adjective describes the overall normalisation of the spectrum and not its shape. Thus, it is possible to have hard, weak emission (such as that from starburst galaxy *M82* which has a spectral index of $2.5 \pm 0.6_{\text{stat}} \pm 0.2_{\text{sys}}$ and a steady-state flux of $\sim 0.9\%$ Crab above 700 GeV [134]), or soft, strong emission (like the extragalactic source *PG 1553+113* which has a spectral index $4.33 \pm 0.09_{\text{stat}}$ and has been reported to flare at the $\sim 18\%$ Crab level [135]), or any other combination.

There are a number of science goals for which the increased energy threshold intrinsic to observing under bright moonlight does not hamper the potential science goals of the observing program. For example, observations of Pulsar Wind Nebulae (PWNe). A PWN is a nebula whose emission is being driven by the emission from the pulsar left over from a supernova. Note that they are distinct from supernova remnants (SNR), which also form from supernovae (and are known to be VHE emitters) and that it is possible for a PWN to be found inside a SNR [136]; these are known as composite SNR.

PWNe are well-known VHE emitters; there is evidence that the majority of unidentified[1] VHE sources are probably PWNe; [137] demonstrated that pulsars with a large spin-down power ($\dot{E}$) tend to have TeV signals within $\lesssim 0.5^\circ$ of their positions. It is unknown if the emission from PWNe is leptonic or hadronic in nature, unlike supernova remnants, for which the gamma-ray emission is thought to be hadronic, due to π^0 decay [138]. Understanding this would provide insight into the sources of high energy cosmic rays, which cannot be directly traced back to their emitters due to the presence of magnetic fields within the galaxy which causes the trajectories of charged particles to curve.

PWNe make good moonlight targets because they have hard spectra typically extending from GeV energies [139] to the VHE regime [140]; most PWNe have spectral indices between 2.0 and 2.5. Deeper exposures and better statistics at high energies on a large population would allow for studies of the VHE emission models to be made; small uncertainties on the spectral points allow constraints on leptonic and hadronic models to be made; there is too much degeneracy between models if the uncertainties are large.

[1] That is, VHE sources without a counterpart at other wavelengths.

10.1.2 Observations of Periodic Sources

There exists a class of VHE emitters known as binaries which are a made up of a compact object (a neutron star or a black hole) and a companion star which loses mass to an accretion disk around the compact object. These objects are of particular interest because of their orbital properties. Binaries have been detected to have periodic variability, which provides a unique laboratory for studying VHE emission.

The first binary to be detected at VHE energies was *LS I +61° 303* (henceforth *LS I*) [141], which consists of a massive star surrounded by a dense circumstellar disk and a compact object (a neutron star or a black hole). *LS I* shows variability across a number of wavelengths, showing variability correlated with both its orbital period of 26.5 days and a superorbital period of 1667 days [142, 143, 144]. Note that the orbital period is close to the period of the lunar cycle. It follows that the observing campaigns of this object are limited by moonlight (*i.e.* exposures are typically made at roughly the same orbital phases).

The ability to follow the object through a full orbit allows for different emission scenarios to be studied, such as when the compact object is at periastron and moving through the star's circumstellar disk. Binaries such as *LS I* have been shown to have spectral variability as a function of orbital phase [145].

As is always the case, the ability to observe under moonlight means that observations can take place in the event that an object is flaring. Indeed, *LS I* flared at the 25% Crab level (above 300 GeV) in 2014 [146]. Furthermore, the relatively hard spectrum ($\Gamma = 2.40 \pm 0.16_{\text{stat}} \pm 0.2_{\text{sys}}$ [147]) of *LS I* makes it a good target for the bright moonlight observing modes. Other binaries detected at VHE energies also have hard spectra [148], making them good candidates for observations for the same reason.

10.1.3 Multiwavelength Campaigns

Increased observing time also benefits multiwavelength campaigns. Many instruments operating at other wavelengths, in particular space-based instruments, are hugely oversubscribed (e.g. the Hubble Space Telescope is oversubscribed by a factor of 9). Thus, observation times are typically very tightly constrained and the scheduling of simultaneous observations is made difficult. Increasing the amount of time *VERITAS* can spend observing both increases the potential for simultaneous multiwavelength observations, which are required in the era of deep exposures where strong constraints on emission models are desired, and simplifies the scheduling of multiwavelength campaigns.

10.2 Active Galactic Nuclei

10.2.1 Description

When the compact region at the centre of a galaxy has an above-average luminosity it is known as an Active Galactic Nucleus (AGN). The radiation and particle outflow from AGNs is believed to be due to the accretion of matter onto a supermassive black hole with a mass between 10^4 and 10^{10} $M_\odot$ at the centre of the galaxy. Accretion can produce jets (see Figures 10.1 to 10.3) of highly collimated, relativistic outflows where the direction of the jet emission is along the black hole's spin axis, perpendicular to the plane of the accretion disk.

The Third *Fermi* AGN Catalogue (3LAC) [34] is the most recent (at time of writing) catalogue of AGNs detected by the *Fermi*-LAT. It is based on the first 4 years of *Fermi* data and contains 1591 AGNs detected at Galactic latitudes $|b| > 10°$, a 71% increase from the Second *Fermi* AGN Catalogue (2LAC) [149]. AGN make up a large percentage of all known VHE emitters to date (59/156 at the time of writing [4]).

10.2.2 Blazars

Blazars, which will be the general focus of this chapter, are generally accepted to be the geometrically selected type of AGN where the object is being viewed directly along the axis of the AGN jet. They are divided into two classes: Flat Spectrum Radio Quasars (FSRQs) and BL Lacertae (BL Lac) objects (named after the prototype object BL Lacertae). They are differentiated by the respective presence or absence of strong emission lines in their UV/optical spectrum [150]. Examples of the spectral lines (and lack thereof) are given in Figure 10.4 and Figure 10.5, respectively. Due to the lack of strong spectral lines, it is difficult to spectroscopically measure the redshifts of BL Lacs; the redshift can be determined if weak emission lines from the AGN or absorption lines from the host galaxy are present. On average, FSRQs are more luminous and more distant than BL Lac objects (see [151] and Figure 10.6).

For both classes, the energy spectrum, also called the spectral energy distribution (SED), is a continuum of emission from radio to gamma rays, with two well-defined peaks at IR-to-X-rays and MeV-to-TeV energies. FSRQs are characterised by a lower frequency of the first peak. BL Lac objects have a number of peak frequencies and are divided into subclasses: low-frequency-peaked BL Lacs (LBL), which have their peak in the IR, high-frequency-peaked (HBL), which have their peak at frequencies in UV and above, and some are referred to as intermediate-frequency-peaked (IBL) which have their peak in UV/optical. For more details on the classification scheme, see [154]. A cartoon of the SED for HBLs and LBLs is shown in Figure 10.7.

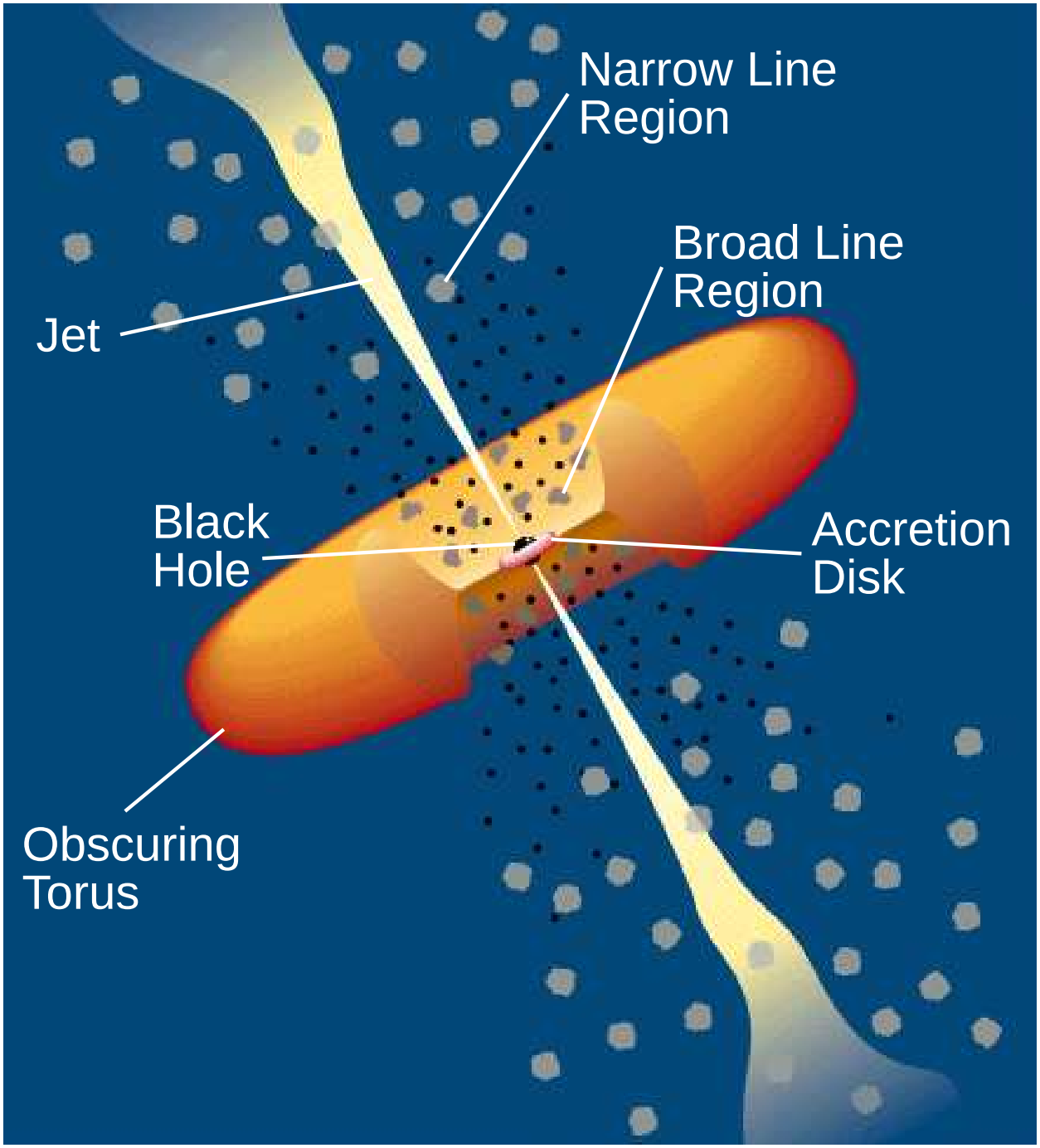

Figure 10.1: Cartoon of an AGN with the various components indicated. The broad (narrow) line region refers to an area in the AGN where broad (narrow) emission lines are seen, corresponding to the presence of high (low) velocity gas near (far from) the AGN. The obscuring torus is made up of gas and dust which obscures emission from the accretion disk. Image credit: C. M. Urry and P. Padovani.

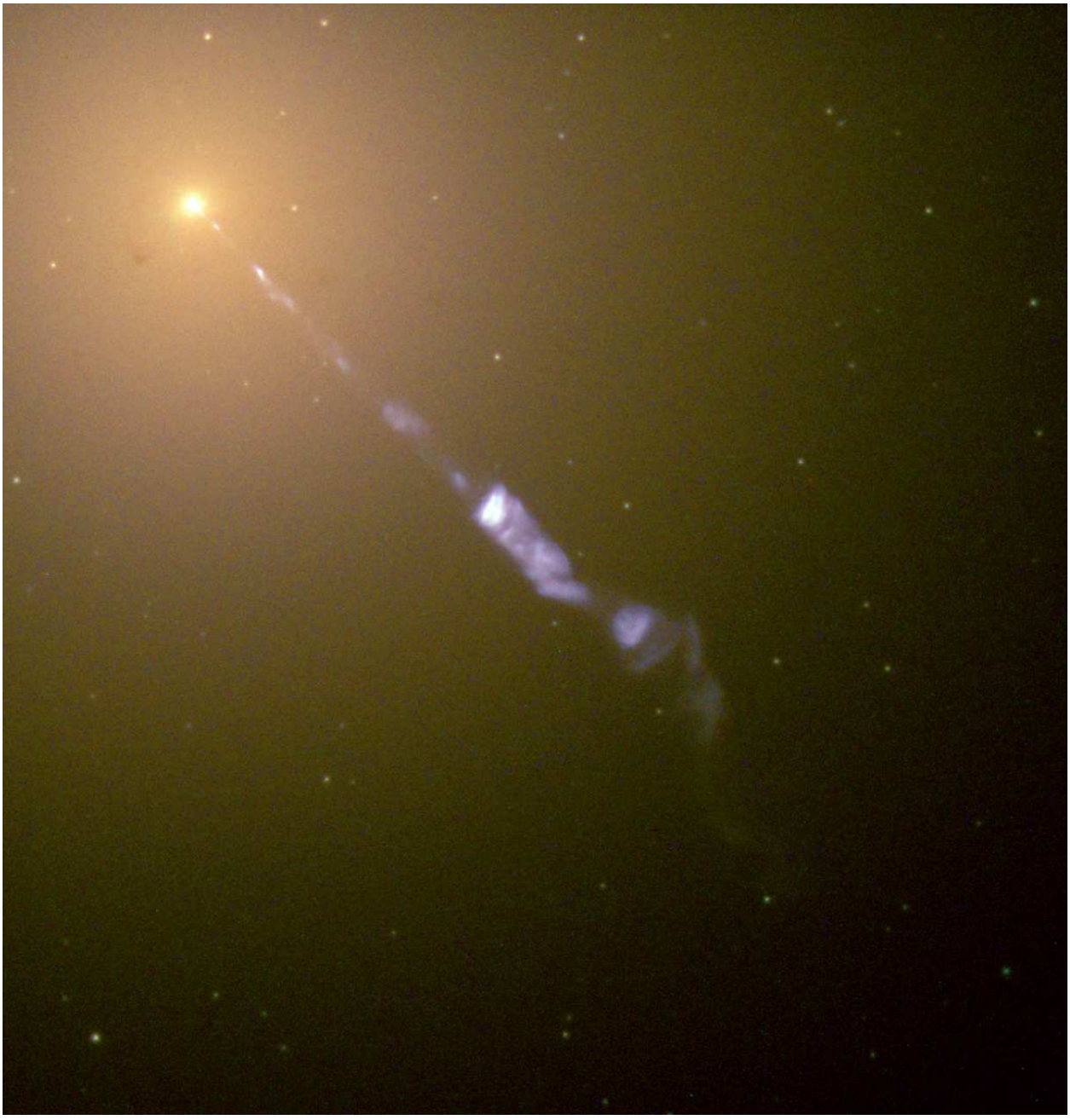

Figure 10.2: Jet from the active galaxy M87. The jet in this image is 5000 light years long. Image credit: "M87 jet" by NASA and The Hubble Heritage Team (STScI/AURA). Licensed under Public Domain via Wikimedia Commons.

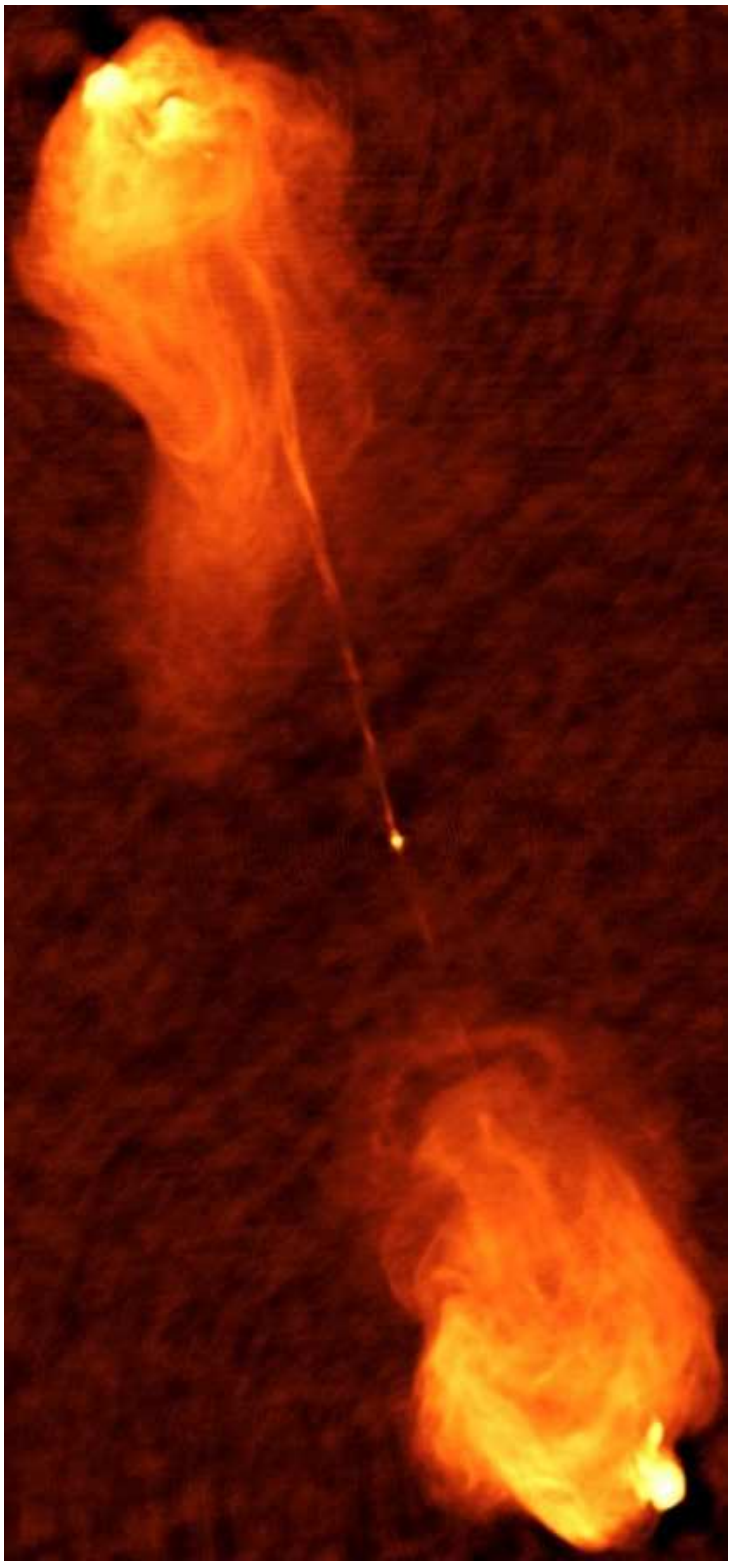

Figure 10.3: The radio source Cygnus A seen at radio wavelengths. Twin jets (originating from an AGN) are visible, with giant radio "lobes" at either end. Image credit: NRAO.

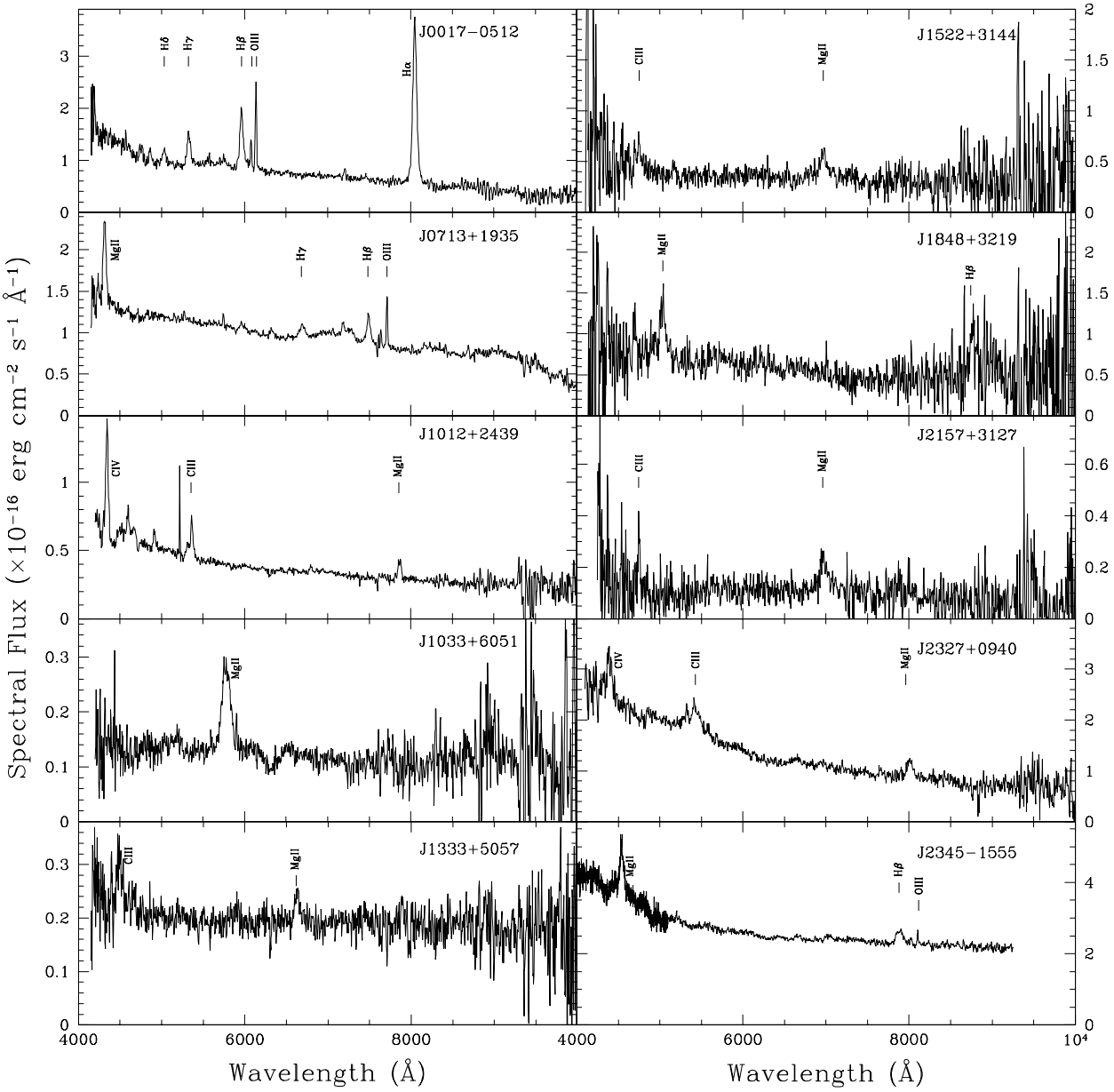

Figure 10.4: Spectra of various FSRQ objects. The different emission lines are indicated. Image credit: Figure 1 in [152].

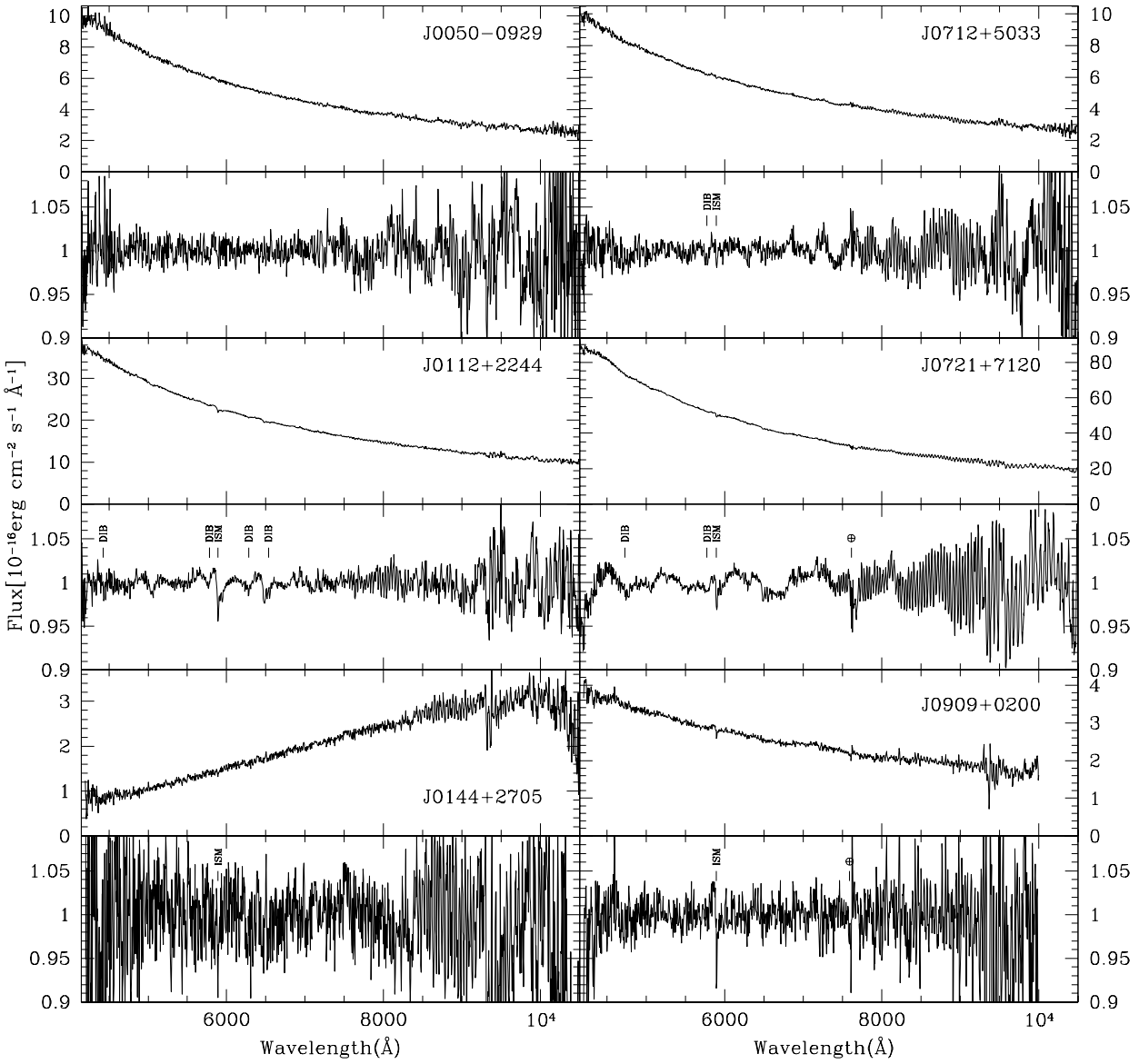

Figure 10.5: Spectra of various BL Lac objects. Each object has a pair of plots: the top panels are the spectra and the bottom panels are normalized by removing the continuum emission. Image credit: Figure 3 in [152].

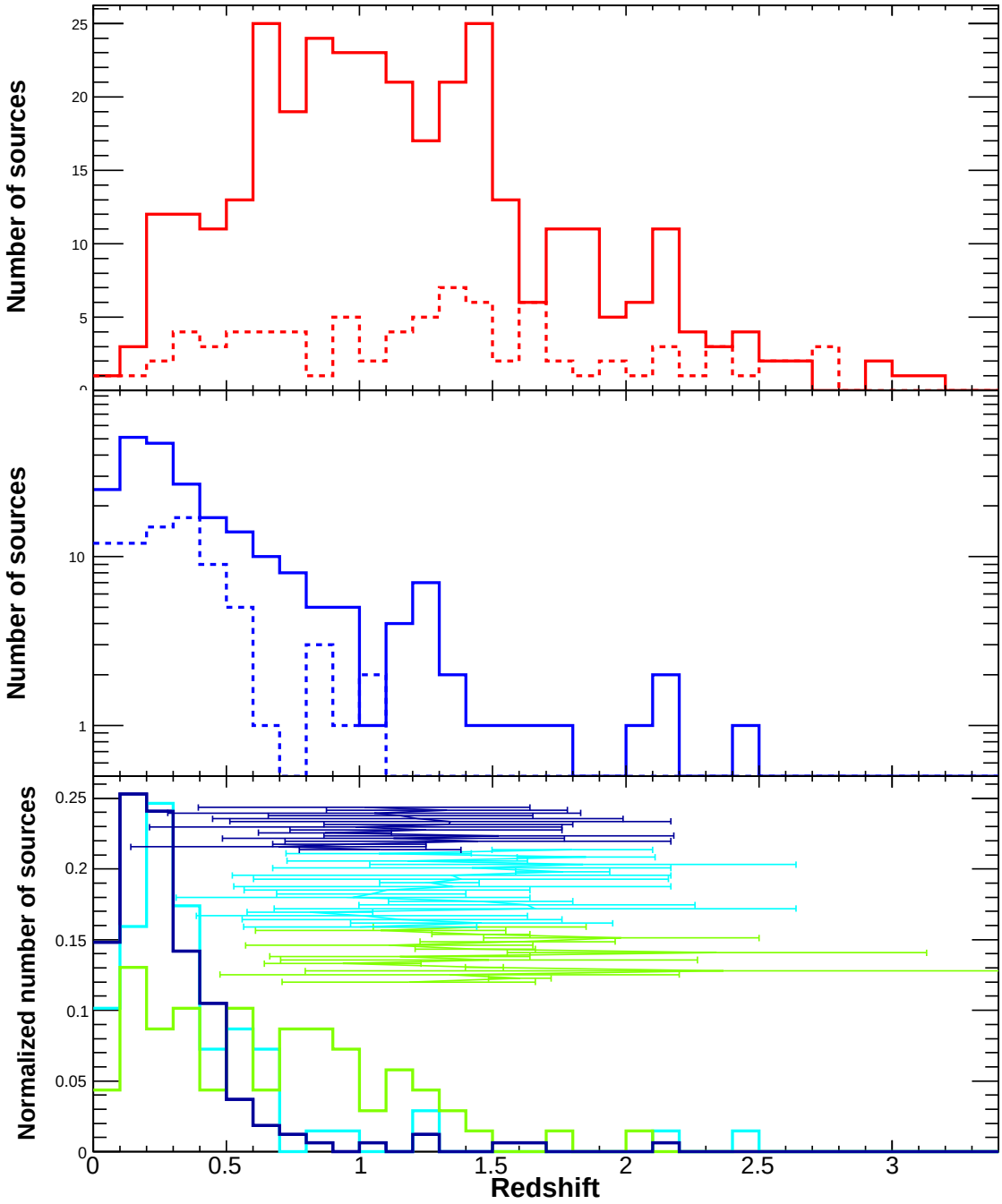

Figure 10.6: Redshift distributions (solid: 2LAC sources; dashed: new 3LAC sources). **Top**: FSRQs. **Middle**: BL Lacs. **Bottom**: Different classes of BL Lac, LSPs (green), ISPs (light blue), HSPs (dark blue). The redshift ranges for the 57 BL Lacs having upper and lower limits are also shown. Note that 50% of the BL Lacs in the 3LAC do not have measured redshifts. Image credit: Figure 12 in [153].

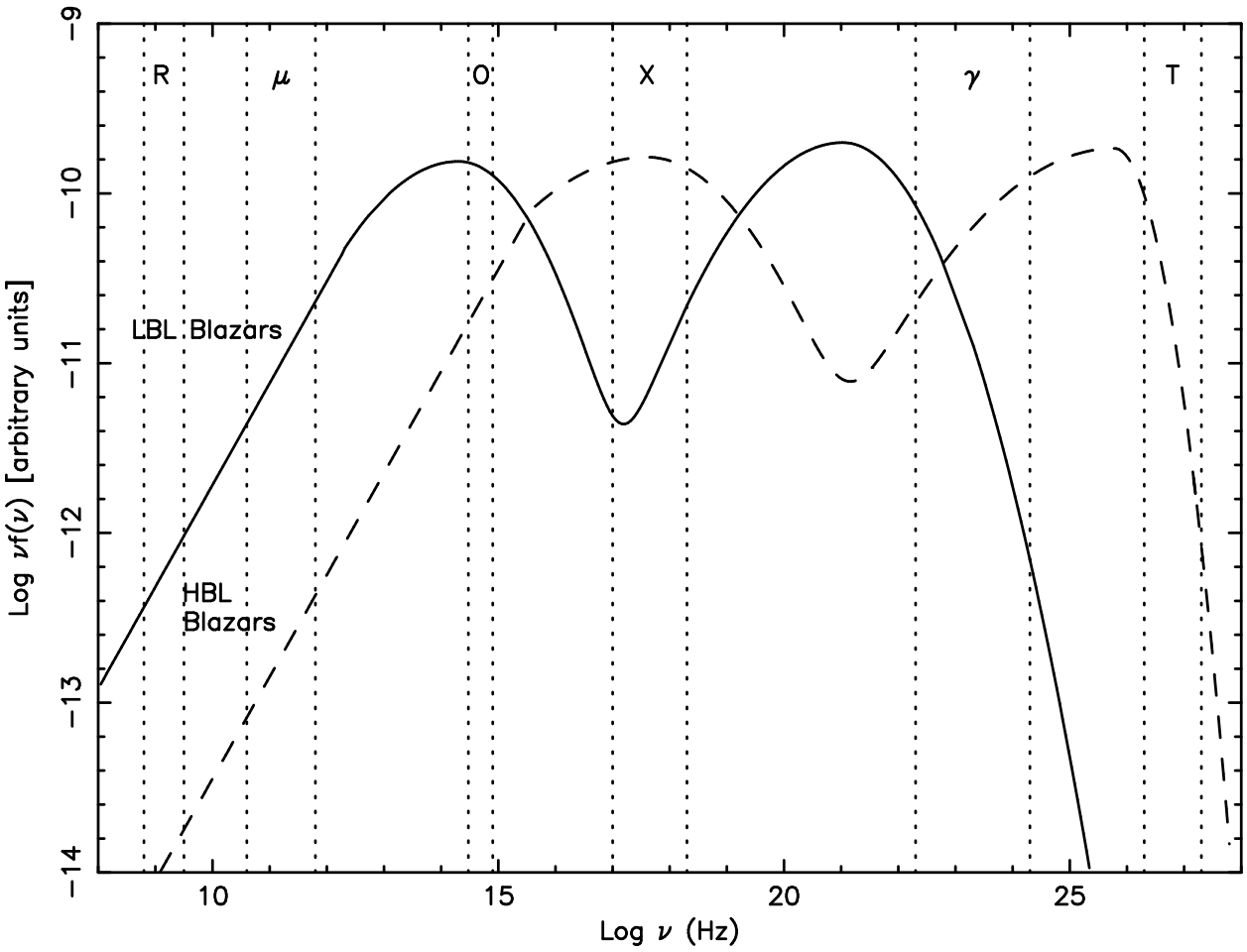

Figure 10.7: Cartoon SED for LBL and HBL objects from radio to gamma ray frequencies. The quantity on the vertical axis is the logarithm of the flux multiplied by the frequency; this has the effect of removing the steep falloff with energy. Image credit: Figure 1 in [155]

BL Lac objects are known to be variable across the entire electromagnetic spectrum. For example, in [156], BL Lacertae was shown to be variable in radio, optical, UV, X-rays, MeV gamma rays and VHE gamma rays (Figure 10.8), with structure in the VHE light curve seen with 4-minute time bins (Figure 10.9). Other blazars are known to undergo periods of massive flaring, such as *Markarian 421* (abbreviated as *Mrk 421*) which currently holds the record for the brightest VHE flare observed to date, at ~ 11 Crab [157]. *Mrk 421* was the second-ever detected VHE gamma-ray source [158] (and the first extragalactic source) detected using the imaging atmospheric Cherenkov technique[2].

[2]An interesting anecdote on the subject of *Mrk 421* is that it is believed that the original detection of *Mrk 421* occurred during an excited state; the story goes that the source was detected one year by the *Whipple* collaboration and then the following year when observations were made of the object but it was no longer detected at VHE energies, they thought that they may have broken the detector, since so little was known about these objects at higher energies.

Variability on such short timescales is interesting as it offers a window into the size of the emission region and allows for a greater understanding of the underlying physics taking place in the object. It is possible to constrain the size of the emitting region via causality arguments. If the emission region is a spherical blob of radius R moving along the jet towards the observer with a Doppler factor δ, then for a variability timescale τ, and redshift z, the size of the emitting region is constrained by [159]

$$R \leq \delta \frac{c\tau}{1+z}. \tag{10.2}$$

10.2.3 VHE Emission Models

In this section, some of the different emission models for blazars are presented. For an in-depth review, see [160]. It is generally accepted that the low-frequency (radio through UV/X-ray) emission in the blazar jet is synchrotron emission from ultra-relativistic electrons[3] moving along the jet. However, the source of the higher energy emission is still uncertain. There are two types of models which assume a different underlying population of accelerated particles responsible for the emission.

10.2.3.1 Leptonic

In leptonic emission models, it is assumed that the radiation output over the entire electromagnetic spectrum is dominated by electrons and positrons with the high-energy component being due to inverse-Compton scattering of the electrons in the AGN's jet with ambient photons. In such models, it is assumed that any protons present in the jet are not sufficiently energetic to significantly contribute to the radiative output. The main idea is that electrons in the jet will produce synchrotron radiation due to interactions with the jet's magnetic field, and some of those synchrotron photons will be up-scattered to gamma-ray energies through inverse-Compton scattering. Thus, it is inverse-Compton scattering of synchrotron photons off the same population of electrons which produced them. This is known as the Synchrotron Self Compton (SSC) model.

Alternatively, the ambient photons could be external, such as the Cosmic Microwave Background or radiation directly from the blazar's accretion disk [e.g. 161]. This is known as an External-Inverse-Compton (EC) model.

[3] "Electrons" meaning electrons and positrons.

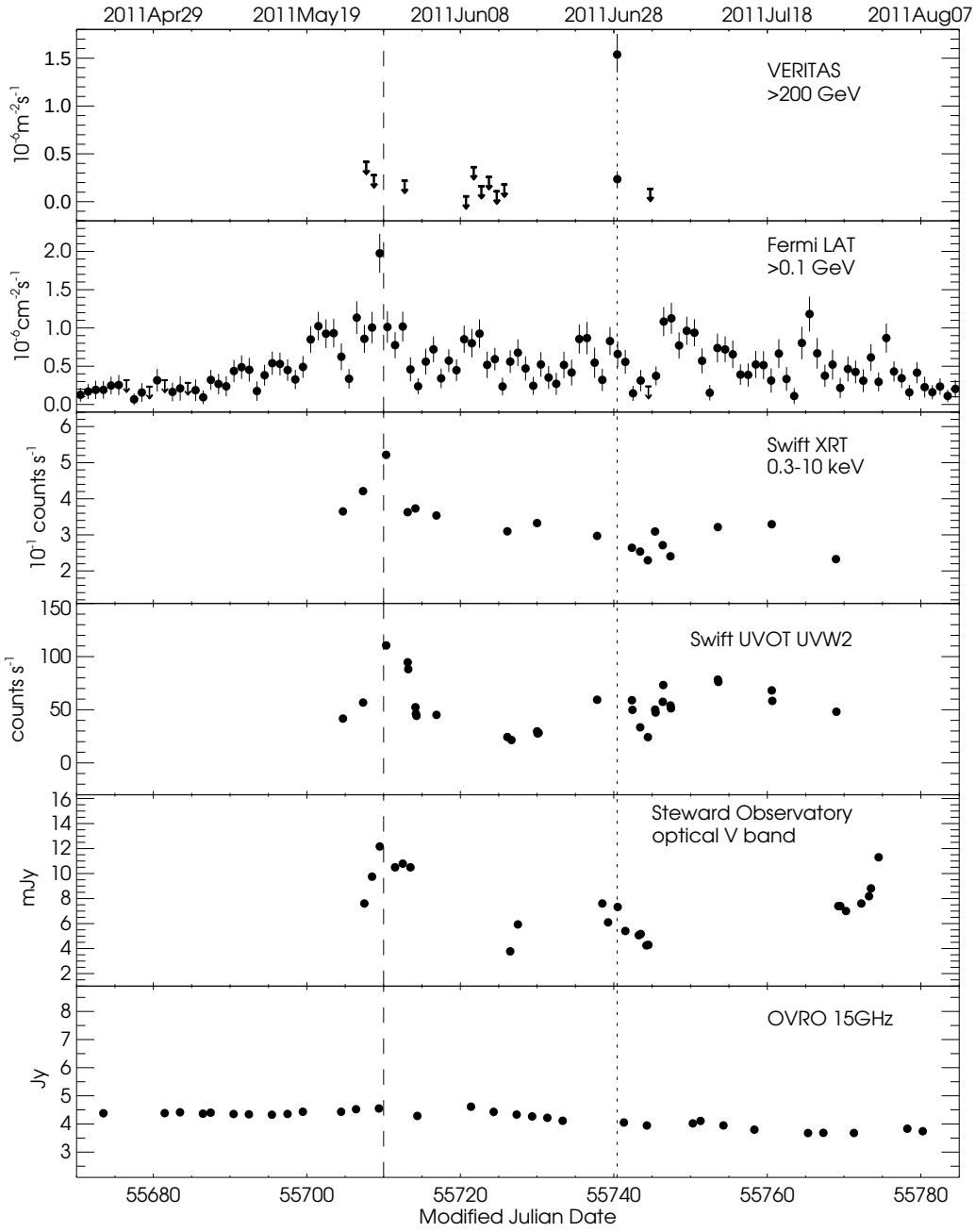

Figure 10.8: Multiwavelength light curves (*i.e.* flux versus time) of BL Lacertae. The dashed line corresponds to a flare seen at *Fermi*-LAT energies, and the dotted line corresponds to a flare detected by *VERITAS*. Variability can be seen across multiple wavelengths, but is not necessarily correlated. Image credit: Figure 4 in [156].

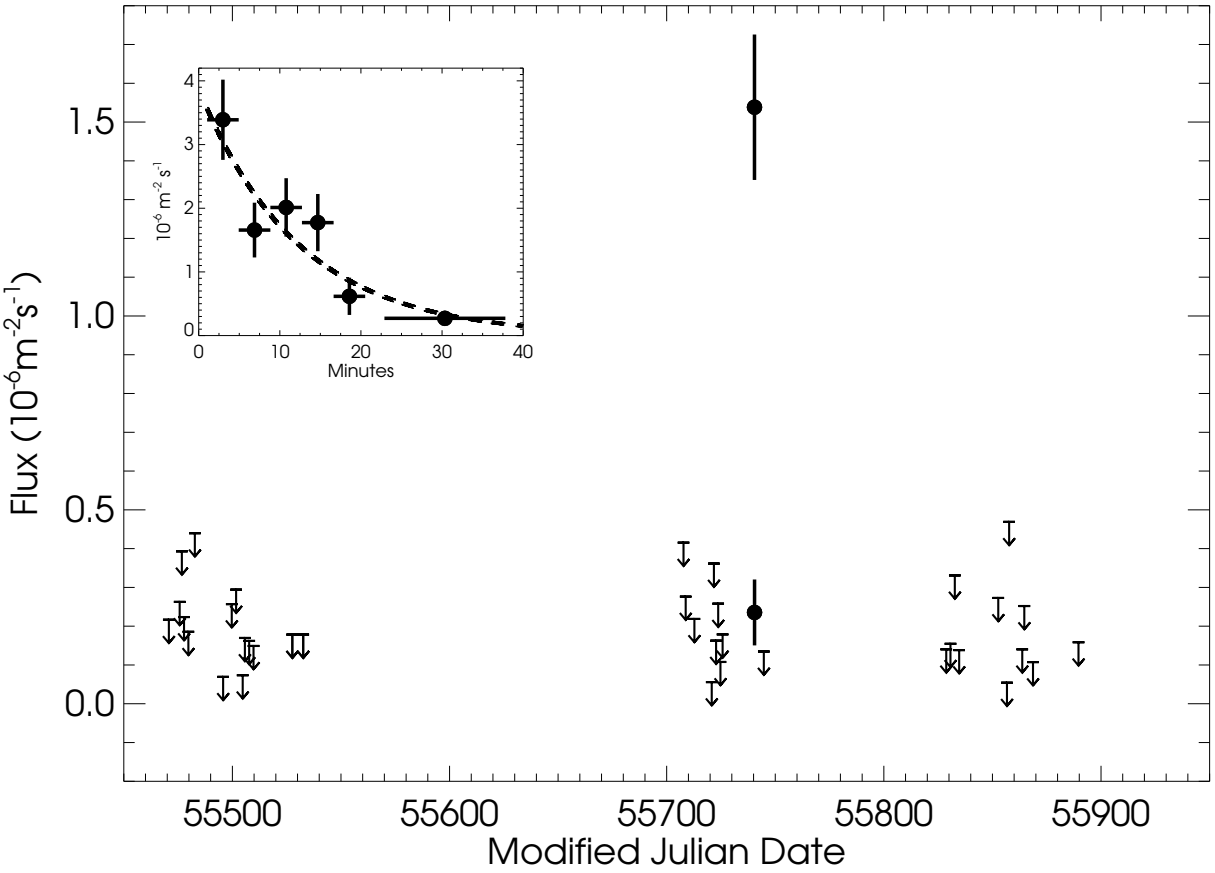

Figure 10.9: Gamma-ray light curve of BL Lacertae for E > 200 GeV. The upper limits are at the 99% confidence level. The insert shows the details of the flare in 4-minute bins for the first data run and a single 16-minute bin for the second. The dashed line is the best fit for an exponential decay. Image credit: Figure 1 in [156].

10.2.3.2 Hadronic

In hadronic models, synchrotron emission from electrons is still primarily responsible for the low-energy peak in the SED. However, to explain the high energy peak it is assumed that both primary electrons and protons are accelerated to ultrarelativistic energies. In order for protons to contribute significantly to the radiative output (via proton synchrotron radiation), the proton energies must be $\geq 10^{19}$ eV and there must be present a large magnetic field ($B \sim 30 - 100$ Gauss) [162].

The high-energy emission is typically modelled by a combination of proton synchrotron, π^0 decay, and emission from the decay products of charged pions [163]; the pions mentioned here are produced in high-energy interactions between protons and the ambient material (e.g. $p + \gamma$ interactions). Due to the complex nature of the interactions and energy-dependent interaction cross sections (see Figure 10.10) hadronic modelling is much more difficult than

leptonic modelling and requires detailed Monte Carlo studies in order to properly understand the distributions of secondary particles. Further information can be found in [164].

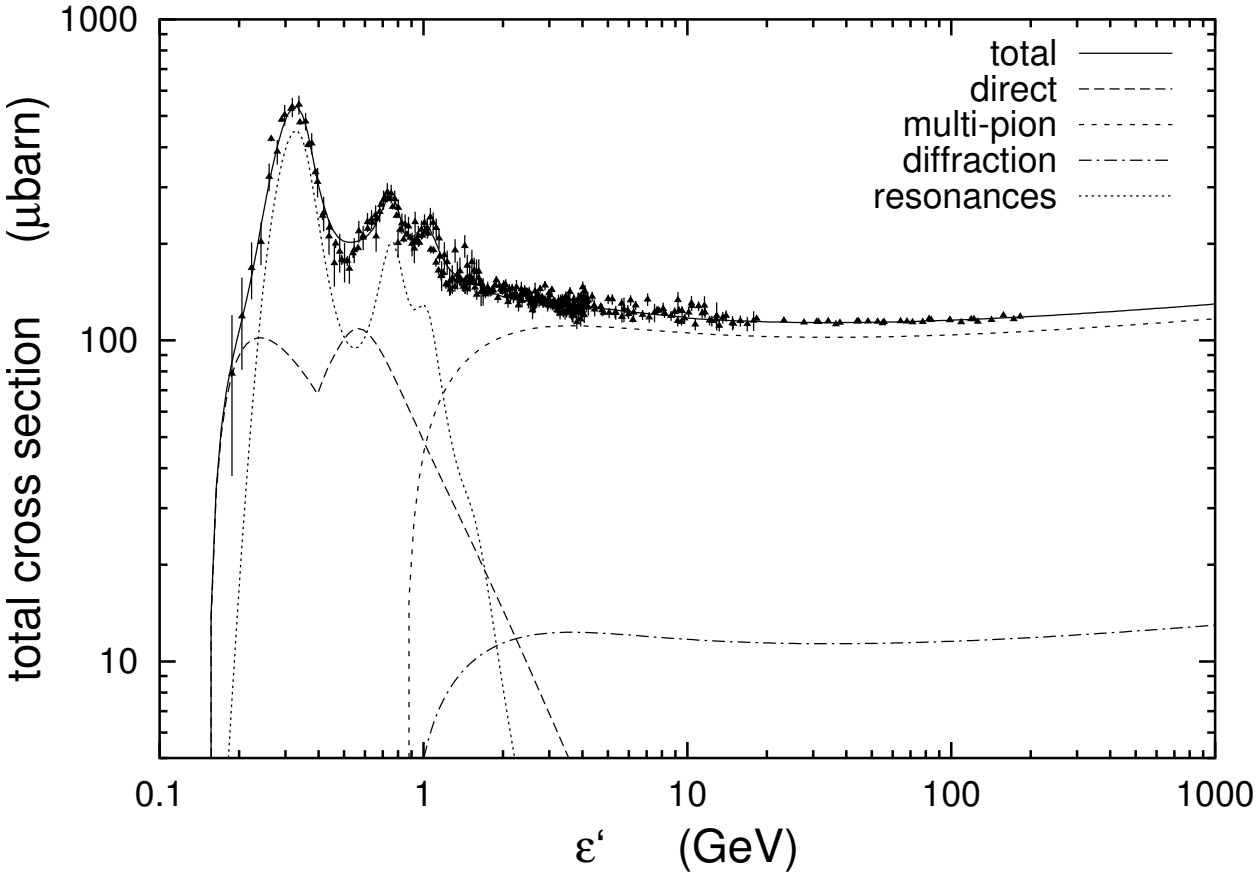

Figure 10.10: The total cross section for $p+\gamma$ interactions with various components indicated. The abscissa is the photon energy in the nucleon rest frame. The data points correspond to direct measurements. Image credit: Figure 1 in [165].

10.2.3.3 Hybrid

Hybrid ("lepto-hadronic") models, which combine leptonic and hadronic emission, exist (e.g. [166]) but for brevity will not be discussed here.

10.3 The Extragalactic Background Light

10.3.1 Effects on Gamma-ray Detection

The Extragalactic Background Light (EBL) was presented earlier in Section 5.2.1.2 as a tiny contribution to the overall night sky background seen by telescopes. The effects of the EBL

become important when doing VHE astronomy at cosmological distances: gamma rays from large distances can pair produce due to an interaction with an EBL photon:

$$\gamma_{\text{VHE}} + \gamma_{\text{EBL}} \rightarrow e^- + e^+. \tag{10.3}$$

Pair production can occur if the centre-of-mass energy of the photon-photon system is greater than twice the rest energy of the electron [167]. Taking E_γ as the energy of the gamma ray, ϵ the energy of the lower energy photon, and θ the collision angle between the two photons, the minimum energy required to produce an electron-positron pair is given by

$$(E_\gamma \epsilon)_{\text{threshold}}(1 - \cos\theta) \geq 2(m_e c^2)^2 \tag{10.4}$$

Thus, for a TeV gamma-ray hitting another photon head-on, $\epsilon \sim 0.5$ eV, corresponding to an infrared photon. The interaction cross-section for pair production is a function of energy, so interactions occur for a range of both E_γ and ϵ. Hence, the optical depth $\tau(E, z)$ depends on the SED of the EBL along the line of sight, and its distribution in z.

In order to understand the intrinsic properties of a source, the effects of the EBL must be deconvolved from the data taken. The effects of the EBL are imprinted on the observed flux as

$$F_{\text{obs}}(E) = F_{\text{int}}(E) e^{-\tau(E,z)}. \tag{10.5}$$

It follows that the more distant an object is, the more the observed flux is attenuated, thus making the detection of high redshift sources challenging. This interaction ultimately leads to a VHE horizon which is defined as the energy at which the optical depth τ becomes unity as a function of redshift. Further details of the VHE horizon can be found in [168].

It follows that at large cosmological distances, $\tau \gg 1$ since the gamma rays are moving through more EBL. The correlation between the redshift of an object and the gamma-ray attenuation is known as the Fazio-Stecker relation [169], demonstrated in Figure 10.11. A plot of optical depth versus gamma-ray energy for a number of redshifts is given in Figure 10.12. It can be seen that the higher energy gamma rays are particularly susceptible to attenuation and that the effect becomes more pronounced with increasing redshift. This effectively limits the redshift (*i.e.* distance) at which VHE emission can be detected.

10.3.2 Constraining the EBL with VHE Data

Estimates of the EBL must take into account all the processes that contribute to the photon field, such as galaxy evolution and structure formation. Furthermore, recall that direct measurements are difficult due to bright foregrounds such as zodiacal light and light from the

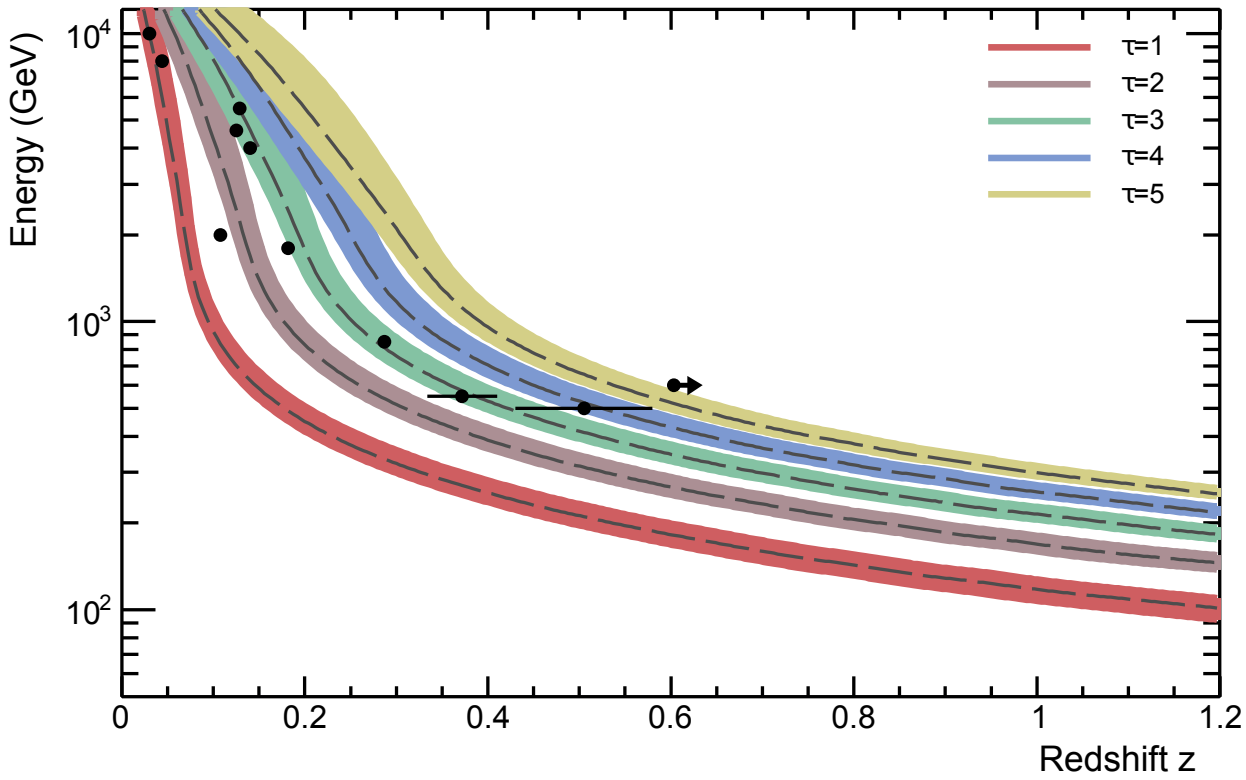

Figure 10.11: For several sources, the energy of the most energetic gamma ray detected from that source is plotted versus the source's redshift. There is a strong anti-correlation; this is the essence of the Fazio-Stecker relation. Each colour band corresponds to a different optical depth (as per the EBL model in [170]. Thus, a data point lying in one of those colour bands represents a measurement that has been made at the corresponding optical depth. Image credit: A. Furniss.

Milky Way. The use of data from VHE observatories to probe the composition of the EBL has been attempted, with some success, since the early days of the field [e.g. 172].

For a sufficiently well-understood intrinsic blazar SED, measurements of objects at VHE energies can be used to constrain the EBL [e.g. 173, 174]. The main assumption needed to place limits on the EBL is the intrinsic spectral shape of the blazar; the usual assumption is that the intrinsic spectrum of a blazar is a power law,

$$\frac{dN}{dE} \propto E^{-\Gamma}, \tag{10.6}$$

with the spectral index Γ no harder than ≈ 1.5. This spectral limitation is derived from the assumption that the VHE photons are produced in shock regions [175]. Recent observations of distant blazars [e.g. 176] which derived intrinsic spectral indices of 1.28 ± 0.2 or harder, are beginning to challenge the conventional models.

The detection of more gamma rays at higher energies and greater redshifts are where the

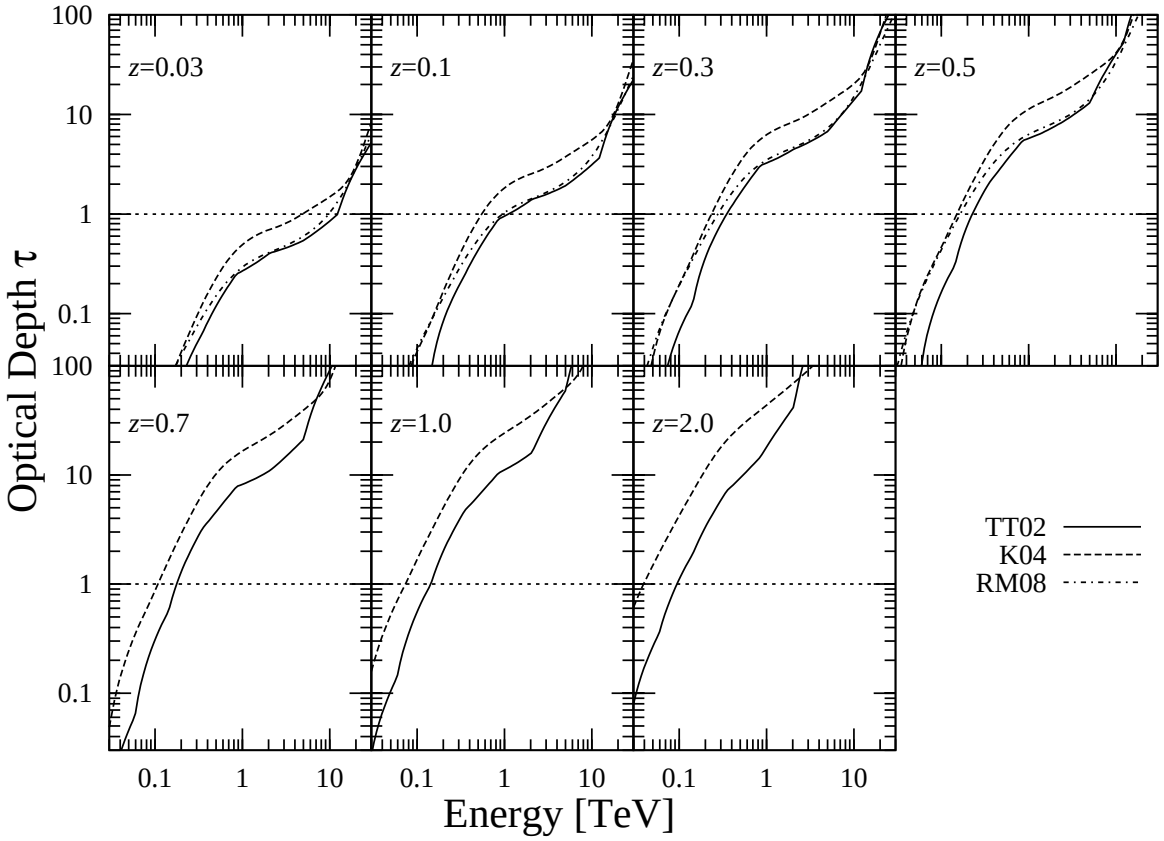

Figure 10.12: Optical depth τ for different gamma-ray energies. Each panel is for a different source redshift. The horizontal line represents the VHE horizon ($\tau = 1$) and the different lines correspond to different models. It can be seen that higher energy photons are more heavily influenced by the EBL and that with increasing redshift the optical depth increases across all energies. TT02, K04, and RM08 correspond to different EBL models. Image credit: Figure 3 in [171].

Bright Moonlight Program comes into play: deep observations at higher energies allow for more constraints to be placed on different energy regions of the EBL SED.

10.4 Results of the Bright Moonlight Program

The following is a brief discussion of a flare from *1ES 1727+502*, a blazar with redshift $z \sim 0.055$ that was discovered to be flaring during observations under bright moonlight. This was a new detection for *VERITAS*. Note that this is distinct from a new *discovery* as the source was discovered at VHE energies by *MAGIC* [177]. That being said, the *VERITAS* detection was the first detection of variability of the source.

1ES 1727+502 was detected in a high flux state on May 1, 2013 (MJD 56413) and data

were taken until May 7, 2013 (MJD 56419). Additional data were taken on May 18, 2013 (56430) and these did not result in a detection. After data quality cuts, there was ~ 6 hours of data available for the science analysis, of which half were taken in RHV mode during the first two nights of the exposure.

The data were analysed using the standard methods presented earlier in Chapter 4. The resulting spectrum is shown in Figure 10.13. The spectrum was corrected for EBL absorption using the model in [178]. Both spectra are well fitted by power-law functions between 0.25 TeV and 1.6 TeV with χ^2/NDF values of 1.66/2 ($P \sim 44\%$) and 1.69/2 ($P \sim 43\%$) for the observed and EBL-corrected spectra, respectively. The observed spectrum is given by

$$\frac{dN}{dE} = (7.8 \pm 1.1) \times 10^{-12} \left(\frac{E}{620 \text{ GeV}}\right)^{-2.1\pm0.3} \text{ cm}^{-2} \text{ s}^{-1} \text{ TeV}^{-1}, \tag{10.7}$$

and the EBL-corrected (*intrinsic*) spectrum is given by

$$\frac{dN}{dE} = (1.1 \pm 0.2) \times 10^{-11} \left(\frac{E}{620 \text{ GeV}}\right)^{-1.8\pm0.3} \text{ cm}^{-2} \text{ s}^{-1} \text{ TeV}^{-1}. \tag{10.8}$$

All the aforementioned errors are statistical only.

At the time of publishing, the systematic errors were conservatively estimated to be 30% on the flux normalisation and 0.3 on the spectral index. This is 50% larger than standard *VERITAS* systematic uncertainties. The increased uncertainty was due to the fact that the RHV mode is not as well understood as the standard configuration. However, based on the studies performed by the author of this work since then (e.g. studies of the energy bias and resolution in Section 8.2.1), there is reason to believe that this 50% increase is probably overestimating the systematic error.

The light curve (*i.e.* flux versus time) for the *VERITAS* observation is shown in Figure 10.14. The light curve between May 01 and May 07 2015 (Modified Julian Date (MJD) 56413 - 56419) can be fitted by a constant resulting in an integral flux

$$F(E > 250 \text{ GeV}) = (1.1 \pm 0.2) \times 10^{-11} \text{ cm}^{-2} \text{ s}^{-1} \tag{10.9}$$

and a $\chi^2/NDF = 4.73/3$ ($P \sim 19\%$). However, when including the upper limit from data taken on on May 18 (MJD 56437), the resulting χ^2/NDF is 12.0/4 ($P \sim 1.8\%$), which excludes a constant flux at the 2.4σ level. Thus, it is likely that the flare ended at some point after the last *VERITAS* detection.

An easy constraint to calculate based on these data is the size of the emission region. Based on the *1ES 1727+502* light curve, a reasonable range for the variability timescale τ is $5.8 - 10$ days. The lower bound is set by the fact that *VERITAS* detected emission from the blazar over this period of time and the upper bound is set by the fact that the flare ended

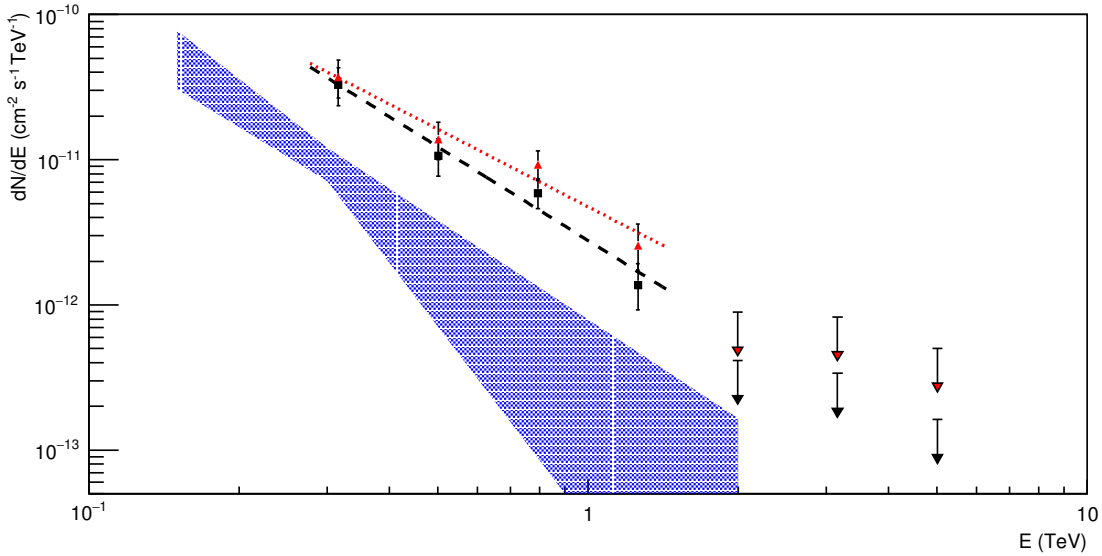

Figure 10.13: Spectra for the complete *1ES 1727+502* dataset. Power-law fits to both the uncorrected (black squares) and EBL-corrected (red triangles) points are provided. The fitted values are given in the text. The blue-shaded region is the spectrum of *1ES 1727+502* from the *MAGIC* discovery paper [177]. Image credit: data from Figure 1 in [1].

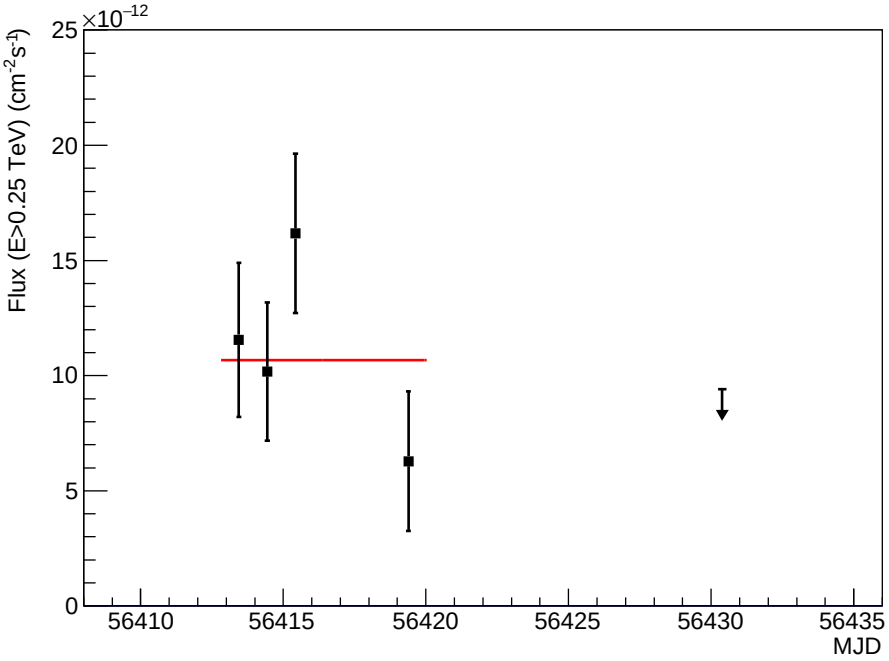

Figure 10.14: The light curve for *1ES 1727+502*. The fit for a constant flux has a value of $(1.1 \pm 0.2) \times 10^{-11}$ cm^{-2} s^{-1}. The arrow is the upper limit from data taken on May 18. Image credit: data from [1].

before May 18. Taking the Doppler factor $\delta = 30$ (a value similar to those typical in SSC models, see (e.g.) [170]), via Equation 10.2 the emitting region can be constrained to have a size $4.3 < R < 7.4$ where R has units of 10^{15} m. The size of the emission region in blazars provides insight into the underlying physics, such as the particle acceleration mechanisms and timescales; for more information see e.g. [179, 180].

For completeness, the full SED for *1ES 1727+502* is given in Figure 10.15 to compare with the cartoon given earlier in Figure 10.7. This SED was produced by M. Cerruti, the other lead author on the paper [1], who also performed the multiwavelength analysis and modeling for the article. The rest of the science gleaned from the study of *1ES 1727+502* can be found in [1]. In short, the SED was fit with a SSC model which allowed for a discussion of the acceleration and cooling mechanisms within the blazar and the underlying particle population.

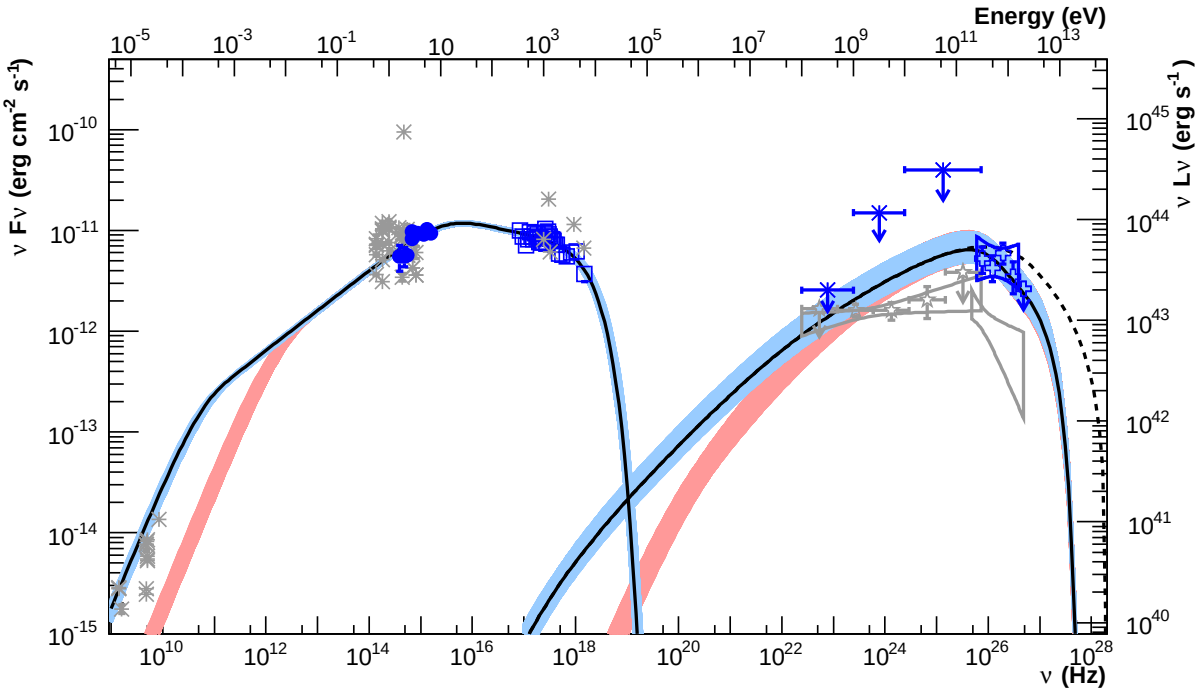

Figure 10.15: The full SED for *1ES 1727+502*. Archival data from various instruments is plotted in gray, and quasi-simultaneous data from the May 2013 flare are given in blue. Image credit: Figure 3 in [1].

10.5 Summary

In this chapter, several of the science benefits of the new bright moonlight observing modes have been presented. The inclusion of bright moonlight data in *VERITAS* analyses offers increased exposures at high energies (useful for probing the EBL), and the overall increase in observing time increases the chances of detecting a transient event (which has been demonstrated in the detection of the flare from *1ES 1727+502*). It follows that the opposite is also true; it is now possible to follow a transient detected during dark time into moonlight and determine the length of the transient. Based on this success, bright moonlight data is now beginning to be used by the collaboration at-large.

Chapter 11

Conclusions

Two new observing modes for *VERITAS* have been devised to increase the amount of observing time available to the experiment. The reduced high voltage (RHV) observing mode has been shown to have an energy threshold and sensitivity very similar to a standard analysis. This makes the observing mode useful for a large number of *VERITAS* primary science goals (all but those requiring the lowest energy thresholds, in fact). Based on database logs of the different data types, RHV provides an additional $\sim 13\%$ observing time for a given observing season. The use of UV filters (UVF) has been shown to allow *VERITAS* to operate through very bright moonlight, at the cost of a higher energy threshold and significantly reduced sensitivity. Still, this observing mode is useful for monitoring targets for flaring, or making dedicated measurements of certain astrophysical phenomena which require pointing very close to the moon. The UVF mode yields an additional $\sim 16\%$ observing time a year. A summary of the performance of each of the observing modes is given in Table 11.1.

Mode	Time to Detection (min) Crab Flux Fraction			Energy Threshold	Sensitivity
	1	0.05	0.01	(GeV)	($\sigma/\sqrt{\text{hr}}$)
NOM	1.14	124	2670	140	36.5
RHV	1.19	109	2290	160	36.4
UVF	4.89	842	19500	320	17.7

Table 11.1: Compilation of the performance values for the different observing modes for the analysis cuts used in this thesis.

The first science publication resulting from the Bright Moonlight Program is now in print [1] and the data products resulting from this work are beginning to be used by the collaboration. The RHV data type is quickly being assimilated into standard analyses. The

UVF mode still requires a bit more understanding (e.g. systematic uncertainties relating to the energy reconstruction bias and the energy-dependant shift in the MSCW distributions) but is still capable of being integrated into a standard analysis.

In terms of practicality, switching to the RHV observing mode is trivial; it requires a single command. Installing the UV filters, however, requires modifying the telescopes and is thus somewhat more cumbersome. By optimising target selection, it is possible to trade off some UVF time for RHV time; this is beneficial considering the substantially higher sensitivity and energy threshold of the RHV mode. Thus, RHV observations are more appealing, but it is important to note that some measurements can only be made using the filters.

Bibliography

[1] S. Archambault, A. Archer, M. Beilicke, et al. "VERITAS Detection of γ-Ray Flaring Activity From the BL Lac Object 1ES 1727+502 During Bright Moonlight Observations". *ApJ*, **808**:110, August 2015. [ADS]

[2] P. Morrison. "On gamma-ray astronomy". *Il Nuovo Cimento*, **7**(6): pp. 858–865, 1958. ISSN 0029-6341. [LINK]

[3] T. C. Weekes, M. F. Cawley, D. J. Fegan, et al. "Observation of TeV gamma rays from the Crab nebula using the atmospheric Cerenkov imaging technique". *ApJ*, **342**: pp. 379–395, July 1989. [ADS]

[4] S. Wakely and D. Horan, "TeVCat VHE Source Catalog". [LINK] (Accessed: 2015-06-03).

[5] http://www.mpi-hd.mpg.de/hfm/HESS/

[6] https://magic.mpp.mpg.de/

[7] http://veritas.sao.arizona.edu/

[8] http://isdc.unige.ch/fact/

[9] H. Bethe and W. Heitler. "On the Stopping of Fast Particles and on the Creation of Positive Electrons". *Royal Society of London Proceedings Series A*, **146**: pp. 83–112, August 1934. [ADS]

[10] M. S. Longair. "High Energy Astrophysics". February 2011. [ADS]

[11] T. Weekes. "Very high energy gamma-ray astronomy". Series in Astronomy and Astrophysics. CRC Press, 2003. ISBN 9781420033199. [LINK]

[12] C. Amsler, M. Doser, M. Antonelli, et al. "Review of Particle Physics". *Physics Letters B*, **667**: pp. 1–6, September 2008. [ADS]

[13] S. R. Kelner, F. A. Aharonian, and V. V. Bugayov. "Energy spectra of gamma rays, electrons, and neutrinos produced at proton-proton interactions in the very high energy regime". *Phys. Rev. D*, **74**(3):034018, August 2006. [ADS]

[14] F. Aharonian, A. G. Akhperjanian, U. Barres de Almeida, et al. "Energy Spectrum of Cosmic-Ray Electrons at TeV Energies". *Physical Review Letters*, **101**(26):261104, December 2008. [ADS]

[15] W. F. Meggers and C. G. Peters. "Measurements on the Index of Refraction of Air for Wave-Lengths from 2218 A to 9000 A". *ApJ*, **50**: pp. 56–71, July 1919. [ADS]

[16] N. C. Gerson. "Variations in the index of refraction of the atmosphere". *Geofisica Pura e Applicata*, **13**: pp. 88–101, September 1948. [ADS]

[17] H. J. Völk and K. Bernlöhr. "Imaging very high energy gamma-ray telescopes". *Experimental Astronomy*, **25**: pp. 173–191, August 2009. [ADS]

[18] A. McCann. "Discovery of Emission above 100 GeV from The Crab Pulsar With VERITAS". PhD thesis, McGill University (Canada), 2012. [ADS]

[19] J. Kildea, R. W. Atkins, H. M. Badran, et al. "The Whipple Observatory 10 m gamma-ray telescope, 1997 2006". *Astroparticle Physics*, **28**: pp. 182–195, October 2007. [ADS]

[20] D. Horns for the HEGRA collaboration. "Observations with the HEGRA stereoscopic system". *Proceedings of the XXIst Rencontres de Moriond*, March 2001. [ADS]

[21] https://www.cta-observatory.org/

[22] R. Atkins, W. Benbow, D. Berley, et al. "Milagrito, a TeV air-shower array". *Nuclear Instruments and Methods in Physics Research A*, **449**: pp. 478–499, July 2000. [ADS]

[23] A. A. Abdo, B. Allen, D. Berley, et al. "TeV Gamma-Ray Sources from a Survey of the Galactic Plane with Milagro". *ApJ*, **664**: pp. L91–L94, August 2007. [ADS]

[24] http://www.hawc-observatory.org/

[25] A. U. Abeysekara, R. Alfaro, C. Alvarez, et al. "Sensitivity of the high altitude water Cherenkov detector to sources of multi-TeV gamma rays". *Astroparticle Physics*, **50**: pp. 26–32, December 2013. [ADS]

[26] W. L. Kraushaar and G. W. Clark. "Search for Primary Cosmic Gamma Rays with the Satellite Explorer XI". *Physical Review Letters*, **8**: pp. 106–109, February 1962. [ADS]

[27] W. L. Kraushaar, G. W. Clark, G. P. Garmire, et al. "High-Energy Cosmic Gamma-Ray Observations from the OSO-3 Satellite". *ApJ*, **177**: p. 341, November 1972. [ADS]

[28] R. W. Klebesadel, I. B. Strong, and R. A. Olson. "Observations of Gamma-Ray Bursts of Cosmic Origin". *ApJ*, **182**: p. L85, June 1973. [ADS]

[29] C. E. Fichtel, R. C. Hartman, D. A. Kniffen, et al. "High-energy gamma-ray results from the second small astronomy satellite". *ApJ*, **198**: pp. 163–182, May 1975. [ADS]

[30] D. A. Kniffen, C. E. Fichtel, R. C. Hartman, et al. "Distribution of cosmic gamma rays in the galactic anticenter region as observed by SAS-2". *International Cosmic Ray Conference*, **1**: pp. 100–105, August 1975. [ADS]

[31] B. N. Swanenburg, K. Bennett, G. F. Bignami, et al. "Second COS B catalog of high-energy gamma-ray sources". *ApJ*, **243**: pp. L69–L73, January 1981. [ADS]

[32] C. Meegan, G. Lichti, P. N. Bhat, et al. "The Fermi Gamma-ray Burst Monitor". *ApJ*, **702**:791, September 2009. [ADS]

[33] W. B. Atwood, A. A. Abdo, M. Ackermann, et al. "The Large Area Telescope on the Fermi Gamma-Ray Space Telescope Mission". *ApJ*, **697**: pp. 1071–1102, June 2009. [ADS]

[34] F. Acero, M. Ackermann, M. Ajello, et al. "Fermi Large Area Telescope Third Source Catalog". *ApJS*, **218**:23, June 2015. [ADS]

[35] Hammamatsu, "Photomultiplier tubes basics and applications". [LINK] (Accessed: 2015-02-17).

[36] W. Haynes. "CRC Handbook of Chemistry and Physics, 96th Edition". (ISC)2 Press. Taylor & Francis, 2015. [LINK]

[37] M. Suyama and K. Nakamura. "Recent progress of photocathodes for PMTs". *Proceedings of the International Workshop on New Photon Detectors, Japan*, 2009. [LINK]

[38] W. B. Nottingham. "Thermionic Emission". *Handbuch der Physik*, **21**: pp. 1–175, 1956. [ADS]

[39] ET Enterprises, "Understanding Photomultipliers". [LINK] (Accessed: 2015-07-06).

[40] Hammamatsu, "Photomultiplier tubes and related products". [LINK] (Accessed: 2015-11-18).

[41] M. Bautista. "An investigation of the plate scale of the *VERITAS* telescopes". MSc thesis, McGill University (Canada), 2009. [LINK]

[42] N. A. Otte et al. "The Upgrade of VERITAS with High Efficiency Photomultipliers". *Proceedings of the 32nd International Cosmic Ray Conference*, October 2011. [ADS]

[43] T. Nagai, R. McKay, G. Sleege, et al. "Focal Plane Instrumentation of VERITAS". *International Cosmic Ray Conference*, **3**: pp. 1437–1440, 2008. [ADS]

[44] R. Winston. "Light Collection within the Framework of Geometrical Optics". *Journal of the Optical Society of America (1917-1983)*, **60**: pp. 245–247, February 1970. [ADS]

[45] S. Griffin. "VERy TRenDy: The VERITAS Transient Detector". MSc thesis, McGill University (Canada), 2011. [ADS]

[46] J. M. Davies and E. S. Cotton. "Design of the quartermaster solar furnace". *Solar Energy*, **1**: pp. 16–22, April 1957. [ADS]

[47] C. Deil, C. van Eldik, A. Förster, et al. "H.E.S.S. II-Telescope Structure, Reflector and Drive System". In F. A. Aharonian, W. Hofmann, and F. Rieger, editors, "American Institute of Physics Conference Series", volume 1085 of *American Institute of Physics Conference Series*, pp. 693–695. December 2008. [ADS]

[48] E. Roache, R. Irvin, J. S. Perkins, et al. "Mirror Facets for the VERITAS Telescopes". *Proceedings of the 30th International Cosmic Ray Conference*, **3**: pp. 1397–1400, 2008. [ADS]

[49] J. Hall, V. V. Vassiliev, D. B. Kieda, et al. "VERITAS CFDs". *International Cosmic Ray Conference*, **5**: p. 2851, July 2003. [ADS]

[50] B. Zitzer et al. "The VERITAS Upgraded Telescope-Level Trigger Systems: Technical Details and Performance Characterization". *Proceedings of the 33rd International Cosmic Ray Conference*, July 2013. [ADS]

[51] A. Weinstein et al. "The VERITAS Trigger System". *Proceedings of the 30th International Cosmic Ray Conference*, **3**: pp. 1539–1542, 2008. [ADS]

[52] OPTEK, "OPTEK OVLGx0CyB9 Series LED Datasheet". [LINK] (Accessed: 2015-06-26).

[53] D. Hanna, A. McCann, M. McCutcheon, et al. "An LED-based flasher system for VERITAS". *Nuclear Instruments and Methods in Physics Research A*, **612**: pp. 278–287, January 2010. [ADS]

[54] J. R. Prescott. "A statistical model for photomultiplier single-electron statistics". *Nuclear Instruments and Methods*, **39**: pp. 173–179, January 1966. [ADS]

[55] C. Fruck, M. Gaug, R. Zanin, et al. "A novel LIDAR-based Atmospheric Calibration Method for Improving the Data Analysis of MAGIC". *ArXiv e-prints*, March 2014. [ADS]

[56] M. McCutcheon. "Search for VHE gamma-ray emission from the globular cluster M13 with VERITAS". PhD thesis, McGill University (Canada), 2012. [LINK]

[57] S. Griffin and D. Hanna. "Using Raster Scans of Bright Stars to Measure the Relative Total Throughputs of Cherenkov Telescopes". *Proceedings of the 33rd International Cosmic Ray Conference*, July 2013. [ADS]

[58] A. M. Hillas. "Cerenkov light images of EAS produced by primary gamma". *International Cosmic Ray Conference*, **3**: pp. 445–448, August 1985. [ADS]

[59] E. Lorenz and R. Wagner. "Very-high energy gamma-ray astronomy. A 23-year success story in high-energy astroparticle physics". *European Physical Journal H*, **37**: pp. 459–513, August 2012. [ADS]

[60] S. LeBohec, C. Duke, and P. Jordan. "Minimal stereoscopic analysis for imaging atmospheric Cherenkov telescope arrays". *Astroparticle Physics*, **24**: pp. 26–31, September 2005. [ADS]

[61] M. Ackermann, M. Ajello, A. Albert, et al. "The Spectrum of Isotropic Diffuse Gamma-Ray Emission between 100 MeV and 820 GeV". *ApJ*, **799**:86, January 2015. [ADS]

[62] K. Egberts, F. Brun, S. Casanova, et al. "Diffuse TeV Gamma-Ray Emission in the H.E.S.S. Galactic Plane Survey". *ArXiv e-prints*, August 2013. [ADS]

[63] G. Maier. "Monte Carlo studies of the VERITAS array of Cherenkov telescopes". *International Cosmic Ray Conference*, **3**: pp. 1413–1416, 2008. [ADS]

[64] F. A. Aharonian, A. G. Akhperjanian, J. A. Barrio, et al. "The temporal characteristics of the TeV gamma-radiation from MKN 501 in 1997. I. Data from the stereoscopic imaging atmospheric Cherenkov telescope system of HEGRA". *A&A*, **342**: pp. 69–86, February 1999. [ADS]

[65] D. Berge, S. Funk, and J. Hinton. "Background modelling in very-high-energy γ-ray astronomy". *A&A*, **466**: pp. 1219–1229, May 2007. [ADS]

[66] B. Zitzer et al. "The VERITAS Dark Matter Program". *Proceedings of the 2014 Fermi Symposium*, March 2015. [ADS]

[67] T.-P. Li and Y.-Q. Ma. "Analysis methods for results in gamma-ray astronomy". *ApJ*, **272**: pp. 317–324, September 1983. [ADS]

[68] P. Cogan. "VEGAS, the VERITAS Gamma-ray Analysis Suite". *International Cosmic Ray Conference*, **3**: pp. 1385–1388, 2008. [ADS]

[69] https://znwiki3.ifh.de/CTA/Eventdisplay%20Software

[70] http://www.physics.utah.edu/gammaray/GrISU/GrISU/Documentation/grisu.html

[71] http://otte.gatech.edu/care/

[72] D. Heck, J. Knapp, J. N. Capdevielle, et al. "CORSIKA: a Monte Carlo code to simulate extensive air showers." February 1998. [ADS]

[73] M. K. Daniel. "Application of radiosonde data to VERITAS simulations". *International Cosmic Ray Conference*, **3**: pp. 1329–1332, 2008. [ADS]

[74] C. Leinert, S. Bowyer, L. K. Haikala, et al. "The 1997 reference of diffuse night sky brightness". *A&AS*, **127**: pp. 1–99, January 1998. [ADS]

[75] M. S. Bessell. "UBVRI passbands". *PASP*, **102**: pp. 1181–1199, October 1990. [ADS]

[76] M. S. Bessell. "Standard photometric systems". *Annual Review of Astronomy and Astrophysics*, **43**(1): pp. 293–336, 2005. [LINK]

[77] J. D. Fernie. "On the variability of Vega". *PASP*, **93**: pp. 333–337, June 1981. [ADS]

[78] F. Roach and J. Gordon. "The light of the night sky". Geophysics and Astrophysics Monographs. An international Series of fundamental Textbooks. Springer, 1973. ISBN 9789027702937. [LINK]

[79] P. S. Wesson. "Olbers's paradox and the spectral intensity of the extragalactic background light". *ApJ*, **367**: pp. 399–406, February 1991. [ADS]

[80] G. N. Toller. "The extragalactic background light at 4400 Å". *ApJ*, **266**: pp. L79–L82, March 1983. [LINK]

[81] Y. Matsuoka, N. Ienaka, K. Kawara, et al. "Cosmic Optical Background: The View from Pioneer 10/11". *ApJ*, **736**:119, August 2011. [ADS]

[82] S. Cole, M.-A. Treyer, and J. Silk. "The faint galaxy contribution to the diffuse extragalactic background light". *ApJ*, **385**: pp. 9–25, January 1992. [ADS]

[83] C. W. Allen. "Astrophysical quantities". 1973. [ADS]

[84] T. N. Chatterjee and T. K. Das. "Relation between solar UV flux and 10.7-cm radio emission". *MNRAS*, **274**: pp. 858–860, June 1995. [ADS]

[85] F. Patat. "UBVRI night sky brightness during sunspot maximum at ESO-Paranal". *A&A*, **400**: pp. 1183–1198, March 2003. [ADS]

[86] P. Massey, C. Gronwall, and C. A. Pilachowski. "The spectrum of the Kitt Peak night sky". *PASP*, **102**: pp. 1046–1051, August 1990. [ADS]

[87] C. R. Benn and S. L. Ellison. "Brightness of the night sky over La Palma". *New A Rev.*, **42**: pp. 503–507, November 1998. [ADS]

[88] A. Levasseur-Regourd, I. Mann, R. Dumont, et al. *Optical and Thermal Properties of Interplanetary Dust*, pp. 57–94. Astronomy and Astrophysics Library. Springer Berlin Heidelberg, 2001. [ADS]

[89] J.-D. Cassini. "Découverte de la lumière qui paroist dans le zodiaque". Académie royale des sciences (Paris), 1685. [LINK]

[90] J.-J. Dortous de Mairan and P. Simonneau. "Traité physique et historique de l'aurore boréale". Suite des Mémoires de l'Académie Royale des Sciences. Imprimerie Royale (Paris), 1733. [LINK]

[91] B. L. Cooper, H. A. Zook, and A. E. Potter. "Clementine Photographs of the Inner Zodiacal Light". **104**: p. 333, 1996. [ADS]

[92] M. S. Hanner, J. L. Weinberg, L. M. DeShields, II, et al. "Zodiacal light and the asteroid belt: The view from Pioneer 10". *J. Geophys. Res.*, **79**: p. 3671, 1974. [ADS]

[93] G. N. Toller and J. L. Weinberg. "The change in near-ecliptic zodiacal light brightness with heliocentric distance". In "IAU Colloq. 85: Properties and Interactions of Interplanetary Dust", volume 119 of *Astrophysics and Space Science Library*, pp. 21–25. 1985. [ADS]

[94] J. F. James, T. Mukai, T. Watanabe, et al. "The morphology and brightness of the zodiacal light and gegenschein". *MNRAS*, **288**: pp. 1022–1026, July 1997. [ADS]

[95] M. Ishiguro, H. Fukushima, D. Kinoshita, et al. "The isophote maps of the gegenschein obtained by ccd observations". *Earth, Planets and Space*, **50**(6-7): pp. 477–480, 1998. ISSN 1343-8832. [LINK]

[96] "2012 City of Tucson/Pima County Outdoor Lighting Code". [LINK] (Accessed: 2015-08-12).

[97] P. Massey and C. B. Foltz. "The Spectrum of the Night Sky over Mount Hopkins and Kitt Peak: Changes after a Decade". *PASP*, **112**: pp. 566–573, April 2000. [ADS]

[98] K. F. Neugent and P. Massey. "The Spectrum of the Night Sky Over Kitt Peak: Changes Over Two Decades". *PASP*, **122**: pp. 1246–1253, October 2010. [ADS]

[99] R. L. Berry. "Light Pollution in Southern Ontario". *JRASC*, **70**: p. 97, June 1976. [ADS]

[100] R. L. Wildey and H. A. Pohn. "The Normal Albedo of the Apollo 11 Landing Site and Intrinsic Dispersion in the Lunar Heiligenschein". *ApJ*, **158**: p. L129, November 1969. [ADS]

[101] Y. G. Shkuratov, M. A. Kreslavsky, A. A. Ovcharenko, et al. "Opposition Effect from Clementine Data and Mechanisms of Backscatter". *Icarus*, **141**: pp. 132–155, September 1999. [ADS]

[102] A. Jones, S. Noll, W. Kausch, et al. "An advanced scattered moonlight model for Cerro Paranal". *A&A*, **560**:A91, December 2013. [ADS]

[103] H. H. Kieffer and T. C. Stone. "The Spectral Irradiance of the Moon". *AJ*, **129**: pp. 2887–2901, June 2005. [ADS]

[104] K. Krisciunas and B. E. Schaefer. "A model of the brightness of moonlight". *PASP*, **103**: pp. 1033–1039, September 1991. [ADS]

[105] F. Patat. "Observing During Bright Time: Tips and Tricks". *The Messenger*, **118**: pp. 11–14, December 2004. [LINK]

[106] A. Walker. *NOAO Newsletter*, **10**(16), 1987.

[107] A. N. Cox. "Allen's astrophysical quantities". 2000. [ADS]

[108] J. Elias. "Estimating lunar phase requirements". *NOAO Newsletter*, **37**, 1994. [LINK]

[109] L. Valcarcel. "VERITAS, 1ES 1218 + 30.4 and the extragalactic background light". PhD thesis, McGill University (Canada), 2008. [ADS]

[110] M. Urban, M. C. Chantell, P. Fleury, et al. "The use of an ultra-violet camera in the atmospheric Cherenkov technique". *Nuclear Instruments and Methods in Physics Research A*, **368**: pp. 503–511, February 1996. [ADS]

[111] D. Pomarède, P. J. Boyle, M. Urban, et al. "Search for shadowing of primary cosmic radiation by the moon at TeV energies". *Astroparticle Physics*, **14**: pp. 287–317, January 2001. [ADS]

[112] M. C. Chantell, C. W. Akerlof, H. M. Badran, et al. "A hybrid version of the Whipple observatory's air Cherenkov imaging camera for use in moonlight". *Astroparticle Physics*, **6**: pp. 205–214, February 1997. [ADS]

[113] D. Kranich, R. Mirzoyan, D. Petry, et al. "TeV γ-ray observations of the Crab and Mkn 501 during moonshine and twilight". *Astroparticle Physics*, **12**: pp. 65–74, October 1999. [ADS]

[114] J. Albert et al. "Very high energy gamma-ray observations during moonlight and twilight with the MAGIC telescope". *ArXiv Astrophysics e-prints*, February 2007. [ADS]

[115] E. Aliu, S. Archambault, T. Aune, et al. "A Search for Enhanced Very High Energy Gamma-Ray Emission from the 2013 March Crab Nebula Flare". *ApJ*, **781**:L11, January 2014. [ADS]

[116] A. M. Hillas, C. W. Akerlof, S. D. Biller, et al. "The Spectrum of Teravolt Gamma Rays from the Crab Nebula". *ApJ*, **503**: pp. 744–759, August 1998. [ADS]

[117] J. Grube et al. "Observations of the Crab Nebula with the Whipple 10 m Telescope". *ArXiv e-prints*, September 2007. [ADS]

[118] C. Masterson and CAT Collaboration. "Observations of the Crab Nebula with the CAT Imaging Atmospheric Čerenkov Telescope". In "American Institute of Physics Conference Series", volume 558 of *American Institute of Physics Conference Series*, p. 753. April 2001. [ADS]

[119] F. Aharonian, A. Akhperjanian, M. Beilicke, et al. "The Crab Nebula and Pulsar between 500 GeV and 80 TeV: Observations with the HEGRA Stereoscopic Air Cerenkov Telescopes". *ApJ*, **614**: pp. 897–913, October 2004. [ADS]

[120] F. Aharonian, A. G. Akhperjanian, A. R. Bazer-Bachi, et al. "Observations of the Crab nebula with HESS". *A&A*, **457**: pp. 899–915, October 2006. [ADS]

[121] J. Albert, E. Aliu, H. Anderhub, et al. "VHE γ-Ray Observation of the Crab Nebula and its Pulsar with the MAGIC Telescope". *ApJ*, **674**: pp. 1037–1055, February 2008. [ADS]

[122] J. Aleksić, S. Ansoldi, L. Antonelli, et al. "Measurement of the Crab Nebula spectrum over three decades in energy with the MAGIC telescopes". *Journal of High Energy Astrophysics*, pp. –, 2015. ISSN 2214-4048. [LINK]

[123] B. Bartoli, P. Bernardini, X. J. Bi, et al. "Crab Nebula: Five-year Observation with ARGO-YBJ". *ApJ*, **798**:119, January 2015. [ADS]

[124] M. Tluczykont, G. Fontaine, M. Ouchrif, et al. "A second level trigger for HESS phase 2". pp. 509–517, 2005. [LINK]

[125] SCHOTT, "UG-11 Datasheet". [LINK] (Accessed: 2014-09-29).

[126] SCHOTT, "Glass filter definitions". [LINK] (Accessed: 2014-09-30).

[127] U. S. D. of Energy and L. L. N. Laboratory. "Laser program annual report". v. 1. Lawrence Livermore National Laboratory., 1980. [LINK]

[128] ASTM, "Standard Tables for Reference Solar Spectral Irradiances: Direct Normal and Hemispherical on 37° Tilted Surface". [LINK] (Accessed: 2015-08-27).

[129] Thorlabs, "Thorlabs LED341W Datasheet". [LINK] (Accessed: 2015-06-17).

[130] Thorlabs, "Thorlabs LED370E Datasheet". [LINK] (Accessed: 2015-06-17).

[131] F. Krennrich, I. H. Bond, S. M. Bradbury, et al. "Discovery of Spectral Variability of Markarian 421 at TeV Energies". *ApJ*, **575**: pp. L9–L13, August 2002. [ADS]

[132] J. Albert, E. Aliu, H. Anderhub, et al. "Observations of Markarian 421 with the MAGIC Telescope". *ApJ*, **663**: pp. 125–138, July 2007. [ADS]

[133] V. A. Acciari, E. Aliu, T. Arlen, et al. "TeV and Multi-wavelength Observations of Mrk 421 in 2006-2008". *ApJ*, **738**:25, September 2011. [ADS]

[134] VERITAS Collaboration, V. A. Acciari, E. Aliu, et al. "A connection between star formation activity and cosmic rays in the starburst galaxy M82". *Nature*, **462**: pp. 770–772, December 2009. [ADS]

[135] E. Aliu, A. Archer, T. Aune, et al. "VERITAS Observations of the BL Lac Object PG 1553+113". *ApJ*, **799**:7, January 2015. [ADS]

[136] D. J. Helfand and R. H. Becker. "G0.9 + 0.1 and the emerging class of composite supernova remnants". *ApJ*, **314**: pp. 203–214, March 1987. [ADS]

[137] S. Klepser, S. Carrigan, E. de Oña Wilhelmi, et al. "A Population of Teraelectronvolt Pulsar Wind Nebulae in the H.E.S.S. Galactic Plane Survey". *ArXiv e-prints*, July 2013. [ADS]

[138] M. Ackermann, M. Ajello, A. Allafort, et al. "Detection of the Characteristic Pion-Decay Signature in Supernova Remnants". *Science*, **339**: pp. 807–811, February 2013. [ADS]

[139] F. Acero, M. Ackermann, M. Ajello, et al. "Constraints on the Galactic Population of TeV Pulsar Wind Nebulae Using Fermi Large Area Telescope Observations". *ApJ*, **773**:77, August 2013. [ADS]

[140] O. Kargaltsev, B. Rangelov, and G. G. Pavlov. "Gamma-ray and X-ray Properties of Pulsar Wind Nebulae and Unidentified Galactic TeV Sources". *ArXiv e-prints*, May 2013. [ADS]

[141] J. Albert, E. Aliu, H. Anderhub, et al. "Variable Very-High-Energy Gamma-Ray Emission from the Microquasar LS I +61 303". *Science*, **312**: pp. 1771–1773, June 2006. [ADS]

[142] P. C. Gregory. "Bayesian Analysis of Radio Observations of the Be X-Ray Binary LS I +61°303". *ApJ*, **575**: pp. 427–434, August 2002. [ADS]

[143] Andrew W. Smith for the VERITAS Collaboration. "VERITAS Observations of TeV Binaries". *ArXiv e-prints*, July 2013. [ADS]

[144] M. Ackermann, M. Ajello, J. Ballet, et al. "Associating Long-term γ-Ray Variability with the Superorbital Period of LS I +61°303". *ApJ*, **773**:L35, August 2013. [ADS]

[145] J. Aleksić, E. A. Alvarez, L. A. Antonelli, et al. "Detection of the γ-Ray Binary LS I +61°303 in a Low-flux State at Very High Energy γ-Rays with the MAGIC Telescopes in 2009". *ApJ*, **746**:80, February 2012. [ADS]

[146] J. Holder. "VERITAS Detection of Historically Bright TeV Flares From LS I +61 303". *The Astronomer's Telegram*, **6785**: p. 1, December 2014. [ADS]

[147] V. A. Acciari, M. Beilicke, G. Blaylock, et al. "VERITAS Observations of the γ-Ray Binary LS I +61 303". *ApJ*, **679**: pp. 1427–1432, June 2008. [ADS]

[148] G. Dubus. "Gamma-ray binaries and related systems". *A&A Rev.*, **21**:64, August 2013. [ADS]

[149] M. Ackermann, M. Ajello, A. Allafort, et al. "The Second Catalog of Active Galactic Nuclei Detected by the Fermi Large Area Telescope". *ApJ*, **743**:171, December 2011. [ADS]

[150] J. R. P. Angel and H. S. Stockman. "Optical and infrared polarization of active extragalactic objects". *ARA&A*, **18**: pp. 321–361, 1980. [ADS]

[151] P. Padovani. "A statistical analysis of complete samples of BL Lacertae objects". *A&A*, **256**: pp. 399–407, March 1992. [ADS]

[152] M. S. Shaw, R. W. Romani, S. E. Healey, et al. "Optical Spectroscopy of Bright Fermi LAT Blazars". *ApJ*, **704**: pp. 477–484, October 2009. [ADS]

[153] M. Ackermann, M. Ajello, W. Atwood, et al. "The Third Catalog of Active Galactic Nuclei Detected by the Fermi Large Area Telescope". *ArXiv e-prints*, January 2015. [ADS]

[154] P. Padovani and P. Giommi. "The connection between x-ray- and radio-selected BL Lacertae objects". *ApJ*, **444**: pp. 567–581, May 1995. [ADS]

[155] P. Giommi, S. Colafrancesco, E. Cavazzuti, et al. "Non-thermal cosmic backgrounds from blazars: the contribution to the CMB, X-ray and γ-ray backgrounds". *A&A*, **445**: pp. 843–855, January 2006. [ADS]

[156] T. Arlen, T. Aune, M. Beilicke, et al. "Rapid TeV Gamma-Ray Flaring of BL Lacertae". *ApJ*, **762**:92, January 2013. [ADS]

[157] J. Cortina and J. Holder. "MAGIC and VERITAS detect an unprecedented flaring activity from Mrk 421 in very high energy gamma-rays". *The Astronomer's Telegram*, **4976**: p. 1, April 2013. [ADS]

[158] M. Punch, C. W. Akerlof, M. F. Cawley, et al. "Detection of TeV photons from the active galaxy Markarian 421". *Nature*, **358**: p. 477, August 1992. [ADS]

[159] K. Nalewajko, M. C. Begelman, and M. Sikora. "Constraining the Location of Gamma-Ray Flares in Luminous Blazars". *ApJ*, **789**:161, July 2014. [ADS]

[160] M. Böttcher. "Modeling the emission processes in blazars". *Ap&SS*, **309**: pp. 95–104, June 2007. [ADS]

[161] C. D. Dermer and R. Schlickeiser. "Model for the High-Energy Emission from Blazars". *ApJ*, **416**: p. 458, October 1993. [LINK]

[162] F. A. Aharonian. "TeV gamma rays from BL Lac objects due to synchrotron radiation of extremely high energy protons". *New A*, **5**: pp. 377–395, November 2000. [ADS]

[163] W. Cui. "TeV gamma-ray astronomy". *Research in Astronomy and Astrophysics*, **9**: pp. 841–860, August 2009. [ADS]

[164] M. Böttcher, A. Reimer, K. Sweeney, et al. "Leptonic and Hadronic Modeling of Fermi-detected Blazars". *ApJ*, **768**:54, May 2013. [ADS]

[165] A. Mücke, J. P. Rachen, R. Engel, et al. "Photohadronic Processes in Astrophysical Environments". *PASA*, **16**: pp. 160–166, August 1999. [ADS]

[166] M. Cerruti, A. Zech, C. Boisson, et al. "Lepto-hadronic modelling of blazar emission". *SF2A-2011: Proceedings of the Annual meeting of the French Society of Astronomy and Astrophysics*, pp. 555–558, December 2011. [ADS]

[167] R. J. Gould and G. P. Schréder. "Opacity of the Universe to High-Energy Photons". *Physical Review*, **155**: pp. 1408–1411, March 1967. [ADS]

[168] A. Domínguez, J. D. Finke, F. Prada, et al. "Detection of the Cosmic γ-Ray Horizon from Multiwavelength Observations of Blazars". *ApJ*, **770**:77, June 2013. [ADS]

[169] G. G. Fazio and F. W. Stecker. "Predicted High Energy Break in the Isotropic Gamma Ray Spectrum: a Test of Cosmological Origin". *Nature*, **226**: pp. 135–136, April 1970. [ADS]

[170] F. Tavecchio, G. Ghisellini, G. Ghirlanda, et al. "TeV BL Lac objects at the dawn of the Fermi era". *MNRAS*, **401**: pp. 1570–1586, January 2010. [ADS]

[171] Y. Inoue, T. Totani, and M. Mori. "Prospects for a Very High-Energy Blazar Survey by the Next-Generation Cherenkov Telescopes". *PASJ*, **62**: pp. 1005–, August 2010. [ADS]

[172] F. W. Stecker, O. C. de Jager, and M. H. Salamon. "TeV gamma rays from 3C 279 - A possible probe of origin and intergalactic infrared radiation fields". *ApJ*, **390**: pp. L49–L52, May 1992. [ADS]

[173] M. Schroedter. "Upper Limits on the Extragalactic Background Light from the Very High Energy Gamma-Ray Spectra of Blazars". *ApJ*, **628**: pp. 617–628, August 2005. [ADS]

[174] F. Aharonian, A. G. Akhperjanian, A. R. Bazer-Bachi, et al. "A low level of extragalactic background light as revealed by γ-rays from blazars". *Nature*, **440**: pp. 1018–1021, April 2006. [ADS]

[175] F. W. Stecker, M. G. Baring, and E. J. Summerlin. "Blazar γ-Rays, Shock Acceleration, and the Extragalactic Background Light". *ApJ*, **667**: pp. L29–L32, September 2007. [ADS]

[176] F. Krennrich, E. Dwek, and A. Imran. "Constraints on Energy Spectra of Blazars based on Recent EBL Limits from Galaxy Counts". *ApJ*, **689**: pp. L93–L96, December 2008. [ADS]

[177] J. Aleksić, L. A. Antonelli, P. Antoranz, et al. "Discovery of very high energy gamma-ray emission from the blazar 1ES 1727+502 with the MAGIC Telescopes". *A&A*, **563**:A90, March 2014. [ADS]

[178] A. Franceschini, G. Rodighiero, and M. Vaccari. "Extragalactic optical-infrared background radiation, its time evolution and the cosmic photon-photon opacity". *A&A*, **487**: pp. 837–852, September 2008. [ADS]

[179] M. C. Begelman, A. C. Fabian, and M. J. Rees. "Implications of very rapid TeV variability in blazars". *MNRAS*, **384**: pp. L19–L23, February 2008. [ADS]

[180] J. Tammi and P. Duffy. "Particle-acceleration time-scales in TeV blazar flares". *MNRAS*, **393**: pp. 1063–1069, March 2009. [ADS]

[181] E. W. Weisstein. "Millimeter/submillimeter Fourier Transform Spectroscopy of Jovian Planet Atmospheres". PhD thesis, California Institute of Technology, 1996. [ADS]

Appendices

Appendix A

The Winston Cone Equation

The following is a derivation of the equations which describe the surface of a Winston-type light concentrator. [181] has been used as the reference for the derivation.

A Winston cone is in essence a parabola which has been tilted and revolved around its axis. Consider a parabola with focal length f whose surface is described in r' and z' coordinates, where the r' and z' axes are rotated from r and z by an angle θ as depicted in Figure A.1.

The surface of this parabola is (as usual) defined by

$$(r' - r'_0)^2 = 4f(z' - z'_0). \tag{A.1}$$

If the parabola is defined such that the parabola's origin is at $(0, -f)$, this simplifies to

$$(r')^2 = 4f(z' + f) \tag{A.2}$$

using a rotation matrix, this can then be expressed in (r, z) coordinates:

$$\begin{pmatrix} r \\ z \end{pmatrix} = \begin{pmatrix} \cos\theta & -\sin\theta \\ \sin\theta & \cos\theta \end{pmatrix} \begin{pmatrix} r' \\ z' \end{pmatrix} - \begin{pmatrix} a' \\ 0' \end{pmatrix}, \tag{A.3}$$

which can be rearranged to yield

$$\begin{pmatrix} r' \\ z' \end{pmatrix} = \begin{pmatrix} \cos\theta & \sin\theta \\ -\sin\theta & \cos\theta \end{pmatrix} \begin{pmatrix} r + a' \\ z \end{pmatrix} = \begin{pmatrix} (r + a')\cos\theta + z\sin\theta \\ -(r + a')\sin\theta + z\sin\theta \end{pmatrix}. \tag{A.4}$$

Finally, by inserting Equation A.2 into the above expression, after simplification we have the expression for the surface of the Winston cone:

$$\begin{aligned} S(r, z, \theta) = {} & (r\cos\theta + z\sin\theta)^2 + a'r(1 + \sin\theta)^2 \\ & - 2a'z\cos\theta(1 + \sin\theta) - (a')^2(3 + \sin\theta)(1 + \sin\theta) = 0. \end{aligned} \tag{A.5}$$

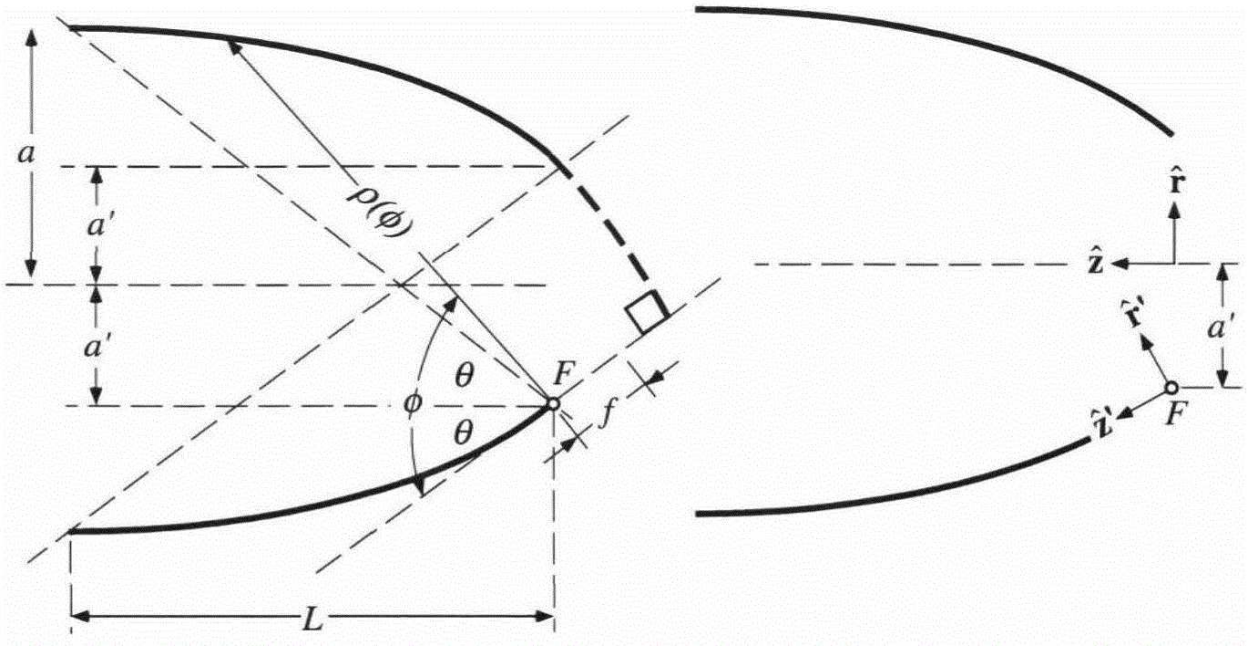

Figure A.1: Diagram of a 2D Winston cone. The entrance and exit radii are given by a and a', respectively. The tilt angle of the parabola which defines the geometry is θ, where θ is also the cutoff angle of the light cone. The length of the cone is L. Image credit: Figure B.1 in [181].

That for this expression, which is valid in cylindrical coordinates, $r = \rho \equiv \sqrt{x^2 + y^2}$, but θ in the above equation is *not* the polar angle, but the tilt angle of the parabola. This has been stated explicitly to avoid any confusion the reader may come across while skimming through this thesis in the future.

This expression has the solution

$$z(r) = \cot(\theta)(2a' \csc(\theta) + a' - r) - 2\csc^2(\theta)\sqrt{a'(\sin(\theta) + 1)(a' - r\sin(\theta))} \tag{A.6}$$

where a' is the light cone exit aperture radius. Note that this equation is only valid for $a' \leq r \leq a$, with a the entry aperture radius.

Of the four parameters which are indicated in Figure A.1 (length L, and a, a', and θ as previously defined) The entire geometry of a Winston cone can be described by two parameters: the exit aperture a' and the tilt angle θ:

$$\sin\theta = \frac{a'}{a}, \tag{A.7}$$

$$L = (a + a')\cot\theta. \tag{A.8}$$

Appendix B

Ray Tracing Algorithm

The idea behind ray tracing is that given a ray (usually a photon in the real-life system) with position $\vec{R}_0$ and direction $\vec{V}$, the intersection point with a surface $\vec{S}$ must be found. This is done by solving the following system of equations:

$$\vec{S} = \vec{R}_0 + t\vec{V}. \tag{B.1}$$

Conceptually, this is similar to a linear regression of the form $y = b + ax$, but instead there are N equations and N unknowns, where N is determined by the number of dimensions in the vectors.

In the case where multiple reflections with the surface is possible (e.g. in the case of a light concentrator, or dual-mirror system), the following process is performed iteratively to completely track the ray's movement through the system.

1. Locate intersection point $P_i = [x_i, y_i, z_i]$ of a ray with incident direction $\vec{I}$ with surface $S(x, y, z)$ with normal $\hat{N}_S(x_i, y_i, z_i)$.

2. Reflect ray around $\hat{N}_S(x_i, y_i, z_i)$. For a ray $\vec{I}$ incident on a surface with a normal vector $\hat{N}$, the reflected ray $\vec{V}$ can be computed as

$$\vec{J} = \vec{I} - 2\hat{N}_S\left(\vec{I} \cdot \hat{N}_S\right). \tag{B.2}$$

3. Calculate intersection point based on new velocity and position. If no solution is found stop. Otherwise, repeat steps 1-3.

In the specific case of a Winston cone with entry radius a and exit radius a', where the cone's optic axis is the z-axis, the surface components S_i of the Winston cone is defined as

$$\begin{pmatrix} S_x \\ S_y \\ S_z \end{pmatrix} = \begin{pmatrix} \rho\cos\phi \\ \rho\sin\phi \\ z(\rho) \end{pmatrix} = \begin{pmatrix} \rho(x,y)\cos\phi \\ \rho(x,y)\sin\phi \\ z(\rho(x,y)) \end{pmatrix} \tag{B.3}$$

with $\rho \equiv \sqrt{x^2+y^2}$ is the standard radial component in a cylindrical coordinate system and ϕ is the polar around the z-axis. The function $z(\rho)$ is defined by the equation of a light cone:

which is valid over $a' \leq \rho \leq a$.

Thus, using these values as the surface of intersection in Equation B.1 the system of equations to solve is

$$\begin{pmatrix} \rho(x,y)\cos\phi \\ \rho(x,y)\sin\phi \\ z(\rho(x,y)) \end{pmatrix} = \begin{pmatrix} x_0 \\ y_0 \\ z_0 \end{pmatrix} + t \begin{pmatrix} v_x \\ v_y \\ v_z \end{pmatrix}. \tag{B.4}$$

The unknowns that must be solved for are x, y, and t: the first two allow for the z position to be calculated and t is the absolute distance from the ray's origin to the surface along the direction vector. Note that ϕ is not unknown as it can be calculated from x and y as follows:

$$\begin{aligned} 0; & \qquad x = y = 0 \\ \arctan(\frac{y}{x}); & \qquad x \geq 0 \\ -\arcsin(\frac{y}{\rho}) + \pi; & \qquad x < 0 \end{aligned} \tag{B.5}$$

When implementing the definition of ϕ in software, in a number of programming languages which contain functions that can return the correct value of θ given x and y (e.g. `atan2(y,x)` in $C/C{+}{+}$).

For the Winston cone, there are two different conditions for ceasing to follow the cone. First (the obvious one) is that the ray has a velocity vector that will take it through the exit aperture of the cone. Second, is if the ray has been reflected such that its direction vector has a positive z component. If $v_z > 0$, then the ray has begun to exit the light cone; this is how light cones work. All rays that enter the cone at angles greater than the cutoff angle defined by the geometry of the cone will be reflected back out again. For a demonstration of this see Figure B.1.

Note that *VERITAS* cones are not *true* light cones: they are in fact hexagonal to reduce dead space between PMTs and morph into traditional light cones at their exit aperture. The details of the light cones simulated in this thesis are listed below.

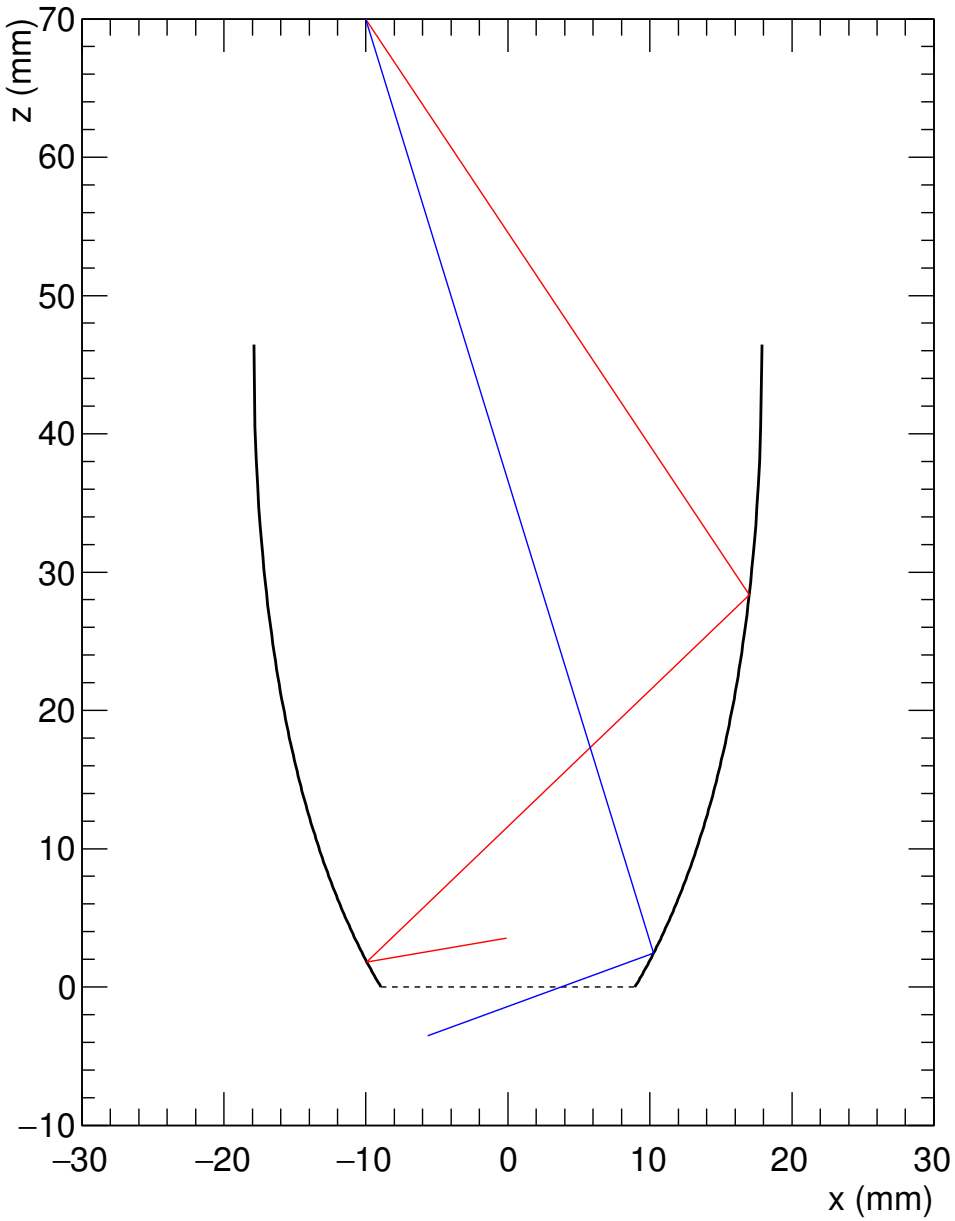

Figure B.1: Two rays from the same point of origin enter a Winston cone with angles above and below the cutoff angle. The blue ray with the shallow incoming angle $\theta < \theta_{\max}$ proceeds to exit the bottom of the cone after a single reflection. The red ray with angle $\theta > \theta_{\max}$ is rejected by the cone; it reflects several times before starting an upwards trajectory which will bring it back through the top of the cone.

- D_{out}: 17.9 mm. This is the size of the exit aperture of the *VERITAS* light cones.
- θ_{max}: 30°. This is the maximum photon arrival angle for photons reflecting off the dish. Note that this is slightly smaller than the acceptance of the *VERITAS* light cones which have an acceptance angle $\theta_V = \arcsin(17.9/31.4) = 34.75°$. This is consistent with ensuring that *all* the light from the dish is collected.
- D_{in}: 35.8 mm. This is slightly larger than the pixel-to-pixel spacing in the *VERITAS* camera but required in order to limit θ_{max} to 30°. Note that $D_{\text{in}} = 2a'$.

Appendix C

List of Acronyms

2FGL Second *Fermi*-LAT catalog

2LAC Second *Fermi* AGN Catalogue

3LAC Third *Fermi* AGN Catalogue

AGN active galactic nucleus

Az-El azimuth-elevation

BL Lac BL Lacertae

CFD constant fraction discriminator

CGRO Compton Gamma Ray Observatory

CPL curved power law

CR cosmic ray

CTA Cherenkov Telescope Array

d.c. digital counts

DAQ data acquisition system

EA effective area

EBL extragalactic background light

EC external inverse Compton

EM electromagnetic

FADC flash analog-to-digital converter

FoV field of view

FPGA field programmable gate array

FSRQ flat spectrum radio quasar

FWHM full width half maximum

GBM Gamma-ray Burst Monitor

GLAST Gamma-ray Large Area Space Telescope

GRBs gamma-ray bursts

HAWC High-Altitude Water Cherenkov Observatory

HESS High Energy Stereoscopic System

IACT imaging atmospheric Cherenkov technique

IRF instrument response function

LAT Large Area Telescope

LUT lookup table

MAGIC Major Atmospheric Gamma Imaging Cherenkov

MJD Modified Julian Date

NOM nominal

NSB night sky background

OSS optical support structure

p.e. photoelectron

PDE photon detection efficiency

PL power law

PLWC power law with cutoff

PMT photomultiplier tube

PSF point spread function

PWN pulsar wind nebula

QE quantum efficiency

RFB rate feedback

RHV reduced high voltage

ROI region of interest

S/N signal to noise

SED spectral energy distribution

SNR supernova remnants

SPE single photoelectron

SSC synchrotron self Compton

TD threshold discriminator

TOA time of arrival

UVF UV filter

VERITAS Very Energetic Radiation Imaging Telescope Array System

VHE very high energy

VPM *VERITAS* pointing monitor

ZCD zero crossing discriminator